SANS investigations of the flux line lattice in unconventional superconductors

Jonathan Stuart White

A thesis submitted to
The University of Birmingham
for the degree of
DOCTOR OF PHILOSOPHY

Condensed Matter Physics
School of Physics and Astronomy
The University of Birmingham
October 2009

ABSTRACT

Small-angle neutron scattering has been used to study the flux line lattice (FLL) in the d-wave superconductors $YBa_2Cu_3O_7$ and $CeCoIn_5$. Our studies on the High-T_c superconductor $YBa_2Cu_3O_7$ were carried out using a twin-free sample, and we present the *first* observations of the *intrinsic* FLL structure in this material, with a magnetic field applied parallel to the crystal **c**-axis ($H \parallel \mathbf{c}$). We observe a sequence of field-driven FLL structure transitions, the detailed physics of which can be broadly described in terms of field-induced non-locality, the potency of which is perhaps increased by the anisotropy of the order-parameter. The heavy-fermion superconductor $CeCoIn_5$ exhibits an exotic ground state that combines unconventional superconductivity with strong paramagnetism. With $H \parallel \mathbf{c}$, these properties contribute towards both a rich FLL structure phase diagram, and new behaviour of the FLL form factor. Most notably, we observe the form factor to increase with field, in strong contrast to the monotonic decrease expected from predictions made using more conventional theories. These results can be qualitatively described by calculations made within the framework of the quasiclassical Eilenberger theory, which indicate the increase in the form factor as due to field-induced Pauli paramagnetic effects which manifest most strongly within the flux line cores.

for Kathy and Mike White

ACKNOWLEDGEMENTS

First and foremost I would like to acknowledge my supervisor Ted Forgan, for all of the advice and support I have received over the last three years. I feel lucky to have experienced first-hand Ted's infectious enthusiasm for physics and research, and my lasting impressions are of a scientist who possesses a vast knowledge of physics, is a dedicated hands-on experimentalist, and is the master of the pun. I also wish to acknowledge the many opportunities Ted has generated for me to participate in both experiments and international conferences, which I feel has greatly enhanced my PhD experience.

I have had a fantastic time being a member of the Condensed Matter (CM) Group, and surrounded by people from whom I have learnt a great deal. I especially wish to acknowledge the other members of the Big Facilities Physics subgroup; Silvia Ramos for her good spirits, encouragement and advice, Mark Laver for the crash courses in flux line lattice physics, and providing somewhere nice for us to live during our final few months in Birmingham, Rich Lycett for his down to earth character, sense of humour, and for never providing a dull moment, and Charlotte Bowell for always be a good sounding board, and someone with which I have had many discussions on physics and The X Factor. I acknowledge Rich Heslop for always having something to talk about, often answering the questions on Life, the Universe and Everything during a single lunch break (even if the answers are different every day) and for the endless similes. Finally, I wish to acknowledge Elizabeth Blackburn, who epitomises the hard work, dedication and capacity required of a young physicist, and from whom I have learnt a lot about neutron scattering and how to stay positive in the face of no experimental signal.

I thank the rest of the CM Group for making my time in Birmingham so memorable. In particular, I acknowledge Chris Muirhead and Mark Colclough, both of

whom were involved at various stages of my studies, over my entire undergraduate and postgraduate period. I thank the other members of the group, including Suz Gildert, Jo Healey, Christian Schuppler, Dom Walliman and Phil Baker for providing a stimulating working environment, full of good humour and often bizarre conversation. I also acknowledge briefer interactions with the more recent arrivals, Georgina Klemencic, Josh Lim, Alistair Cameron and Alex Holmes.

I have had the pleasure to interact with scientists from many different places. In particular, I have especially enjoyed working with Morten Eskildsen, who combines refreshingly honest views with a sharp insight and a cutting sense of humour. I greatly benefited from working with Morten's graduate students, firstly Lisa DeBeer-Schmitt, and more recently Pinaki Das, in trying to make sure we all understood what was happening in $CeCoIn_5$. I further benefited from working with Andrea Bianchi, Michel Kenzelmann, Jorge Gavilano, Joel Mesot, Simon Gerber and Nikola Egetenmeyer. A special mention goes to Markus Zolliker, who is far more indispensable to the success of the $CeCoIn_5$ experiments than he thinks. I thank Vladimir Hinkov for his enthusiastic participation in the experiments on $YBa_2Cu_3O_7$, and for a tutorial on crystallographic twinning. From the ILL, I acknowledge Bob Cubitt for the sound effects, and Charles Dewhurst for keeping my feet on the ground; 'Jonny, you're an idiot..'

Finally, I wish to thank the people behind the scenes who in so many ways have made this thesis possible. I give massive thanks to my Mum and Dad for always being there for me, and offering their guidance and support for any decision I have made. It is to them that this thesis is dedicated. I also thank Liz, Rob and my grandparents for their support, and with who I feel lucky to have such a close family. Last, but by no means least, I say a big thank you to my wonderful girlfriend Christel, who has provided me with unquestioning support, strong motivation and a lot of love over the last two years, all of which were vital in helping me to finish this thesis.

Contents

List of Figures

List of Tables

Introduction and theory

The clearest distinction between the two classes of superconductor, type-I and type-II, is seen on observing their behaviour under an applied magnetic field. Figure 1.1 shows the ideal bulk magnetisation curves for both types, and the intrinsically different behaviour. In type-I superconductors the magnetisation curve is characterised by the Meissner effect. This describes the almost complete expulsion of internal fields from the bulk of the superconductor, barring a surface depth of characteristic dimension λ_L, which is the London penetration depth. As $\mathbf{B} = \mu_0(\mathbf{M}+\mathbf{H})$, and $\mathbf{B} = 0$ inside the bulk, the magnetisation follows $\mathbf{M} = -\mathbf{H}$ for all fields less than the thermodynamic critical field, H_c. On increasing the field beyond H_c, the ideal system undergoes a first-order transition into the normal state, as there is a finite latent heat. In the absence of an external field, there is no latent heat, and so on increasing the temperature, the transition to the normal state is second-order.

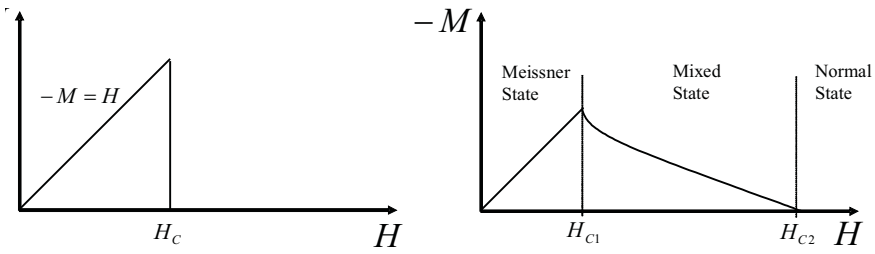

Figure 1.1: The ideal bulk magnetisation versus applied field curves for (a) a type-I superconductor and (b) a type-II superconductor.

Type-II superconductors possess two characteristic critical fields, the lower critical field, H_{c1} and the upper critical field, H_{c2}. Below H_{c1}, the sample exhibits the full Meissner state and behaves as if it were a type-I material. On increasing the field beyond H_{c1} the system becomes unstable to the admission of magnetic flux into the bulk, and the magnetisation increases as more flux enters with increasing field. The magnetisation becomes zero on passing through H_{c2}, where there is typically a second-order transition into the normal state.

The region between H_{c1} and H_{c2} is a distinct thermodynamic phase called the mixed state. In this phase, there is a more delicate balance between a lowering of the system free energy on admission of magnetic flux, and an increase due to a reduction in the condensation energy. This energy balance results in magnetic flux being partially admitted into the bulk of the superconductor in the form of magnetic flux lines; a phenomenon first predicted to occur by Abrikosov (1957). Each flux line carries a total flux of one magnetic flux quantum, $\Phi_0 = h/2e$, that mostly exists within a core region where the superconductivity is suppressed. In the ideal and isotropic situation, the flux lines arrange under the propensity of their own interaction into a regular hexagonal flux line lattice (FLL). However, in anisotropic materials, it is well known that a lower free energy is often associated with a FLL coordination that deviates from this ideal. This is one example where observations of the FLL allow an examination of the physics of the host material; a key theme of the studies presented here.

1.1 London theory

The London equations (London and London, 1935) provided the first phenomenological electrodynamic description of the superconducting state, consistent with the observations of perfect conductivity (Onnes, 1911) and the Meissner effect (Meissner and Ochsenfeld, 1933). From the quantum mechanical perspective, the canonical momentum of a superconducting particle of velocity $\mathbf{v}_s$, mass $\hat{m}$ and electric

charge $\hat{e}$ [1] can be written as

$$\mathbf{p} = \hat{m}\mathbf{v}_s + \hat{e}\mathbf{A} \tag{1.1}$$

where **A** is the vector potential. In the absence of an applied field, it is expected that in the ground state the particle will have zero momentum, and the current density can be written as

$$\mathbf{j}_s = n_s\hat{e}\langle\mathbf{v}_s\rangle = -\frac{n_s\hat{e}^2}{\hat{m}}\mathbf{A} \tag{1.2}$$

where $\langle\mathbf{v}_s\rangle$ is the average velocity, and n_s is the superconducting particle density. This is the London equation, and is only true if we assume that the ground state is somewhat rigid to the perturbation of a finite external field, such that $\langle\mathbf{p}\rangle = 0$. This condition is achieved by specifying the gauge to be $\nabla \cdot \mathbf{A} = 0$ (the London gauge), so that on substitution into equation 1.2, $\nabla \cdot \mathbf{j}_s = 0$ due to continuity. On taking the time-derivative of equation 1.2 we find the first London equation which implies persistent current flow,

$$\mathbf{E} = \frac{\hat{m}}{n_s\hat{e}^2}\frac{\mathrm{d}\mathbf{j}_s}{\mathrm{d}t} \tag{1.3}$$

where **E** is the electric field. On taking the curl of equation 1.2, we obtain the second London equation

$$\nabla^2\mathbf{B} = \frac{1}{\lambda_L^2}\mathbf{B} \tag{1.4}$$

where **B** denotes the internal field, and we have introduced the London penetration depth length-scale $\lambda_L = \sqrt{\hat{m}/\mu_0 n_s\hat{e}^2}$. The solutions to this equation show that for time-varying and time-independent magnetic fields applied parallel to a superconducting surface, the field normal to the surface will decay exponentially over the length λ_L.

The London equations embody empirical limiting approximations to a classical electrodynamic theory. As a consequence, it is not possible to use them to predict the existence of the FLL, which represents an emergent quantum phenomenon on the macroscopic scale. Despite this, the London theory is relevant for materials where $\lambda_L \gg \xi$, where ξ is the characteristic size of the flux line core. These are

[1] The 'hat' symbols for both the mass and charge of the superconducting particle indicate that the values of these variables are not simply those expected for a single electron.

strongly type-II superconductors, and as the subject materials of this thesis fall into this category, it is useful to consider the description of the FLL within this London limit. For a single flux line at the origin, we insert the flux line by hand using a δ-function source term

$$\lambda_L^2 \nabla^2 \mathbf{B} - \mathbf{B} = \Phi_0 \hat{\mathbf{z}} \delta^{(2)}(\mathbf{r}). \tag{1.5}$$

Here, $\delta^{(2)}$ is a two-dimensional delta function describing the position of the flux line in the plane perpendicular to the unit vector $\hat{\mathbf{z}}$, which is parallel to the axis of the flux line. The exact solution of equation 1.5 gives the spatial variation of the magnetic field for a single flux line as

$$B_z(r) = \frac{\Phi_0}{2\pi\lambda_L^2} K_0\left(\frac{r}{\lambda_L}\right) \tag{1.6}$$

where r is the radial distance from the singularity and K_0 is the zeroth order modified Bessel function. For small x, $K_0(x) \sim -\ln x$, whilst for large x, $K_0(x) \sim (\pi/2x)^{(1/2)}\mathrm{e}^{-x}$ yielding

$$B_z(r) = \begin{cases} \frac{\Phi_0}{2\pi\lambda_L^2} \ln\left(\frac{\lambda_L}{r}\right) & r \ll \lambda_L \\ \frac{\Phi_0}{2\pi\lambda_L^2}\sqrt{\frac{\pi\lambda_L}{2r}} \exp\left(-r/\lambda_L\right) & r \gg \lambda_L \end{cases}. \tag{1.7}$$

We see that far from the flux line core, the field distribution takes on a form consistent with the solutions of equation 1.4. The solution at small distances assumes the flux line core to be infinitesimally narrow, in accordance with the δ function source term. This means that on the approach to the flux line axis, an integral evaluation of the flux line free energy $\mathcal{F}$ (Ketterson and Song, 1999),

$$\mathcal{F} = \frac{1}{2\mu_0} \int \left[B^2 + \lambda_L^2 \left(\nabla \times \mathbf{B}\left(\mathbf{r}\right)\right)^2\right] \mathrm{d}^3\mathbf{r} \tag{1.8}$$

is logarithmically divergent, which reflects the divergence of the field as $r \to 0$ [2]. This indicates that the rough approximations of the London model do not allow an accurate evaluation of the free energy. In reality, sustaining divergent fields requires increasingly large supercurrents, which when large enough will increase the free energy by exciting quasiparticles out of the condensate. In order to reduce the

[2] The term in square brackets is equivalent to the left hand side of equation 1.5.

free energy penalty of a divergent field, the flux contained within the core is spread over a finite area. However, the divergence of the integral reflects the inherent assumption of the London theory; that the supercurrent density $\mathbf{j}_s$ at a point $\mathbf{r}$ yields the vector potential $\mathbf{A}$ at the same point. This relationship is embodied in equation 1.2, and represents the local limit. In general, this relationship is only achieved for the extreme type-II material, where the core-size is negligible compared to the penetration depth λ_L, i.e. the original London assumption. For more realistic type-II materials, the core exhibits a finite size, and the supercurrent density and magnetic vector potential enjoy a *non-local* relationship (see section 1.1.2).

In the London limit however, the London model can still provide a useful description of the FLL, and a reference for beginning to understand experimental observations. Extending equation 1.5 to describe an ideal FLL we obtain

$$\lambda_L^2 \nabla^2 \mathbf{B} + \mathbf{B} = \Phi_0 \hat{\mathbf{z}} \sum_i \delta^{(2)}(\mathbf{r} - \mathbf{r}_i) \tag{1.9}$$

with the positional sum being taken over *i* flux lines. By definition, the lattice implies periodicity such that the internal field distribution is position dependent and $\mathbf{B}(\mathbf{r})$ can be expanded as a Fourier series,

$$\mathbf{B}(\mathbf{r}) = \sum_{\mathbf{G}} \mathbf{B}_{\mathbf{G}} e^{i\mathbf{G}\cdot\mathbf{r}} \tag{1.10}$$

where $\mathbf{G}$ represents the reciprocal lattice vector derived from the real space arrangement of the flux lines, and $\mathbf{B}_{\mathbf{G}}$ are the Fourier coefficients. Substituting equation 1.10 into equation 1.9 and integrating over the unit cell, yields the expression for the Fourier coefficients,

$$\mathbf{B}_{\mathbf{G}} = \frac{\Phi_0 n_L}{1 + \lambda_L^2 \mathbf{G}^2} = \frac{\langle B \rangle}{1 + \lambda_L^2 \mathbf{G}^2} \tag{1.11}$$

where n_L is the areal density of vortices, which multiplied by Φ_0 gives the mean induction, $\langle B \rangle$. The Fourier coefficients can be measured experimentally, allowing direct access to a measure of λ_L.

1.1.1 Anisotropic London theory

The London theory outlined in the previous subsection can be extended to allow for an effective mass anisotropy whilst leaving the integral evaluation of the free energy invariant. This is achieved by generalising the effective mass term $\hat{m}(\propto m^*)$ in the expression for λ_L, and substituting it with the normalised effective mass tensor m_{ij} (Kogan, 1981)

$$\mathcal{F} = \frac{1}{2\mu_0} \int \left[B^2 + \lambda_L^2 m_{ij} \left(\nabla_i \times \mathbf{B} \right) \left(\nabla_j \times \mathbf{B} \right) \right] \mathrm{d}^3\mathbf{r} \tag{1.12}$$

where the effective mass term in λ_L is replaced by a geometric mean mass, $\overline{m}$. If the principal directions of the mass tensor are chosen to coincide with the crystal axes, the normalised effective mass tensor is diagonal with components $m_{xx} = m_a/\overline{m}$, $m_{yy} = m_b/\overline{m}$ and $m_{zz} = m_c/\overline{m}$. Hence, for normalising the effective mass tensor, $\overline{m}^3 = m_a m_b m_c$.

For fields parallel to $\hat{\mathbf{z}}$, an inequality in m_a and m_b indicates a penetration depth anisotropy, and the FLL structure distorts along the direction of longest penetration depth. In this thesis, we define the penetration depth as $\lambda_i \propto \sqrt{m_i^*}$, where currents along i screen against fields that vary along the j or k directions. For example λ_a screens field variations along the **b**-direction. Figure 1.2 provides a visualisation of this structural distortion, the measure of which is encapsulated by the measurable parameter $\gamma_{ab} = \lambda_a/\lambda_b$. For $\gamma_{ab} = 1$ (figure 1.2 (a)), the hexagonal FLL structure is isotropic and the flux line distribution can be overlaid by a circle. For $\gamma_{ab} \neq 1$, the FLL coordination is subject to a scale transformation of $\left(\sqrt{\gamma_{ab}}\right)^{-1}$ along **a** and $\sqrt{\gamma_{ab}}$ along **b** (Thiemann et al., 1989). In figure 1.2 (b) we show the scale transformation for $\gamma_{ab} = 1.5$, where the flux line distribution can be overlaid by an ellipse.

In the diagonal situation, where the effective mass components of the flux line frame are co-incident with the crystal frame, the diagrams shown in figure 1.2 are somewhat misleading as they imply there is a preferred FLL orientation. As the distorted FLL can always be mapped back to the isotropic FLL by a scale transformation, any flux line distribution around the circle or ellipse that represents a valid hexagonal FLL coordination is energetically equivalent (Campbell et al., 1988). It

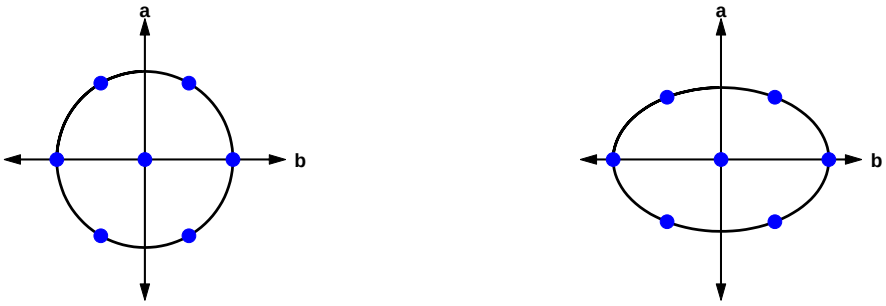

(a) $\gamma_{ab} = 1$ (b) $\gamma_{ab} = 1.5$

Figure 1.2: Schematic real-space depictions of a hexagonal FLL structure for (a) $\gamma_{ab} = 1$ and (b) $\gamma_{ab} = 1.5$ in the London regime. The blue spots represent flux lines, and we show enough nearest neighbours to capture the hexagonal symmetry. In (b), the FLL structure is distorted along the direction of longest penetration depth, which is λ_b.

is worth noting that within the local London theory presented here, there is no preferred orientation for the FLL. However, when the field is applied at an arbitrary angle to the crystal frame of a uniaxial material, by taking higher order terms into account Campbell et al. (1988) were able to show that the London theory does make a prediction as to the preferred alignment of the FLL. In this case, the FLL is predicted to align such that the flux line nearest neighbour direction is perpendicular to the axis of rotation.

1.1.2 Non-local London theory

The London theory outlined above is a local theory; the supercurrent density $\mathbf{j}_s(\mathbf{r})$ is proportional to $\mathbf{A}(\mathbf{r})$ at any point $\mathbf{r}$. However, Pippard (1953) proposed that from a more general perspective, the supercurrent density and the magnetic vector potential enjoy a non-local relationship. Pippard proposed an integral relation, whereby the value of $\mathbf{j}_s$ at $\mathbf{r}$ is determined by contributions due to $\mathbf{A}$ within a volume of dimension ξ_0 centred on $\mathbf{r}$. This characteristic dimension ξ_0, referred to as the Pippard coherence length, was later shown to be of the same order as the

spatial dimension of the supercarriers in the complete microscopic theory of superconductivity (Bardeen et al., 1957). If the value of $\mathbf{A}(\mathbf{r})$ varies from its full value over this volume, for example as would happen in the vicinity of a flux line core, the supercurrent response is weaker. This results in an enhanced penetration of the field over a distance larger than λ_L expected from the local London theory. For the case where $\lambda_L < \xi_0$, $\mathbf{A}(\mathbf{r})$ can vary rapidly over a distance less than ξ_0. This is the situation for type-I superconductors, and superconductors that are only just type-II ($\lambda_L \sim \xi_0$), for which it is always necessary to consider non-local corrections. For strongly type-II superconductors, where $\lambda_L \gg \xi_0$, the non-local corrections become less important, and vanish for the case $\lambda_L/\xi_0 \rightarrow \infty$, where the local London limit is recovered.

However, even for strongly type-II superconductors, where λ_L/ξ_0 is large, the theoretical work carried out by Kogan and collaborators (Kogan et al., 1996, 1997a,b) predict non-local corrections to the London equations to have consequences for the FLL coordination. By considering an isotropic superconductor, they derive the London equation from the microscopic viewpoint of the Eilenberger equations (Eilenberger, 1968), which provide a quasiclassical description (see section 1.5.1) of the microscopic theory outlined in section 1.3. On making a leading order expansion of the integral kernel, in reciprocal space the general form of the London equation becomes

$$\mu_0 j_i = -\lambda^{-2} \left(m_{ij}^{-1} - \lambda^2 n_{ijlm} \mathbf{G}_l \mathbf{G}_m \right) a_j \tag{1.13}$$

where the vector potential is encapsulated by $\mathbf{a} = \mathbf{A} + \Phi_0 \nabla\theta/2\pi$, with Φ_0 the flux quantum, and θ the phase of the microscopic order parameter. m_{ij} is the normalised inverse mass tensor and λ the geometrically averaged penetration depth $= (\lambda_a \lambda_b \lambda_c)^{1/3}$. The power of the non-local theory lies in the term dependent on the fourth rank tensor n_{ijlm}, which couples the supercurrents of the FLL to microscopic properties of the Fermi surface according to

$$n_{ijlm} = \frac{\hbar^2 \langle v_i v_j v_l v_m \rangle \gamma\left(T, \tau\right)}{4\Delta_0^2 \lambda^2 \mathrm{det} \langle v_i v_j \rangle^{1/3}} \tag{1.14}$$

where i is the ith component of the Fermi velocity, γ is a temperature-dependent

factor dependent on impurity scattering and the size of the energy gap Δ_0 (see section 1.3) and brackets$\langle \ldots \rangle$ indicate an angular average over the Fermi surface. We see that the size of the tensor depends on the fourth moment of the Fermi velocity which couples any crystal anisotropy into the properties of the FLL. This tensor coupling results in a preferred orientation of the FLL for any field orientation.

To determine the preferred orientation of the FLL, equation 1.13 is used to evaluate the Fourier components of the field distribution for a particular FLL coordination. Using these Fourier components, the free energy density is then numerically computed, with the preferred FLL coordination that which gives the free energy minimum, $\mathcal{F}_m$. For the case where the field is applied perpendicular to a fourfold crystal plane (Kogan et al., 1997a), the free energy density is calculated according to

$$\mathcal{F} = \frac{B^2}{2\mu_0} \sum_{\mathbf{G}} \frac{1}{1 + \lambda^2 \mathbf{G} + \lambda^4 \left(n_2 \mathbf{G}^4 + (2n_1 - 6n_2)\, \mathbf{G}_1^2 \mathbf{G}_2^2 \right)} \tag{1.15}$$

where the degree of Fermi surface anisotropy that can affect $\mathcal{F}_m$ is included in the term involving $\mathbf{G}_1^2 \mathbf{G}_2^2$. Here, $n_1 \propto \langle v_1^4 \rangle \equiv \langle v_2^4 \rangle$, and $n_2 \propto \langle v_1^2 v_2^2 \rangle$. Figure 1.3 show the predictions of calculations made by Kogan et al. (1997a) relevant for both the cases of field perpendicular to a fourfold symmetry plane, and field perpendicular to a twofold symmetry plane of the borocarbide superconductor $LuNi_2B_2C$ (Kogan et al., 1997a). At each field, the possible shape of the FLL primitive cell is describable in terms of two basis vectors, separated by an angle β. Kogan et al. (1997a) vary β and find the coordination that gives the $\mathcal{F}_m$ at each field. From the figure, we see that for the case of field perpendicular to a fourfold plane, on increasing the field there is a first-order 45° reorientation transition of the FLL primitive cell at H_1, before the FLL structure stabilises into a square FLL structure at field H_2. Note the nearest neighbour directions of this square phase are aligned along the directions corresponding to the Fermi velocity minima. For the twofold situation, no reorientation transitions are predicted to occur, though at high enough fields the FLL structure is predicted to stabilise at a certain β. This theory has been successful in describing the observed behaviour in YNi_2B_2C (Paul et al., 1998) and to some

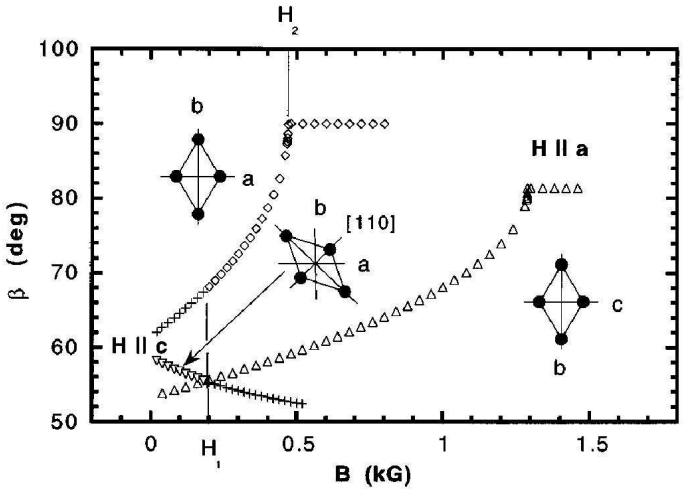

Figure 1.3: Calculations of the field-dependence of the preferred FLL structure for the cases of fields perpendicular to both fourfold ($H \parallel \mathbf{c}$) and twofold ($H \parallel \mathbf{a}$) symmetry planes. The angle β is that which lies between the two basis vectors of the FLL primitive cell. After Kogan et al. (1997a).

extent that seen in cubic V_3Si (Yethiraj et al., 1999).

1.2 Ginzburg-Landau theory

The Ginzburg-Landau (GL) theory is also a phenomenological description of superconductivity. However, unlike the London description, GL theory is based on a thermodynamic description of the superconducting state, with a judiciously chosen complex order parameter that describes the collective behaviour of the supercarriers. Here, we follow the treatments of Ketterson and Song (1999) and Annett (2004).

The GL theory builds on Landau's theory of the second-order phase transition. This theory introduces the concept of an order parameter which, above a certain critical temperature, T_c is zero, but is finite below this temperature. As the order parameter varies continuously from zero as one goes below T_c, this allows the expansion of the free energy in terms of a power series of the order parameter. Ginzburg and Landau developed their idea that within this theoretical framework, an order parameter might describe the superconducting state, thus incorporating their assumption that superconductivity can be defined by an all-encompassing and

coherent macroscopic quantum state. They chose the order parameter to be a spatially variant and complex quantum wavefunction, $\psi(\mathbf{r})$. As the wavefunction is a complex entity, only even power terms enter the expansion for the free energy density

$$F = F(T) + \alpha(T)|\psi(\mathbf{r})|^2 + \frac{\beta}{2}|\psi(\mathbf{r})|^4 + \dots \tag{1.16}$$

The free energy density for both the cases of above T_c, where $\psi = 0$ and below T_c where $|\psi| > 0$, can be minimised by giving the constant α a temperature dependence such that it changes sign on passing through T_c. In the simplest case, we leave β as a constant. Thus if

$$\alpha(T) = a(T - T_c) \tag{1.17}$$

then on minimising equation 1.16 we find

$$|\psi(\mathbf{r})| = \begin{cases} 0 & T > T_c \\ \sqrt{\frac{a(T_c - T)}{\beta}} & T < T_c \end{cases} \tag{1.18}$$

Equation 1.16 does not provide a complete picture of a truly spatially dependent order parameter, as spatial deformations will cause an increase in the free energy density. The ability to account for this spatial variance of $\psi(\mathbf{r})$, and its associated energy cost, is an inherent strength of the GL theory, and its ultimate ability to predict the emergence of the FLL. To account for an inhomogeneous order parameter, a gradient energy term is incorporated, the form of which is directly analogous to the kinetic energy term of the Hamiltonian describing the interaction between charged particles and an electromagnetic field. With **A** being the magnetic vector potential, this term takes the form

$$\frac{\hbar^2}{2\hat{m}}|\nabla\psi(\mathbf{r})|^2 = \frac{\hbar^2}{2\hat{m}}\left|\left(\nabla - \frac{i\hat{e}\mathbf{A}}{\hbar}\right)\psi(\mathbf{r})\right|^2 \tag{1.19}$$

such that the total free energy density, including the magnetic field energy, to fourth order is now written as

$$F = F(T) + \frac{\mathbf{B}^2}{2\mu_0} + \alpha(T)|\psi(\mathbf{r})|^2 + \frac{\beta}{2}|\psi(\mathbf{r})|^4 + \frac{\hbar^2}{2\hat{m}}\left|\left(\nabla - \frac{i\hat{e}\mathbf{A}}{\hbar}\right)\psi(\mathbf{r})\right|^2. \tag{1.20}$$

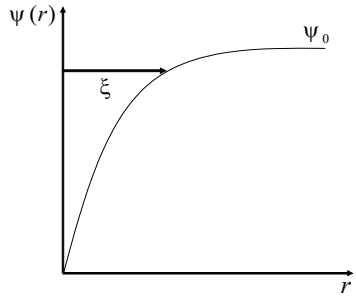

Figure 1.4: A depiction of the shortest distance r over which the order parameter can deform from *nearly* its bulk value ψ_0 to zero. The distance over which this occurs is of the order ξ.

The minimisation of equation 1.20 is achieved by performing a functional differentiation and minimising with respect to $\psi(\mathbf{r})$ and $\psi^*(\mathbf{r})$. This yields the first Ginzburg-Landau equation

$$-\frac{\hbar^2}{2\hat{m}}\left(\nabla - \frac{i\hat{e}\mathbf{A}}{\hbar}\right)^2 \psi(\mathbf{r}) + \alpha(T)\psi(\mathbf{r}) + \beta|\psi(\mathbf{r})|^2\psi(\mathbf{r}) = 0. \tag{1.21}$$

On considering the supercurrents due to the magnetic field, and again taking the functional derivative of the free energy but this time with respect to the magnetic vector potential, we obtain the second Ginzburg-Landau equation

$$\mathbf{j}_s = -\frac{i\hat{e}\hbar}{2\hat{m}}\left(\psi^*(\mathbf{r})\nabla\psi(\mathbf{r}) - \psi(\mathbf{r})\nabla\psi^*(\mathbf{r})\right) - \frac{\hat{e}^2}{\hat{m}}|\psi(\mathbf{r})|^2\mathbf{A}. \tag{1.22}$$

Equations 1.21 and 1.22 can be used to provide definitions of the Ginzburg-Landau length scales. On solving the one-dimensional form of equation 1.21, and in the absence of an electromagnetic field, the Ginzburg-Landau coherence length is obtained and defined as

$$\xi(T) = \sqrt{\frac{\hbar^2}{2\hat{m}|\alpha(T)|}} \tag{1.23}$$

which can be physically interpreted as the shortest distance over which the order parameter can deform from nearly the bulk value to zero. This is shown schematically in figure 1.4. We note that the GL coherence length is a related, but still distinct, quantity to the Pippard coherence length, ξ_0 which is essentially temperature independent (Pippard, 1953). Well away from T_c for clean materials, it turns out that $\xi(T) \sim \xi_0$, but near to T_c they will be different as $\xi(T)$ diverges due to the temperature-dependence of $\alpha(T)$.

The second GL length-scale is obtained from equation 1.22. In the limit close to T_c, the first two terms of the left hand side of the equation do not contribute, and the remainder is equivalent to the local London relation

$$\mathbf{j}_s = -\frac{\hat{e}^2}{\hat{m}}|\psi(\mathbf{r})|^2\mathbf{A}. \tag{1.24}$$

where we identify $|\psi(\mathbf{r})|^2$ as equivalent to n_s, the density of superconducting carriers. This observation is further suggestive that the complex order parameter provides a description of the superconducting state. Thus if

$$n_s = |\psi(\mathbf{r})|^2 = \frac{\alpha(T)}{\beta}, \tag{1.25}$$

the GL penetration depth, $\lambda(T)$ is given by

$$\lambda(T) = \sqrt{\frac{\hat{m}\beta}{\mu_0\hat{e}^2\alpha(T)}} \tag{1.26}$$

which exhibits the same form as the London penetration depth derived earlier, and the same temperature-dependence as $\xi(T)$. We further see that within the GL theory, the dimensionless ratio

$$\kappa = \frac{\lambda(T)}{\xi(T)} \tag{1.27}$$

is temperature independent.

1.2.1 The first Ginzburg-Landau equation and the Abrikosov solution

For most type-II superconductors, the transition between the normal and superconducting states is second-order. Therefore, we can assume that the GL order-parameter ψ is small just below H_{c2}, and zero at H_{c2}. If we are infinitesimally below H_{c2}, then as ψ is small we can drop the cubic $|\psi(\mathbf{r})|^2\psi(\mathbf{r})$ term, and linearise the first GL equation. For fields $\mathbf{B} = (0, 0, B)$ and choosing the Landau gauge $\mathbf{A} = (0, Bx, 0)$, the first GL equation becomes

$$\left(-\frac{\hbar^2}{2\hat{m}}\nabla^2 - \hbar\omega_c ix\frac{\partial}{\partial y} + \frac{\hat{m}\omega_c^2}{2}x^2\right)\psi(\mathbf{r}) = |a|\psi(\mathbf{r}) \tag{1.28}$$

where ω_c is the cyclotron frequency $\omega_c = \hat{e}B/\hat{m}$. Equation 1.28 is equivalent to the Schrödinger equation for a charged particle in a magnetic field, and has Landau

level solutions for the allowed energy eigenvalues. The trial function of the form $\psi(\mathbf{r}) = \exp(i(k_y y + k_z z))\, f(x)$, which describes the plane wave combinations along y and z and some unknown $f(x)$, can be substituted into equation 1.28 to obtain

$$-\frac{\hbar^2}{2\hat{m}}\frac{\mathrm{d}^2 f}{\mathrm{d}x^2} + \frac{\hat{m}\omega_c^2}{2}\left(x + \frac{\hbar k_y}{\hat{m}\omega_c}\right)^2 f = \left(|a| - \frac{\hbar^2 k_z^2}{2\hat{m}}\right) f. \tag{1.29}$$

Equation 1.29 has the form of the Schrödinger equation for a simple harmonic oscillator (SHO), with energy eigenvalues

$$\left(n + \frac{1}{2}\right)\hbar\omega_c + \frac{\hbar^2 k_z^2}{2\hat{m}} = |a|, \tag{1.30}$$

thus showing $f(x)$ to have the form of the wavefunction for the SHO. The lowest Landau level solution will have $n = 0$ and $k_z = 0$, which on substituting back in the cyclotron frequency ω_c can be used to find the upper critical field

$$\mu_0 H_{c2} = B_{c2} = \frac{\Phi_0}{2\pi\xi^2(T)}; \tag{1.31}$$

a result that implies the existence of one flux quantum Φ_0 per unit area $2\pi\xi^2(T)$. This result also can be used to identify the difference between the type-I and type-II superconductors within the GL theory. Equation 1.16 can be solved in order to express the condensation energy of the superconductor as $\mu_0 H_c/2 = \alpha^2/2\beta$, (where H_c is the thermodynamic critical field) and by direct substitution with equation 1.31 show that

$$H_{c2} = \sqrt{2}\kappa H_c. \tag{1.32}$$

Therefore, for $\kappa > 1/\sqrt{2}$, $H_{c2} > H_c$ and the order parameter grows continuously from zero at fields just below H_{c2}. This is characteristic for the type-II superconductor. Conversely for type-I materials, $\kappa > 1/\sqrt{2}$, $H_{c2} < H_c$ and there is a discontinuity in the order parameter at the thermodynamic critical field.

The examination of equation 1.21 a little further below H_{c2} was first carried out by Abrikosov (1957) for a type-II material. Now the cubic term $|\psi(\mathbf{r})|^2\psi(\mathbf{r})$ can now no longer be neglected and the non-linear equation becomes more difficult to solve. However, based on the SHO form of the solution to the linearised version

of equation 1.21, Abrikosov expected the form of the solution to the non-linear equation to resemble this, and that only the lowest Landau level ($n = 0$ and $k_z = 0$) solutions would be significant. In this lowest Landau level approximation, the trial function now becomes

$$\psi(\mathbf{r}) = C\mathrm{e}^{(i(k_y y))}\mathrm{e}^{-(x-x_0)/\xi(T)^2} \tag{1.33}$$

where C is a normalisation constant that vanishes at H_{c2}, x_0 is the shift in the lowest Landau level and is equal to $-\hbar k_y/m\omega_c$, and we use the fact that the ground state SHO wavefunction has a gaussian form, with a width which happens to be of order the GL coherence length $\xi(T)$. However, this form of $\psi(\mathbf{r})$ is highly degenerate as there are an infinite number of possible k_y values. Abrikosov circumvented this by looking for a solution that was periodic in y with period l_y, such that the possible k_y values were limited to $k_y = 2\pi n/l_y$, with n any integer. By correcting the Landau level shift for this periodicity condition, $x_0 = -2\pi\hbar n/m\omega_c l_y = -\Phi_0 n/Bl_y$, the trial function becomes

$$\psi(\mathbf{r}) = \sum_{n=-\infty,\infty} C_n\mathrm{e}^{i(2\pi n y/l_y)}\mathrm{e}^{-(x+n\Phi_0/Bl_y)/\xi(T)^2} \tag{1.34}$$

where C_n are a series of parameters that can be chosen to minimise the free energy of the system. The form of the solution shown in equation 1.34 is periodic in y but not definitively periodic in x. Periodicity in x can be generated by enforcing the periodicity condition $C_{n+\nu} = C_n$, for integer ν, where the period $l_x = \nu\Phi_0/Bl_y$. For the simple square arrangement $\nu = 1$, whilst $\nu = 2$ for the simple hexagonal lattice. These periodicity conditions in the wavefunction correspond to the nucleation of the FLL close to H_{c2}, with a single flux quantum per unit cell.

Abrikosov (1957) used the trial function to perturbatively solve the first GL equation for the square lattice. The resulting free energy density for the Abrikosov FLL can be written as (Ketterson and Song, 1999)

$$\mathcal{F} = \mathcal{F}_0 + \frac{1}{2\mu_0}\left(B^2 - \frac{(B-\mu_0 H_{c2})^2}{1+\beta_A(2\kappa^2-1)}\right) \tag{1.35}$$

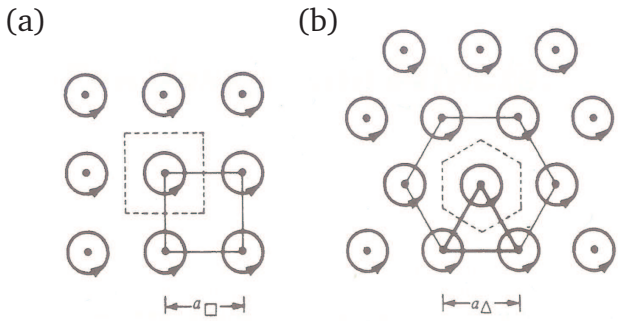

Figure 1.5: Schematics of the (a) square and (b) hexagonal Abrikosov FLL coordinations with the lattice parameters indicated. The dashed lines represent the FLL primitive cells. Adapted after (Ketterson and Song, 1999).

where the value of the Abrikosov parameter β_A, which is evaluated using values of C_n and k that minimise it, is calculated to be 1.16 (Kleiner et al., 1964) for the hexagonal coordination, and 1.18 (Abrikosov, 1957) for the square coordination. Therefore, the square lattice is of slightly higher free energy than the hexagonal lattice coordination (Kleiner et al., 1964). However, as the free energy difference between the two types of lattice is only ∼2%, even a weak anisotropy in the system will lead to the establishment of lattice shapes other than the isotropic hexagon. Schematic diagrams of the hexagonal and square coordinations are shown in figure 1.5.

Finally, Brandt (1995) examined the solutions to the GL equations close to T_c, providing a prediction of the field-dependence of the FLL form factor on the approach to T_c. Valid for any value of $\kappa > 1/\sqrt{2}$, the FLL form factor for a $\{h, k\}$ Bragg reflection of the reciprocal FLL is given by

$$F_{hk} = \frac{(-1)^\nu \mathrm{e}^{-\pi\nu/\sqrt{3}}\,(B - B_{c2})}{1 + 1.16\,(2\kappa^2 - 1)} \qquad \text{where} \qquad \nu = \left(h^2 + hk + k^2\right). \tag{1.36}$$

Thus within the Abrikosov model, the FLL form factor falls linearly to zero on the approach to T_c, a prediction strongly supported by small-angle neutron scattering measurements of the form factor close to T_c in elemental Nb (Forgan et al., 2002).

1.2.2 The Clem model

The inherent limitation of the London theory is that the field is predicted to diverge on the approach to the flux line axis. In an effort to the correct the London model for this unphysical effect, Clem (1975) solved the second GL equation for a *single* flux line using a variational approach. Within a cylindrical coordinate system where $\rho = (x^2 + y^2)^{1/2}$, $\phi = \tan^{-1}(y/x)$ and z, and with field parallel to z, Clem starts from the second GL equation, which is written as

$$j_\phi = -\mu_0 \lambda^{-2} \left(a_\phi - \frac{\Phi_0}{2\pi\rho} \right) f^2. \tag{1.37}$$

Here, j_ϕ and a_ϕ are respectively the supercurrent density and magnetic vector potential along unit vector $\hat{\phi}$, with the vector potential satisfying both the requirements of the London gauge, and that it vanishes at the flux line axis. ρ is the radial coordinate, and f represents a radial variation of the order parameter ψ,

$$\psi(\rho) = f(\rho) \exp(-i\phi) = \left(\frac{\rho}{R} \right) \exp(-i\phi). \tag{1.38}$$

where $R = (\rho^2 + \xi_\nu^2)^{1/2}$. ξ_ν is a variational parameter which is related to ξ_{GL}, and which Clem shows gives the form of ψ closest to the form of the GL solution that minimises the GL free energy. The later numerical solutions of the GL equations proposed by Brandt (1997) show that Clem's approximation is indeed close, thus indicating the validity of this approach. Using $\mathbf{B} = \nabla \times \mathbf{A}$ and Maxwell's 4^{th} equation in combination with equation 1.37, an equation for a_ϕ is obtained

$$\frac{\mathrm{d}}{\mathrm{d}\rho} \left[\frac{1}{\rho} \frac{\mathrm{d}}{\mathrm{d}\rho} (\rho a_\phi) \right] - \frac{f^2}{\lambda^2} a_\phi = -\frac{\Phi_0 f^2}{2\pi\lambda^2\rho} \tag{1.39}$$

with solution

$$a_\phi = \frac{\Phi_0}{2\pi\rho} \left[1 - \frac{R K_1(R/\lambda)}{\xi_\nu K_1(\xi_\nu/\lambda)} \right] \tag{1.40}$$

where $K_n(x)$ is the modified Bessel function. The corresponding magnetic flux density is

$$B_z = \left(\frac{\Phi_0}{2\pi\lambda\xi_\nu} \right) \frac{K_0(R/\lambda)}{K_1(\xi_\nu/\lambda)} \tag{1.41}$$

and by taking the Fourier transform of the flux density, the expression for the Fourier components becomes

$$F_z(\mathbf{G}) = \frac{\Phi_0 K_1\left(\xi_\nu\left(\mathbf{G}^2+\lambda^{-2}\right)^{1/2}\right)}{\left(\mathbf{G}^2+\lambda^{-2}\right)^{1/2}\lambda K_1(\xi_\nu/\lambda)}. \tag{1.42}$$

Equation 1.42 can be written more conveniently in the limit of large κ as

$$F_z(\mathbf{G}) = \langle B\rangle \frac{gK_1(g)}{\left(1+\mathbf{G}^2\lambda^2\right)}, \qquad g = \frac{\xi_\nu}{\lambda}\left(1+\mathbf{G}^2\lambda^2\right)^{1/2} \tag{1.43}$$

where $\langle B\rangle$ is the mean induction. Equation 1.43 essentially amounts to the London model with a $gK_1(g)$ factor in the numerator to account for the existence of the cores. Despite being obtained from GL theory, and therefore valid only close to T_c, there is a close resemblance between the form of the Clem model and the London model of equation 1.11. This coincidence derives from the common assumption of the adequacy of local electrodynamics. The effect of the $gK_1(g)$ term is to cause the free energy to converge by suppressing contributions at short distances from the flux line axis.

1.3 Microscopic theory

Bardeen, Cooper and Schrieffer (BCS) (Bardeen et al., 1957) provided the first successful description of the microscopic mechanism behind superconductivity in the conventional superconductors. Whilst, the subject compounds of this thesis are unconventional in comparison, we outline a description of conventional superconductivity in order to provide a basis on which to describe an unconventional superconductor. Here, we follow the treatments of Ketterson and Song (1999) and Tinkham (1996).

The BCS theory was built upon the important insight of Fröhlich (1950), that due to electron-phonon coupling, the effective forces between electrons could sometimes be attractive. Using this idea, Cooper (1956) subsequently showed that two such electrons interacting just above a filled Fermi surface could form a bound-state for an arbitrarily weak interaction potential. The two particle wavefunction of such

a 'Cooper pair' is

$$\psi(\mathbf{r}_1, \mathbf{r}_2) = \phi_{\mathbf{q}}(\rho) \mathrm{e}^{i\mathbf{q}\cdot\mathbf{R}} \chi(\sigma_1, \sigma_2). \tag{1.44}$$

where $\mathbf{R}$ is the centre of mass coordinate, $\mathbf{R} = (|\mathbf{r}_1 - \mathbf{r}_2|)/2$, $\rho = (|\mathbf{r}_1 - \mathbf{r}_2|)$ and σ_1, σ_2 are the electron spins. The term $\phi_{\mathbf{q}}(\rho)$ represents the spatial component of the wavefunction. If the lowest energy state has zero total momentum, the two electrons will have equal and opposite momenta such that the Bloch expansion of the spatial component of the wavefunction will be symmetric with respect to particle interchange. This is achieved if the two electrons have equal and opposite momenta. $\chi(\sigma_1, \sigma_2)$ represents the spin part of the wavefunction which, to conserve fermionic antisymmetry of the overall wavefunction, must be antisymmetric with respect to particle interchange. This implies a spin singlet wavefunction

$$\chi(\sigma_1, \sigma_2) = \frac{1}{\sqrt{2}} \left(|\uparrow\downarrow\rangle - |\downarrow\uparrow\rangle \right). \tag{1.45}$$

Therefore the simplest pairing state consists of electrons with equal and opposite momenta, and opposing spin. This is an s-wave state implying that there is no intrinsic angular momentum of the pair, i.e. $\ell = 0$. We also see that the mass of a Cooper pair is $2m_e$ and its charge is $2e$. These are equivalent to the terms $\hat{m}$ and $\hat{e}$ used until now in this thesis.

BCS realised that if there is such an effective interaction close to the Fermi surface, this means *all* the electrons at the Fermi surface are unstable with respect to the formation of Cooper pairs. The description of many Cooper pairs according to a single coherent wavefunction is a defining feature of superconductivity. The coherent many particle wavefunction that describes every electron being one of a pair at the Fermi level is written as

$$|\Psi_{BCS}\rangle = \prod_{\mathbf{k}} \left(u_{\mathbf{k}}^* + v_{\mathbf{k}}^* \hat{P}_{\mathbf{k}}^\dagger \right) |0\rangle \tag{1.46}$$

where $\hat{P}_{\mathbf{k}}^\dagger$ is a pair creation operator equal to $c_{\mathbf{k}\uparrow}^\dagger c_{\text{-}\mathbf{k}\downarrow}^\dagger$, which are operators that create a pair of electrons of zero total crystal momentum and opposite spin. $|0\rangle$ is a vacuum state, and the complex functions $|u_{\mathbf{k}}|^2$ and $|v_{\mathbf{k}}|^2$ represent the probability that

a pair state is occupied or unoccupied respectively. The normalisation condition $\langle \Psi_{BCS} | \Psi_{BCS} \rangle = 1$ forces $|u_{\mathbf{k}}|^2 + |v_{\mathbf{k}}|^2 = 1$. If $v_{\mathbf{k}} = 1$ for $|\mathbf{k}| < k_F$, or if $u_{\mathbf{k}} = 1$ for $|\mathbf{k}| > k_F$ the wavefunction describes the Fermi sphere. However, for finite values of $v_{\mathbf{k}}$ and $u_{\mathbf{k}}$, the occupation becomes smeared in energy at Fermi surface over a width, which in terms of reciprocal space, is of order ξ_0^{-1} in $\mathbf{k}$. This distance ξ_0 is equivalent to the Pippard coherence length introduced in section 1.1.2, and is effectively equivalent to the size of a Cooper pair.

The proposed wavefunction can be used to minimise the energy of the BCS Hamiltonian

$$\hat{H} = \sum_{\mathbf{k},\sigma} \left(\frac{\hbar^2 \mathbf{k}}{2m} - \mu \right) c^{\dagger}_{\mathbf{k}\sigma} c^{\dagger}_{\text{-}\mathbf{k}\sigma} + \frac{1}{2} \sum_{\mathbf{kk'}} c^{\dagger}_{\mathbf{k}\uparrow} c^{\dagger}_{\text{-}\mathbf{k}\downarrow} V_{\mathbf{k'k}} c_{\mathbf{k'}\uparrow} c_{\text{-}\mathbf{k'}\downarrow} \tag{1.47}$$

which is the BCS Hamiltonian for paired electrons, $V_{\mathbf{k'k}}$ is the matrix element that describes the two-particle interaction, and μ is the chemical potential. To solve the BCS Hamiltonian, the functions $u_{\mathbf{k}}$ and $v_{\mathbf{k}}$ are treated as variational parameters, and values are sought that minimise the total energy. Minimisation yields the expression for the excitation energy spectrum for single quasiparticles added to the BCS ground state

$$E_{\mathbf{k}} = \sqrt{\left(\frac{\hbar^2 \mathbf{k}}{2m} - \mu \right)^2 + |\Delta_{\mathbf{k}}|^2}, \tag{1.48}$$

where $\Delta_{\mathbf{k}}$ arises as the superconducting gap function. Whilst $\Delta_{\mathbf{k}}$ is strictly momentum-dependent, in BCS theory the gap is uniform in $\mathbf{k}$-space. BCS further showed that two times this energy gap is of order the binding energy of a Cooper pair, and that the zero temperature magnitude of $|\Delta|$ is related to the superconducting transition temperature T_c:

$$2\Delta\,(0) = 3.52 k_B T_c. \tag{1.49}$$

The temperature-dependence of the BCS energy gap shows that $|\Delta|$ falls to zero at T_c, analogous to the behaviour of the GL order parameter ψ. For this reason the terms 'order-parameter' and 'gap function' are often used interchangeably. It was Gor'kov (1958) who showed that the gap function was directly related to the

GL order parameter, and that a physical interpretation of ψ is that it represents the wavefunction for the centre of mass motion of the Cooper pairs.

Equation 1.48 is important, as it introduces the concept of an energy gap of magnitude Δ over the *entire* Fermi surface, below which single particle states are inaccessible. Single particle states are accessible for energies greater than Δ, but their nature is dependent on the value of $u_{\mathbf{k}}$ and $v_{\mathbf{k}}$ at the position in momentum space. It turns out that a state is predominantly electron-like well below the Fermi surface $|v_{\mathbf{k}}|^2 \simeq 1$ and predominantly hole-like above $|u_{\mathbf{k}}|^2 \simeq 1$. However, nearer to the Fermi surface such quasiparticles exhibit mixed electron- and hole-like character. Due to this mixed character, quasiparticle excitation energies can only be found after using the following Bogoliubov-Valatin fermion annihilation and creation operators (Ketterson and Song, 1999)

$$\hat{\gamma}^{\dagger}_{\text{-}\mathbf{k}\downarrow} = u_{\mathbf{k}} c^{\dagger}_{\text{-}\mathbf{k}\downarrow} + v_{\mathbf{k}} c_{\mathbf{k}\uparrow} \tag{1.50}$$

$$\hat{\gamma}_{\mathbf{k}\uparrow} = u^{*}_{\mathbf{k}} c_{\mathbf{k}\uparrow} - v^{*}_{\mathbf{k}} c^{\dagger}_{\text{-}\mathbf{k}\downarrow} \tag{1.51}$$

to diagonalise the relevant Hamiltonian, where precisely the same gapped energy excitation spectrum (equation 1.48) is found, as on using the BCS wavefunction to diagonalise the BCS Hamiltonian. Therefore, we have a microscopic theory that can explain not only the emergence of the superconducting gap, but also the behaviour of the single particle excitations at energies above Δ.

So far we have outlined the theory of uniform superconductivity in an ideal system. In order to be useful for describing real systems, a microscopic theory of superconductivity must allow for inhomogeneities such as crystal imperfections, scattering centres, and flux lines. Allowing for spatial inhomogeneities within the Hamiltonian that describe the quasiparticles, such as scatterers with potential $U(\mathbf{r})$, and variations in the superconducting gap $\Delta(\mathbf{r})$ due to flux line cores, means that plane-wave operators represented by quantum number $\mathbf{k}$ are no longer appropriate, and need to be replaced by position-dependent functions (de Gennes, 1989). It is possible to define more generalised fermionic operators after another Bogoliubov

transformation

$$\hat{\Psi}_{\uparrow}(\mathbf{r}) = \sum_{n} \left[u_n(\mathbf{r})\hat{\gamma}_{n\uparrow} - v_n^*(\mathbf{r})\hat{\gamma}_{n\downarrow}^{\dagger} \right] \tag{1.52}$$

$$\hat{\Psi}_{\downarrow}(\mathbf{r}) = \sum_{n} \left[u_n(\mathbf{r})\hat{\gamma}_{n\downarrow} + v_n^*(\mathbf{r})\hat{\gamma}_{n\uparrow}^{\dagger} \right] \tag{1.53}$$

where $\hat{\Psi}$ are annihilation operators for the *position* dependent functions u_n and v_n rather than the momentum dependent functions $u_{\mathbf{k}}$ and $v_{\mathbf{k}}$ defined earlier. The values of u_n and v_n are again determined as those that diagonalise the Hamiltonian, which means that u and v satisfy the coupled Bogoliubov-de Gennes equations

$$\hat{H}u_n(\mathbf{r}) + \Delta(\mathbf{r})v_n(\mathbf{r}) = E_n u_n(\mathbf{r}) \tag{1.54}$$

$$-\hat{H}^* v_n(\mathbf{r}) + \Delta^*(\mathbf{r})u_n(\mathbf{r}) = E_n v_n(\mathbf{r}) \tag{1.55}$$

where $\hat{H}$ is the mean-field complex Hamiltonian. To seek solutions to such a pair of coupled equations, it is necessary to compute $\Delta(\mathbf{r})$ from the allowed sets of u and v functions. These equations were used successfully to examine the quasiparticle excitations for the case where Δ varies rapidly over a distance of size the Ginzburg-Landau coherence length $\xi\,(0)$, i.e. over a flux line core. It was shown that in the limit of high-κ, there are a group of low-lying excitations with wavefunctions $u(\mathbf{r})$ and $v(\mathbf{r})$ localised near the flux line core, i.e. bound states (Caroli et al., 1964; Bardeen et al., 1969), thus providing a microscopic basis for the existence of single particle states within flux line cores.

1.4 d-wave superconductivity

The BCS theory describes the conventional superconductivity of a singlet pairing state with $\ell = 0$. On moving from the normal state into the superconducting state, the establishment of an energy gap function $\Delta_{\mathbf{k}}$ defines a coherent *phase* relationship between all Cooper pairs described by the pair wavefunction. The energy cost of any phase gradients is minimised by making the phase as constant as possible throughout the system. The 'long-range order' of quantum mechanical phase is said to break gauge symmetry. This broken symmetry is the minimal requirement for the

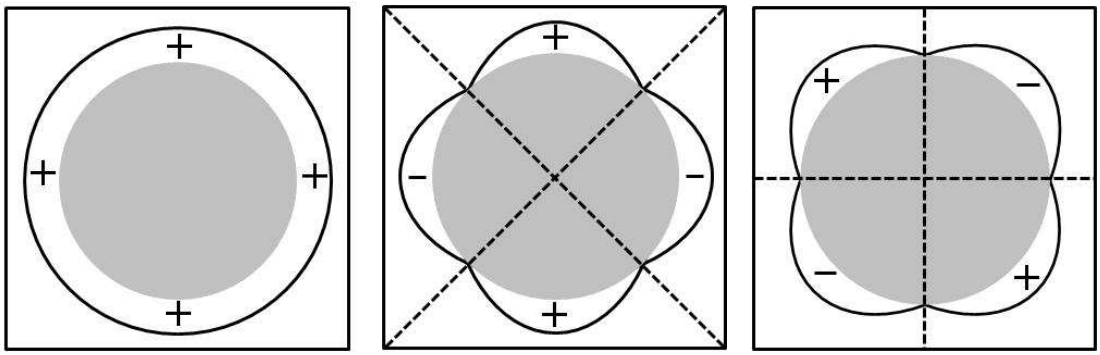

(a) s (b) $d_{x^2-y^2}$ (c) d_{xy}

Figure 1.6: Schematic **k**-space diagrams of three possible superconducting phases for a tetragonal superconductor exhibiting (a) BCS s-wave pairing, (b) $d_{x^2-y^2}$ pairing and (c) d_{xy} pairing. The diagrams attempt to show the form of the superconducting energy gap over the Fermi surface, and the relevant superconducting phase indicated by $+$ and $-$ signs. The dashed lines represent mirror planes where symmetry is broken

realisation of the superconducting wavefunction, and is the only symmetry broken within the BCS theory of conventional materials. In contrast, unconventional superconductors are those where the superconducting state breaks extra symmetries, such as parity, or on rotation or reflection transformations.

In figure 1.6 we consider the nature of the superconducting gap function over a two-dimensional Fermi surface of a tetragonal superconductor, with $\langle 100 \rangle$ directions vertical and horizontal. Figure 1.6 (a) shows a schematic form of the energy gap over the Fermi surface analogous to that predicted by BCS theory. The form of the gap function $\Delta_{\mathbf{k}}$ is a constant and it exhibits uniform phase. Clearly the gap function will remain unchanged for all possible symmetry operations. In contrast, the anisotropic gap functions of figures 1.6 (b) and (c) break extra symmetries; both are odd under 90° rotational symmetry and mirror reflections about the indicated dotted lines. These d-wave gap functions have the same symmetry properties as the atomic spherical harmonic functions $d_{x^2-y^2}$ and d_{xy}, and correspond to a singlet pairing state with $\ell = 2$. We see from figures 1.6 (b) and (c) that for the d-wave pairing states the magnitude of $\Delta_{\mathbf{k}}$ falls to zero at nodal points on the Fermi surface. This suggests that in these superconductors, the gap function is strongly anisotropic,

and quasiparticle states are accessible at arbitrarily low temperatures.

An experimental distinction between s- and d-wave superconductors is provided by examining the quasiparticle response at low temperatures. This can be achieved via measurements of the London penetration depth. According to equation 1.26, $\lambda(T)$ varies with the superfluid density $n_s(T)$ according to $n_s(T)$=$n_s(0) - n_n(T)$ where $n_s(0)$ is the zero-temperature superfluid density, and n_n is the normal, or quasiparticle, density. For the s-wave state, BCS theory predicts, $n_n \sim \exp(2|\Delta|/k_BT)$, so the quasiparticle density is very low at low temperatures. For the nodal gap, it is always possible to excite quasiparticles at all temperatures, and the dependence is $n_n \sim T$. Therefore, the markedly different T-dependence of the measured penetration depth allows a distinction between the s- and d-wave pairing states. Distinguishing between different d-wave pairing states involves probing the anisotropy of the phase degree of freedom of the gap function. The most convincing evidence for a particular orientation of d-wave gap function is provided by electron tunnelling (Renner and Fischer, 1995) and phase sensitive (Tsuei and Kirtley, 2000) experiments that are able to measure the change in phase of the superconducting wavefunction between different crystal directions.

1.5 d-wave superconductivity and the flux line lattice

The effect on the FLL of an anisotropic d-wave gap function has been extensively studied. The early study of Soininen et al. (1994) investigated the detailed structure of a single flux line in a $d_{x^2-y^2}$ superconductor on solving the Bogoliubov-de Gennes equations for the quasiparticles. The calculations predict the structure of the flux line in the core vicinity to be remarkably detailed, and consist of three different regions that can support fermionic states. The inner core region supports localised states resembling those of an s-wave flux line Caroli et al. (1964). The outer core region is composed of a gapped excitation spectrum due to co-existence of d- and s-wave order-parameter components. The relative phase between these two components is non-zero except along orthogonal directions where the gap falls

to zero due to destructive interference between them. The third region outside the core is an asymptotic d-wave state. The outer core region is of most interest, as the rotational symmetry of the field distribution is reduced to fourfold, which is the same as that of spatial variation of the d-wave gap function. This will necessarily induce an anisotropy in the interactions between flux lines.

The prediction for the nucleation of both s- and d-wave gap components within a rich core region led Berlinsky et al. (1995) to propose the following GL free energy expansion that can be solved to reproduce this phenomenon.

$$F = \alpha_s|s|^2 + \alpha_d|d|^2 + \beta_1|s|^4 + \beta_2|d|^4 + \beta_3|s|^2|d|^2 + \beta_4\left(s^{*2}d^2 + d^{*2}s^2\right) \\ +\gamma_s|\Pi s|^2 + \gamma_d|\Pi d|^2 + \gamma_\nu\left[\left(\Pi_y s\right)^*\left(\Pi_y d\right) - \left(\Pi_x s\right)^*\left(\Pi_x d\right) + \text{c.c.}\right]. \qquad (1.56)$$

The expansion is essentially the sum of two expansions for s and $d_{x^2-y^2}$ order parameters, described by terms with coefficients α_s, α_d, β_1, β_2,γ_s and γ_d. The other terms provide the coupling between the two order-parameters, with that of coefficient γ_ν including mixed higher-order gradient terms, which are responsible for the nucleation of the s-wave components at the core region. The morphology of these s-wave components is shown by Franz et al. (1996) to be in the form of five core-like regions, one located at the flux line centre, and four oppositely wound cores located symmetrically about this centre core at a distance a few coherence lengths away. Although the amplitudes of such components are calculated to be just a few percent the size of the d-wave component, they reduce the symmetry of the field distribution to four-fold, for distances far beyond the positions of these s-wave cores. Both Berlinsky et al. (1995) and Franz et al. (1996) show that the precise FLL coordination is strongly dependent on both the coupling strength of the mixed gradient terms and on the magnetic field. In the limit of vanishing coupling terms, and at low fields, the induced s-wave components vanish and the FLL coordination tends towards being isotropic and hexagonal. Increasing either the coupling strength or the field promotes the continuous distortion of the isotropic hexagonal FLL coordination towards a square FLL structure. It was shown by Franz et al. (1996) that the square FLL structure has a free energy minimum, $\mathcal{F}_m$ when

the flux line nearest neighbours lie parallel to the nodal directions of the $d_{x^2-y^2}$ gap function. This same prediction for a similarly oriented square FLL structure at high fields is also reproduced by the GL theories of Xu et al. (1996) and Shiraishi et al. (1999).

The GL models can be used to predict the intricate structure of a flux line, and ultimately the preferred $\mathcal{F}_m$ of the FLL. However, they are limited in being technically valid only near to T_{c2}, and difficult to use as there are many free parameters. This motivated Affleck et al. (1997) to develop a simpler, more generalised London model. Starting from the GL free energy expansion proposed by Berlinsky et al. (1995) (equation 1.56), the authors simplify the expression by integrating out the s-wave components in favour of higher-order derivatives expressed in terms of d-wave components. Whilst these higher order terms capture the inherent gap anisotropy, the simplification results in the intricate details associated with the flux line core structure being lost. However, these details are experimentally difficult to access, and the expected fourfold anisotropy of the magnetic field distribution around the core is retained. Affleck et al. (1997) subsequently calculate the free energy density assuming the London limit of $\lambda \gg \xi$, and the expression for the FLL Fourier components is shown to be

$$B\left(\mathbf{G}\right) = \langle B \rangle \frac{\exp\left(-G^2\xi^2/2\right)}{1 + \lambda_0^2 G^2 + 4\epsilon\lambda_0^2\xi^2\left(G_x G_y\right)^2}. \tag{1.57}$$

The term $\epsilon = 3\left(\alpha_d \gamma_v^2 / \alpha_s \gamma_d^2\right)$ is a dimensionless parameter that determines the strength of the s-d coupling which generates the fourfold anisotropy, and is assumed to be < 1. Evaluating the free energy as a function of field shows that for both increasing field and ϵ, there is an increased propensity for the FLL to adopt a square structure with the nearest neighbour direction parallel to the nodal directions. These predictions agree with those of the more detailed GL theories. Also searching for a more tractable theory were Franz et al. (1997). Similar to Kogan et al. (1996), the authors start from a microscopic viewpoint and derive a non-local London expression for the free energy density. Unlike Kogan et al. (1996) however, the model is generalised to allow for a gap anisotropy. Franz et al. (1997) subsequently derive

the expression for the Fourier components to be

$$B\left(\mathbf{G}\right) = \langle B \rangle \frac{\exp\left(-G^2\xi^2/2\right)}{1 + \lambda^2 G^2 + \lambda^2 \xi^2 \left(c_1 G^4 + c_2 G_x G_y\right)^2}. \tag{1.58}$$

Parameters c_1 and c_2 are dimensionless coefficients dependent on the magnitude and momentum-dependence of the gap function, the temperature, and the Fermi velocity averages. As a function of increasing field, and as a consequence of the gap anisotropy, Franz et al. (1997) predict that the isotropic hexagonal structure smoothly distorts towards a square structure. At higher temperatures, they further show that the non-local corrections become weaker, and the FLL structure tends toward being isotropic and hexagonal.

We note that the general forms of the expressions for the Fourier components according to s-wave non-local theory (Kogan et al., 1996, 1997a), d-wave non-local theory (Franz et al., 1997; Affleck et al., 1997), and the GL models (Berlinsky et al., 1995; Franz et al., 1996) are all comparable, and make broadly similar predictions. From this point of view, if a high field square FLL structure is observed experimentally, for certain cases, it can be difficult to determine whether the underlying anisotropy that causes this can be interpreted in terms of non-local corrections to the London equation, or to higher order terms of the GL free energy expansion.

1.5.1 Quasiclassical Eilenberger theory

In section 1.3 we outlined the Bogoliubov-de Gennes (BdG) equations, which can be used to describe the quasiparticle states of a spatially inhomogeneous superconductor. More powerful methods of dealing with inhomogeneous superconductivity borrow from quantum field theory in the form of Green's functions, which are used to describe the correlations of creation and annihilation operators. These techniques were shown to be useful by Gor'kov (1958), who applied them to the BCS theory and re-derived the BdG equations. The use of such expressions in describing a real system is a rather complex process. However, the calculations can be simplified somewhat by assuming the quasiclassical limit. This involves ignoring the short-wavelength variations of the quasiparticle functions, as this length-scale $1/k_F$

is typically less than the coherence length ξ (or $\Delta \ll E_F$). Using this assumption, Eilenberger realised that the Gor'kov theory could be approximated to treat single quasiparticle states self-consistently, and developed a set of transport-like equations that describe the quasiparticle motion (Eilenberger, 1968). The use of the Eilenberger equations has been shown in recent years to be extremely effective in understanding the behaviour of the FLL (see for example, Ichioka et al. (1996),Ichioka et al. (1999),Nakai et al. (2002),Ichioka and Machida (2007)). The main principle of the calculations is to obtain the quasi-classical Greens functions that describe the quasiparticle states at each point of a grid across a unit cell of the FLL. At each point, an iteration technique is adopted such that the pairing potential and vector potential are determined self-consistently. The self-consistent parameters are then used to calculate the current density and internal field distributions, and the spatial distribution of the low energy density of quasiparticle states.

An early application of the theory looked at the case of a single flux line in a $d_{x^2-y^2}$ superconductor. In contrast to the GL theories, Ichioka et al. (1996) show the field distribution around the flux line core is fourfold symmetric, without the necessity for the nucleation of any s-wave components in the core vicinity. Therefore, the fourfold symmetry of the field distribution around the core was shown to be an intrinsic feature of a flux line in a $d_{x^2-y^2}$ superconductor. The calculations also reveal that the spatial distribution of the low energy quasiparticle states also has a fourfold symmetry, with extended 'tails' that propagate along the nodal directions over long distances far from the cores. These tails are a unique consequence of the the $d_{x^2-y^2}$ flux line, and arise due to the fourfold core structure, which reflects the spatial symmetry of the order parameter.

The effect of the low energy quasiparticle tails on the overall FLL structure was investigated in Ichioka et al. (1999). Here, the authors consider the role of quasiparticle states from three viewpoints: (i) quasiparticles that form the tails that propagate along the nodal directions, (ii) core quasiparticles which are bound inside the flux line core and (iii) quasiparticle tunnelling between flux line cores. The role of the quasiparticle tunnelling becomes more important at high fields, when the

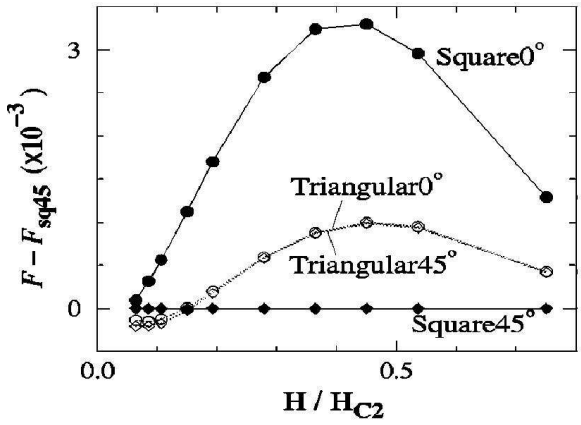

Figure 1.7: The results of the free energy calculations within the quasiclassical Eilenberger theory of Ichioka et al. (1999). The free energy is measured relative to a square FLL orientation with nearest neighbours parallel to the nodal directions (Square45°). The other square coordination, Square0° has nearest neighbours parallel to the antinodal directions. Triangular0° and triangular45° coordinations indicate isotropic hexagonal FLL structures with nearest neighbours respectively along the antinodal and and nodal directions. The calculations were carried out at $0.5T_c$.

core regions begin to overlap. When this occurs, Ichioka et al. (1999) calculate that the lower energy FLL configurations correspond to a square FLL structure, with the nearest neighbour directions parallel to the nodal $\langle 110 \rangle$ directions. At lower inductions, when the flux lines are not in close proximity, the influence of the core anisotropy is weaker such that the FLL configuration is typically triangular. Figure 1.7, shows the predicted field-dependence of the structural free energy for four different FLL coordinations in the $d_{x^2-y^2}$ superconductor. At low fields, the preferred FLL structure is predicted to be lie with the isotropic hexagonal coordination, with very little difference between the free energies of the two considered orientations. However, at $\sim 0.15H_{c2}$ the free energy minimum crosses over to the square FLL structure with nearest neighbours parallel to the nodal directions. The nature of the transition is predicted to be first-order. We also note that these calculations were carried out at $0.5T_c$, with calculations at lower temperature unpublished.

The power of the quasiclassical Eilenberger theory lies with its generality; it is sensitive to microscopic variables such as the symmetry of both the Fermi surface and the superconducting gap function, and most promisingly, the theory is valid

for any field and temperature. Unfortunately, with the greater generality comes the associated cost of the increased complexity for the non-specialist. For this reason, unless dedicated calculations can be carried out, only qualitative comparisons between experimental results and existing published calculations are made.

1.6 The upper critical field in type-II superconductors

The destruction of superconductivity in the mixed state can be achieved via two distinct mechanisms on the application of magnetic field. The first, and most common, is through the application of a field larger than the orbital-limiting critical field. The second, and less common, occurs for fields larger than the Pauli paramagnetically limited critical field. Whichever field is lower is determined by the material properties.

Orbital limiting actually leads to the emergence of the FLL, whereby supercurrents circulate [3] the flux lines cores somewhat screening the bulk from the flux inside the core. As the field is increased, the orbital limiting field is reached when the flux line density is such that the flux line cores begin to overlap. Thus, the material can be thought of as simply composed of core regions, and hence not superconducting. The orbitally limited critical field was found previously after linearising the first Ginzburg-Landau equation 1.21, and is

$$\mu_0 H_{c2}^{Orb} = B_{c2}^{Orb} = \frac{\Phi_0}{2\pi\xi^2(T)}. \tag{1.59}$$

The Pauli paramagnetic upper critical field arises due to the Zeeman splitting of single electron energy levels. If a magnetic field is applied in the normal state, electrons are polarised because the Fermi surface splits into a part composed of spins aligned with the field, and a part with spins anti-aligned with the field. For certain superconductors, such as $TmNi_2B_2C$ (DeBeer-Schmitt et al., 2007) and $CeCoIn_5$ (see Chapter 4), the Fermi surface splitting is enhanced due to an exchange interaction between the field-induced localised moments of the rare earth sub-lattice and the

[3] These supercurrents exhibit a finite vorticity about the flux line axis, and in the literature 'flux line lattice' and 'vortex lattice' are used interchangeably. In this thesis, we choose to use the former.

conduction electron moments. This interaction results in increased Pauli paramagnetic effects, and can contribute toward the realisation of a Pauli-limited upper critical field. For the singlet superconducting state, in order to maintain the superconductivity, the Cooper pairs exhibit negligible spin susceptibility. To polarise the paired electrons, a magnetic field energy larger than the condensation energy must be applied in order to break the Cooper pair, and destroy the superconductivity. This field is the Pauli-limited upper critical field, the estimation of which is (Chandrasekhar, 1962; Clogston, 1962)

$$\mu_0 H_{c2}^P = \frac{\sqrt{2}\Delta}{g\mu_B}. \tag{1.60}$$

Here, Δ is the magnitude of the superconducting energy gap, g is the electron g-factor, which is 2, and μ_B is the Bohr magneton.

In general, the nature of the upper critical field is dependent on a combination of both the orbital and paramagnetic effects. The Maki parameter describes the relative importance of each effect to the destruction of superconductivity, being defined as

$$\alpha_M = \sqrt{2}\frac{B_{c2}^{Orb}}{B_{c2}^P}. \tag{1.61}$$

For most superconductors, α_M is much less than unity, and this indicates a small influence of the paramagnetic effect in the destruction of superconductivity. However, for materials where the carriers exhibit an enhanced effective mass, such as heavy-fermion materials, α_M can be larger than unity, which indicates a dominant paramagnetic effect. The most distinctive feature between the two methods of destroying the superconductivity is the order of the associated phase transition at H_{c2}. The orbitally-limited superconductor exhibits a second-order phase transition, whilst the Pauli limited superconductor shows a first-order phase transition.

Small-angle neutron scattering by the flux line lattice

The periodic nature of the flux line lattice (FLL) makes it an ideal candidate for neutron diffraction experiments. Neutrons are an excellent probe of the FLL; the intrinsic magnetic moment of the neutron interacts with the spatially varying magnetic potential of the FLL field distribution via the dipolar interaction. Moreover, neutrons are insensitive to sample surface quality, and provide an imaging of the FLL in the sample bulk over a large sample volume. The resulting diffraction patterns unambiguously provide an image of the FLL structure and orientation, and the absolute intensities of Bragg diffraction spots provide information about the field distribution. Both of these directly reflect the underlying microscopic state, the characterisation of which plays a crucial role in the studies on the materials reported in this thesis.

2.1 Introduction to small-angle neutron scattering (SANS)

The observation that each FLL unit cell contains a single magnetic flux quantum Φ_0, dictates the d-spacing of the FLL. The expression for the generalised d-spacing is

$$d = \sqrt{\frac{\Phi_0}{B}\sin(\beta)} \tag{2.1}$$

where B is the internal induction, and β is the characteristic opening angle of the FLL primitive cell. Therefore, for the limiting cases of isotropic hexagonal and square FLL coordinations, $\beta = 60^\circ$ and $\beta = 90^\circ$ respectively. For the isotropic hexagonal coordination at 1 T, the d-spacing is $\sim$40 nm. This is much larger than

the atomic lattice spacings of the host crystal, and indicates that cold neutrons are required to probe this periodicity. We will see in what follows that the scattering from the FLL is elastic and described by Bragg's Law

$$(n)\lambda_n = 2d\sin(\theta) \tag{2.2}$$

where n refers to the order of diffraction, λ_n is the neutron wavelength, d is the d-spacing of the FLL and θ is the Bragg angle. Taking the example of the isotropic hexagonal FLL coordination at 1 T, using a neutron wavelength of 10 Å the Bragg 2θ is just 1.35°. The small angle of scatter leads to the 'small-angle neutron scattering' (SANS) nomenclature used in this thesis. The small θ also necessitates large sample-to-detector distances (of order 10 m), so that diffracted neutrons can separate out from the undiffracted beam and be distinguished.

2.1.1 Scattering from an arbitrary periodic potential

We start from the viewpoint of quantum mechanics and consider the neutron Hamiltonian and its interaction with an arbitrary scattering system. A description of a neutron can be made in terms of the time-independent Schrödinger equation,

$$\left[-\frac{\hbar^2}{2m_n}\nabla^2 + V(\mathbf{r})\right]\Psi(\mathbf{r}) = E\Psi(\mathbf{r}). \tag{2.3}$$

Here, m_n is the neutron mass, E is its energy, and $\Psi(\mathbf{r})$ is the position-dependent wavefunction. $V(\mathbf{r})$ is the interaction potential and, for the case of weak scattering, the first Born approximation holds, which treats $V(\mathbf{r})$ as a perturbation (Schiff, 1968). This essentially means that the scattering amplitude is proportional to the spatial Fourier transform of the scattering potential, with respect to $\mathbf{q}$. The probability for the scattering potential to cause a change in the neutron momentum, can be expressed in terms of Fermi's Golden Rule

$$W_{\mathbf{k}\to\mathbf{k}'} = \frac{2\pi}{\hbar}\rho_{\mathbf{k}'}\left|\langle\mathbf{k}'|V(\mathbf{r})|\mathbf{k}\rangle\right|^2 \tag{2.4}$$

where $|\mathbf{k}\rangle$ is the neutron wavefunction, $\mathbf{k}$ and $\mathbf{k}'$ are respectively the initial and final neutron wavevectors, and $\rho_{\mathbf{k}'}$ is the density of final neutron states [4]. Here, we have

[4]For completeness, we should also consider energy conservation of the overall system of the neutron and scatterer, in addition to the initial and final quantum states of the scatterer. We will see

neglected the dependence on neutron spin, so that the neutron wavefunction is defined entirely by its momentum. The time-independent partial differential cross-section is defined as the probability for neutron to be scattered into solid angle $\mathrm{d}\Omega$,

$$\frac{\mathrm{d}\sigma}{\mathrm{d}\Omega} = \frac{1}{\phi_n}\frac{1}{\mathrm{d}\Omega}\sum_{\mathbf{k}'\in\mathrm{d}\Omega} W_{\mathbf{k}\to\mathbf{k}'} \tag{2.5}$$

where ϕ_n is the incident neutron flux. By inserting the plane wave representation of the neutron wavefunction, equation 2.5 can be written as

$$\frac{\mathrm{d}\sigma}{\mathrm{d}\Omega} = \left(\frac{m_n}{2\pi\hbar^2}\right)^2 \left|\int \exp\left(-i\mathbf{k}'\cdot\mathbf{r}\right) V\left(\mathbf{r}\right) \exp\left(i\mathbf{k}\cdot\mathbf{r}\right) \mathrm{d}\mathbf{r}\right|^2 . \tag{2.6}$$

where the prefactor arises due to normalisation in the calculation of $\rho_{\mathbf{k}'}$ (Squires, 1996). To evaluate the matrix element, we describe $V(\mathbf{r})$ according to the periodic array of N weak scatterers centred at $\mathbf{R}_j$ with the same non-overlapping potential,

$$V = \sum_j^N \hat{V}\left(\mathbf{r}-\mathbf{R}_j\right). \tag{2.7}$$

If we define $\mathbf{r}' = \mathbf{r} - \mathbf{R}_j$, then we can evaluate equation 2.6 to obtain

$$\frac{\mathrm{d}\sigma}{\mathrm{d}\Omega} = \left(\frac{m_n}{2\pi\hbar^2}\right)^2 \left|\int \hat{V}\left(\mathbf{r}'\right) \exp\left(i\mathbf{q}\cdot\mathbf{r}'\right) \mathrm{d}\mathbf{r}' \sum_j^N \exp\left(i\mathbf{q}\cdot\mathbf{R}_j\right)\right|^2 . \tag{2.8}$$

where we have introduced

$$\mathbf{q} = \mathbf{k} - \mathbf{k}' \tag{2.9}$$

with $\mathbf{q}$ being the scattering vector. Equation 2.8 is valid for any weak scattering system, and can be written more concisely as

$$\frac{\mathrm{d}\sigma}{\mathrm{d}\Omega} = \left|F\left(\mathbf{q}\right)\right|^2 S\left(\mathbf{q}\right). \tag{2.10}$$

$F\left(\mathbf{q}\right)$ describes the scattering amplitude of a *single scatterer* and is termed the form factor. It is defined as the normalised Fourier transform of the scattering potential,

$$F\left(\mathbf{q}\right) = \frac{m_n}{2\pi\hbar^2}\int \hat{V}\left(\mathbf{r}\right) \exp\left(i\mathbf{q}\cdot\mathbf{r}\right) \mathrm{d}\mathbf{r}. \tag{2.11}$$

that it is not important to consider these elements for neutron scattering from the FLL.

$S(\mathbf{q})$ is the structure factor which provides a description of *how* the neutrons are scattered by the periodic potential of the lattice

$$S(\mathbf{q}) = \left| \sum_{j}^{N} \exp(i\mathbf{q} \cdot \mathbf{R}_j) \right|^2 . \tag{2.12}$$

2.1.2 Scattering from the flux line lattice

Neutrons can interact with matter via the nuclear potential, or the dipole potential of the neutron magnetic moment within a magnetic field $B(\mathbf{r})$. As the FLL is a magnetic entity, we develop equation 2.10 in this context. As the scattering process of the neutron by the FLL does not depend on the neutron spin, the scattering potential can be given by

$$\hat{V}(\mathbf{r}) = -\gamma \mu_N B(\mathbf{r}) \tag{2.13}$$

where μ_N is the nuclear magneton which is equal to $e\hbar/2m_p$, e is the electron charge, and m_p is the proton rest mass. γ is a dimensionless constant equal to 1.91, and $B(\mathbf{r})$ is the field distribution of the FLL.

For parallel fields everywhere $B = (0, 0, B)$, as is expected for the ideal FLL, the elastic differential cross-section for magnetic scattering becomes

$$\frac{\mathrm{d}\sigma}{\mathrm{d}\Omega} = \left(\frac{m_n}{2\pi\hbar^2} \right)^2 \gamma^2 \mu_N^2 \left| \int B(\mathbf{r}) \exp(i\mathbf{q} \cdot \mathbf{r}) \, \mathrm{d}\mathbf{r} \right|^2 S(\mathbf{q}) . \tag{2.14}$$

The structure factor term of the partial differential cross-section is calculated by summing over the scattering potentials of the FLL at their positions $\mathbf{R}_j$. As we treat the flux lines as macroscopic rods that are parallel to the field direction, we describe the two-dimensional positional array of flux line scattering potentials by the vector $\mathbf{R}_j = \mu a \hat{\mathbf{x}} + \nu b \hat{\mathbf{y}}$. The structure factor $S(\mathbf{q})$ therefore becomes

$$S(\mathbf{q}) = \left| \sum_{j} \exp(i\mathbf{q} \cdot \mathbf{R}_j) \right|^2 = \left| \sum_{\mu=0}^{M-1} \exp(i\mu a q_x) + \sum_{\nu=0}^{M-1} \exp(i\nu b q_y) \right|^2 \tag{2.15}$$

where $M^2 = N$, and N represents a finite number of scatterers in the system. Each of these exponential sums represents a geometric series, allowing the structure

factor to be written as

$$S(\mathbf{q}) = \frac{\sin^2(aq_xM/2)}{\sin^2(aq_x/2)}\frac{\sin^2(bq_yM/2)}{\sin^2(bq_y/2)}. \tag{2.16}$$

For large N, equation 2.16 is sharply peaked at locations given by

$$\mathbf{G}_{h,k} = 2\pi\left(\frac{h}{a}, \frac{k}{b}\right) \tag{2.17}$$

where $\mathbf{G}_{h,k}$ corresponds to a reciprocal lattice vector of the scattering system at the Miller indices h and k. Away from this condition, $S(\mathbf{q})$ is essentially zero. Thus we can write for N flux lines in the sample,

$$S(\mathbf{q}) = N\left|\sum_j \exp(i\mathbf{q}\cdot\mathbf{R}_j)\right|^2 = N\frac{(2\pi)^3}{V}\sum_{\mathbf{G}}\delta^{(2)}(\mathbf{q}-\mathbf{G}). \tag{2.18}$$

The prefactor on the right hand side of equation 2.18 is obtained by integrating over a unit cell of the reciprocal lattice unit cell of volume V (Squires, 1996). Substituting equation 2.18 into equation 2.14 the partial differential cross-section becomes

$$\frac{\mathrm{d}\sigma}{\mathrm{d}\Omega} = N\left(\frac{\gamma}{4}\right)^2\frac{(2\pi)^3}{V}\frac{1}{\Phi_0^2}\sum_{\mathbf{G}}|F(\mathbf{G})|^2\,\delta^{(2)}(\mathbf{q}-\mathbf{G}) \tag{2.19}$$

with some re-arrangement of the pre-factor, which allows us to introduce the magnetic flux quantum $\Phi_0 = h/2e$. $F(\mathbf{G})$ is the FLL form factor, defined as the two-dimensional Fourier transform of the field-distribution for the FLL unit cell. The delta function in equation 2.19 embodies the condition for elastic scattering; the partial differential cross section will only be finite for a momentum transfer where $\mathbf{q} = \mathbf{G}$. When this relation holds, it is often said the 'Bragg condition' is satisfied, alluding to the fact that for the elastic scattering, $|\mathbf{k}| = |\mathbf{k}'|$ and that in this case equation 2.9 corresponds to Bragg's Law.

Equation 2.19 indicates that the partial differential cross-section is only finite when the argument of the delta-function is zero. In reality however, a Bragg reflection exhibits a finite size in reciprocal space due to both the resolution of the instrument, and imperfections in the FLL (see section 2.3). This means the partial differential cross-section is finite over a volume in reciprocal lattice, and on satisfying the Bragg condition over this volume, diffracted intensity can be observed at

the detector. In a real experiment however, the partial differential cross-section is not measured, rather instead we measure the integrated intensity as the reciprocal lattice vector is *rotated* through the Ewald sphere. The calculation of the integrated intensity involves integrating the partial differential cross-section over all directions in space to obtain the total cross-section σ_{tot}, and then integrating σ_{tot} as a function of the reciprocal lattice rotation angle. Example calculations can be found in many places (see for example, Squires (1996),Eskildsen (1998) or Laver (2007)). Here, we re-state the final result for the integrated intensity of a Bragg spot of order $\{h, k\}$

$$I(\mathbf{G}_{h,k}) = 2\pi V \phi_n \left(\frac{\gamma}{4}\right)^2 \frac{\lambda_n^2}{\Phi_0^2 \mathbf{G}_{h,k} \cos(\zeta)} |F(\mathbf{G}_{h,k})|^2, \tag{2.20}$$

where, essentially we have multiplied the magnitude of the partial differential $|\mathrm{d}\sigma/\mathrm{d}\Omega|$ by a factor

$$I(\mathbf{G}_{h,k}) = \left|\frac{\mathrm{d}\sigma}{\mathrm{d}\Omega}\right| \frac{\lambda_n^2 \phi_n}{(2\pi)^2 \mathbf{G}_{h,k} \cos(\zeta)} \tag{2.21}$$

where λ_n is the neutron wavelength and $\cos(\zeta)$ is the Lorentz-factor. The angle ζ is that which lies between the reciprocal lattice vector and the direction normal to the rotation axis. In Appendix A, we outline the common experimental practice adopted in order to carry out SANS measurements and obtain the integrated intensity for a Bragg spot, and also how the integrated intensity data is analysed in order to obtain the FLL form factor. The appendix also includes an example of some raw rocking-curve data.

It is also customary to define the absolute reflectivity, which is normalised to the incident neutron flux,

$$R(\mathbf{G}_{h,k}) = \frac{I(\mathbf{G}_{h,k})}{\phi A} = 2\pi t \left(\frac{\gamma}{4}\right)^2 \frac{\lambda_n^2}{\Phi_0^2 \mathbf{G}_{h,k} \cos(\zeta)} |F(\mathbf{G}_{h,k})|^2 \tag{2.22}$$

where we have assumed the volume $V = At$, where A is the illuminated sample area, and t the mean sample thickness. ϕ is subsequently the neutron flux *per unit area*. We see from equations 2.20 and 2.22 that for a given Bragg spot, with all other variables constant, both the integrated intensity and absolute reflectivity are proportional to the square of the form factor modulus, $|F(\mathbf{G})|^2$ and inversely proportional to the length of the scattering vector $\mathbf{G}$.

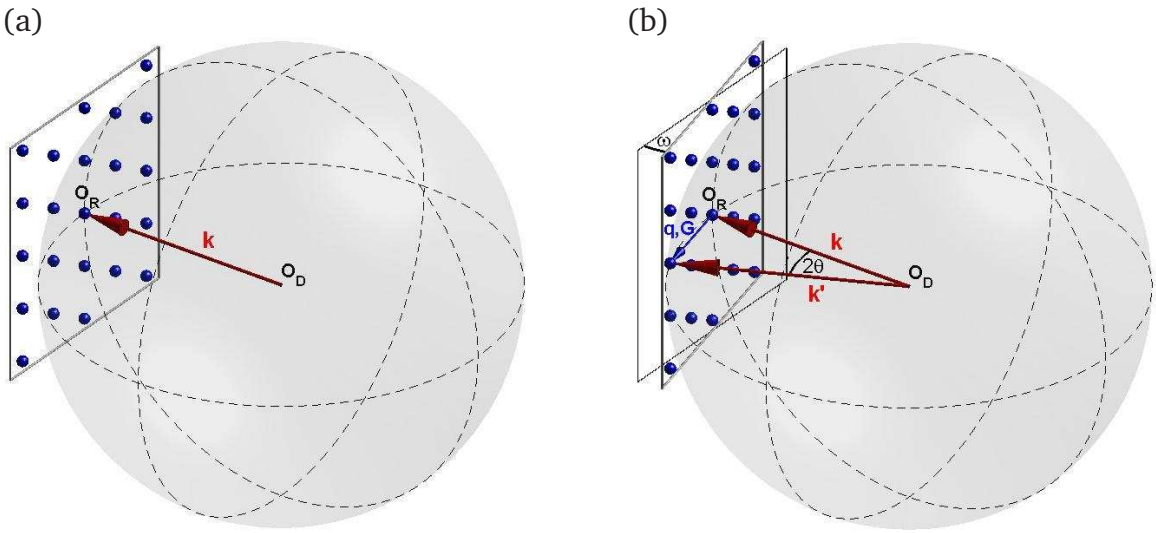

Figure 2.1: In (a), the Ewald sphere is shown in grey, and the incoming wavevector **k** is parallel to the field direction. This wavevector is defined as that spanning the origin of diffraction O_D (which is also the origin of the Ewald sphere), to the origin of reciprocal space, O_R. The reciprocal lattice of the FLL is shown as the array of blue spots, with the frame around it representing the sample of the plane of reciprocal space. In this scenario, none of the Bragg spots satisfy the Bragg condition. In (b) we have rotated the reciprocal lattice by an angle ω about the vertical axis, such that a reciprocal lattice vector **G** (or **q**) forms a chord of the Ewald sphere. This is shown by the blue arrow. The vector **k'** is the distance from O_D to end of **G**. The angle between **k** and **k'** is given by the Bragg 2θ. These diagrams are exaggerated for clarity. In reality ω is of order 1°.

2.1.3 The Ewald sphere

The Ewald sphere construction provides a geometrically appealing picture from which it is possible to visualise the application of the elastic scattering theory outlined in the previous two subsections. The sphere is defined in reciprocal space according to incoming and outgoing wavevectors **k** and $\mathbf{k}'$. If these vectors point from a common origin, the ends of all possible **k** and $\mathbf{k}'$ will lie on the surface of a sphere. Figure 2.1 shows an interpretation of the Ewald sphere construction for the specialised case of the flux line lattice. The incoming wavevector is defined as that which spans the distance from the origin of the sphere, which is termed the origin of diffraction, to the origin of reciprocal space. Initially, the plane of the reciprocal FLL lies perpendicular to **k**, and is tangent to the sphere at this point. This

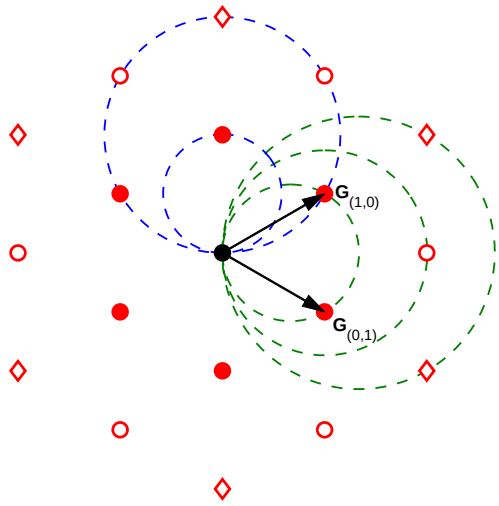

Figure 2.2: A schematic diagram showing the circular sampling region that exists for a finite rotation of the reciprocal FLL. The dashed circles correspond to the points where the plane of the reciprocal FLL touches the surface of the Ewald sphere. Larger dashed circles indicate larger rotation angles of the reciprocal FLL. In the figure, green (blue) dashed circles correspond to the cuts of the Ewald sphere surface for the case where the reciprocal lattice is rotated about a vertical (horizontal) axis. Around the circumference of each circle, the Bragg condition is satisfied, and diffracted intensity is observed on the detector. The diagram serves to illustrate that more than one Bragg reflection can satisfy the Bragg condition simultaneously. The black circle corresponds to the origin of reciprocal space, filled red circles the $\{1,0\}$ spots of a hexagonal FLL, empty circles the $\{1,1\}$ diffraction spots, and empty diamonds the $\{2,0\}$ diffraction spots.

situation (shown in figure 2.1 (a)) realises no diffracted intensity for any of the reciprocal lattice points, as the delta function of equation 2.19 is not satisfied. To satisfy the requirement of the delta function, it is necessary to rotate the reciprocal lattice by an angle ω, which brings a reciprocal lattice point to the surface of the Ewald sphere. This is depicted in figure 2.1 (b). When this situation occurs, the delta function, and consequently the Bragg condition, is satisfied. The **q**-vector is equal to a reciprocal lattice vector **G** and diffracted intensity will be observed at the detector. The angular difference between the incoming and resulting outgoing wavevectors, **k** and **k'** is the Bragg 2θ which for SANS is usually of order a degree.

In figure 2.2 we highlight an interesting consequence that can arise for the pla-

nar two dimensional reciprocal FLL. When the reciprocal FLL plane is rotated about an axis, be it horizontal or vertical, it slices through the surface of the Ewald sphere. The points where the reciprocal FLL plane cut the surface of the Ewald sphere are those where it is possible to simultaneously satisfy the Bragg condition. These points trace out a circle. As the rotation angle of the reciprocal lattice increases, this sampling circle becomes larger. Clearly, for a certain direction of rotation of the reciprocal lattice, the points at lower **q** will be satisfied at smaller rotation angles. However, as the angle of rotation increases, and as can be seen in figure 2.2, there is an increased possibility to simultaneously satisfy the diffraction condition of multiple reciprocal lattice vectors. The satisfying of multiple reciprocal lattice vectors at once is often deliberately carried out in SANS measurements.

2.2 Instrumentation

The large-scale instrumentation, coupled with the need for a source of neutrons, means that the SANS measurements reported in this thesis were carried out at dedicated international facilities. The results reported in this thesis made use of three SANS instruments, the D11 diffractometer at the Institut Laue-Langevin (ILL), Grenoble, France, and the SANS-I and SANS-II instruments at the Paul Scherrer Institut (PSI), Villigen, Switzerland. All of these instruments were used in the same way, and have qualitatively the same layout, summarised schematically in figure 2.3.

The neutrons required for SANS experiments from the FLL are provided either by a reactor source, as at ILL, or a spallation source, as at PSI. For the former, hot fission neutrons are moderated by liquid deuterium in order to obtain cold neutrons. At PSI, the neutrons are supplied by the process of bombarding a heavy metal target with high-energy protons. Liquid deuterium is again used as the moderator. Deuterium is the chosen moderator due to its low neutron absorption cross-section, light mass, and high scattering cross-section. This provides an efficient moderation of the high energy neutrons produced in fission or spallation processes (of energy

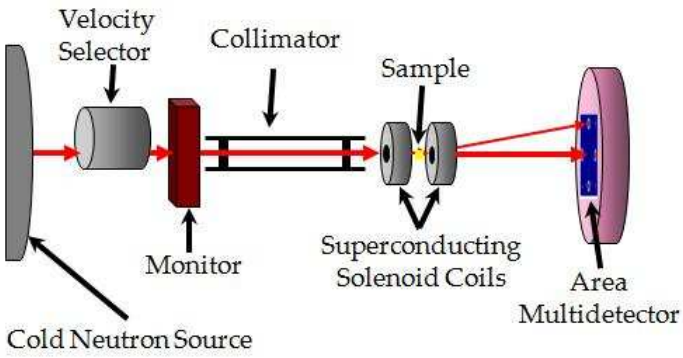

Figure 2.3: A schematic diagram of a typical SANS instrument. Typically the length of the collimator section is approximately equal to the distance between the sample and the area multidetector, in the traditional pinhole geometry. This distance can be up to ∼40 m on the D11 instrument at ILL. Typically shorter distances are used, especially for larger momentum transfers.

$\sim$ 1 MeV) down to cold ($\sim$ 1 meV) energies. For both types of source, cold neutrons are directed towards the instrument via guides which are internally coated with a highly polished 'supermirror' layer (Ni-coated multi-layer). This inner surface is reflective to grazing incidence neutrons, as the critical angle is a few degrees for cold neutrons. Therefore, neutrons are guided towards the instrument via multiple critical angle reflections.

The neutrons that emerge from the ends of the guides possess a range of energies. In order to select a single energy, and hence wavelength, a helical tilt slot mechanical velocity selector is used. The velocity selector is composed of a turbine that rotates about its long axis. Neutron absorbing blades that are approximately parallel to the long axis exist on the outside, but are helically rotated about the axis of the turbine. This means that the centre point between two adjacent blades is not parallel to the turbine axis between the entrance and exit of two blades. By rotating the turbine at a certain frequency, only neutrons of a certain energy will be able to pass through between the blades, whilst higher and lower energy neutrons will become absorbed. In reality, the selector allows a distribution of wavelengths to pass with a typical FWHM spread $\Delta\lambda_n/\lambda_n$ of $\sim$ 10 %.

Selected neutrons then pass through a low-efficiency detector which acts as the

monitor. The monitor is used for the normalisation of the diffracted neutrons in order to provide a measure of the incident neutron beam. As PSI is a spallation source, it is known that the neutron flux is often prone to fluctuations with time. Therefore, in deciding how long to carry out a measurement, the best measurement unit is not absolute time, but rather *standard monitor*, where a standard monitor represents a fixed number of counts recorded by the low-efficiency detector. If the number of neutrons corresponding to one monitor is known, then it is logical to choose to carry out a measurement for a set number of monitors. The real benefit for normalisation according to standard monitor comes in analysis, where individual measurements recorded over a different number of monitors can be directly compared (though attention must be paid towards obtaining the correct statistical accuracy). In contrast, at the reactor source of the ILL, the neutron beam flux is very stable with time, meaning that normalisation according to a standard time is a reasonable alternative to standard monitor.

Neutrons that pass through the monitor then pass into the collimation section. This section is composed of a length of guide divided into discrete sections, where each section can be adjusted by the user to be either a section of supermirror neutron guide or a section of collimation. In contrast to the neutron guide sections, the inner walls of the collimation sections are strongly neutron absorbent. Typically section sizes are of order between 1 m and 3 m in length. The purpose of collimation to control the angular divergence of the beam that emerges from the velocity selector. This divergence can be reduced by progressively replacing neutron guide sections with collimation sections on moving upstream from the sample. Inserting a collimation section essentially moves the source aperture further upstream from the sample. Subsequently, the angular divergence of the neutron beam reduces, as neutrons are absorbed by the walls of the collimation sections. Reduced angular divergence contributes to improvements in all aspects of the resolution of the resultant diffraction patterns (see section 2.3), however the improvements come at the expense of neutron flux at the sample position. Therefore, the decision on the collimation length should be carefully considered in order to achieve the best

compromise between resolution and flux.

Between the end of the collimation section and the detector section lies the sample and sample environment. The details associated with this are described in section 2.2.1. Both diffracted and undiffracted neutrons that pass through the sample environment section will pass into the detector section. This section is composed of an evacuated detector tank that houses a position adjustable, two-dimensional multidetector. The position of the multidetector within the tank can be adjusted continuously over a maximum distance of order the maximum collimation length. A neutron is detected through its interaction with ^{3}He, which has a high neutron absorption cross-section. The capture of a neutron by ^{3}He produces a triton, a proton and 764 keV of energy. The charged decay products ionise the gas in the chamber, ultimately producing a charge pulse that is detected by a grid of high potential wires. Each wire has a horizontal and vertical index, allowing the determination of the location of the charge pulse associated with the neutron detection event. Each wire also has a finite size, which contributes to the binning of the data into pixels. There is a finite dead-time associated with each neutron detection event, typically of order $\sim 10\ \mu s$. This implies a maximum count-rate of order ~ 100 kHz, though precise values depend on the instrument. However, at the short wavelengths accessible to SANS, these count-rates are too low to process all of the events associated with an un-diffracted and un-attenuated beam. Therefore, in order not to overload the detector and be able to count the diffracted neutrons, a strongly neutron absorbent Cd beam-stop is placed over the detector to intercept the un-diffracted beam.

2.2.1 Sample and sample environment

To examine the FLL of a type-II superconductor, the material needs to be mounted appropriately into a sample environment that provides cryogenic temperatures and uniform magnetic fields. Fortunately, these sample environment requirements can be achieved by making use of cryomagnet facilities that are local to the institutes. A cryomagnet assembly houses both a variable temperature insert (VTI) and a split

pair of superconducting solenoid coils. The VTI provides a space within which the sample can be loaded and cooled using He exchange gas. The solenoid coils provide the magnetic field which is used to create the FLL inside a sample. This field is at its most uniform at the midpoint between the coils, and it is at this point the sample should be placed. In order to achieve this, the bottom of the VTI lies at this midpoint between the coils, providing a space where the sample can be positioned on the end of a sample stick. The coil arrangement indicated in figure 2.3 is typical of most experimental arrangements, with the field at the midpoint of the split pair parallel to the neutron beam. At ILL, the available horizontal fields can reach a maximum of 7 T, whilst at PSI magnetic fields up to 11 T are available. Both cryomagnet environments can provide sample temperatures down to 1.5 K. However, similarly at both institutes there is the option to load the sample onto the cold tail of a dilution refrigerator insert, and place this inside the VTI. Whilst this is possible at PSI with the 11 T SANS cryomagnet, at ILL a dilution insert can only be loaded into the VTI of a 2 T cryomagnet suitable for SANS. At all facilities, the cryomagnet assembly can be mounted onto goniometer tables so that the sample can be positioned so that it will intercept the neutron beam. The table and cryomagnet can then be rotated and titled through small angles using computer control, which is a necessity in order to carry out rocking curve measurements.

As we make extensive use of the dilution refrigerator (DR) system for the measurements described in chapter 4, we take a moment to describe the physics behind its operation in a little more detail. The cooling provided by a DR system relies on the phase separation of a mixture of ^{3}He and ^{4}He on cooling below a certain temperature. Figure 2.4 (a) shows a phase diagram describing the mixture of the stable isotopes of He, ^{3}He and ^{4}He, as functions of ^{3}He fraction and temperature. For temperatures below the tri-critical point at 0.86 K, the mixture spontaneously separates into a ^{3}He rich phase which is mostly ^{3}He, and a dilute phase which is mostly ^{4}He. We see from figure 2.4 (a) that below 0.86 K, and $T \rightarrow 0$, there will always be a finite fraction ($\sim$ 6 %) of ^{3}He within the dilute phase. As the ^{3}He rich phase has a lower density than the ^{3}He dilute phase, the rich phase floats above

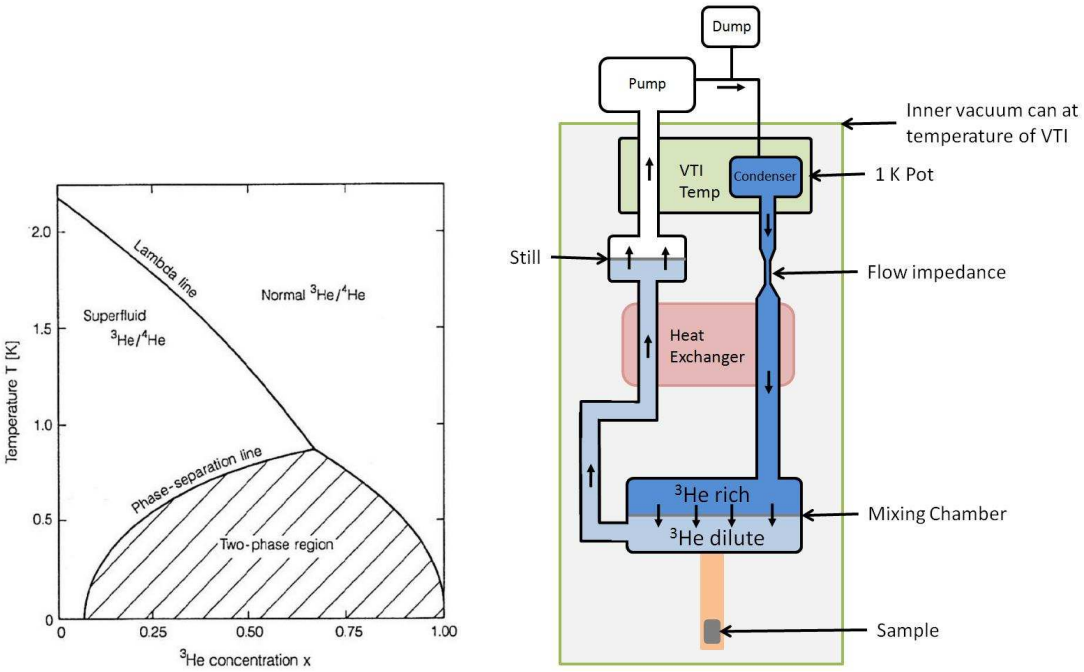

(a) ^{3}He/^{4}He phase diagram (b) Schematic layout of a dilution refrigerator

Figure 2.4: In (a) we show a phase diagram indicating the properties of the ^{3}He/^{4}He mixture, as functions of both temperature and molar fraction of ^{3}He (taken from *http://www.cresst.de*). In (b) we show a schematic diagram of a dilution refrigerator insert analogous to that used in the VTI of the 11 T SANS cryomagnet at PSI. The green box indicates the inner vacuum can which is placed inside the VTI of the cryomagnet. The pumps at the top indicate the gas handling system at room temperature.

the dilute phase, and the two phases are separated by a phase boundary. If we consider the ^{4}He in the dilute phase as inert and essentially non-interacting, the phase boundary represents a separation between an almost pure and ordered ^{3}He phase, and a dilute and more disordered ^{3}He phase. By pumping on the vapour above the dilute phase, ^{3}He atoms preferentially evaporate over ^{4}He atoms. This breaks the equilibrium of the dilute phase such that ^{3}He atoms from the rich phase are able to cross the phase boundary. However, in order to cross the boundary and reach the disordered phase, energy in the form of heat is required, which can be obtained from the walls of the chamber where the phase separated mixture is held (the mixing chamber). This chamber makes the thermal contact with the sample. In order to replenish the ^{3}He that moves across the phase boundary, ^{3}He is added to

the rich phase via a continuous cycle process. This continuous cooling process can occur for all temperatures, as figure 2.4 (a) shows the fraction of ^{3}He in the dilute phase always remains finite. A continuous cycle mode was adopted when we used the DR for the SANS experiments.

In figure 2.4 (b) we show a schematic diagram of the dilution refrigeration system and the major components involved in the continuous cycle mode of operation. The 1 K pot is used to condense the ^{3}He/^{4}He mixture, though sitting at the VTI temperature of 1.2 K, it does not provide sufficient cooling power to cause the phase separation of the mixture at 0.86 K. The extra cooling is provided by the still via a series of heat exchangers as the ^{3}He heads towards the mixing chamber. It is crucial for cooling to base temperature that the ^{3}He/^{4}He balance of the mixture is chosen such that the phase separation boundary lies inside the mixing chamber, and the liquid surface of the dilute phase lies in the still. This allows the pumping above the liquid surface of the dilute phase where the ^{3}He preferentially evaporates over the from the ^{4}He. Carefully heating the still can also accelerate the evaporation of ^{3}He gas, and accelerate the cooling rate. The ^{3}He gas evaporated is pumped to a gas-handling system at room temperature, where it is recycled and cleansed on passing through a cold trap held at 77 K. It is then cycled back to the 1 K pot to re-condense. The flow impedance below the 1 K pot ensures there is a sufficiently high pressure for the gas to condense.

When loading any sample onto a sample stick, or onto the cold tail of the DR, in order to keep background scattering as low as possible it is important to minimise the amount of material that the neutron beam encounters. The main sources of background scattering include the cryomagnet itself, the sample and sample mounting. To minimise the scattering from the cryomagnet, purpose built sapphire windows are placed at the neutron entry and exit points which allow access through the walls of the otherwise Al construction. The plate upon which the sample mounted, and the sample holders which hold the plates, are typically made of pure and thin Al. Pure Al is chosen as it is free of precipitates which contribute to the small-angle

background scattering, and it has a low absorption cross-section. The adhesive used to attach the sample to the sample plate is typically diluted down, and the applied layer as thin as possible in order to keep the background scattering low and maintain good thermal contact between the plate and the sample. The sample itself can contribute to the background in the form of 'metallurgical' scattering. This arises due to imperfections in the sample such as planar defects, and is sometimes seen clearly in the background. Reflections from sample edges can also be observed on the detector and sometimes look like convincing Bragg spots. However, these can be suppressed by identifying the likely reflecting edges on the sample, and painting over them with strongly neutron absorbing Gd_2O_3 paint. It is also common to place a neat fitting Cd window around the sample in order to define the illumination area. This helps limit the illumination area of the beam and help reduce unnecessary background signal. Typically, this Cd window placed on the sample holder defines the sample aperture. Therefore, the aperture at the sample end of the collimation section is then slightly larger than this so that the illumination area of the sample is defined by this sample aperture.

2.3 Resolution effects

As mentioned in section 2.1.2 the δ-function description of the FLL described by equation 2.19 is not realised. Due to contributions from both the instrument and FLL in the sample itself, Bragg spots exhibit a finite size in reciprocal space. This is represented in figure 2.5 where we show a schematic diagram of the usual SANS experimental setup, with field parallel to the neutron beam. In this geometry we see that a Bragg spot exhibits characteristic dimensions W_l, W_r and W_a which can all be measured.

Quantitative treatments of the resolution and resolution function are described by Cubitt et al. (1992) and Brown (2005). In particular, Cubitt et al. (1992) developed a convenient model where contributions to the finite widths of the observed diffraction spots can be represented as gaussian functions, each with a standard de-

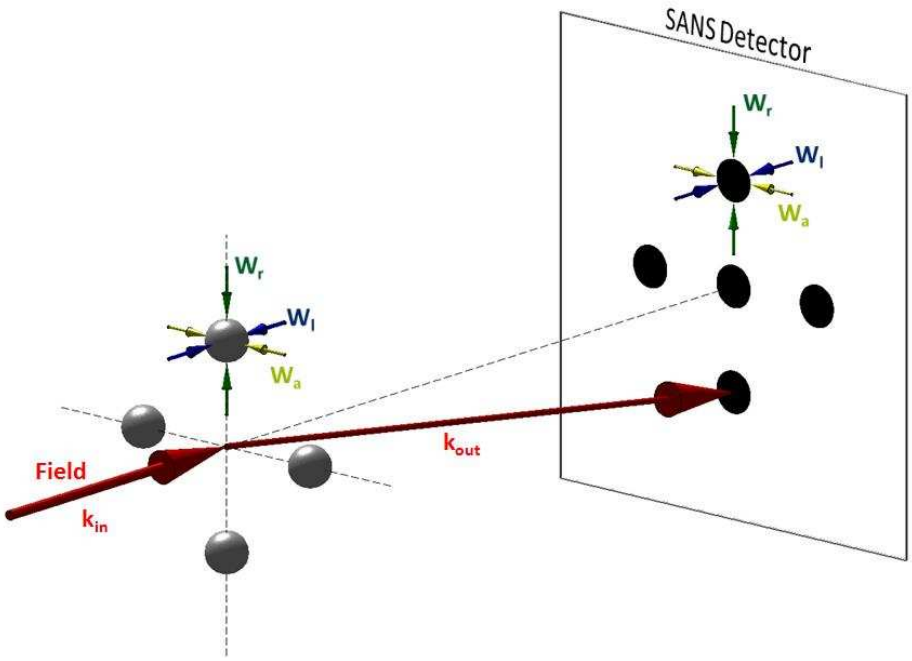

Figure 2.5: A schematic diagram of the parallel field SANS geometry. For this arrangement the field is approximately parallel to the incoming wavevector, $\mathbf{k}_{in}$. The arrangement of spheres represents a square FLL coordination in reciprocal space. The use of spheres is to indicate the finite size of a three-dimensional Bragg spot in recpirocal space. The small paired arrows indicate the angular width of the Bragg spot along three directions; W_l is the longitudinal width, W_r is the radial width and W_a is the azimuthal width. The detector image represents a projection of the reciprocal FLL as would be observed on the detector. W_l is measured out of the plane, whilst W_r and W_a are measured in the detector plane.

viation representative of the actual distribution. The overall distribution represents a convolution of the instrument contributions and those from the FLL within the sample.

The length of the collimation section, and the dimensions of the source and sample apertures, determines the angular spread, or beam divergence, a of the incoming beam. If s_o and s_a respectively denote the widths of the source and sample apertures, and l_c and l_d respectively denote the collimation length between the apertures and the distance between the sample aperture and detector, Pedersen et al. (1990) show that the FWHM spread a can be represented as

$$a \simeq \begin{cases} s_o/l_c & \text{if } s_o/(l_c+l_d) \geq s_a/l_d \\ s_a\left(l_c^{-1}+l_d^{-1}\right), & \text{otherwise.} \end{cases} \tag{2.23}$$

For circular apertures, Pedersen et al. (1990) calculate small corrections to equation 2.23.

The second FWHM spread, denoted b, arises due to the imperfection of the FLL in the sample, and indicates the effective spread b of the Bragg plane angle away from the mean. In reciprocal space this translates into an angular spread of **G** both within, and normal to the scattering plane. For the parallel field geometry shown in figure 2.5, b indicates a measure of the longitudinal correlations of the flux lines along the field direction. Similarly, any mosaic spread in FLL crystallites within a sample will also contribute to the spread in the b.

The FWHM spread in c reflects the spread in Bragg angle θ_B, which appears in reciprocal space as a spread in the magnitude of the scattering vector. The major contribution to c arises due to the wavelength spread of the beam that emerges from the velocity selector. Strictly, c also includes a measure of the spread Bragg plane spacing $\Delta G/G$,

$$\left(\frac{c}{\theta_B}\right)^2 = \left(\frac{\Delta\lambda_n}{\lambda_n}\right)^2 + \left(\frac{\Delta G}{G}\right)^2. \tag{2.24}$$

However, as the spread in θ_B is small for small-angle scattering, it is rather difficult to measure the contribution due to the spread in the Bragg plane spacing.

At the Bragg peak, Cubitt et al. (1992) derive the following expression for the radial width of the Bragg spot W_r as shown in figure 2.5,

$$W_r^2 = \frac{a^2c^2 + a^2b^2 + 4b^2c^2}{a^2 + b^2 + c^2}. \tag{2.25}$$

which represents the spread of the measured exit angle. The expression for the width of the Bragg spot that lies out of the plane of the reciprocal lattice (rocking curve width) W_l is derived to be

$$W_l^2 = a^2 + b^2 + c^2, \tag{2.26}$$

whilst finally the azimuthal spread W_a is shown to be

$$W_a^2 = a^2 + (2\theta_h r_t)^2, \tag{2.27}$$

where $2\theta_h$ describes the rotation angle of the Bragg planes about the beam axis, whilst r_t is the FWHM of the angular spread of the reciprocal lattice vector about this axis. We see that within equations 2.25 to 2.27, the instrumental contribution to the size of a Bragg spot can be found by evaluating the widths a and c, and setting all other terms, which are associated with the FLL, to zero.

Flux line lattice structure transitions in twin-free $YBa_2Cu_3O_7$

We report new results from SANS studies of the flux line lattice (FLL) in the maximally doped High-T_c superconductor $YBa_2Cu_3O_7$. Using a near perfectly twin-free sample, our measurements reveal the intrinsic FLL structure with the field applied parallel to the crystal **c**-axis ($H \parallel$ **c**). Our results at 2 K show that at low fields, the FLL structure is composed of a single distorted hexagonal domain aligned with the crystal axes. On increasing the field, at 2.3 T we observe a first-order 90° reorientation transition into a different single domain hexagonal structure. We suggest this transition is driven by the increasing prominence with field of non-local effects combined with a Fermi surface anisotropy. At 6.7 T we observe another first-order transition into a rhombic structure phase which could be driven by the increasing prominence of the order-parameter anisotropy. The observed distortion of the rhombic structure is orthogonal to that of the hexagonal structures, possibly providing evidence for a high-field s-wave component to the predominantly $d_{x^2-y^2}$ order parameter. However, an equally possible interpretation for the emergence of the high field structure phase is that it is due to the increasing prominence of further Fermi surface effects.

Measurements of the FLL form factor in the low field structure phase show our results are describable using a phenomenological model. However, at higher fields the model breaks down, and it is necessary to introduce several assumptions in order to understand the data. We discuss the field- and temperature-dependence of the form factor data within the framework of the predictions of the available theories and other experimental data.

3.1 Introduction to $YBa_2Cu_3O_{7-\delta}$

The initial discovery of High-T_c superconductivity in cuprate materials was made by Bednorz and Müller (1986), at $\sim$35 K in the $La_{1.85}Ba_{0.15}CuO_4$ (LBCO) system. The discovery caused great excitement, as the record of the highest T_c in *any* material had leapt from 23.2 K (held by the alloy Nb_3Ge) to $\sim$35 K in LBCO. However, more quickly followed with the synthesis of, and observation of superconductivity in, a Y-Ba-Cu-O system in 1987 (Wu et al., 1987). Their samples exhibited critical temperatures within the range of 80 K to 93 K, being above that of the boiling point of liquid nitrogen at 77 K, a coolant that is cheaper, more plentiful, and easier to handle than liquid helium. Therefore, it is perhaps the discovery of superconductivity in the Y-Ba-Cu-O system, and other cuprates shortly afterwards that possess even higher critical temperatures, (e.g. $Bi_2Sr_2Ca_nCu_{n+1}O_{2n+6-\delta}$ (BSCCO) ($T_c > 105$ K) (Maeda et al., 1988) and $Tl_mBa_2Ca_{n-1}Cu_nO_{2n+m+2+\delta}$ ($T_c > 120$ K) (Sheng and Hermann, 1988)), that were responsible for stimulating the ongoing worldwide research effort into understanding, and manipulating these materials.

To aid the ensuing discussion on the more important chemical and physical properties of $YBa_2Cu_3O_{7-\delta}$, we briefly review the crystal structure. We note that δ in the chemical formula is variable between 1, which is oxygen deficient $YBa_2Cu_3O_6$, and 0, which is stoichiometric $YBa_2Cu_3O_7$. The crystal structures for both of these phases are shown in figure 3.1. Within the structures there are clear layers; a CuO_2 bilayer sandwiching an Y atom, and BaO planes sandwiching a Cu plane (or CuO plane (figure 3.1 (b)). The Y and Ba atoms serve as fixed charges and stabilise the crystal structure. The electronic nature of the CuO_2 planes is important as, within the superconducting phase, the majority of the low lying energy states that govern the overall macroscopic behaviour originate from the Cu-O bonds here. Furthermore, as the common constituent unit of *all* cuprates is the CuO_2 plane, we concentrate our initial discussion here.

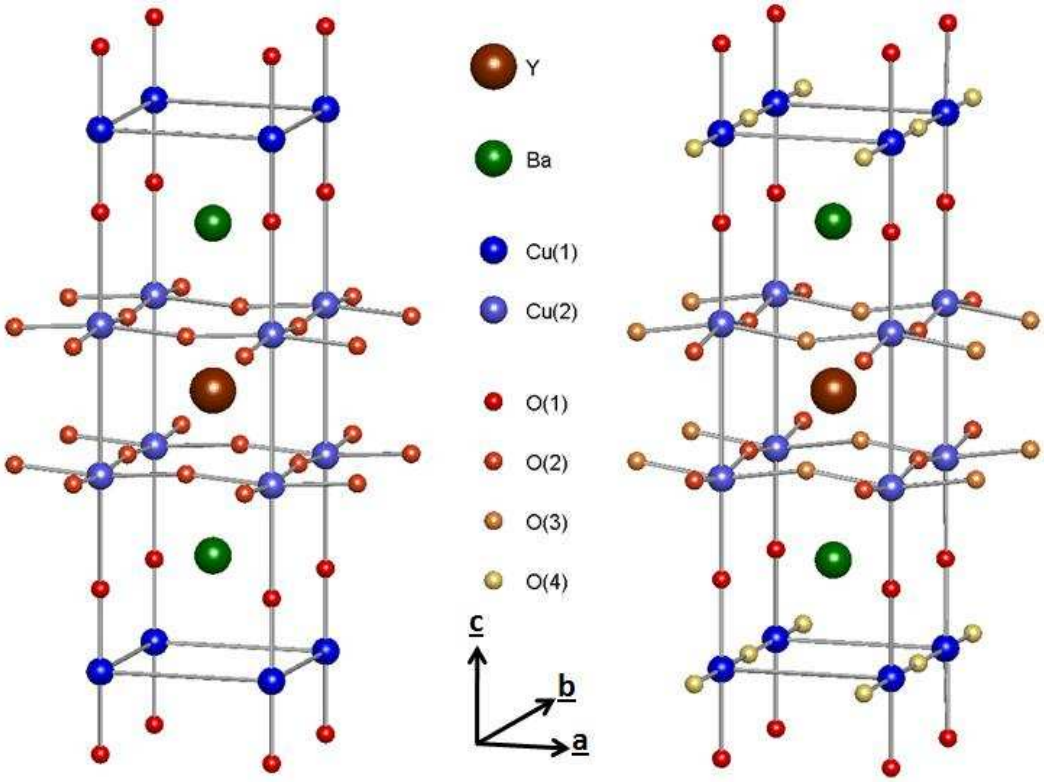

(a) $YBa_2Cu_3O_6$ (b) $YBa_2Cu_3O_7$

Figure 3.1: The crystal structures of (a) $YBa_2Cu_3O_6$ and (b) $YBa_2Cu_3O_7$. The crystal axes and key between the two figures apply to both, and indicate that there are just two inequivalent oxygen sites in $YBa_2Cu_3O_6$, as opposed to four in $YBa_2Cu_3O_7$.

3.1.1 CuO_2 planes and the metal-insulator transition

Consider the CuO_2 plane as shown on the left hand side of figure 3.2. When electrically neutral, all the Cu^{2+} ions in the CuO_2 planes have nine electrons in their $3d$ shell. However, under the influence of crystal field effects within the host cuprate, the energy degeneracy of the $3d$ states is broken. Eight of the electrons in the $3d$ orbital are paired off at lower energy, leaving an unpaired electron in the higher energy $d_{x^2-y^2}$ orbital. It is generally accepted that this orbital and its interactions are responsible for the majority of the low energy physical phenomena in the cuprates. This orbital strongly hybridises with the relevant $2p_{x,y}$ orbitals of the in-plane O^{2-} ligands to form three bands. These respectively correspond to bonding, non-bonding and anti-bonding orbital configurations as depicted in Fig 3.2.

Band structure calculations based solely on the CuO_2 plane predict the bonding

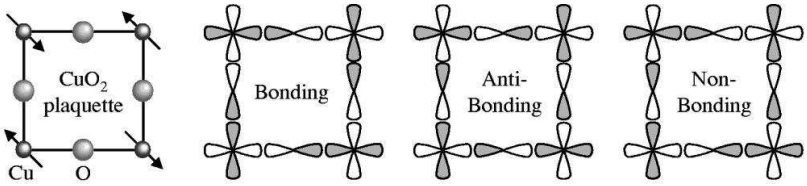

Figure 3.2: Schematic diagram showing the various possible combinations of wave-function symmetry induced by the hybridisation of oxygen and copper orbitals in the CuO_2 plane. After Damascelli et al. (2003).

and non-bonding bands to be full, and the anti-bonding band to be half filled at the Fermi energy (Damascelli et al., 2003). As the carrier density for each CuO_2 planar unit cell is a single hole, in the absence of interactions, these should delocalise and the planes should show metallic behaviour. However, this phase is well-known to be a Mott-type insulator, exhibiting commensurate $S = \frac{1}{2}$ antiferromagnetism ($T_N > 400$ K in $YBa_2Cu_3O_6$, as verified by neutron scattering (Tranquada et al., 1988)) with the large on site repulsion U, originating from the Cu ions. However, the energy difference Δ, between the Cu d levels and the O p levels is less than the on-site repulsion energy U. Hence, the lowest energy excitation is of order the charge transfer energy, thus characterising the plane more correctly as a charge transfer insulator. Most models predict the detailed band structure between an empty upper band and nearest filled energy band as having an energy gap of order Δ (see for example, Zhang and Rice (1988)).

It lies beyond the scope of this thesis to go into the details of the theories that attempt to model the insulating and antiferromagnetic situation. Here, we attempt to highlight the strongly-correlated nature of the charge carrier interactions within the planes. In $YBa_2Cu_3O_{7-\delta}$, the addition of oxygen atoms dopes holes into the apical O(1) atoms and subsequently into the CuO_2 planes. Initially for low dopings, figure 3.3 (b) shows that $YBa_2Cu_3O_{7-\delta}$ remains insulating. This is because the holes doped into the planes localise with the oxygen ions rather than the copper ions, even though most of the latter have a half-filled d-orbital. As the doping increases, interactions between the doped holes and the Cu spins eventually allow spins to delocalise, thus causing the antiferromagnetic correlations to become increasingly

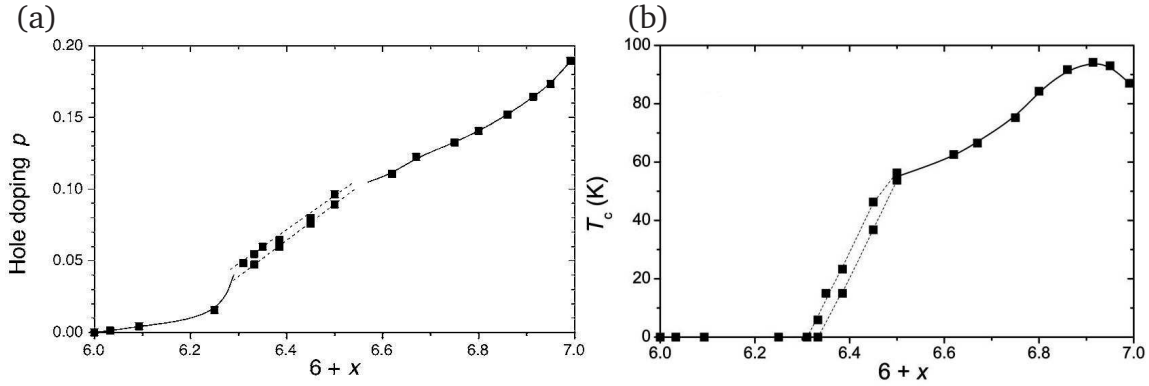

Figure 3.3: Results of a systematic investigation of the oxygen doping dependence in $YBa_2Cu_3O_{7-\delta}$ in terms of (a) the number of holes doped per Cu planar atom into a CuO_2 plane p, and (b) the zero-field T_c, as reported by Liang et al. (2006). In both cases, the horizontal axis is shown as $6 + x$, which is equivalent to $7 - \delta$ notation used in the text, where $x = 1 - \delta$.

unstable. By $7 - \delta \sim 6.3$, or $p \sim 0.04$, the commensurate Néel state collapses, and the system becomes more metal-like, and ultimately superconducting. The collapse of the commensurate Néel state with hole doping does not represent the disappearance of *underlying* antiferromagnetic charge or spin correlations within the superconducting phase. Some believe (Zaanen and Gunnarsson, 1989) the added holes contribute to the formation of low-dimensional and incommensurate charge/spin 'stripes' (strongly supported by experiment (Tranquada et al., 1995; Mook et al., 2000; Hoffman et al., 2002; Hinkov et al., 2004)) that co-exist and compete with superconductivity in the under-doped regime [5]. As the hole-doping increases the superconductivity becomes more potent, exhibiting a maximum zero-field T_c of ~ 92 K for $7 - \delta \sim 6.93$, or $p \sim 0.165$. This is referred to as optimal doping, and here (and for larger p - over-doping) antiferromagnetic correlations finally become negligible (Orenstein and Millis, 2000), and Fermi liquid-like behaviour is recovered.

The under-doped regime of $YBa_2Cu_3O_{7-\delta}$, where $p < 0.165$, is where most research is performed. This is due to the fundamental nature of the questions being asked such as those concerning the descriptions of spin dynamics, the structure and

[5] In this context, we mention that, in addition to solving the outstanding problem of the microscopic mechanism of High-T_c superconductivity, a major contribution towards this is thought to lie with a description of how the low energy quasiparticle states emerge from the insulating state as a function of planar hole-doping.

evolution of the Fermi surface as a function of doping, and the character of the 'pseudogap' phase in the 'normal' state above T_c. The work presented in this thesis has been obtained from measurements on a over-doped sample of $YBa_2Cu_3O_7$, and we mention in passing that under-doped materials command a lot of attention in the literature. For optimally- and over-doped cuprates, the physics appears to be reasonably consistent with a Fermi liquid-like picture, where the materials possess large and coherent Fermi surfaces.

3.1.2 Doping dependence of the single crystal structure

The insulating parent compound is $YBa_2Cu_3O_6$ (Fig 3.1 (a)) and, as there is no chemical distinction between the **a** and **b** directions, the crystal structure is tetragonal and of type $P4/mmm$. Initially for low hole dopings, the oxygen atoms randomly occupy interstitial sites between the Cu(1) ions that lie between the BaO planes. Again due to a lack of distinction between the crystal directions, the occupied sites lie along both the **a** and **b** directions (contrary to exclusively along **b** as indicated in Fig 3.1 (b)). Therefore, initially for large δ, the structure remains tetragonal. However, coincident with the emergence of superconductivity at $p \sim 0.04$, the **a**-**b** symmetry is broken, and oxygen atoms preferentially occupy O(4) sites. The resulting direction where the average length of the Cu(1)-O(4) chains is longest is assigned the crystal **b**-direction, and the crystal structure undergoes a transition to a lower symmetry orthorhombic structure of space group $Pmmm$. This transition in structure is a crucial detail with respect to crystallographic twinning, the effects of which on the flux line lattice are discussed later. At room temperature for $YBa_2Cu_3O_{6.93}$, the lattice parameters of the orthorhombic structure are **a** = 3.822 Å, **b** = 3.887 Å, and **c** = 11.680 Å (Jorgensen et al., 1990).

For a certain doping, the percolation of the CuO chains within the orthorhombic structure allows the formation of various oxygen ordered superstructures. Examples of these are shown in figure 3.4, with figure 3.4 (c) representative of the long-range ortho-I (OI) oxygen order of the sample studied in this thesis. Other dopings exhibit different orderings which essentially correspond to a different periodicity along the

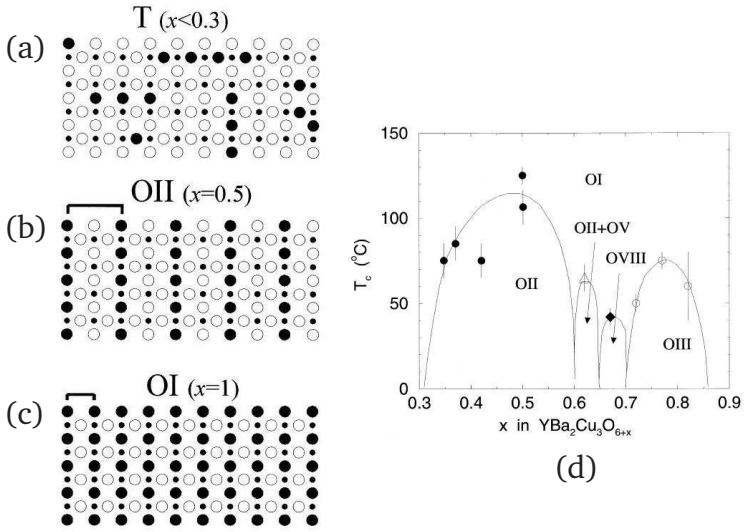

Figure 3.4: Various ordering configurations of the CuO chains are shown in (a) - (c). In all figures, small filled circles correspond to Cu atoms, whilst large filled and large empty circles correspond to occupied and unoccupied oxygen sites respectively. In (a) is shown the proliferation of short CuO chains in the insulating and tetragonal phase. In (b) and (c) the CuO chain ordering is shown for the $YBa_2Cu_3O_{6.5}$ and $YBa_2Cu_3O_7$ structures respectively. In (d) is a phase diagram showing the dopings at which different superstructures appear. The phase boundaries mark the transition points between the high temperature tetragonal crystal structure and the low temperature orthorhombic structures. After Andersen et al. (1999) and references therein.

a-axis between alternating full CuO chains and empty Cu chains. For example, the oxygen ordered CuO chains of $YBa_2Cu_3O_{6.5}$ have a periodicity of 2**a** for the ortho-II (OII) phase - see figure 3.4 (b). Figure 3.4 (d) shows a 'phase diagram' of the doping dependence of the various types of oxygen ordering superstructures. The figure shows that for any doping, there is a transition from a high symmetry tetragonal phase to a lower symmetry orthorhombic phase that occurs on cooling during the sample preparation. At high temperatures ($T > 400$ K), regardless of the doping, the structure is in an OI phase as finite length chain fragments align at high temperature (Andersen et al., 1999).

The superconductivity that emerges is particularly sensitive to the quality of the oxygen ordering for a given superstructure. This is unsurprising, as the CuO chains can be considered as one-dimensional systems, which are highly sensitive

to the effects of disorder. Disordered and fragmented chains are known to degrade the superconductivity within the CuO_2 planes (due to a reduction in the hole-doping) (McCormack et al., 1992) meaning that often from the oxygen-doping alone it is not possible to predict the value that T_c will take. For example, in $YBa_2Cu_3O_{6.4}$ a high degree of chain disorder can drive a sample insulating (Veal and Paulikas, 1991), whilst in $YBa_2Cu_3O_{6.5}$, disrupting the OII order can depress T_c by as much as 6 K (Bobowski et al., 2007). However, the problem is somewhat alleviated through the observation of an empirical relationship between value of the **c**-axis lattice parameter and the hole doping per Cu planar atom, p (and hence T_c) (Liang et al., 2006).

3.1.3 Twin planes in orthorhombic $YBa_2Cu_3O_{7-\delta}$

For oxygen dopings where $7 - \delta > 6.3$, the system is superconducting and the crystal structure is orthorhombic. The degree of orthorhombicity is determined by the doping (Jorgensen et al., 1990), though for all dopings the inequality of the **a** and **b** lattice parameters is relatively small, being of order 2 % for optimally-doped $YBa_2Cu_3O_{6.93}$. However, this difference does have important experimental consequences regarding the effects of crystallographic twinning. Due to the inequality of the **a** and **b** directions, as-grown samples of $YBa_2Cu_3O_{7-\delta}$ naturally decompose from a single crystal domain at high temperature into 'twin' domains on cooling.

The twin domains occupy different regions of the crystal and possess mutually orthogonal orientations of the **a** and **b** crystal axes. Domains of each orientation nucleate at various places and, dependent on the thermal history of a sample, can vary between nanometres and fractions of millimetres in size. Due to this vast variation in length scale, and the sensitivity of a domain size to specific preparation conditions, the physical effects associated with twins suffer from a lack of reproducibility between samples. Dependent on the orientation of a certain twin, the boundary between the two orientations of single crystal form along the [110] or [1-10] crystallographic directions. Hence there are two orthogonal twin-domain regions within a sample. Figure 3.5 (a) shows a photograph of a sample containing

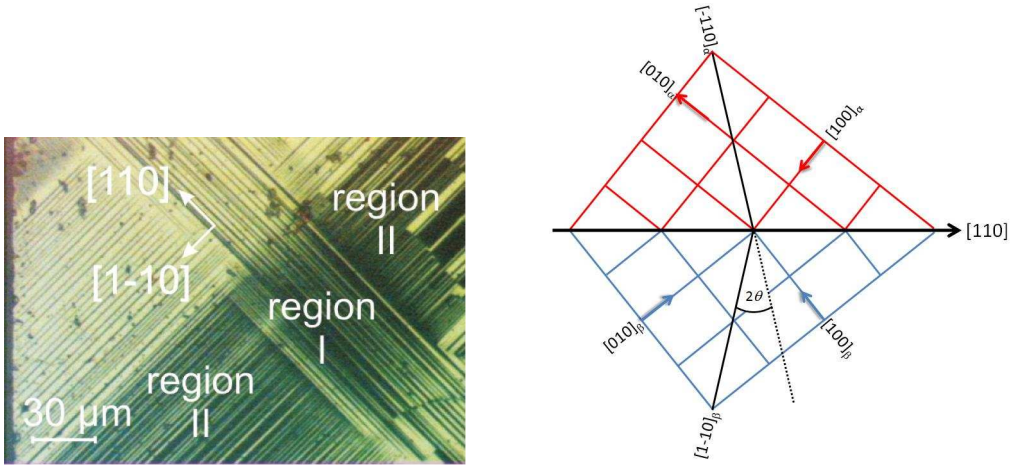

(a) (b)

Figure 3.5: In (a) we show a photograph of the (001) surface of a twinned sample of $YBa_2Cu_3O_{7-\delta}$ illuminated using polarised light. The two regions labelled as 'Region I' and 'Region II' indicate regions where the twin boundaries are aligned along [110] or [1-10] respectively. In (b) we show a schematic diagram of an ideal border region in real-space between two crystal domains labelled α and β. The angle 2θ is the shear angle between the $[-110]_\alpha$ and $[1-10]_\beta$ directions. Note the sketch in (b) corresponds to a section of Region I from (a). Photograph in (a) courtesy of C.T. Lin, MPI Stuttgart.

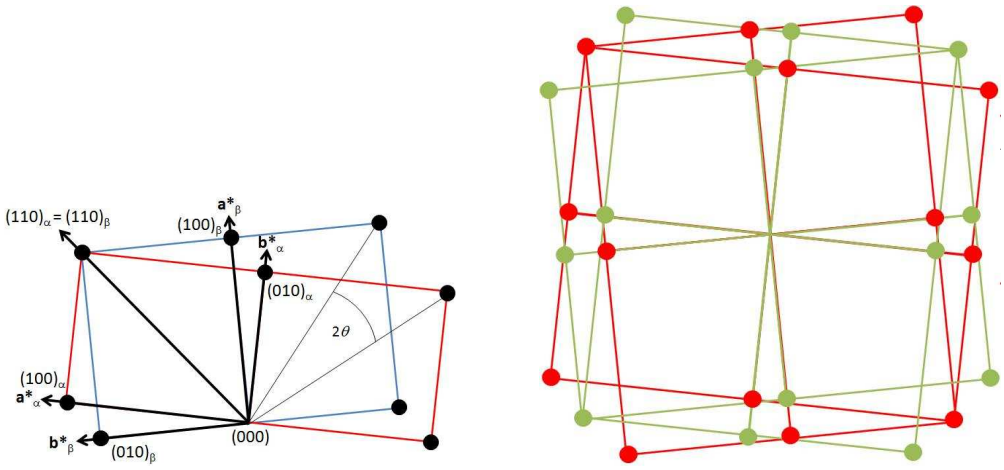

(a) (b)

Figure 3.6: Schematic diagrams demonstrating (a) the reciprocal space atomic lattice from the twin-domain Region I of figure 3.5 (b). The reciprocal space lattice of domain of the α domain is in red, whilst it is in blue for the β domain. In (b) we show the overall reciprocal atomic lattice for both twin domain regions. The reciprocal space lattice of Region I is shown in red, whilst that of Region II is shown in green.

these two region types where the twin boundaries of Region I are aligned along [110] and those of Region II aligned along [1-10].

Figure 3.5 (b) shows an ideal real-space representation of a twin-boundary in the twin-domain of Region I depicted in figure Figure 3.5 (a). This figure also shows the shear angle between the [110] directions of the two domains labelled as α and β [6]. On rotating the crystal structure in Region I to obtain the resulting real- or reciprocal-space crystal lattice of Region II, the lattice of Region I should be rotated by $90^\circ \pm \epsilon$, where $\epsilon \sim \theta$. In heavily twinned samples, even the value of ϵ can vary in the same sample, which results in many slightly differently oriented domains; the discussion here concentrates on lightly twinned samples. Figure 3.6 (a) shows the atomic lattice in reciprocal space for the twin domain of Region I shown in figure 3.5 (b). Here it is clear to see that within a twin domain region, there are two orientational states of the reciprocal atomic lattice. Accounting for the other twin-region, Region II, figure 3.6 (b) shows that in total there are four orientational states of the crystal lattice, with the α and β domains of Region I at an angle of $\sim 2\theta$ to the equivalent domains in Region II.

In experiments on twinned samples, the four orientational states contribute to the observations equally. Therefore, the conclusions drawn from studies on twinned samples of $YBa_2Cu_3O_{7-\delta}$, particularly those studies examining various anisotropies within the plane, are often limited by being unable to distinguish between the intrinsic physical effects and those influenced by the twinned nature of the crystal lattice. FLL studies are no exception, as the orientations of equivalent FLL structures will be different according to which orientational state they occupy. Furthermore, flux lines are susceptible to pinning effects arising from twin boundaries. In reality, the boundaries both within a twin domain and between different twinned regions can be regarded as regions of both long-range point-like disorder, and also where the superconducting order parameter is depressed from the bulk value. Hence, flux

[6] The angle 2θ is found from

$$2\theta = 2\left(90 - 2.\tan^{-1}\left(\frac{\mathbf{a}}{\mathbf{b}}\right)\right) \tag{3.1}$$

and for optimally-doped $YBa_2Cu_3O_{6.93}$, $2\theta \sim 1.8^\circ$.

lines can preferentially pin to these defects to minimise their free energy. Scanning tunnelling microscopy (STM) shows clear evidence in real-space for flux lines pinning to a twin-boundary (Maggio-Aprile et al., 1997; Shibata et al., 2003). Bulk evidence is provided through the reciprocal space studies of numerous SANS measurements (Yethiraj et al., 1993b,a; Keimer et al., 1994; Johnson et al., 1999; Simon et al., 2004; Brown et al., 2004; White et al., 2008). From the SANS studies, the results indicate that pinning to twin boundaries is strongly influential in determining the long-range positional coordination of the FLL structure, as the FLL specifically orients in regions away from twin boundaries to accommodate the alignment of flux line planes parallel to the direction of the twin-plane. This is supported by the STM study of Shibata et al. (2003), which shows the FLL coordination to be influenced by flux line planes pinned to a twin boundary for distances up to 1 μm away.

3.1.4 Band structure of $YBa_2Cu_3O_7$

For maximally doped YBCO, the theoretical picture of the low energy states provided by band structure calculations appears to be well established, and reasonably consistent across different calculational techniques (Pickett et al., 1990; Andersen et al., 1995; Elfimov et al., 2008). The results of the linear augmented plane wave (LAPW) calculations of Pickett et al. (1990) are shown in figure 3.7.

Note that for $YBa_2Cu_3O_7$, the first Brillouin zone is centred on S, and not Γ, as the principal carriers are holes. Figure 3.7 (c) shows that the Fermi surface is predicted to be comprised of four bands. Two large, concentric and distorted cylinders centred on S/R, that cross the YS/TR and XS/UR boundaries, originate from within the CuO_2 planes. The band labelled 'b' corresponds to the symmetric (about the mirror plane of the CuO_2 bilayer) linear combinations of the planar $pd\sigma$ antibonding orbitals ($O(2)_y$ - $Cu(2)_{x^2-y^2}$ - $O(3)_x$). This band is called the bonding band and has a lower energy than the band labelled 'a' which corresponds to the antisymmetric linear combination of bonding wavefunctions. Hence, the 'a' band is called the antibonding band. The bands labelled 'c' and 's' are the 'chain' and 'stick' bands, which are predominantly associated with the CuO chains that form

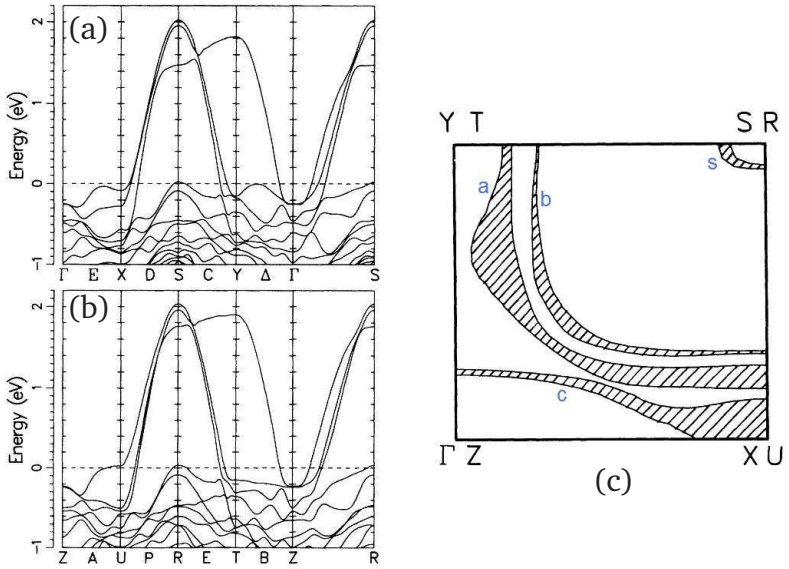

Figure 3.7: The results of band structure calculations performed by Pickett et al. (1990). In (a) and (b) the calculated band structure is shown at (a) $k_z = 0$ and (b) $k_z = \pi/\mathbf{c}$. In (c) we show the irreducible quadrant of the first Brillouin zone derived from the results shown in (a) and (b). In (c), k_x is horizontal and k_y vertical, with the shaded regions indicating the degree of k_z dispersion between k_z and $k_z = \pi/\mathbf{c}$, but projected onto the $k_x - k_y$ plane. The labels, 'a','b','c' and 's' refer to bands discussed in the text.

along the crystal **b**-direction. The essential orbitals for the 'c' band are the chain $pd\sigma$ antibonding orbital made from $O(4)_y$ and the $pd\sigma$ antibonding dumbbell orbital $O(1)_z$ - $Cu(1)_{z^2-y^2}$ - $O(1)_z$. The stick band is composed of a rather more complicated bonding combination of two chain $pd\pi$ antibonding dumbbell orbitals ($O(1)_x$ - $Cu(1)_{xz}$ - $O(1)_x$ and $O(1)_y$ - $Cu(1)_{yz}$ - $O(1)_y$) and an antibonding linear combination of $O(4)_z$ with the $pd\pi$ bonding dumbbell orbital $O(1)_y$ - $Cu(1)_{yz}$ - $O(1)_y$. Experimental evidence in favour of the theoretical model of the Fermi surface is available from angle-resolved photoemission spectroscopy (ARPES) studies, which clearly observe the bonding, antibonding, and chain bands (Schabel et al., 1998; Zabolotnyy et al., 2007; Hossain et al., 2008). Evidence for the stick band is more controversial, with Schabel et al. (1998) claiming to observe it, but the more recent study of Zabolotnyy et al. (2007) arguing otherwise. It is possible the band is at lower binding energy than that shown in the predictions of figure 3.7 (a), though

this would have to be appreciably lower than predicted to escape detection by the ARPES measurements. In spite of this uncertainty, the contribution of the stick sheet to the supercurrent density is expected to be small and is thus not considered from this point on.

An important consequence of the low energy band structure is that there is a noticeable anisotropy between various moments of the Fermi velocity distribution within the plane. This is directly relevant to the interpretation of observations of the FLL structure within both the local and non-local London regimes. To a leading order approximation, the strongest contribution to the in-plane anisotropy of the Fermi velocity originates from the near one-dimensional dispersion associated with CuO chains that runs effectively parallel to ΓX - see figure 3.7 (c). As the dispersion is strongest along k_x, corresponding to the real-space crystal **b**-axis (the CuO chain direction), this results in an anisotropy in the second moment of the Fermi velocity such that $\langle v_{F,y}^2 \rangle > \langle v_{F,x}^2 \rangle$. A similar contribution from bands 'a' and 'b' is expected to be much less, as for these bands, allowing for small deviations in the detailed band structure, $\langle v_{F,y}^2 \rangle \sim \langle v_{F,x}^2 \rangle$. Therefore, the overall anisotropy of the second moment of the Fermi velocity is dominated by the contribution of the chain band. Within the framework of local anisotropic London theory, this results in a non-identity effective mass tensor (as $m_{ij}^{-1} = \langle v_i v_j \rangle / \left(\det \langle v_i v_j \rangle\right)^{1/3}$ (Kogan et al., 1997a)) and an anisotropy of the in-plane London penetration depth γ_{ab} (Campbell et al., 1988; Thiemann et al., 1989; Daemen et al., 1992), of which a quantitative estimate can be obtained from the measure of the distortion of hexagonal FLL structures at low fields.

To next order approximation, the square-like distortion of the bonding and anti-bonding bands *is* important, as the higher moment components of the Fermi velocity play in a role in models that extend the anisotropic London theory through the incorporation of non-local corrections (Kogan et al., 1997a; Franz et al., 1997). The symmetry of the distortion of these bands (again to a simple approximation) leads to $\langle v_{F,x}^4 \rangle \sim \langle v_{F,y}^4 \rangle > \langle v_{F,x}^2 v_{F,y}^2 \rangle$, i.e. a smaller Fermi velocity along [110] than along either x or y. For the non-local theories of Kogan et al. (1997a) and Franz et al.

(1997), and the numerical work of Nakai et al. (2002), such an anisotropy in the fourth moment of the Fermi velocity is vitally important for both the stabilisation and orientation of a square FLL structure at high-field.

We note that the band structure calculations predict none of the main bands to be closed in the **c**-axis direction, implying that the component of the carrier group velocity v_g ($\nabla_{\mathbf{k}} E$, where E is the carrier energy) in this direction is small. Figures 3.7 (b) and (c) further show that whilst the bonding, antibonding and stick bands are predicted to be weakly dispersive in the k_z direction, the k_z dispersion of the chain band is predicted to be larger, particularly around the X/U point. Therefore, whilst the band-structure calculations predict the major part of the electronic character to be well described as two-dimensional, the chain k_z dispersion is thought to account for the smaller out-of-plane in-plane resistivity anisotropy, ρ_c/ρ_{ab} observed in $YBa_2Cu_3O_{7-\delta}$ than, for example, in chain free BSCCO. Early normal-state resistivity measurements taken just above T_c as functions of both temperature and crystal direction reveal ρ_c/ρ_{ab} to be $\sim$ 70 for optimally-doped $YBa_2Cu_3O_{6.93}$. For underdoped $YBa_2Cu_3O_{6.82}$, ρ_c/ρ_{ab} was observed to be $\sim$ 1,700 (Ito et al., 1991). As a comparison, a similar estimate of ρ_c/ρ_{ab} in optimally doped $Bi_2Sr_2CaCu_2O_{8+\delta}$ (where $\delta = 0.24$) is $\sim$ 100,000 (Watanabe et al., 1997). Whilst this shows optimally- and over-doped $YBa_2Cu_3O_{7-\delta}$ to be relatively more three-dimensional than CuO chain free BSCCO, we conclude that at least part of this originates from the contribution of the chain band dispersion, the prevalence of which is consistent with the doping dependence. However, as mentioned in the previous section, the components of the dispersion originating from the chain band will be strongly dependent on the quality of the O(4) atom ordering of the CuO chains.

3.1.5 Multi-band superconductivity in $YBa_2Cu_3O_{7-\delta}$

Overdoped samples of $YBa_2Cu_3O_{7-\delta}$ exhibit classic characteristics of strongly type-II materials. For example, at low fields and temperatures, the in-plane penetration depth is $>$100 nm, and the in-plane coherence length is just $\sim$2 nm, implying $\kappa \sim$

50. Taking 2 nm as a measure of the Ginzburg-Landau coherence length ξ_{GL}, H_{c2} is $\sim$ 100 T. Due to the difficulty in reaching H_{c2} experimentally, estimates of the actual value of H_{c2} vary (Ichioka et al., 1999; Sekitani et al., 2004). Therefore, in this thesis, we will use a typical value of $H_{c2} = 100$ T for field perpendicular to the plane.

$YBa_2Cu_3O_{7-\delta}$ exhibits a clear anisotropy of the in-plane superconductivity which is experimentally well established. For samples of $YBa_2Cu_3O_7$, the penetration depth measurements of Basov et al. (1995) find $\lambda_a/\lambda_b \sim 1.5$ and attribute this anisotropy as evidence that a significant fraction of the superconducting condensate resides on the **b**-axis oriented, and one-dimensional, CuO chains states. ARPES studies show the chain bands to be far from half-filling (Schabel et al., 1998; Zabolotnyy et al., 2007), and hence they are expected to exhibit metallic behaviour (Basov and Timusk, 2005). This is in contrast to the strongly correlated superconductivity of the CuO_2 plane states (see section 3.1.1). For this reason amongst others,[7] other studies question whether superconductivity is a true ground state of the chains. For example, nuclear quadrupole resonance measurements observe the onset of charge-density wave (CDW) order on the chains in the superconducting state (Grévin et al., 2000) which the authors claim to rule out the existence of a chain superfluid.

However, strong evidence in favour of a superconducting chain ground state is derived from further penetration depth measurements, which suggest that superconductivity within both plane and chain states occurs at a single critical temperature T_c (Zhang et al., 1994), and that these states exhibit a similar temperature-dependence (Hardy et al., 1993). Such observations provide support for models that predict the superconductivity of the chains as induced by proximity effect from the CuO_2 planes (Atkinson and Carbotte, 1995; Xiang and Wheatley, 1996; O'Donovan and Carbotte, 1997; Atkinson, 1999; Atkinson and Sonier, 2008). The models of Atkinson and co-workers (Atkinson and Carbotte, 1995; Atkinson,

[7] Such as a consideration of the large difference in the dimensionality of the low energy bands associated with the chain and plane states, and the fact that the chains are not expected to be intrinsically superconducting.

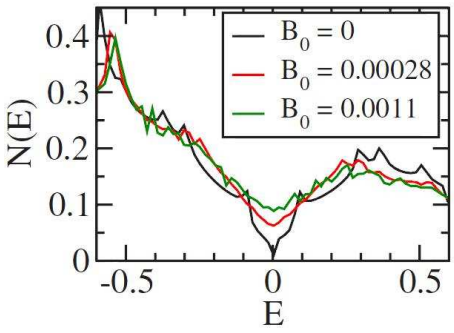

Figure 3.8: The low-energy spectrum of the projected density of chain states at different fields. At zero field, there exist two distinct energy scales associated with the proximity effect induced chain superconductivity, with gap features at $E_1 \sim 0.1$ and $E_2 \sim 0.3$. The magnitude of the field is presented in dimensionless units defined in the model. After Atkinson and Sonier (2008).

1999; Atkinson and Sonier, 2008), contain an intrinsic d-wave pairing interaction V within a CuO_2 plane band, no pairing interaction on the CuO chain band, and a band hybridisation that allows carriers to move between plane and chain states via single-particle hopping. The details of the band hybridisation are non-trivial due to the strong anisotropy between them in momentum space. As a consequence, it is not possible to attach a single superconducting gap function, with an associated symmetry, to the one-dimensional chain states (Atkinson and Sonier, 2008). By calculating the field-dependence of the chain density of states, figure 3.8 shows that Atkinson and Sonier (2008) predict there to be multiple pairing energy scales associated with the chain states. Here, the superconducting pairing energy scales show up as two coherence peaks, or gap-like features, in the zero-field spectrum of the chain-projected density of states. Multiple pairing energy-scales turn out to be a generic feature of the proximity effect models. The small energy scale is associated with a more one-dimensional hybridisation of the plane and chain states, and is closer to being fully gapped. The larger energy scale reflects a more three-dimensional hybridisation, and as such the superconductivity can be described as being more anisotropic. However, as mentioned just previously, attaching a symmetry to the superconductivity is subtle, and possible suggestions are not proposed in the theoretical work. Experimentally, the existence of the smaller

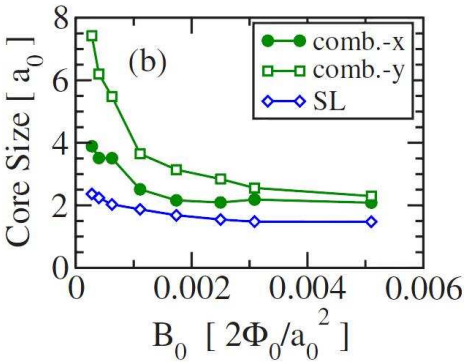

Figure 3.9: Results of proximity-effect model calculations of the vortex core size. The x and y directions respectively correspond to the **a** and **b**-axes. The results shown are obtained by combining the results over both the plane and chain layers of the bilayer model. For comparison, the single layer (SL) model calculation is also presented. For reference, $0.001B_0 = 1.5$ T. After Atkinson and Sonier (2008).

energy scale is expected to be manifested as a low temperature inflection point on the temperature-dependent superfluid density. Such inflection points have been observed in μSR studies of the temperature-dependence of the superfluid density in $YBa_2Cu_3O_{7-\delta}$ (Khasanov et al., 2007) and $YBa_2Cu_4O_8$ (Khasanov et al., 2008). Other evidence is provided by a scanning tunnelling spectroscopy study that claim to observe subgap features in the density of states (Ngai et al., 2007).

Atkinson and Sonier (2008) also use their theory to investigate how the flux line core size varies with field. On calculating the current distribution, $\mathbf{J}(\mathbf{r})$ within the system, they define the size of the flux line core according to the vorticity, $\omega(\mathbf{r})=\nabla\times\mathbf{J}(\mathbf{r})$. Some results of their calculations are shown in figure 3.9. They predict there to be a strong, field-dependent, anisotropy in core size between the x (real-space **a**) and y (real-space **b**) directions, in essence meaning that $\xi_b > \xi_a$. In the x-direction, the major contribution to the core size originates from the plane layer, and the core size is only weakly field-dependent. The dominant field-dependence to the core-size along the y direction originates from the CuO chain layer. The reduced rate of core contraction shown in figure 3.9 is apparently correlated with a suppression of the E_1 chain energy scale. However, we point out experimental evidence for such a core contraction is controversial. The theoretical study of Atkinson and Sonier (2008) was motivated by μSR studies of $YBa_2Cu_3O_{7-\delta}$

(see for example, Sonier et al. (1999)), which are apparently able to show the core-size to fall as a function of increasing field. However, the ability of the μSR technique to extract a reliable measure of the core-size remains questioned in the literature (Landau and Keller, 2007; Maisuradze et al., 2009).

Finally, we discuss the precise details of the overall in-plane order-parameter symmetry in zero field. Due to the orthorhombic distortion of the basal plane, group theory dictates that the symmetry of the superconducting ground state *must* necessarily contain a symmetry conserving admixture (Tsuei and Kirtley, 2000). The precise details surrounding such a component have been a topic of recent interest. Both the electron-tunnelling study of Smilde et al. (2005) and the phase sensitive measurements of Kirtley et al. (2006) deduce that the in-plane order-parameter symmetry for optimally- and overdoped $YBa_2Cu_3O_{7-\delta}$ is composed of a significant s-wave admixture to a predominantly $d_{x^2-y^2}$ order parameter symmetry. Tsuei and Kirtley (2000) show that the functional form of such a gap function is $\Delta(\mathbf{k}) = d\left(k_x^2 - k_y^2\right) + s\left(k_x^2 + k_y^2\right)$ where s and d respectively represent the magnitudes of the $s-$ and $d-$wave subcomponents. If $d/s \geq 1$, then the gap exhibits line nodes at $k_y = \pm\left((d+s)/(d-s)\right)^{1/2} k_x$, indicating that for finite s, the nodes deviate from the expected $\pm 45^\circ$ angles about a principal crystal axis. Smilde et al. (2005) estimate the ratio $d/s \sim 5$ whilst Kirtley et al. (2006) find $d/s \sim 10$ indicating that they observe the nodes to be skewed away from the $\langle 110 \rangle$ directions of a pure $d_{x^2-y^2}$ symmetry. They also find that as a consequence the magnitude of the in-plane gap is anisotropic, with $\Delta_b/\Delta_a \sim 1.2 - 1.5$ Figure 3.10 shows the node skewing pictorially from the work of Kirtley et al. (2006). The magnitude of the order parameter lobe is significantly larger along the **b**-axis, which corresponds to the direction of strong chain dispersion, and the gap nodes lie at angles of $\pm$ 50° about the **b**-axis. A similar measure of node skewing is obtained by Smilde et al. (2005).

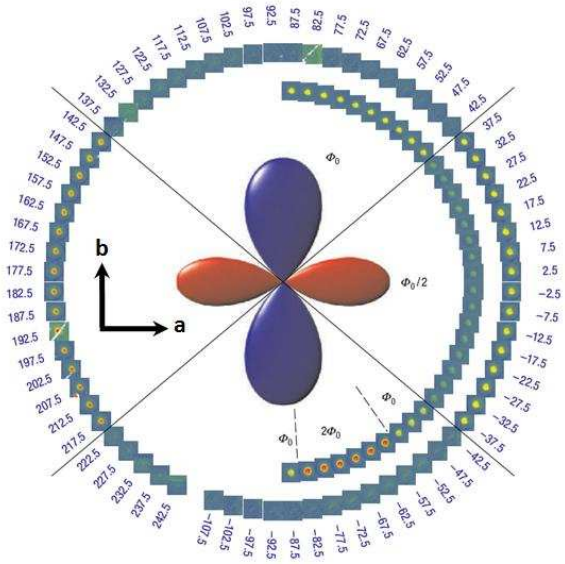

Figure 3.10: A schematic diagram of the angular variation of the sign of the in-plane order parameter in an untwinned sample of optimally doped $YBa_2Cu_3O_{6.93}$. The figure is precisely the same as found in Kirtley et al. (2006), but we have superposed some crystal axis labels to indicate the magnitude of the gap is larger along **b** than **a**.

3.2 Previous studies of the flux line lattice in $YBa_2Cu_3O_{7-\delta}$

Since the discovery of $YBa_2Cu_3O_{7-\delta}$, the FLL structure has been extensively interrogated. The earliest reports were those of Bitter decoration studies, which provide a real-space imaging of the FLL over a small localised surface region of the sample at low fields (Gammel et al., 1987; Dolan et al., 1989a,b). In these studies, for fields up to 170 G, the FLL coordination was observed to be hexagonal, but with clear indications of flux line pinning to both twin boundaries. In particular, Dolan et al. (1989a) also identified an extremely high density of 'unseen' point-like defects of spacing less than 100 nm, which they speculate is associated with the oxygen chain order in their overdoped sample of $YBa_2Cu_3O_7$. This is also suggested by their slightly later study (Dolan et al., 1989b) on the same sample, where the authors were able to deduce an in-plane anisotropy, γ_{ab} $(= \lambda_a/\lambda_b)$ of typically 1.13(2). The value is smaller than other reported low (or zero) field values of γ_{ab} which typically range between 1.2 and 1.5 as obtained across various techniques (Basov et al., 1995; Sun et al., 1995; Ager et al., 2000; Khasanov et al., 2007). Hence, the low

value of Dolan et al. (1989b) likely reflects a certain degree of chain disorder in their samples, in agreement with the conclusion of muon spin relaxation studies that observe such an effect to reduce the in-plane anisotropy (Tallon et al., 1995).

The information yielded from decoration experiments allows a direct view of the FLL structure on a local scale, and can help identify the origin of flux line pinning. Despite this, such studies are limited to small fields, only able to image a relatively small region of the sample surface, and they suffer from a lack of reproducibility between one region of the sample surface to the next. Experimental techniques such as SANS and μSR overcome all of these issues at once. Both can probe the bulk of large volume samples, with measurements possible at much higher applied field. As SANS is the technique adopted for the new measurements reported in this thesis, we concentrate on the discoveries of previous SANS investigations.

The first successful observation by SANS of the FLL in *any* High-T_c material was carried out on a twinned sample of $YBa_2Cu_3O_{7-\delta}$ (Forgan et al., 1990). In a magnetic field of 0.2 T applied approximately to the **c**-axis, and at 20 K, the diffraction pattern showed a reasonable fraction of the diffracted signal to lie along one of the $\{110\}$ directions. This already indicated, and would turn out to be, an orientational effect on the FLL due to flux line pinning to twin planes. The subsequent SANS studies of Yethiraj and co-workers (Yethiraj et al., 1993b,a) confirmed this pinning effect more clearly for $H \parallel \mathbf{c}$, observing 'square-like' diffraction patterns at 0.8 T, and 11 K. Although the square-like pattern showed large peaks in the diffracted intensity with a **q**-vector parallel to the $\{110\}$ directions, the FLL structure was *not* interpreted as intrinsically square. Instead, the major part of the diffracted signal was ascribed to FLL planes aligned with the twin boundaries of the strongly twinned sample. Due to the strong pinning, the authors were unable to deduce a value of γ_{ab}, and were non-committal regarding the details of the intrinsic FLL structure. They did correctly stress that the diffraction pattern is likely a superposition of pinned FLL structures, whose orientations are controlled by the flux line pinning to twin boundaries.

The same group observed that by rotating the twin boundaries out of the direc-

tion of the applied field the pinning effects on the FLL due to twin planes could be somewhat suppressed (Yethiraj et al., 1993a). On rotating the field away from $H \parallel \mathbf{c}$, the two domain FLL structure was observed to become increasingly distorted, indicating the out-of-plane components of the effective mass anisotropy were coupled more strongly into the properties of the FLL. Whilst the measure of the structural distortion was interpreted using anisotropic London theory, the observed orientations of both domains disagreed with the prediction of Campbell et al. (1988) which indicated a preferred orientation to the FLL on rotating the field about **c**. The authors suggest that the orientations of their observed structures remain controlled by pinning to twin boundaries, even for an angle of applied field as high as 70° to the **c**-axis. Similar SANS observations for fields of 0.5 T applied at large angles to the **c**-axis were reported at approximately the same time by Keimer et al. (1993) in their study on a strongly twinned sample.

The disagreement between the observed and predicted structural orientation of the FLL within London theory appears to be consistent with the results of the SANS study of Simon et al. (2004). Using heavily twinned samples of $YBa_2Cu_3O_7$, a systematic approach was taken to investigate the effects of twin plane pinning on the FLL. On increasing the angle of applied field field to **c**, the flux lines deviate from being aligned with the field to being 'locked' via pinning to a twin boundary proliferation path along the crystal **c**-axis. However, above a critical angle θ_B, the flux lines are observed to meander along the direction of the applied field, by allowing parts of their lengths to be pinned to *adjacent* twin boundaries. In this meandering regime, although the orientation of the FLL remains determined by the twin-planes, the overall FLL structure and the measure of its distortion is deemed interpretable in terms of anisotropic London theory. The study of Simon et al. (2004) provides an indication that the orientations of the FLL structures seen in Yethiraj et al. (1993b); Keimer et al. (1993); Yethiraj et al. (1993a) belong to this meandering regime. Using anisotropic London theory, Simon et al. (2004) are also able to extract a value of γ_{ab} of ~ 1.3 from their measurements.

The early studies clearly showed the FLL structural orientation to be strongly in-

fluenced by the crystallographic environment. However, the measure of any structural distortion appears to lie within the anisotropic London theory. In $YBa_2Cu_3O_7$, the agreement with London theory is unsurprising, as for fields $H_{c1} \ll H \ll H_{c2}$, the flux line spacing is much larger than the range over which anisotropic effects that originate from the core region might be expected to extend. At higher field however, where the flux line supercurrents overlap more strongly, other sources of anisotropy are predicted to become increasingly important. Therefore, the local London model might be expected to become inadequate.

Indeed, the first high-field study of Keimer et al. (1994) on a heavily twinned sample of $YBa_2Cu_3O_7$ claimed to observe such a departure. In fields up to 5 T the authors observed an essentially unchanged FLL diffraction pattern that exhibited strong Bragg spots along the $\{110\}$ directions for $H\|$ **c**. There was nothing to distinguish the observations from those previously reported at low fields (Yethiraj et al., 1993b). The authors interpreted the overall FLL structure as being composed of a superposition of four orientations of oblique lattice, with equal length primitive vectors and an opening angle of $73(1)^\circ$. Keimer et al. (1994) suggested these structures were stabilised due to an increasing prominence of the gap anisotropy at high field, and therefore a departure from the London regime. The idea that the overall FLL structure remained composed of a superposition of hexagonal London-like domains, whose alignment remained determined by pinning to twin boundaries, was rejected based on an evaluation of the Gibbs free energy. This evaluation was later shown to be inaccurate by Forgan and Lee (1995), who pointed out that the observations of Keimer et al. (1994) remained consistent with a FLL structure composed of multiple hexagonal structures, with the domain orientations determined by pinning to twin boundaries.

Similarly stimulated into action by the misinterpretations of Keimer et al. (1994) were Walker and Timusk (1995), who were unable to reconcile the observations of Keimer et al. (1994) with their Ginzburg-Landau model. Using arguments of scaling and symmetry, they showed that for FLL primitive vectors to lie along $\langle 110 \rangle$ directions, the primitive cell opening angle of the real-space lattice would need

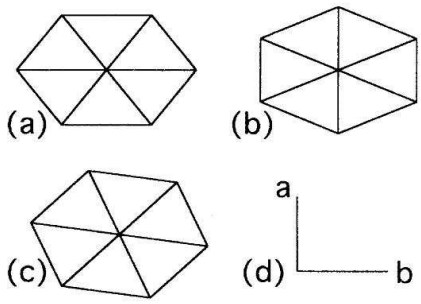

Figure 3.11: In (a) and (b) are the symmetry favoured orientations that the FLL might adopt in real-space for $H\|$ **c**, as predicted by Walker and Timusk (1995). In (c) is one of the FLL domains observed by Keimer et al. (1994), aligned with a Bragg plane along $[110]$. The axes shown in (d) indicate the relative orientations of the FLL structures to those of a single crystal domain.

to be of order 90°, in clear disagreement with the SANS measurements. Walker and Timusk (1995) do use their theory to make a prediction as to the symmetry favoured orientations that the FLL might adopt. The two predicted structures are shown in figure 3.11 (a) and (b).

The desire to deconvolve the effects of twin boundaries on the FLL provided the motivation for a SANS study on a detwinned sample by Johnson et al. (1999). The optimally-doped single crystal sample of $YBa_2Cu_3O_{7-\delta}$ was well detwinned, being characterised as having a majority domain fraction of ∼95 %. Figure 3.12 (a) shows the diffraction pattern obtained at 0.51 T and 1.5 K with $H\|$ **c**. The use of the largely detwinned sample is evident from the resulting twofold symmetry of the diffraction pattern, which reflects the expected intrinsic crystal symmetry of a single crystal domain of $YBa_2Cu_3O_{7-\delta}$. Figure 3.12 (b) shows the decomposition of the FLL diffraction pattern shown in figure 3.12 (a) into four distorted hexagonal domains. The lower two FLL structures are consistent with pinned domains aligned with the residual twin planes in the sample. However, the top two structures observed were new, aligned with the atomic lattice, and suggested to be intrinsic. We note the consistency of these structures with the predictions of Walker and Timusk (1995) (figure 3.11). Using anisotropic London theory, a value of γ_{ab}=1.18(2) is extracted from the entire FLL structure. The physical mechanisms that might stabilise the

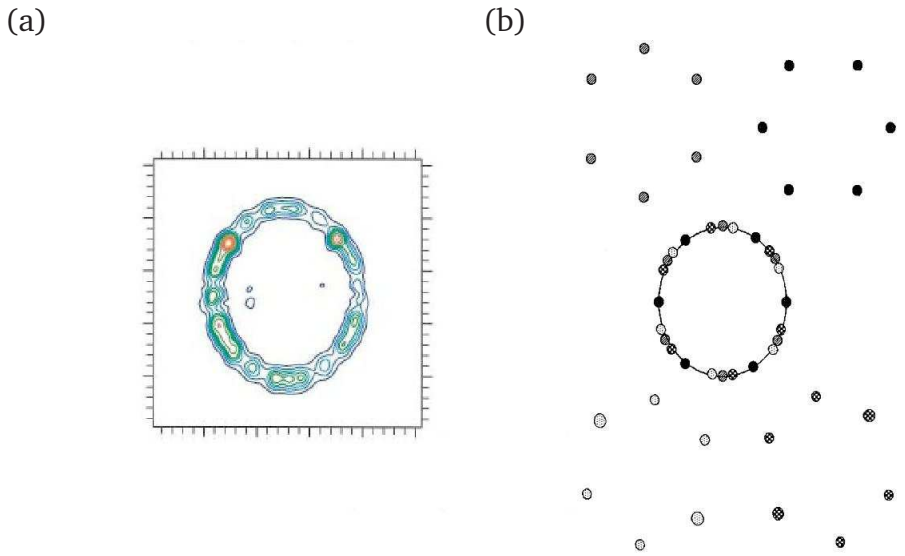

Figure 3.12: In (a) is shown the FLL diffraction pattern obtained by Johnson et al. (1999) at 0.51 T and 2 K. In this image, the field is parallel to the **c**-axis, and the **a**-axis is vertical. Their decomposition of the overall FLL structure shown in (a) into four hexagonal FLL domains is shown in (b).

new and intrinsic FLL structures are not discussed. However, further measurements with field applied at an angle to the **c**-axis show the first clear departure from London theory at higher field. With the field at 33° to **c**, a 90° re-orientation of the FLL structure is observed to occur between the fields of 0.2 T and 3.0 T. The 0.2 T structure has an orientation that agrees with London theory (Campbell et al., 1988), whilst the orientation of the 3.0 T structure is in disagreement. The mechanism behind this 90° re-orientation of the FLL structure remains unexplained, though the authors speculate core anisotropy effects may scale with field to possibly become influential even by fields of 3.0 T.

The clear indication for the FLL structure to depart from a London regime for fields as low as 3.0 T provided one source of motivation for the design and construction of the 11 T SANS cryomagnet facility introduced in section 2.2.1. The subsequent studies of Brown et al. (2004) and White et al. (2008) were the first to report the use of the high field capability in SANS experiments on a 40 mg lightly twinned single crystal sample of $YBa_2Cu_3O_7$. Figures 3.13 (a)-(c) show some of the diffraction patterns obtained within the field range up to 11 T, at 4-5 K and

for $H \parallel \mathbf{c}$. Note that for these images, a $\{110\}$ direction is vertical. The FLL structure shown in figure 3.13 (a) at 1 T is the same as that observed previously for more strongly twinned samples (Yethiraj et al., 1993b; Keimer et al., 1993, 1994), with the fourfold symmetry of the overall diffraction pattern reflecting the averaged fourfold symmetry of the crystal. The high resolution data allow the unambiguous decomposition of the FLL structure into four distinct distorted hexagonal domains, each of which will occupy one of the four orientational crystal states that exist in twinned samples. This decomposition is shown in figure 3.13 (d). Across all of these domain structures, the average value of γ_{ab} extracted from the 1 T data was 1.28(1), in general agreement other bulk measurements. Figure 3.13 (e) shows the FLL structure was observed to change smoothly as a function of field, with the FLL structure being almost perfectly square at the highest field of 11 T. The tendency for a hexagonal FLL to become square-like at high fields cannot be predicted using London theory, and lies in agreement with the theoretical predictions for such a structure to be stabilised by an increasing influence of a $d_{x^2-y^2}$ order parameter symmetry (Ichioka et al., 1999; Berlinsky et al., 1995; Shiraishi et al., 1999; Xu et al., 1996; Affleck et al., 1997).

The report of the high field triangular to square transition by Brown et al. (2004) has become a benchmark study for flux line lattice physicists looking for an example of the manifestation of the d-wave order parameter on the FLL structure. However, as acknowledged in Brown et al. (2004) and discussed in White et al. (2008), the data cannot preclude the possibility that the smooth transition is interpretable in terms an increasing influence of non-local effects coupled with a Fermi surface anisotropy (Kogan et al., 1997a). In particular, the square-like anisotropy of the dominant Fermi surface sheets shown in figure 3.7 (c) is consistent with that required for the stabilisation due to non-local effects of a high-field square FLL structure of the same orientation as observed in figure 3.13 (c). Measurements at higher temperatures on the same sample allowed the mapping out of the high field FLL structure phase diagram for $H \parallel \mathbf{c}$, and this is shown in figure 3.14. The upward curvature of the phase boundary line shows the triangular to square transition to

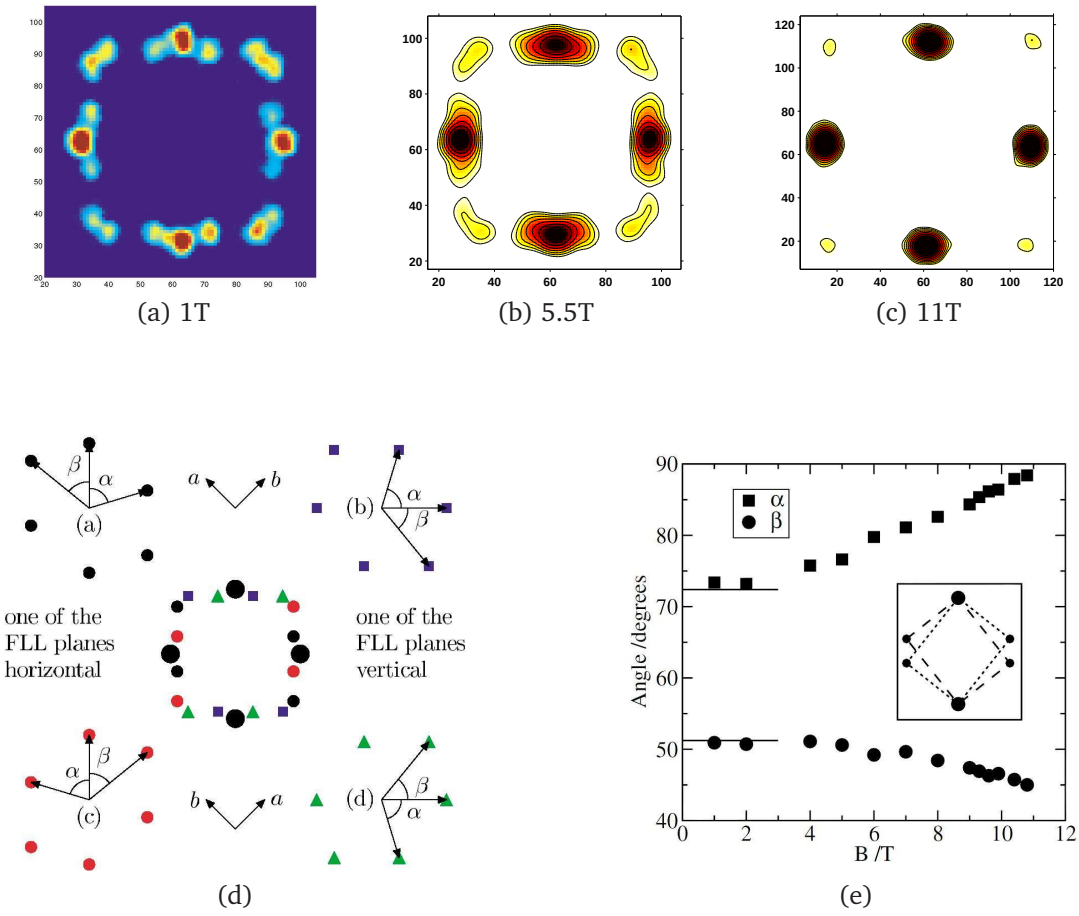

Figure 3.13: Figures (a), (b) and (c) show the observed diffraction patterns obtained in applied fields of 1 T, 5.5 T and 11 T obtained on a lightly twinned sample of $YBa_2Cu_3O_7$. Pattern (a) is shown on a linear intensity scale, whilst those of (b) and (c) are logarithmic, in order to emphasise the weaker spots in the corners. All patterns are obtained at 4 K, with $H \parallel \mathbf{c}$, and in all cases the sample has been mounted with a $\{110\}$ direction vertical. The decomposition of the overall FLL structure in (a) is shown in detail in figure (d), revealing it to be composed of four distinct distorted hexagonal domains. In (e) the field-dependence of the characteristic FLL structure angles α and β is shown, with the definitions of α and β shown in (d). Figures (a), (d) and (e) are after Brown et al. (2004), whilst (b) and (c) are after White et al. (2008).

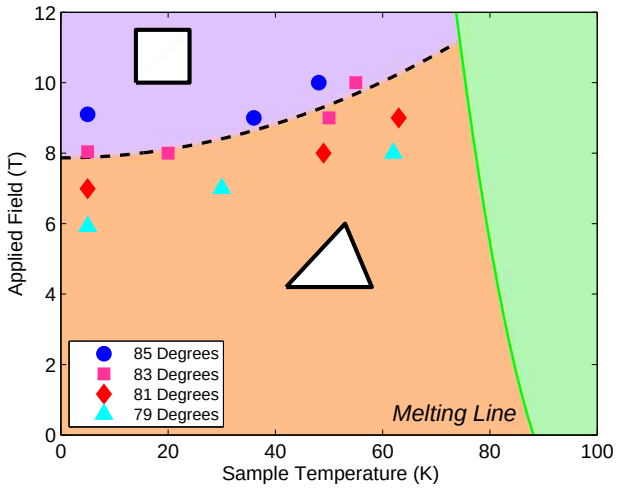

Figure 3.14: The high field FLL structure phase diagram for the lightly twinned $YBa_2Cu_3O_7$ sample discussed in Brown et al. (2004) and White et al. (2008) for $H \parallel \mathbf{c}$. The dashed phase boundary line represents the mid-point of the transition between the limiting cases of the low-field triangular and a perfect square structure. This occurs when the characteristic angle (α as defined in figures 3.13 (d) and (e)) is 83°. The solid melting line is deduced from the data presented in Roulin et al. (1998). After White et al. (2008).

move to higher field with increasing temperature. Such a curvature is consistent with the increasing role of thermal fluctuations in 'smearing' out the stabilising anisotropy of the square FLL structure at high temperature, whether this anisotropy originates due to d-wave or non-local effects.

The final aspect we mention from the SANS studies on the lightly twinned sample (Brown et al., 2004; White et al., 2008) were the observations of intriguing FLL structures when the field was applied at an angle of 10° to both twin boundary directions. At 5 T, figure 3.15 (a) shows the major part of the FLL structure to be composed of two distorted hexagonal domains, one of each occupying a region of the crystal containing approximately orthogonal axes. Although weak scattering is still observed along the $\{110\}$ directions, the orientations of the hexagonal structures were deemed unaffected by twin boundary pinning, and are consistent, within each major crystal domain, with one of the intrinsic FLL structure orientations predicted by Walker and Timusk (1995) and observed by Johnson et al.

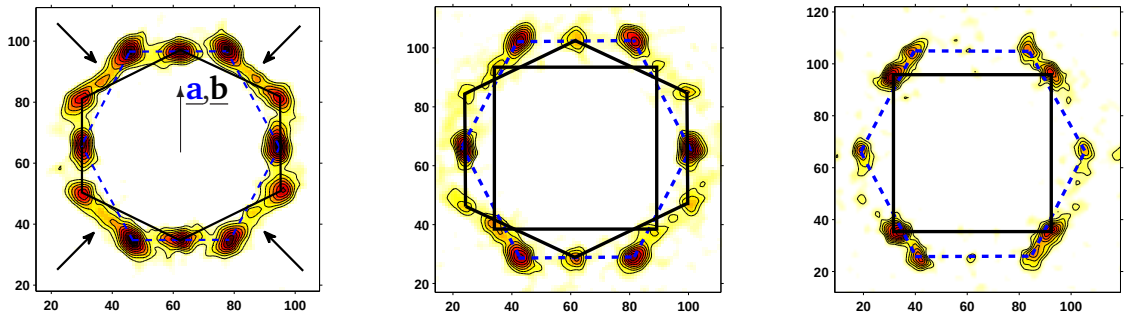

(a) 5T, H 10° **c** (b) 7T, H 10° **c** (c) 8.5T, H 10° **c**

Figure 3.15: FLL diffraction patterns obtained in applied fields of (a) 5 T, (b) 7 T and (c) 8.5 T for the case where the field was applied at 10° to the **c**-axis of the lightly twinned sample used in White et al. (2008). The field rotation axis was chosen such that both twin boundary directions have been rotated out of the field direction. The axis in the centre of (a) indicates that, for all figures, the FLL structures overlaid with blue dashed line patterns occupy a part of the crystal where an **a**-axis is essentially vertical, and the FLL structures overlaid with solid black line patterns correspond to FLL structures occupying the part of the crystal where a **b**-axis is vertical. The arrows in (a) indicate the $\{110\}$ directions.

(1999). Assuming anisotropic London theory is applicable at this field, the measure of the distortion of these two structures in their respective crystal domains shows them to be more isotropic than that measured at 1 T (where $\gamma_{ab} = 1.28(1)$). The equivalent value of γ_{ab} for the domain occupying the part of the crystal with the **a**-axis vertical (blue dashed line structure in figure 3.15 (a)) was 1.14(2), whilst for the other domain it was 1.23(1), suggesting the ab anisotropy is intrinsically suppressed with field when the effects of twin-boundary are suppressed. The origin of the weak scattering along $\{110\}$ is suggested by White et al. (2008) to remain ascribable to the persistence of a remnant and pinned four-hexagonal domain-like FLL structure similar to that seen in figure 3.13 (a). However, such weak scattering is also consistent with the onset at this field of a square-like FLL structure that *co-exists* with the hexagonal structure at 7 T, within the part of the crystal where the **b**-axis is vertical (figure 3.15 (b)). By 8.5 T, figure 3.15 (c) shows the FLL structure in this crystal domain to be entirely square-like, whilst in the other major crystal domain, the FLL structure remains a single distorted hexagon. From such observations of coexistence, it is tempting to deduce that the transition between hexagonal

and square VL structures becomes *first-order* when the effects of twin boundaries are negated.

3.3 Motivation for new SANS studies in detwinned $YBa_2Cu_3O_7$

Each of the major SANS studies of the FLL structure reviewed in the previous section have contributed a series of tantalising clues towards determining the intrinsic FLL structure in the absence of the pinning effects of twin-boundaries, for $H \parallel \mathbf{c}$. We note that many important observations have been made when the field has been applied away from the **c**-axis, and where the effects of pinning to twin boundaries are suppressed. This provides a compelling motivation for new SANS studies on well-detwinned single crystal samples of $YBa_2Cu_3O_7$ with such suppressed pinning to twin boundaries that it is possible to observe the field- and temperature-dependence of the intrinsic FLL structure for $H \parallel \mathbf{c}$. This will allow a new characterisation of the role that the established in-plane anisotropy plays on the FLL structure, without the complication of accounting for the out-of-plane electronic properties that are coupled into the FLL when the field is rotated away from the **c**-axis.

We also note that no study has provided a comprehensive analysis of the field- and temperature-dependence of the FLL form factor in this material. Such measurements are extremely useful for characterising the theoretical regime describing the FLL. For example, of the SANS studies reviewed in this section, it is generally accepted that at the lowest fields, anisotropic London theory is adequate for explaining the measure of the FLL structural distortion (if not the orientation). This assumption can be tested by measuring the form factors of the Bragg spots and comparing them to those expected according to various form factor models. However, the parameter space over which the FLL behaviour departs from the local London regime is not established at all, and measurements of the Bragg spot intensity in fields up to 11 T, and temperatures up to T_{c2}, will provide evidence towards an understanding of this.

3.4 Sample preparation, detwinning, characterisation and mounting

The sample used for the new SANS measurements reported in this thesis was composed of a mosaic of six single crystals of detwinned $YBa_2Cu_3O_7$. Each single crystal of the mosaic was grown by A. Erb at the Walther Meissner Institut, Garching, Germany. Single crystals of $YBa_2Cu_3O_{7-\delta}$ are grown from a molten flux of $BaCO_3$, CuO and Y_2O_3 within $BaZrO_3$ crucibles (Erb et al., 1996). The flux is formed by initially grinding the component oxides in a mortar, and forming the molten flux at 1030°C. The flux is homogenised by holding it at this temperature, within an atmosphere of air, for 10-20 hours. The crystal growth is initiated by cooling the melt slowly to 1005°C. At this temperature, an air-cooled Al rod is bought into contact with one of the crucible walls to provide a temperature gradient over the crucible of 5-10 K. This gradient facilitates by convection the transport of new solute melt to the interface of growing crystals. The temperature is then reduced slowly during crystal growth to 950°, below which the excess flux is decanted away. The furnace is then cooled to room temperature and the single crystals recovered. These as-grown crystals exhibit an ill-defined oxygen concentration and on cooling, as outlined in section 3.1.3, decompose from a high temperature tetragonal structure into a twinned orthorhombic structure. Therefore the crystals need to be detwinned to remove twin boundaries, and annealed to provide samples with the desired oxygen content.

The as-grown single crystals of $YBa_2Cu_3O_{7-\delta}$ were detwinned within the crystal growth group of C.T. Lin at MPI Stuttgart, Germany. Figure 3.16 (a) shows a diagram of the thermo-mechanical equipment used to detwin the crystals. To detwin a single crystal of $YBa_2Cu_3O_{7-\delta}$, the crystal is rectangularly cut so that a uniaxial stress of order $\sim$2 x $10^7 Nm^{-2}$ can be applied by stress plates along a $\langle 100 \rangle$ direction. The stress is initially applied at room temperature and, within a controlled O_2 atmosphere, the temperature is quickly raised (a few mins) to the detwinning temperature of $\sim$500°C (Lin et al., 1991). After 24 hours at this temperature, the sample is cooled to room temperature within $\sim$20 minutes. During the treatment, the

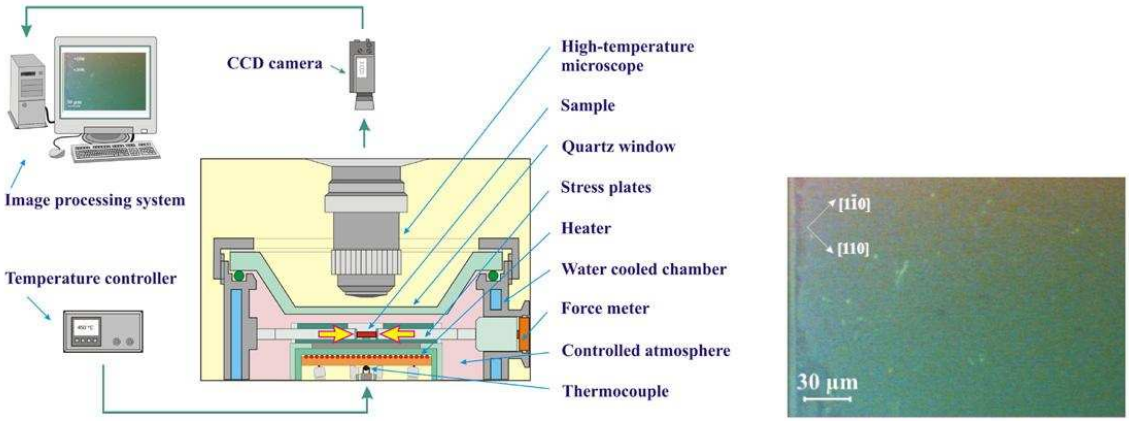

(a) (b)

Figure 3.16: In (a) is a schematic diagram of the detwinning equipment used to detwin the samples used for the SANS measurements reported in this thesis. In (b) is a photograph of a detwinned sample of $YBa_2Cu_3O_{7-\delta}$ taken using polarised light. Figure (a) is courtesy of H. Bender, MPI Stuttgart, whilst (b) is courtesy of C.T. Lin, MPI Stuttgart.

twinning structure at the surface of the sample is observed using polarised light and a microscope capable of operating near to the sample at high temperatures (Lin and Kulakov, 2004). Figure 3.16 (b) shows a region of the surface of a nominal sample of $YBa_2Cu_3O_{7-\delta}$ after the detwinning procedure. In distinction to the photograph of the twinned sample shown in figure 3.5 (a), the polarised light of the microscope is unable to pick out a contrast between regions separated by twin boundaries, suggesting at least the imaged part of the crystal to be single domain.

Finally, the single crystals were returned to A. Erb for oxygen annealing so that they could reach the overdoped O_7 phase. To achieve a homogenous sample oxygenation, the crystals were annealed in a high pressure (100 bar) oxygen atmosphere, at an elevated temperature of 300°C, for 200 hours. The crystals were then quenched rapidly, in approximately just one minute, to room temperature. This was so as to maintain the high temperature oxygen content (Erb et al., 1999).

The zero-field T_c of one of the six crystals that was used for the SANS measurements was measured using a SQUID magnetometer. The mid-point of the transition of the sample bulk was found to be $\sim$89 K, consistent with the sample being maximally doped (c.f. figure 3.3). The six single crystals were mounted, with their

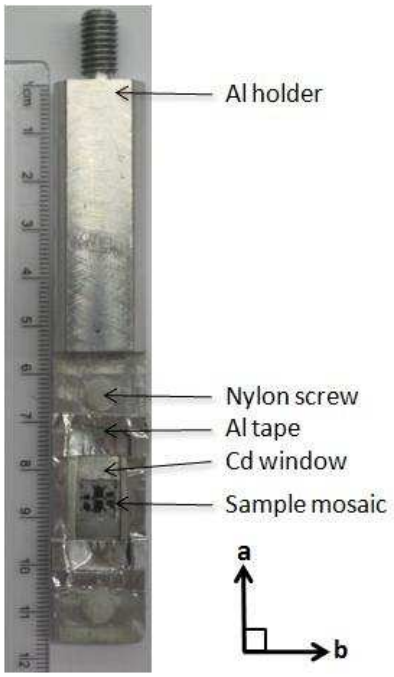

Figure 3.17: An annotated photograph of the $YBa_2Cu_3O_7$ mosaic mounted on a sample holder suitable for use in the 11 T SANS cryomagnet at PSI. The sample region is surrounded by a cadmium window of known dimension which defines the sample aperture. The inset axes indicate those of the sample mosaic, with the **c**-axis lying orthogonal to the **a**-**b** plane (out-of-the-page), and parallel to both the field direction and the neutron beam in the traditional SANS experimental setup.

c-faces flat, onto a ∼1 mm thick Al plate using a diluted adhesive. X-ray Laue photographs showed the mosaicity of the **a**-axes about the **c**-axis to be within 1.5°. A calibrated optical microscope was used to determine the mean thickness of the single crystals to be ∼0.35 mm. This is much less than the $1/e$ length of ∼ 2.0 cm at $\lambda_n = 5$ Å, as indicated in Appendix B, and so neutron absorption is not an issue for these samples. The total mass of the mosaic was estimated to be ∼20 mg. Finally, using the MORPHEUS instrument at PSI, elastic single crystal neutron diffraction was performed on the (100) and (010) reflections to measure the detwinning ratio of the entire sample mosaic. Due to the slight inequality of the **a** and **b** lattice parameters, in a twinned sample it is possible to measure the (100) reflection from one of the twin domains and the (010) reflection from the other twin domain within just one $\theta - 2\theta$ scan. From our measurements, no sign of a signal attributable to a minority twin domain was observed, consistent with the sample possessing a remarkably low minority domain fraction of < 1 %.

A photograph of the sample mounted on a sample holder suitable for use in the VTI of the 11 T SANS cryomagnet at PSI is shown in figure 3.17. The small Al plate containing the mounted $YBa_2Cu_3O_7$ mosaic is itself mounted onto a piece of 0.5 mm

thick pure Al sheet. This second Al sheet is larger, and much easier to attach to the Al sample holder with nylon screws. A cadmium window of known size is placed over the sample region so as to define the sample aperture, and is held in position with diluted Bostik®. As an extra precaution, Al tape is used to support all the glued pieces in their positions. Finally, a thin Al foil (not shown in figure 3.17) is wrapped around the entire sample region, to protect the crystals from condensation that can form if the sample is removed from the cryomagnet whilst still colder than room temperature.

3.5 Flux line lattice structure up to 10.8 T, at 2 K and with $H \parallel$ c

Here, we present our new SANS measurements of the FLL structure in twin-free $YBa_2Cu_3O_7$. In this section we report measurements obtained in applied fields of up to 10.8 T with $H \parallel$ **c**, and at temperatures of 2 K.

3.5.1 Oscillating the field whilst preparing the flux line lattice

Most commonly in SANS experiments, the FLL is prepared by applying the desired measurement field above T_c, and then simply field-cooling to the intended operating temperature. This is the straightforward field-cool (FC), and was the approach adopted for some of the measurements reported here. Another approach found to be important in preparing the FLL was that of oscillating the field whilst cooling, which we term as oscillation field-cool (OFC). Figure 3.18 simplistically shows the differences between these two approaches. In figure 3.18 (a), a graph of sample temperature as a function of time represents the $YBa_2Cu_3O_7$ sample typically cooling from T_c to a low operating temperature, such as 2 K. For an applied field of 1.5 T, figure 3.18 (b) shows the time-dependence of the applied field for the two different approaches of the FC and OFC during the time the temperature is falling. For the FC procedure, the field is held constant for the entire time of the cooling and the measurement at 1.5 T; this is shown by the dark blue line. The OFC preparation is shown by the light blue line, indicating the field to oscillate about the average field, with an amplitude of typically just 0.1 or 0.2 % of this field. When at the

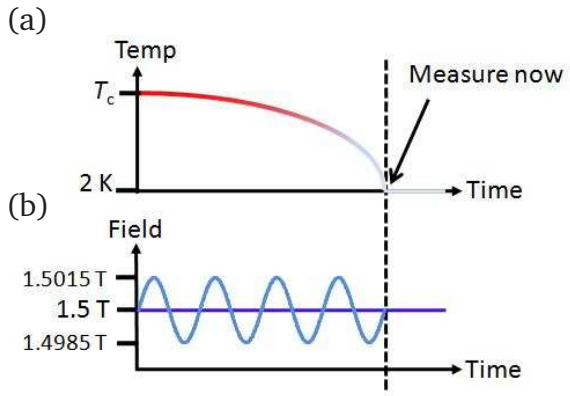

Figure 3.18: In (a) we show the sample cooling from T_c to a low operating temperature, such as 2 K. In (b) we show the difference between the field action for the FC and OFC procedures at a field of 1.5 T. For the FC procedure (dark blue line), the field is held constant whilst cooling. For the OFC procedure (light blue line), the field is made to oscillate in a periodic manner about the intended operating field, with an amplitude typically of 0.1 % of this field. When the operating temperature is reached, the field is raised to the target field, and held stationary for diffraction measurements.

operating temperature, the final action for the field is to be raised to the target field before being held constant for the diffraction measurements [8].

Although in principle a standard FC procedure is sufficient for the formation of the equilibrium FLL structure, competition between the Meissner expulsion of flux and flux line pinning can induce disorder into the FLL and increase its mosaicity. Furthermore, on cooling using the standard FC procedure, such pinning can cause the FLL structure to be 'frozen in' at an irreversibility temperature, which may be higher than the intended operating temperature. Therefore the measured FLL structure might not completely represent that of the intended temperature. In the presence of weak static disorder, it has been observed that the OFC procedure [9] can be successful in allowing the FLL to explore its true orientational free energy minimum, $\mathcal{F}_m$. In essence, the OFC procedure 'anneals' the FLL via periodic compressive and rarefactive forces acting on the FLL, that arise due to the periodic variation of

[8] Note the time-scales between figures 3.18 (a) and (b) are inequivalent and exaggerated for clarity. Typically at PSI, using locally enforced needle valve settings, the time taken to get from a little above T_c ($\sim$95 K) to 2 K is $\sim$45 mins, whilst the field oscillations normally had a frequency of $\sim$2 min^{-1}.

[9] Some refer to the action of field oscillation as 'shaking' or 'wiggling.'

the field.

Evidence for the positive effect of adopting the OFC preparation procedure is deduced from the use of similar methods in other SANS experiments. Typically an improvement in FLL quality is observed, as nicely demonstrated in studies on borocarbide superconductors (Levett et al., 2002; Dewhurst et al., 2006) and in the High-T_c materials $YBa_2Cu_4O_8$ (Bowell, 2008) and $La_{1.83}Sr_{0.17}CuO_{4+\delta}$ (Gilardi et al., 2002). Occasionally after the OFC procedure, the resultant equilibrated FLL structure is revealed to be different to that structure 'frozen-in' after a simple FC procedure. Such an observation in the heavy-fermion superconductor UPt_3 allowed a parameter-space distinction between superconducting states that were described by different order parameter symmetries (Huxley et al., 2000). Sometimes however, the use of an OFC procedure can cause the FLL quality to worsen, if strong pinning is present. On these occasions, even if the variation in the field depins a flux line, it allows the flux line to explore new pinning centres. For this reason, in spite of the logic of utilising an OFC method, its application is something of an experimental dark art. The details of the best OFC procedure to use for preparing the FLL will be sample specific, and a systematic approach should be adopted to deduce how best to take advantage of this.

3.5.2 Low field structure phase

Comparing FC and OFC measurements

Figure 3.19 shows two FLL diffraction patterns obtained within an applied field of 1.5 T. The diffraction pattern shown in figure 3.19 (a) was obtained from a FLL prepared using the FC procedure, whilst the FLL of figure 3.19 (b) was prepared using an OFC procedure. All other experimental conditions were constant.

The diffraction pattern obtained from the OFC measurement shows the intrinsic FLL structure type of the low field range; a distorted and single domain hexagonal structure aligned with the atomic lattice. A deduction of the FLL structure for the FC measurement is less straightforward. However, carefully inspecting the intensity distribution of figure 3.19 (a) allows certain structure to be revealed within the

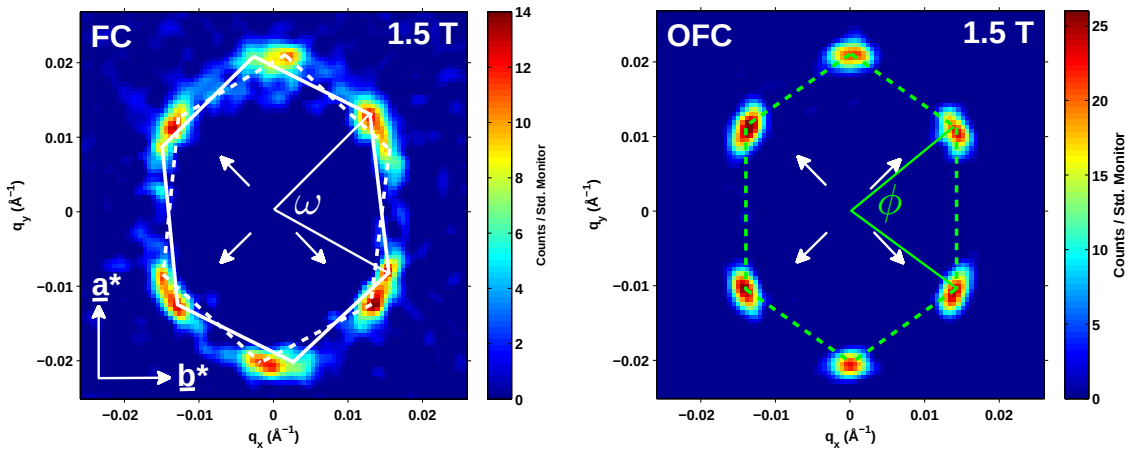

(a) 1.5 T after an FC procedure.

(b) 1.5 T after a 0.1% OFC procedure

Figure 3.19: FLL diffraction patterns recorded in an applied field of 1.5 T, at 2 K and with $H \parallel \mathbf{c}$. Figure (a) shows the FLL structure recorded after a FC procedure, and (b) after a 0.1% OFC procedure. The crystal axes in (a) are valid for both images, and the white arrows indicate the $\{110\}$ directions. Overlaid patterns indicate the suggested FLL structures that make up the overall diffraction pattern. In (a) this is shown by solid and dashed white hexagons, each with two of their corners aligned with $\{110\}$. The characteristic angle ω is valid for both of these structures. In (b), the overlaid green pattern indicates the FLL structure, and the characteristic angle ϕ is that which defines the opening angle of the primitive cell. Both images have background measurements subtracted.

Bragg 'patches' of diffracted intensity. From within these, at least two FLL structures are discernible, and these are indicated in the figure by solid and dashed white hexagons.

The apparent change in precise FLL structure on preparing the FLL using the OFC procedure is also accompanied by improvements in the lattice quality. If we treat one of the 'patches' seen in figure 3.19 (a) as a Bragg spot, then on using the OFC procedure, the mean FWHM azimuthal spread of a 'patch' in figure 3.19 (a) compared to a Bragg spot in figure 3.19 (b) falls by ~ 40 %. However, as the change in overall FLL structure obtained on using the two preparation techniques is only slight, we cannot conclude that the *intrinsic* azimuthal spread of the FLL structure reduces by such an amount. However, this observation is consistent with the proposal that the OFC procedure causes the slight change in FLL structure from the FC

case. A similar analysis of the FWHM of the rocking curves shows the OFC procedure to cause an improvement in the longitudinal order of the FLL in this low field range. Again, on comparing the Bragg patches and the Bragg spots the respective FC and OFC FLL structure, the intrinsic FWHM of the rocking curve is ~ 50 % lower for the Bragg spots prepared using the OFC procedure. Within the statistical accuracy, the integrated intensities for an OFC Bragg spot and the corresponding FC Bragg patch are identical, indicating the sole effect of the OFC procedure is to improve the longitudinal order of the flux lines as compared to the FLL created using the FC procedure.

The orientations of the two FLL structures outlined in 3.19 (a) are consistent with structures observed to exist within twinned samples (Brown et al., 2004; White et al., 2008). However, it is difficult to reconcile the observation of these structures as existing within a sample which is characterised as almost perfectly detwinned.

Origin of the $\{110\}$ alignment potential for the FC FLL structures

Previous SANS studies on twinned samples show that the low field hexagonal structures are distorted along the $\mathbf{a}^*$-axis of their relevant orientational state (see figure 3.13 (d)). From our data, and a knowledge of these four possible orientational states, figure 3.20 identifies the two major orientational states within which FLL structures such as those depicted in figure 3.19 (a) could exist. It might be suggested that the major part of the sample is composed of two such orientational states. These states will originate from different twin regions of the sample and so the twin boundaries along the $\{110\}$ directions of these orientational states will be orthogonal. Hence, FLL structures that occupy one of the two states and whose orientation is controlled by pinning along $\{110\}$, will orient along orthogonal $\{110\}$ directions. Furthermore, the $\mathbf{a}^*$ and $\mathbf{b}^*$ axes of these two states lie close together, and the indicated angle θ in figure 3.20 will only be $\sim 1^\circ$. Hence, even if the OFC procedure does de-pin the two FLL structures shown in figure 3.19 (a), unpinned FLL structures occupying the two states would effectively superpose within the sensitivity of the SANS measurements, giving rise to the observation of the suggested

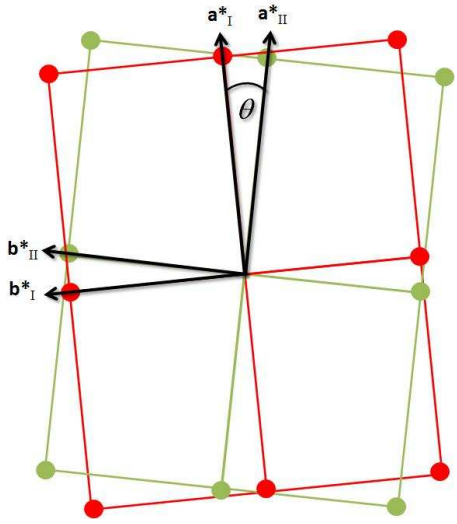

Figure 3.20: A depiction of the two orientational states of the reciprocal atomic lattice from a twinned sample, within which FLL structures such as those shown by the white solid and dashed lines in figure 3.19 (a) (see text for details) could exist. The subscripts I and II indicate that the two orientational states originate from different twin regions of the sample.

intrinsic FLL structure shown in figure 3.19 (b).

However, if the alignment of the structures shown in figure 3.19 (a) is due to remnant twin boundaries, FLL structures populating the two minority orientational states not depicted in figure 3.20 might be expected to give a SANS signal, and contribute to the observation of an overall diffraction pattern similar to that reported at low fields in Brown et al. (2004) and White et al. (2008). Within the sensitivity of the measurements, at no field was a signal from such structures detectable above the background (1 %) level, consistent with that expected from measurements of the twinning ratio of the sample. Due to this consistency however, we can not rule out the possibility that the orientations of the FLL structures indicated in figure 3.19 (a) are influenced by a very small fraction of twin boundaries associated with the presence of minority orientational states of the crystal.

Perhaps more feasible than the effects of twin boundaries in the usual sense, is that these FLL structural orientations are determined by residual defects aligned along $\{110\}$ which remain due to a slight imperfection of the detwinning process. In this scenario, the major part of a crystal is composed of a single orientational state,

but remnant correlated disorder along $\{110\}$ is able to influence the orientations of the low field FLL structures.

Role of the OFC procedure with regard to pinning

Within this low field phase, the improvements in FLL quality induced by the OFC procedure over the FC procedure are accompanied by changes in the observed FLL structure. From this observation, it is tempting to suggest that the OFC preparation procedure acts to reveal the intrinsic FLL structure which cannot be confidently deduced from the FC measurements alone. Clearly the act of oscillating the field will not change the intrinsic orientational $\mathcal{F}_m$ in the ideal material. Therefore, the observed changes must be describable in terms of the OFC procedure allowing pinned flux lines to overcome their pinning barriers, and equilibrate at the preferred coordination of the intrinsic $\mathcal{F}_m$.

In this low field regime, the penetration depth λ_L ($\sim$140 nm) is significantly larger than the FLL lattice parameter a_0 ($\sim$70 nm at 0.5 T). From this consideration, the magnetic interaction of the flux lines, which is the origin of the elastic energy of the FLL, is relatively strong even at low fields. In the short wavelength limit of lattice deformations ($k > 1/\lambda_L$), non-local elasticity theory can account for displacements of the flux line cores towards pinning centres in this strongly interacting regime, by decoupling core displacements from the flux line field profile (Brandt, 1995). Hence, flux lines in High-T_c materials are 'soft', and are able to deviate from the field direction to take advantage of the condensation energy gain provided by a pinning site. The OFC procedure provides a periodic and weakly perturbative variation of the magnetic pressure that is sufficient to depin a flux line from a relatively weak pinning centre and allow the exploration of other local $\mathcal{F}_m$. We see a marked improvement in the order of the FLL despite the field oscillation amplitude being just 0.1 % of the target field. This small amplitude was found to be most effective at depinning flux lines. Larger oscillation amplitudes, for example of order ~ 1 %, generally resulted in a reduction of the FLL order. This suggests that flux lines with a strong pinning centre somewhere along their length are 'bent' and pin to the

next nearest strong pin that the OFC procedure with large amplitude allows it to explore. Unfortunately, a systematic investigation of the optimum OFC amplitude as a function of field was not carried out.

To obtain the intrinsic FLL structure from the pinned FLL structures, essentially a small rotation transformation of $\sim \pm 6^\circ$ is required of the FLL structure about the **c**-axis. Therefore depinned flux lines that relax to positions corresponding to the orientational $\mathcal{F}_m$ are also subject to a shear displacement. This observation, coupled with the improvement in the longitudinal correlation, suggest the shear and tilt moduli are relatively soft, and the pinning barrier of the pinning sites relatively low. It is likely that the FLL in this sample exists within a background of high density but weak point-like pinning sites in the bulk, regardless of the correlated pinning along $\{110\}$. Point-like pinning of flux lines will broaden the rocking curves, which is indeed what is observed from the FC measurements.

From the point of view of the local London theory (Campbell et al., 1988; Thiemann et al., 1989), *all* possible orientations of the hexagonal FLL are predicted to have equivalent free energy. Therefore, assuming that in this field range we are close to the London limit, the intrinsic structural $\mathcal{F}_m$ can reasonably be expected to be shallow with respect to both the orientationally degenerate local London limit, and that provided by the pinning sites. From this respect, it is unsurprising that the apparently weak perturbative action of the OFC procedure is able to equilibrate the FLL structure at low temperatures.

3.5.3 Intermediate field structure phase

Between 2.5 T and 6 T, the intrinsic FLL coordination is composed of a different single domain and distorted hexagonal structure that is aligned with the crystal axes. Figure 3.21 shows diffraction patterns obtained in this structure phase, with measurements at 4 T (figure 3.21 (a)) obtained after a FC procedure, and 6 T (figure 3.21 (b)) obtained after a 0.1% OFC procedure. We see the new structure remains distorted along $\mathbf{a}^*$, but the primitive cell, with its associated opening angle ρ, has rotated 90° about the field axis with respect to the low field structure.

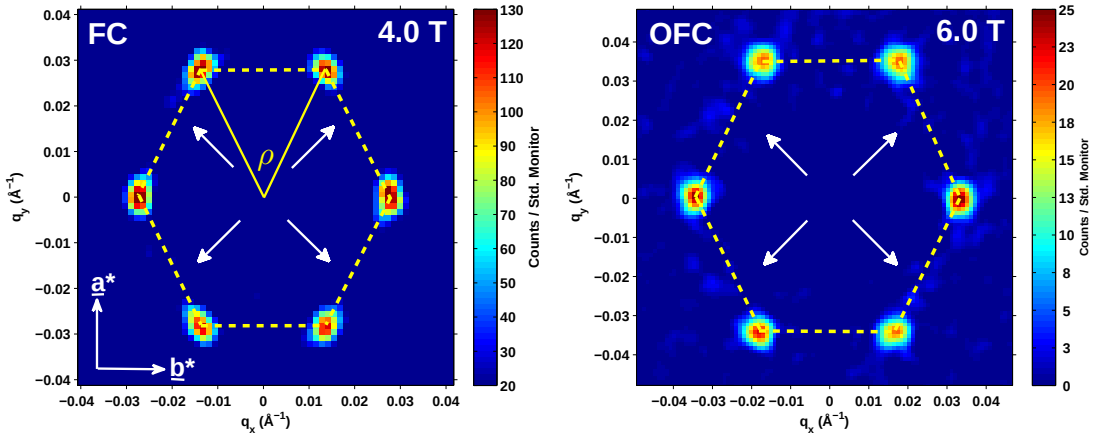

(a) 4 T after a FC procedure

(b) 6 T after a 0.1% OFC procedure

Figure 3.21: FLL diffraction patterns obtained in applied fields of (a) 4.0 T after a FC procedure and (b) 6.0 T after a 0.1% OFC procedure. Both patterns are obtained at 2 K, and with $H \parallel \mathbf{c}$. The axes indicated in (a) are valid for both images, and white arrows indicate $\{110\}$ directions. The FLL structure is indicated by the overlaid yellow dashed line hexagon, and ρ is the characteristic angle of the primitive cell. The two patterns were obtained during different experiments, using different instruments.

Over this field range, there is no discernible difference between the FLL structures created using either the FC or OFC preparation procedures. We understand this as being due to flux line supercurrents overlapping increasingly strongly at higher field, and flux line interactions being dominant in determining the structure and lattice quality. In figure 3.22 we show the increasing propensity with field for improvements in the lattice quality via a series of systematic measurements of FC FLL structures. In figure 3.22 (a) we show the mean Lorentzian FWHM of the rocking-curve to fall monotonically with field. We see a similar field-dependent behaviour of the mean azimuthal FWHM spread of the Bragg spots as shown in figure 3.22 (b)[10]. Here, we have presented the mean azimuthal FWHM angular spread, the quantity defined as the width W_a in section 2.3. For scattering through

[10]Across the field range, two instrument settings were used. λ_n was set to 8 Å for measurements at fields between 2.5 T and 3.5 T, and to 6 Å for measurements at 4 T and higher. The collimation was kept constant at 8 m. Although in figure 3.22 (a) the longitudinal resolution changes as we change λ_n, the dominant contribution to the rocking curve width is due to the mosaic spread of the FLL. Hence, we compare the our measurements across both instrument settings.

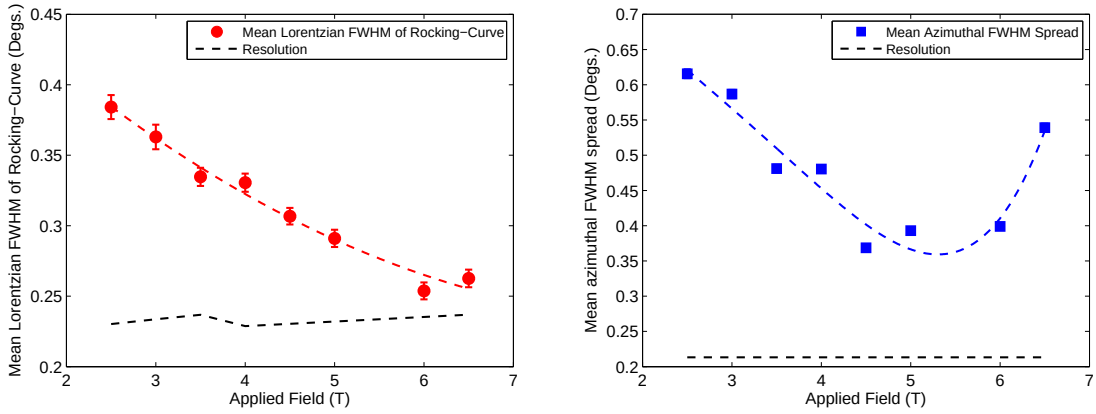

(a) (b)

Figure 3.22: Graphs to investigate the improvement of the FLL order as a function of increasing field. In (a) we show the field-dependence of the FWHM of a Lorentzian lineshape fitted to the rocking-curves. For reference, the black dashed line provides an estimate of the resolution for a Gaussian FWHM. The bump in this line corresponds to a change in λ_n. The red dashed line is a guide to the eye. In (b) we show the field-dependence of the mean FWHM azimuthal width of the Bragg spots, again with a black dashed line indicating the instrumental resolution. The blue dashed line is a guide to the eye. Error bars where not visible are of order the size of the data symbol. For simplicity, we only consider Bragg spots with $\mathbf{q}$ not parallel to a crystal axis.

small angles, this angular spread is obtained from the experimental data using

$$W_a = \tan^{-1}\left(\frac{n\ell_{\text{pix}}}{s_d}\right) \tag{3.2}$$

Here, ℓ_{pix} is the pixel size, and n is the measured FWHM spread in terms of the number of pixels. The distance s_d is strictly that between the middle of the Bragg peak and the sample. However, for a typical instrument configuration, s_d is well approximated by the sample-to-detector distance.

The monotonic decrease with field of both the rocking curve width and the azimuthal spread indicate that, even in the absence of the OFC procedure, the order increases with flux line density. The exception to this is at 6.5 T where both measures of spread are seen to rise again slightly. We associate this with the onset of a structure transition, which we discuss in section 3.5.5. Unfortunately, a systematic comparison between the effects of the FC and OFC procedures has not yet been car-

ried out as a function of field, except for one pair of measurements at 6 T. Between the respective FC and 0.1% OFC measurements at this field, small improvements in lattice quality were observed, suggesting that the OFC procedure has a much smaller, but still noticeably positive effect at higher fields.

3.5.4 High field structure phase

By 7.5 T, the intrinsic FLL structure has completed another transition into a high field structure phase, which persists until the highest accessible fields of 10.8 T. Figure 3.23 shows examples of high field FLL diffraction patterns obtained in fields of 7.5 T and 10.8 T. In this structure phase, the FLL structure appears to be composed of a single domain rhombic structure aligned with the atomic lattice. The term 'rhombic' refers to the fact that the FLL structures observed in the diffraction patterns of figure 3.23, are composed of four Bragg spots of comparable intensity. This is in contrast to the six Bragg spots of the low and intermediate field structures. A noticeable feature of the rhombic lattice is that, relative to a square FLL structure, the structure is distorted along the $\mathbf{b}^*$ direction. This direction is orthogonal to that of the hexagonal structures at lower fields which are distorted along the $\mathbf{a}^*$ direction.

In this structural phase, the effects of the OFC procedure over the FC procedure are found to be unimportant in terms of the measured FLL quality. Similar results are obtained from both preparation techniques, as shown by the systematic investigation of the field-dependences of the mean Lorentzian rocking-curve width (figure 3.24 (a)) and the mean FWHM azimuthal width of the Bragg spots (figure 3.24 (b)). As for the intermediate field phase, both of these FWHM spreads are presented in units of scattering angle. These measurements were all obtained during the same experiment, using identical instrumental conditions ($\lambda_n = 6$ Å and a collimation of 8 m). Figure 3.24 (a) shows that regardless of whether the FLL is prepared by the FC or OFC procedure, the longitudinal correlation becomes noticeably poorer on moving to high fields. Figure 3.24 (b) shows the azimuthal spread

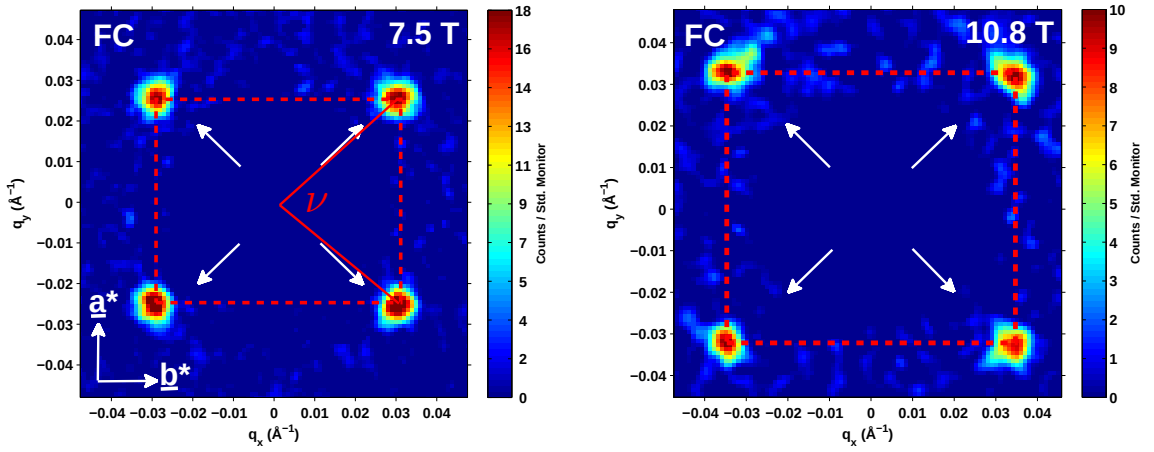

(a) 7.5T after an FC procedure

(b) 10.8T after an FC procedure

Figure 3.23: Flux line lattice diffraction patterns obtained in applied fields of (a) 7.5 T and (b) 10.8 T. Both patterns were obtained at 2 K with $H \parallel \mathbf{c}$, and after an FC procedure. The axes indicates in (a) apply to both figures, and the white arrows show the $\{110\}$ directions. The overlaid red dashed line pattern shows the suggested FLL structure, where the angle ν indicates the opening angle of the FLL primitive cell.

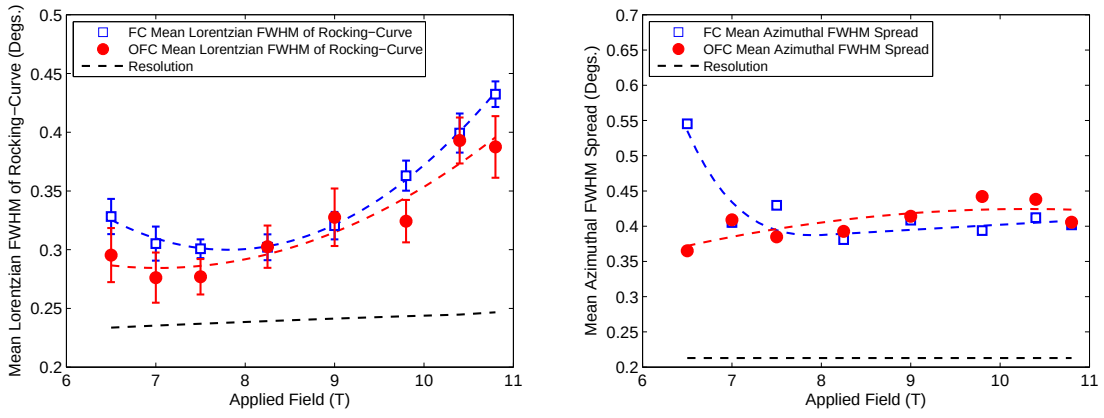

(a)

(b)

Figure 3.24: A comparison between FC and OFC measurements of the high field-dependences of (a) the mean Lorentzian rocking curve width and (b) the mean FWHM azimuthal spread of the Bragg spots. In both cases, the FC data is shown by empty blue squares, the OFC data is shown by filled red circles. The red/blue dashed lines provide guides to the eye. The black dashed lines provide estimates of the resolution. The vertical axes of both (a) and (b) are in units of scattering angle.

of the Bragg spots to be essentially field independent [11]. At these low temperatures and fields, dynamic effects such as FLL melting will not have an effect on the order of the lattice, allowing us to suggest that the reduction in longitudinal correlation is due to the increasing influence of weak static FLL disorder. This was a possible explanation for the similar observation of the field-induced broadening of the rocking curves observed in the high-κ borocarbide superconductors YNi_2B_2C and $LuNi_2B_2C$ (Eskildsen et al., 1997a).

3.5.5 Flux line lattice structure transitions and structural distortion

Transition between the low and intermediate field structures

The field range between 1.5 T and 2.5 T hosts a structure transition between the low field and intermediate field structure phases. To deduce the nature of the transition over this field range, we carried out a systematic investigation of the field-dependence of the FLL structure through the transition, using the OFC procedure at each field. Figures 3.25 (a) to (e) show the results of such an investigation at fields between 1.5 T to 2.5 T. In each figure, just the top right quadrant of reciprocal space was recorded on the detector, as in principle this is all that is needed to construct the overall diffraction pattern. Diagonal rocking scans were carried out to look for diffracted intensity close to the $\{110\}$ direction. A brief inspection of both the low and intermediate field structure types shows that diffracted intensity observed clockwise to the $\{110\}$ direction will be due to the presence of the low field structure, while intensity observed counterclockwise from the $\{110\}$ direction will be due to the presence of the intermediate field structure.

In figures 3.25 (a) and (b) the Bragg spot just below the $\{110\}$ axis indicates the only FLL structure present is the intrinsic hexagonal structure of the low field phase. For figures 3.25 (c) and (d), the azimuthal spread of this spot has noticeably increased, and structure is visible within the diffracted intensity patch. Simple inspection shows this structure to be consistent with that expected from the

[11] This is barring the 6.5 T FC datapoint whose large value can be associated with the effect of the structure transition.

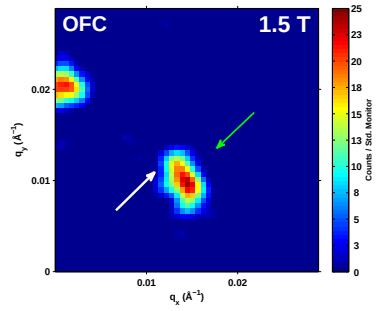

(a) 1.5T after a 0.1% OFC procedure

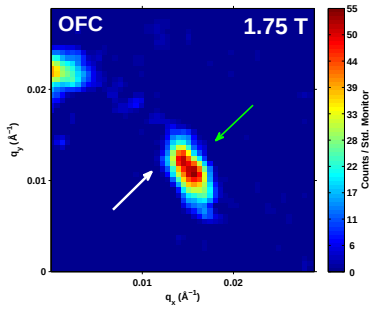

(b) 1.75T after a 0.1% OFC procedure

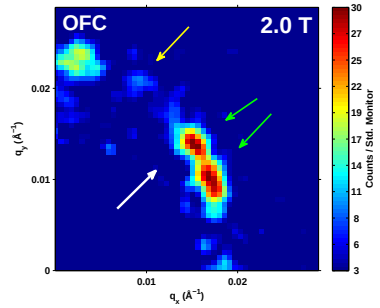

(c) 2.0T after a 0.2% OFC procedure

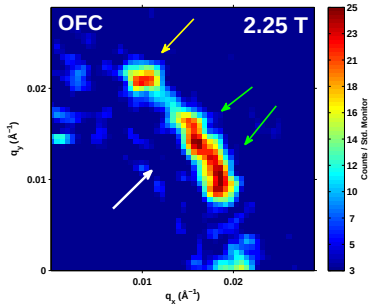

(d) 2.25T after a 0.1% OFC procedure

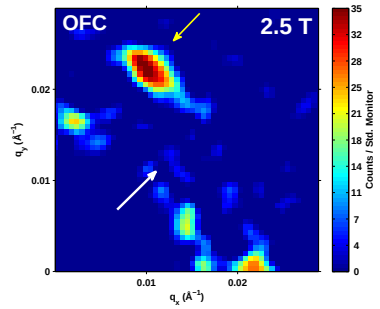

(e) 2.5T after a 0.1% OFC procedure

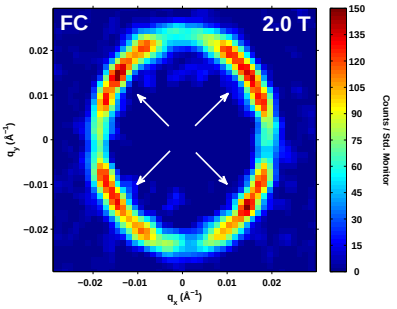

(f) 2.0T after a FC procedure

Figure 3.25: In figures (a) to (e) we show the top right portion of the detector for a series of OFC measurements between the fields of 1.5 T and 2.5 T. These measurements were obtained during the same experiment, and under identical instrument conditions, bar the change in field. Green and yellow arrows indicate regions of diffracted intensity associated with the low and intermediate field structure phases respectively. Figure (f) shows the entire diffraction pattern of an FC measurement at an applied field of 2 T. This was obtained in a different experiment to those patterns shown in (a) to (e). The axes shown in (a) are valid for all figures, and in all cases the white arrows indicate $\{110\}$ directions. All patterns were obtained at 2 K and with $H \parallel \mathbf{c}$.

$\{110\}$ pinned FLL structures observed in the low field FC measurements (c.f. figure 3.19 (a)). For the fields of 2.0 T and 2.25 T, figures 3.25 (c) and (d) show that the re-emergence of the pinned structures is accompanied by the appearance of the intermediate field structure with a Bragg spot counterclockwise to the $\{110\}$ line. This shows that the intermediate field structure phase *co-exists* with low field FLL structures. At 2.5 T, figure 3.25 (e) shows the intermediate field structure phase to be the only structure within the entire sample. Despite the fact that the OFC procedure is unable to prevent the re-emergence of the $\{110\}$ pinned FLL structures during the transition, the distribution of diffracted intensity associated with the low field structures does not smoothly distort to accommodate the emergence of the intermediate field structure phase, leading us to conclude that the transition is likely to be intrinsically *first-order*.

The re-emergence of the $\{110\}$ pinned structures within the vicinity of the structure transition is testament to the shallowness of the intrinsic $\mathcal{F}_m$ of the low field structure phase. On increasing the field, it can be reasonably expected that the $\mathcal{F}_m$ of the low field phase will become yet shallower on approaching the crossover to the orientational $\mathcal{F}_m$ of the intermediate field structure phase. From this perspective, it is unsurprising that the orientational $\mathcal{F}_m$ provided by the $\{110\}$ pinning potential becomes comparable to, and even preferred to, the intrinsic $\mathcal{F}_m$ of the low field phase.

The detrimental role played by weak disorder on a first-order transition is well studied (see for example, Imry and Wortis (1979)). Typically weak disorder smears the sharpness of the transition, whilst strong disorder may be sufficient to completely round the transition so that it appears second-order. In the present case, the role of disorder on the transition may be exaggerated by the fact the transition is between two FLL structures each with Bragg spots relatively close to, but on opposite sides of, the $\{110\}$ pinning potential. Taking this into consideration, it is easy to envisage how the transition between the intrinsic FLL structures might be driven second-order in the presence of $\{110\}$ disorder. Indeed, this is borne out by a diffraction pattern obtained at 2.0 T (figure 3.25 (f)) obtained from a FLL pre-

pared using the standard FC procedure. Although some structure can be loosely discerned from the almost continuous elliptical intensity distribution, the lack of orientational order of the FLL indicates the coexistence of numerous shallow and competing $\mathcal{F}_m$ at the point at which the structure was frozen-in on cooling. This diffraction pattern at 2.0 T ultimately lies at the mid-point between what is observed to be a continuous field-variation of the FLL structure for FC measurements. From this respect, the OFC procedure turns out to be invaluable in promoting the flux lines to order within their local $\mathcal{F}_m$, be it associated with either of the intrinsic structures or that due to the $\{110\}$ pinning. The resulting distinction between either of the low field structures and intermediate field structure, allows us to identify that the field-dependence of the FLL structure through the transition is not intrinsically smooth.

Transition between intermediate and high field structures

Between the field range of 6.0 T to 7.5 T a first-order transition between the intermediate and high field structure types takes place. Determining the nature of this structure transition is simpler than for the case at low fields, as a clear co-existence of the intermediate and high field structures is observed on moving through the transition. As an example of this, figure 3.26 shows a diffraction pattern obtained in an applied field of 6.5 T, after the FLL was prepared by a FC procedure. The co-existence is unaffected by whether or not the FLL is prepared by the OFC or FC procedure; in neither case do the structures smoothly distort into one another as a function of field. Compared to the low field transition, the clarity of the high field transition suggests the $\mathcal{F}_m$ of the intermediate and high field structures are deeper at the point they cross.

Field-dependence of the characteristic primitive cell angle

Although a co-existence of different FLL structures provides a clear indicator for a first-order transition, a more quantifiable viewpoint is shown in figure 3.27 where we present the field-dependence of the FLL primitive cell opening angle. These

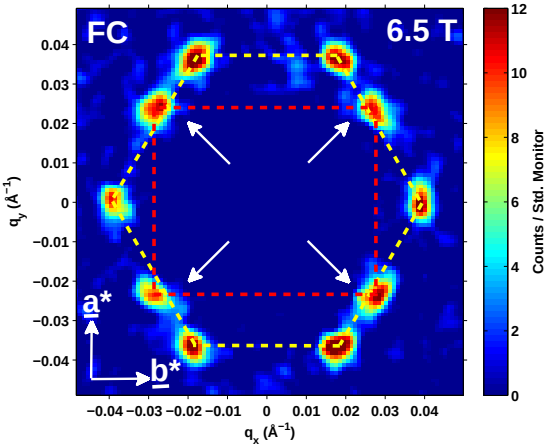

Figure 3.26: A FLL diffraction pattern obtained in an applied field of 6.5 T, at 2 K and with $H \parallel \mathbf{c}$. The FLL has been prepared using a FC procedure. White arrows indicate the $\{110\}$ directions. The overlaid yellow and red dashed line patterns indicate the co-existence of the intermediate and high field structure types respectively.

angles have been defined in previous subsections, and are indicated within the small schematic diagrams of the *real space* primitive cell orientation contained within the figure.

The first-order nature of the FLL structural transitions is again clear on inspecting figure 3.27; the structure does not change smoothly with field on passing through either transition. The graph also allows a quantifiable estimation of the field region of structural co-existence, being ≤ 0.5 T for both transitions. The co-existence likely indicates a small amount of inhomogeneity between the different crystals of the mosaic. From the size of these regions however, we estimate the transition fields as 2.0(2) T for the low field transition, and 6.7(2) T for the high field transition.

We also see from figure 3.27 that within the high field structure phase, there is a clear difference between the FC and OFC FLL structures, with the OFC preparation method promoting a structure that is closer to the perfect square. Within the intermediate field phase however, there is no clear difference between the shapes of the FLL prepared by the FC and OFC procedures. We initially proposed that the results obtained using the OFC method reveal the FLL coordination below the temperature

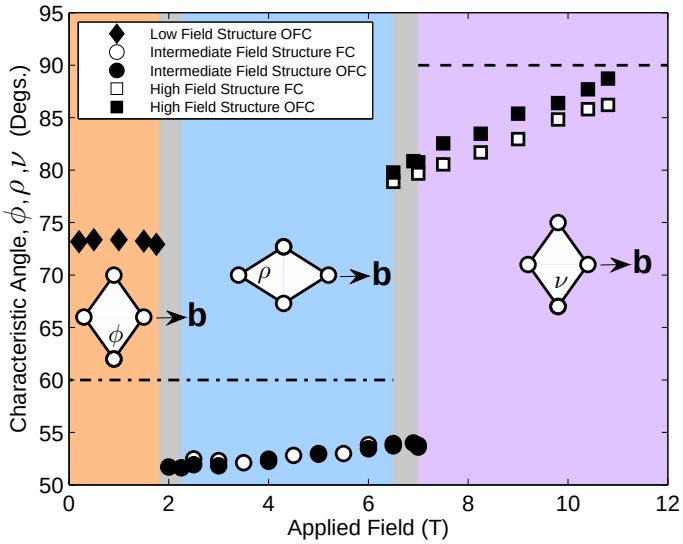

Figure 3.27: The field-dependence of the FLL primitive cell opening angle for the various FLL structures at 2 K, for fields up to 10.8 T applied parallel to the **c**-axis. For clarity, we only consider the intrinsic FLL structures. The inset schematic diagrams show the *real-space* orientation of each primitive cell with respect to the crystal axes, with the **b**-axis indicated. The angles indicated in these schematics are consistent with those defined previously. Grey shading indicates the field regions over which co-existing FLL structures are observed. The dashed line represents the opening angle of 90° as expected for a perfect square FLL structure, whilst the dash-dot line represents an opening angle of 60° as expected for an isotropic hexagonal structure. Error bars (not visible) are of order the size of the data points.

at which the FC structure is frozen in. We will see later in section 3.8, that the differing behaviour between the structure phases is consistent with slightly different temperature-dependences between the two structure types.

Distortion of FLL structures

The hexagonal FLL structures that we observe are distorted from the isotropic hexagon, with a long axis of distortion parallel to $\mathbf{a}^*$. A quantitative measure of this distortion can be described geometrically in terms of the axial ratio η of the ellipse that overlays the distribution of Bragg spots. In Appendix C we derive the geometric rules that relate η directly to the characteristic angles of the FLL structure. In figure 3.28, we show the field-dependence of η obtained across all hexagonal structures observed up to 7.0 T. In the low field phase, where the FLL is close to

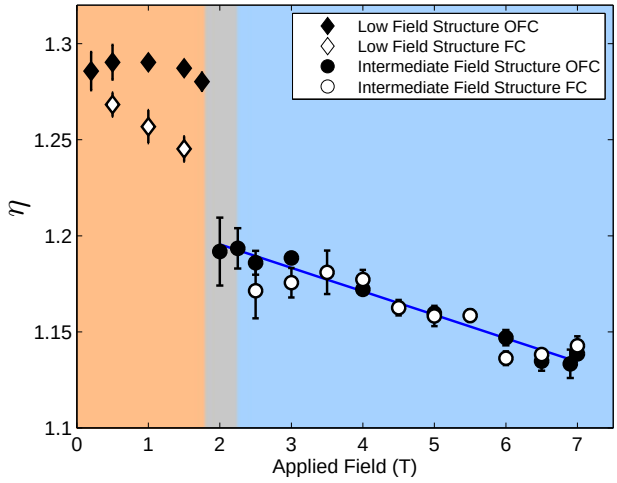

Figure 3.28: A graph showing the field-dependence at 2 K of the distortion parameter η for the low field (diamonds) and intermediate field (circles) structure phase types. The distinction between FC and OFC measurements is made by empty and filled symbols respectively. The solid blue line is a simple linear fit to the OFC data of the intermediate field structure phase.

being describable by anisotropic London theory, the value of η *equals* the in-plane penetration depth anisotropy $\gamma_{ab}\,(=\lambda_a/\lambda_b)$ (Thiemann et al., 1989). Our analysis shows this value to be essentially constant in the low field phase with a mean value 1.28(1); a value that compares favourably with those obtained from other bulk studies on overdoped samples (Ager et al., 2000; Brown et al., 2004; Khasanov et al., 2007). Figure 3.28 also shows that the first-order transition between the low and intermediate field structures manifests as a clear discontinuity in the value of η obtained from OFC measurements. Care must be taken in interpreting this discontinuity as an abrupt change in either of λ_a or λ_b within the London picture, as it may be necessary to invoke non-local corrections to both lengths, thus rendering the local London theory invalid. However, in the intermediate field phase we clearly see that the measure of the structural distortion is monotonically suppressed with field. The easiest interpretation of this is a field-induced suppression of the proximity-effect induced superconductivity on the chains.

Figure 3.28 also shows that, within the low field phase there is a noticeable difference between the FC and OFC value of η. It is difficult to see why there should be

a discrepancy at low fields as the measure of the structural distortion is an intrinsic effect of the Fermi surface anisotropy, which will be the same for both techniques of FLL preparation. Taking this into account, it seems that extrinsic effects originating from the residual $\{110\}$ disorder play a role in causing the apparent reduction of the FC values of η. As the FLL is close to a first-order transition, the reduced values can likely be attributed to the disorder rounding the sharpness of the transition so as to make the field-variation of η appear more continuous. This again highlights the benefit of the OFC procedure over the FC procedure in the low field range.

In the high field rhombic phase, we characterise the structural distortion in terms of the field-dependence of the aspect ratio of the rectangle that overlays the four Bragg spots of the structure. The aspect ratio is directly related to the primitive cell opening angle ν by

$$\text{Aspect Ratio} = \frac{1}{\tan\left(\frac{180-\nu}{2}\right)} \tag{3.3}$$

where the angle ν is as defined in figure 3.23 (a). Referring to a diffraction pattern of the high field structure, the aspect ratio is equivalent to the ratio of the height of the rectangle divided by the length. In figure 3.29 we plot the field-dependence of the aspect ratio of the rhombic structure for both FC and OFC measurements. The aspect ratio of such a FLL structure is seen to approach smoothly the value of unity expected for a perfect square. Clearly, the structural distortion is still changing up to the currently highest available fields, and it remains unclear from our measurements whether the FLL is close to a stable 'lock-in' structure phase or not.

3.5.6 Discussion of the field-dependence of the FLL structure at 2 K

Our results show that the *intrinsic* FLL structure at low field is single domain and distorted hexagonal structure, aligned with the crystal lattice. The physical mechanism that gives rise to this specific orientation is currently unexplained in the literature. Strictly within the local London theory, no preferred orientation of the FLL exists (Campbell et al., 1988; Thiemann et al., 1989). However, since all FLL

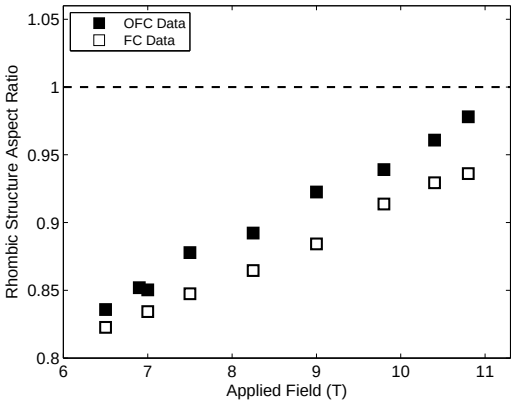

Figure 3.29: A graph showing the field-dependence of the aspect ratio of the rhombus that overlays Bragg spot distribution of the rhombic FLL structure of the high field phase. The aspect ratio is computed from the characteristic angle ν of the primitive cell. The black dashed line corresponds to an aspect ratio of 1, which is the perfect square. Error bars in the aspect ratio can be considered of order the size of the data points.

orientations are predicted to be degenerate, any additional effect, such as a weak non-local interaction between the FLL and the Fermi surface, will be sufficient to provide a preferred orientation, if pinning is not too strong. It also seems reasonable that our observed structure is consistent with one of the two expected according to the symmetry of the crystal (Walker and Timusk, 1995).

The first-order transition between the low and intermediate field structures reflects a crossover from one dominant $\mathcal{F}_m$ to another. In order to explain the occurrence of such a transition, it is necessary to invoke the onset of non-local effects at higher fields. The incorporation of non-local effects into the London theory takes the form of higher-order terms in $\mathbf{q}$ that couple the FLL to the anisotropies of the Fermi surface (Kogan et al., 1997a), and also the gap function (Franz et al., 1997). However, these theories typically only incoporate terms up to fourth order in $\mathbf{q}$, as these are all that is necessary to deduce the role of non-local effects for the commonly considered fourfold symmetric system. As a consequence, field-driven first-order structure transitions are predicted, but only for a 45° re-orientation of the primitive cell. Within such theories, to obtain a 90° re-orientation transition, it is necessary to consider higher-order terms that further break the fourfold sym-

metry. However, including these terms is cumbersome and calculations have not been reported. This results in it being difficult for us to determine the precise Fermi surface origin of the non-local component of the flux line-flux line interaction that directly causes the structure transition.

However, our results clearly indicate there are at least two non-local components to the flux line-flux line interaction that favour orthogonal orientations of the primitive cell. The effect on the FLL due to each component will depend on how each component couples to the anisotropies of the various Fermi surface sheets, and also how this changes with field. We suggest that the different orientations of the primitive cell reflect the influence of Fermi surface sheets that exhibit a markedly different anisotropy. Essentially this comes down to one primitive cell orientation being determined by the anisotropy of the plane bands, and the orthogonal orientation being ascribed to the chain bands. Similar qualitative arguments such as these were offered by Cubitt et al. (2003) in order to explain the re-orientation transition observed in the two band superconductor MgB_2. However, they mention that the assignation of different FLL structures according to different bands requires careful calculations within an appropriate theoretical framework. Unfortunately, such calculations have not yet been carried out for $YBa_2Cu_3O_7$. We also mention that according to Franz et al. (1997) another possible origin for a non-local component can be ascribed to the gap anisotropy.

The first-order transition at high field between a hexagonal structure at intermediate fields, and a rhombic structure at high field can be understood as due to an increasing prominence of the order parameter anisotropy. Only within the numerical calculations of Ichioka et al. (1999) are the free energies of hexagonal and square FLL structures predicted to *cross*, indicating a first-order transition between them. They predict the transition field to be 0.15 H_{c2}, which is higher than our observed transition field. However, these calculations were carried out at T =0.5T_c which is higher than that at which we performed our experiments. It is possible that this field will fall at lower T, and quasiparticles are forced to selectively occupy the nodal regions. For such a high field phase that is stabilised by the gap anisotropy,

the nearest neighbour directions of the FLL structure are predicted to be correlated to the nodal directions of the order parameter (Xu et al., 1996; Berlinsky et al., 1995; Ichioka et al., 1999). Therefore, if the rhombic shape of our FLL structure is stabilised by the gap anisotropy, our results indicate that the order-parameter is not purely $d_{x^2-y^2}$. This is in agreement with the results obtained at low fields (Smilde et al., 2005; Kirtley et al., 2006), which show there to be a noticeable s-wave admixture to the overall symmetry. Both of these studies predict the nodal directions to lie at angles of $\pm 50^\circ$ about the **b**-axis, in qualitative agreement with the nearest neighbour directions of our rhombic structure. We showed in figure 3.29 that the aspect ratio of the rectangle that overlays the rhombus smoothly approaches unity on increasing the field. Within the framework of the d-wave theories, this would suggest the s-wave admixture becomes suppressed with field, and the pure $d_{x^2-y^2}$-symmetry is recovered. However, evidence for a field-driven change in the nodal positions is lacking in the literature.

Although this explanation may seem possible, our results cannot rule out that the stabilisation of the rhombic structure is due to the onset of further non-local effects. The dominant square-like bands of the Fermi surface associated with the plane states have the expected symmetry for the stabilisation of a rhombic structure with nearest neighbours close to the $\{110\}$ directions (Franz et al., 1997; Kogan et al., 1997a). Unfortunately, $YBa_2Cu_3O_7$ is an example of a material where the predicted orientations of high field square FLL structures are qualitatively similar, whether stabilised by non-local effects or the order parameter anisotropy (Franz et al., 1997; Kogan et al., 1997a; Ichioka et al., 1999; Nakai et al., 2002). From this perspective, it seems that disentangling the two effects is somewhat inappropriate, as both are intimately related to the symmetry of the Fermi surface. However, dedicated calculations investigating the physical origins behind our FLL structure transitions are yet to be investigated theoretically.

3.6 Flux line lattice form factor up to 10.8 T, at 2 K and with $H \parallel \mathbf{c}$

To gain further insight into the behaviour of the FLL, it is reasonable to suggest that the physics behind the FLL structure and structure transitions will be manifested in measurements of the FLL form factor. In this section we provide the first analysis of the form factor in this material.

3.6.1 Flux line lattice form factor analysis

The modulus form factor, $|F(\mathbf{q})|$ for a specific Bragg spot is analysed in accordance with the details contained in Appendix A. For reasons that will become apparent, in our analysis we distinguish between the form factors of different types of Bragg spot, whilst the form factor values for equivalent Bragg spots are averaged. For simplicity, we only consider the form factor values of the intrinsic FLL structures created by the OFC preparation procedure.

In figure 3.30 we show our measurements of the modulus form factor collected over the entire field range up to 10.8 T and at 2 K. Figure 3.30 (a) shows the field-dependence of the form factors obtained within the low field phase. In this phase, two Bragg spots have $\mathbf{q} \parallel \mathbf{a}^*$, whilst those of the other four spots are off-axis. We see that the average form factors for the different types of Bragg spot are equivalent within the experimental error. Within the intermediate field phase, figure 3.30 (b) shows a clear anisotropy between the form factors of the spots with $\mathbf{q} \parallel \mathbf{b}^*$, and those of the off-axis spots. The field-dependence of the form factor ratio across the low and intermediate field phases is presented in figure 3.31. For the low field phase, we plot the field-dependence of the ratio $|F(\mathbf{q} \parallel \mathbf{a}^*)|/|F(\mathbf{q} \nparallel \mathbf{a}^*)|$, whilst for the intermediate field phase we plot the ratio $|F(\mathbf{q} \parallel \mathbf{b}^*)|/|F(\mathbf{q} \nparallel \mathbf{b}^*)|$. We clearly see that the first-order transition between the two structure phases further corresponds to an observed change in form factor behaviour. We also mention that unusually, the weaker form factor corresponds to the Bragg spot of the *shorter* $\mathbf{q}$-vector. In the high field rhombic phase, the four spots are equivalent, and in figure 3.30 (c) we

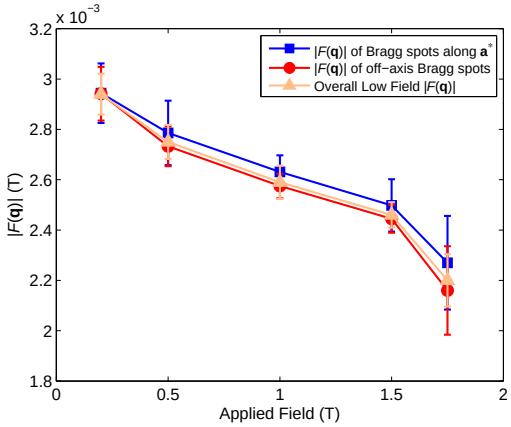

(a) Low Field Structure Phase

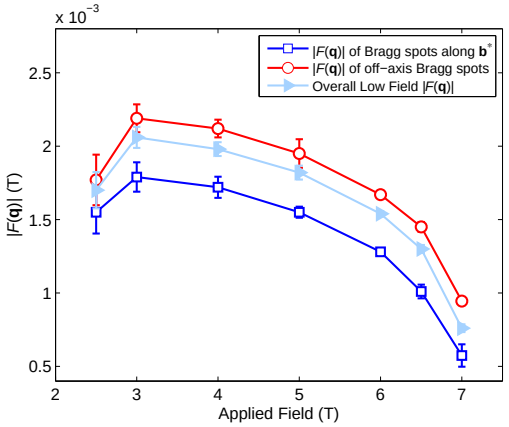

(b) Intermediate Field Structure Phase

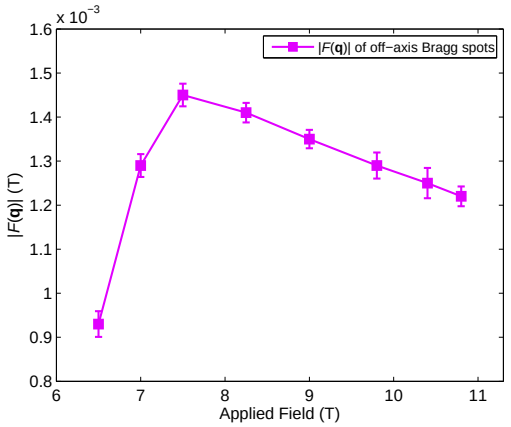

(c) High Field Structure Phase

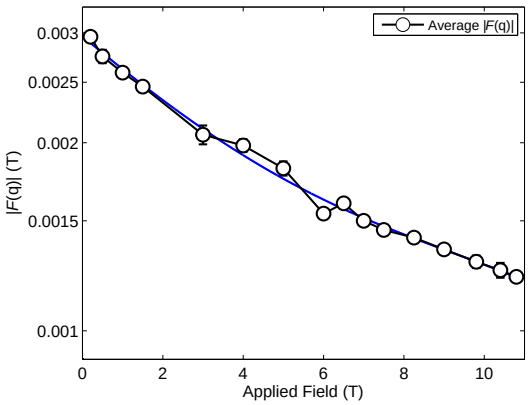

(d) Overall

Figure 3.30: Measurements of the FLL form factor at 2 K and with $H \parallel \mathbf{c}$. All measurements are obtained from FLLs prepared with the OFC technique. The results for the low field phase are shown in (a), the intermediate field phase in (b) and the high field phase in (c). In (a) and (b) we distinguish between the different types of Bragg spot, and further provide an average value of $|F(q)|$ taken over all six Bragg spots. In (d) we combine the results across all three structure phases in plotting the field-dependence of $|F(q)|$. At each field, the average form factor values of figures (a) and (b) are presented, along with the form factor values from figure (c). We exclude data at 1.75 T and 2.5 T, as the measures of the form factor data are unduly affected by the low field structure transition. For the fields of 6.5 T and 7.0 T, due to a clear co-existence of the FLL structures, we can account for all of the diffracted intensity. At these fields, the overall form factor is obtained by $|F(q)| = \sqrt{|F(q)_{int}|^2 + |F(q)_{rho}|^2}$, where $|F(q)_{int}|^2$ and $|F(q)_{rho}|^2$ are respectively the average values of $|F(q)|$ for the intermediate field and rhombic structures. The blue solid line in (d) is a guide to the eye.

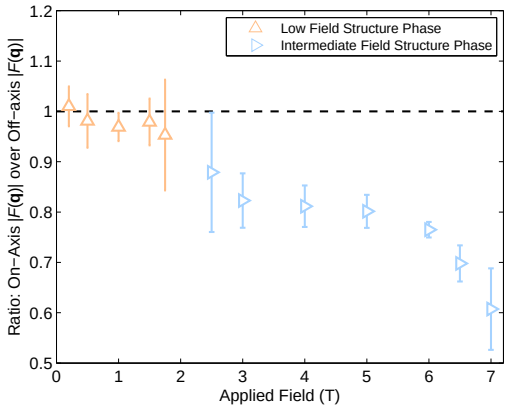

Figure 3.31: A graph showing the field-dependence of the form factor ratio between the inequivalent Bragg spots across the low and intermediate field structure phases. For the details of the ratios obtained in each phase, see the text.

present the mean form factor at each field. In figure 3.30 (d), we show the entire field-dependence of the form factor across all structure phases.

3.6.2 Emergence of non-local effects with increasing field?

The interpretation of our form factor data is not straightforward, as it is not immediately obvious which model we might use. In Appendix D we briefly compare the commonly used phenomenological models; the simple London model, the Clem model, and the Hao-Clem (HC) model. We decide the Clem model (equation 1.43) is the most appropriate with which to proceed. For a biaxial material such as $YBa_2Cu_3O_7$, the Clem model can be extended to allow for an anisotropy in both the length scales of λ and ξ_{GL}. For a Bragg spot with a **q**-vector lying in any direction, the field profile depends on λ and ξ_{GL} along both the **a** and **b**-axes. Therefore, the general expression for the form factor of any Bragg spot can be written as

$$F(\mathbf{q}) = \langle B \rangle \frac{gK_1(g)}{\mathrm{q}_x^2\lambda_a^2 + \mathrm{q}_y^2\lambda_b^2}, \qquad g = \sqrt{2}\left(\mathrm{q}_x^2\xi_{GL,b}^2 + \mathrm{q}_y^2\xi_{GL,a}^2\right)^{1/2} \tag{3.4}$$

where the 1 that appears in the denominator is dropped, as $1 \ll q_y^2\lambda_b^2$ and $1 \ll q_x^2\lambda_a^2$. This also allows us to write the expression for g in the more general form above. In reference to our measurements, x and y respectively indicate the $\mathbf{b}^*$ and $\mathbf{a}^*$ directions on the detector.

The application of the model remains complicated however, as there are four unknown parameters that are each possibly field-dependent. However, we note that within the low and intermediate field phases, there are Bragg spots with **q** parallel to a crystal axis. This simplifies matters, as if q_x or q_y is equal to zero, two parameters are eliminated. The method of analysis adopted for the low field structure phase is as follows:

1. We analyse the Bragg spots with $\mathbf{q} \parallel \mathbf{a}^*$. These spots are sensitive to λ_b and $\xi_{GL,a}$. We assume a reasonable starting value for $\xi_{GL,a}$ of 1.81 nm (taken from $H_{c2} = 100$ T), and use the Clem model to fit the data for λ_b. The values for q_y are those determined experimentally.

2. On the reasonable assumption that we are close to the London regime, we find λ_a by assuming that $\lambda_a = \gamma_{ab}\lambda_b$. The values for γ_{ab} are taken to be equivalent to the values of η as shown in figure 3.28.

3. To test if the Clem model can describe our data, we use the model in order to predict the form factor values for the other Bragg spots with $\mathbf{q} \nparallel \mathbf{a}^*$. At this stage, we have values for $\xi_{GL,a}$, λ_a and λ_b, but not $\xi_{GL,b}$. We make the assumption that the anisotropy in ξ_{GL} is drawn from the effective mass, in the same way as for λ, such that $\xi_{GL,b} = \gamma_{ab}\xi_{GL,a}$. This is the common case for single band materials. Whilst this will not be the case for multi-band $YBa_2Cu_3O_7$, our assumption does mean that $\xi_{GL,b} > \xi_{GL,a}$, which is qualitatively consistent with the predictions of Atkinson and Sonier (2008) shown in figure 3.9. At each field, using the values for the length-scales and the experimentally measured values of q_x and q_y, we use the Clem model to predict the form factors for the Bragg spots with $\mathbf{q} \nparallel \mathbf{a}^*$, and compare the results with the experimental data.

Figure 3.32 shows the fit of the experimental form factor data for $\mathbf{q} \parallel \mathbf{a}^*$ (filled blue squares) on using the Clem model (open light blue squares). The fitted value for λ_b is 105(2) nm. This value is used with γ_{ab} to obtain λ_a and $\xi_{GL,b}$. As γ_{ab} varies

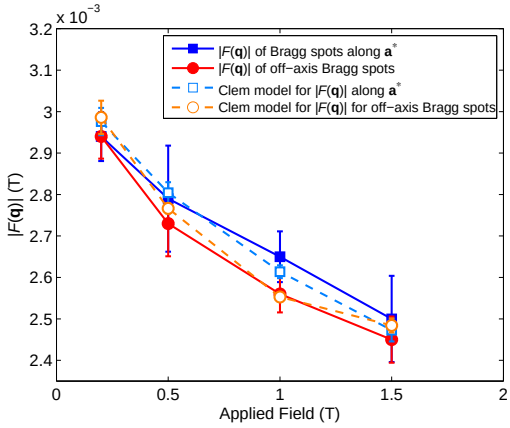

Figure 3.32: A graph showing the application of the Clem model described in the text, to the form factor data of symmetry inequivalent Bragg spots of the low field structure phase.

little over the field range, the values for $\lambda_a = 135(2)$ nm and $\xi_{GL,b} = 2.33(3)$ nm remain constant within the uncertainty. This is as expected if we are close to the London regime. We note that our values for λ_a and λ_b are comparable to other reported values (Basov et al., 1995; Johnson et al., 1999), though perhaps a little shorter. This may indicate our overdoped sample to be of higher quality. On applying the Clem model to predict the form factors for the Bragg spots with $\mathbf{q} \nparallel \mathbf{a}^*$ [12], the empty orange circles in figure 3.32 indicate a reasonable agreement with the experimental data (red filled circles) over the narrow field range.

The form factor data of the intermediate field phase provides a stiffer test of the Clem model and our assumptions. Initially, we maintain our original assumptions that the anisotropies of λ and ξ_{GL} are related by the London parameter γ_{ab}. We continue to take the values of γ_{ab} as equivalent to η shown in figure 3.28. However, this figure shows that η falls monotonically with field in this phase, which we suggested was most naturally associated with a suppression of the chain superconductivity. Hence, in order to continue using the Clem model, we allow the length-scales affected by the chain states, which are those associated with the **b**-axis, to vary with field. We subsequently assume that λ_a and $\xi_{GL,a}$ retain their respective values of

[12] We only consider fields up to 1.5 T, as by 1.75 T the measured form factors are likely affected by the onset of the structure transition into the intermediate field phase.

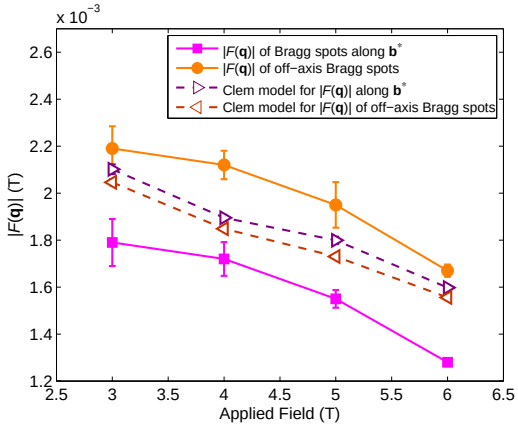

Figure 3.33: A simple application of the Clem model to the form factor data of the Bragg spots of the intermediate field structure phase. The model values are calculated using the method described in the text.

135 nm and 1.81 nm as found/used in the low field phase, and that these values remain field-independent. As we can calculate the values of all four length-scales, we simply use the Clem model, and the experimentally measured **q**-values, to predict the form factors for two types of Bragg spot. Unfortunately, figure 3.33 shows the Clem model provides a poor description for our data.

To proceed in using the Clem model, it seems further assumptions associated with the length-scales are required. Let us consider the Bragg spots with $\mathbf{q} \parallel \mathbf{b}^*$. The predictions made using the Clem model overestimate the value of the form factor. The estimation can be reduced if we let λ_a and/or $\xi_{GL,b}$, be field-dependent such that they *increase* with field. However, on studying the available theoretical work it seems that an increasing core-size is rather unlikely. Numerical calculations based on the Eilenberger theory predict the core-size within a d-wave superconductor to quickly become suppressed with increasing field (Ichioka et al., 1999); a prediction also consistent with the calculations of Atkinson and Sonier (2008) shown in figure 3.9. Furthermore, the Hao-Clem expression (equation D.3) for the field-dependence of the core-size indicates that over our field range, the core-size is expected to fall slightly with increasing field. Based on this evidence, we decide to rule out a field-induced core expansion, and instead consider the possibility that λ_a increases.

If λ_a increases with field, then if the London relationship $\lambda_a = \gamma_{ab}\lambda_b$ remains valid, λ_b will also increase. However, for realistic values of $\xi_{GL,a}$ and $\xi_{GL,b}$, an increase in λ_b causes the predictions made using the Clem model to fall further into disagreement with the experimental data for Bragg spots with $\mathbf{q} \nparallel \mathbf{b}^*$. Therefore, we conclude that any change in λ_a cannot be directly mapped onto a change in λ_b using the London parameter γ_{ab}. Similarly, γ_{ab} is unlikely to be able to describe the relationship between $\xi_{GL,a}$ and $\xi_{GL,b}$. We note that according to the predictions of Atkinson and Sonier (2008) shown in figure 3.9, the field-dependence of the core size is anisotropic, and for fields of ~ 3 T and higher, to a good approximation, the core is closer to being isotropic. On assuming that $\xi_{GL,a} = \xi_{GL,b} = 1.81$ nm within the entire intermediate field phase, this allows an easier investigation of the behaviour of the penetration depths. While this might seem like a gross simplification, it is at least consistent with theoretical work that is directly applicable to this material. It can also be shown that any sensible anisotropy in ξ_{GL} has a weaker effect on the predictions made using the Clem model, than the anisotropy in λ.

We now repeat the analysis of the intermediate field structure phase using the constant core size parameters, and the experimentally measured **q**-vectors. We can fit the form factor data for the Bragg spots with $\mathbf{q} \parallel \mathbf{b}^*$ to obtain $\lambda_a = 151(4)$ nm. Using this knowledge, we subsequently fit the form factors for the off-axis spots to find that $\lambda_b = 104(4)$ nm. Figure 3.34 shows a comparison between the Clem model fits to the experimental data.

There appear to be two contradictory outcomes of this analysis. Firstly, we find the anisotropy between λ_a and λ_b to be larger than at low field, and that naively expected from the measure of hexagonal distortion in the London regime. Secondly, we find λ_a is now significantly longer than at low field, but λ_b remains unchanged. The latter must be the case in order to understand the form factor anisotropy in terms of the Clem model. However, if we are correct in our assumption that field-dependences of λ and ξ_{GL} are independent, then in the absence of the precise knowledge of these dependences are, we have resulted in finding some seemingly counterintuitive results.

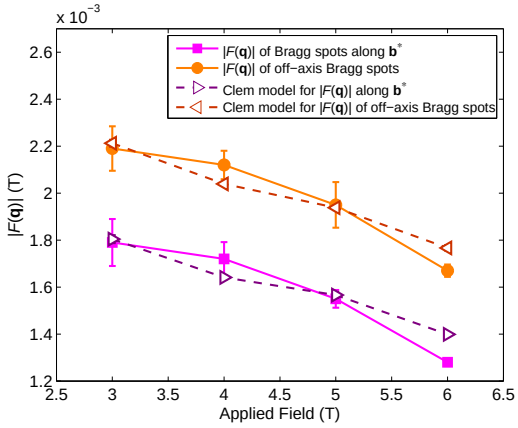

Figure 3.34: An application of the Clem model to the form factor data of the intermediate field structure phase, after making further assumptions described in the text. Here we have assumed that $\xi_{GL,a} = \xi_{GL,b} = 1.81$ nm, for all fields. Using the experimentally measured **q**-vectors and the Clem model to fit the data, we find that $\lambda_a = 151(4)$ nm, and $\lambda_b = 104(4)$ nm.

We also re-analysed the low and intermediate field data using the HC model outlined in Appendix D, which inherently ascribes a field-dependence to ξ_{GL}. Very similar results to those above were obtained. An alternative approach taken by Bowell (2008), was to quantitatively compare the form factor predictions of the various phenomenological models with the predictions made using the quasiclassical Eilenberger theory (Ichioka et al., 1999; Ichioka and Machida, 2007). Over the low field region, and for the most relevant microscopic calculations carried out at $T = 0.1T_c$ (Ichioka and Machida, 2007), the phenomenological (and biaxial) form factor model that gave the best approximation to the numerical calculations was

$$F(\mathbf{q}) = \langle B \rangle \frac{\exp\left(-0.44\left(\mathrm{q}_x^2\xi_{GL,b}^2 + \mathrm{q}_y^2\xi_{GL,a}^2\right)\right)}{\mathrm{q}_x^2\lambda_a^2 + \mathrm{q}_y^2\lambda_b^2}. \tag{3.5}$$

This model is essentially the London model with a core-correction term of the form, $\exp(-C\xi^2q^2)$, where $C = 0.44$ is specifically identified as that which gives agreement to the microscopic theory. On re-analysing our data using this model, we find it provides a poorer description that that given by the Clem model. This is because the core-correction term underestimates the rate at which the form factor falls at low field (i.e. the factor 0.44 is too small). We could adjust the value of 0.44 to improve the fit, but this amounts to a fifth free parameter, and as we have seen,

four is already rather too many.

However, based on our analysis using the Clem model, discounting any unexpected behaviour of $\xi_{GL,a}$ and $\xi_{GL,b}$, it seems likely that λ_a and λ_b do not enjoy a simple London-like relationship at intermediate fields. We find λ_a to lengthen noticeably, whilst λ_b remains robust across the FLL structure transition.

The apparent lengthening of an experimentally obtained λ has been reported before in μSR measurements on $YBa_2Cu_3O_{7-\delta}$ (Sonier et al., 1994, 1999). In these studies, the muon precession signal is fitted according to a model based on the Fourier transform of the calculated field distribution for the expected FLL structure. The 'effective' penetration depth, λ_{eff}, is that which fits the data. Note that whilst λ_{eff} is of order the actual λ in length, the term 'effective' implies it is ultimately determined by the *measured* field-distribution and the analysis routines. At high field, these experiments claim to observe an increase in the in-plane λ_{eff} [13]. Dedicated theoretical work was subsequently carried out within a London/GL framework in order to explain the lengthening of λ_{eff}, and the suggested explanation was that it is due to the onset of non-linear and non-local effects at high field (Franz et al., 1997; Amin et al., 1998, 2000). Non-linear effects are associated with a field-induced adjustment of the quasiparticle spectrum at the nodes. Under an applied field, quasiparticle states move below the Fermi energy, and induce a component in the quasiparticle current flow in the opposite direction to the main supercurrent. This leads to a non-linear relationship between the supercurrent density and its velocity, which weakens the supercurrent response, and increases λ (Amin et al., 1998). However, the onset of non-local effects is considered to be more important that non-linear effects (Franz et al., 1997; Amin et al., 1998, 2000). This is due to the achievement of the extreme non-local limit at the gap nodes, where the non-local length scale $\xi_0(\mathbf{k}) = v_F/\pi\Delta(\mathbf{k})$, formally diverges. Within the nodal vicinity, and for a non-uniform field as exists in the mixed state, a larger ξ_0 results in a larger

[13] Note that the authors do not discriminate between the **a** and **b**-axes in experiment nor theory, and so consider an average over the plane. They also assume the FLL exhibits a field-independent isotropic hexagonal structure.

volume over which to average the field, in order to find the supercurrent density. This weakens the supercurrent response, and thus increases λ. In essence, in the context of the μSR experiments, Amin et al. (1998, 2000) show that non-local effects modify the field-distribution, which result in an increased λ_{eff}.

The possible role that non-local effects may play on SANS measurements of the FLL has not yet been considered theoretically. However, SANS, like μSR, is also sensitive to the field distribution within the material, and if non-local effects do modify this distribution at low temperature, we speculate a modification of the measured λ could be induced in an analogous way as for the μSR studies. If our observations can be understood in terms of theories of Amin et al. (1998, 2000), we are sensitive to 'd-wave non-locality,' the effects of which will be most prominent for the plane states. However, we note any non-local modification of the field-distribution that affects the measured value of λ_a, would also be expected to affect the component of λ_b drawn from the plane supercurrents. As λ_b draws components from both plane and chain states, and we do not observe a change in λ_b across the structure transition, we speculate that due to a complex hybridisation between the plane and chain states (Atkinson and Sonier, 2008), λ_b is more robust to the effects of non-locality compared to λ_a.

In summarising, we acknowledge our analysis relies on a series of assumptions, our discussion is speculative, and that we have no dedicated theoretical support. In spite of these criticisms, and drawing on the available literature, it does seem plausible that 'd-wave non-local effects' will become increasingly important at intermediate fields. New theoretical calculations of the form factor are required, which would allow use to understand the SANS measurements. The most promising theoretical path involves dedicated calculations carried out using the quasiclassical Eilenberger theory. At the time of writing, the first calculations have recently been carried out by M. Ichioka of Okayama University, Japan, and reproduce the form factor anisotropy that we observe in the intermediate field phase.

3.7 Higher order Bragg spots at 2 K

Due to the large value of λ in $YBa_2Cu_3O_7$, higher-order Bragg spots are difficult to observe experimentally. Some effort was spent in trying to observe the next order $\{1,1\}$ Bragg spots. Within the hexagonal phases a systematic investigation of the $\{1,1\}$ spots has not yet been carried out, as such spots are only *just* observable for fields up to 3 T. Here, we focus on our observations in the high field phase.

Figure 3.35 shows a FLL diffraction pattern obtained in a field of 7.5 T. We observe clear $\{1,1\}$ spots with $\mathbf{q} \parallel \mathbf{a}^*$, that are of visibly weaker intensity than the four $\{1,0\}$ spots of the rhombic structure. However, at the time of writing, we have not yet made clear observations of the expected $\{1,1\}$ Bragg spots with $\mathbf{q} \parallel \mathbf{b}^*$. This disparity needs to be understood. This is especially the case considering that our intermediate field phase exhibits an anisotropy between the $\{1,0\}$ spots, with the weaker spots lying at shorter $\mathbf{q}$. This is most unusual, as weaker spots are commonly considered as higher-order. However, for our intermediate field phase, it seems difficult to ascribe the low $\mathbf{q}$ spots as higher-order than $\{1,0\}$. However, without observing the $\{1,1\}$ Bragg spots with $\mathbf{q} \parallel \mathbf{b}^*$, it might be suggested the high field structure is actually distorted hexagonal, exhibiting 'weak' first-order spots with $\mathbf{q} \parallel \mathbf{a}^*$.

In order to understand the nature of the $\{1,1\}$ spots with $\mathbf{q} \parallel \mathbf{a}^*$, full rocking-curve measurements were carried out in order to obtain the field-dependence of the form factor. In figure 3.36 (a) we show the form factor for the $\{1,1\}$ and $\{1,0\}$ types of spot. In figure 3.36 (b), we show the field-dependence of the ratio $|F(\mathbf{q} \parallel \mathbf{a}^*)|/|F(\mathbf{q} \nparallel \mathbf{a}^*)|$, i.e. $|F(\mathbf{q}\ \{1,1\})|/|F(\mathbf{q}\ \{1,0\})|$. We see that the $\{1,1\}$ spots with $\mathbf{q} \parallel \mathbf{a}^*$ genuinely do correspond to a weaker field modulation, and this modulation becomes progressively weaker with increasing field. This corresponds to the expected situation for higher-order spots. However, it is important to understand the disparity between the ability to measure $\{1,1\}$ spots with $\mathbf{q} \parallel \mathbf{a}^*$, and the apparent difficulty in measuring $\{1,1\}$ Bragg spots with $\mathbf{q} \parallel \mathbf{b}^*$.

To understand this, we re-examine our form factor measurements in terms of the

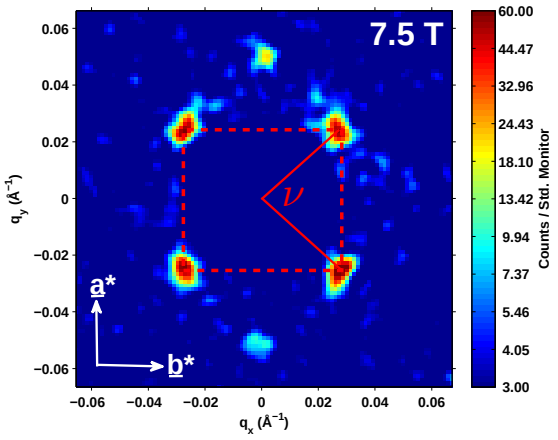

Figure 3.35: A FLL diffraction pattern obtained in an applied field of 7.5 T, a temperature of 2 K, and with $H \parallel \mathbf{c}$. The red dashed line indicates the rhombic structure accompanied by $\{1,1\}$ Bragg spots with $\mathbf{q} \parallel \mathbf{a}^*$. Due to the apparent weakness of these Bragg spots, in this figure, we use a logarithmic intensity scale. Note the absence of corresponding $\{1,1\}$ Bragg spots with $\mathbf{q} \parallel \mathbf{b}^*$. The angle ν has precisely the same definition as the characteristic angle of the rhombic structure shown in figure 3.23 (a).

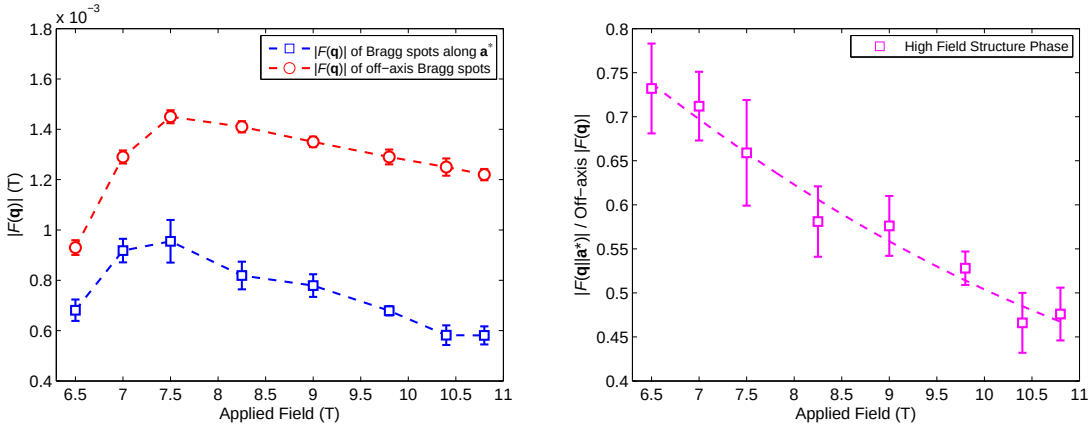

(a) (b)

Figure 3.36: In (a) we show the field-dependence of the form factor for the two different spot types of Bragg spot observed in the high field phase. The form factors for the off-axis Bragg spots correspond to those values shown earlier in figure 3.30 (c). In (b) we show the field-dependence of the ratio between the different Bragg spots observed in the high field structure phase. The form factor ratio plotted is $|F(\mathbf{q} \parallel \mathbf{a}^*)|/|F(\mathbf{q} \nparallel \mathbf{a}^*)|$. All data were obtained at 2 K, and with $H \parallel \mathbf{c}$. The dashed lines are guides to the eye.

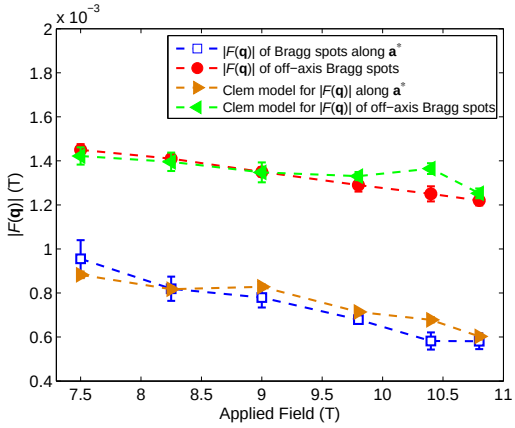

Figure 3.37: The best fits of the Clem model to the experimental data in the high field structure phase. The fitted values for the penetration depths are $\lambda_a = 159(2)$ nm and $\lambda_b = 131(2)$ nm.

description afforded by the Clem model (equation 3.4). In doing so, we adopt a similar approach as done previously for the hexagonal phases. We maintain our high-field assumption that the core-sizes $\xi_{GL,a} = \xi_{GL,b} = 1.81$ nm are field-independent. This is in reasonable agreement to the predictions shown in figure 3.9. We then use the Clem model, and the experimentally measured **q**-values, to fit the form factor data for the $\{1,1\}$ spots with $\mathbf{q} \parallel \mathbf{a}^*$ for fields of 7.5 T and above [14]. The fitted value of $\lambda_b = 131(2)$ nm. We now use this value in order to fit the form factor data for the $\{1,0\}$ spots and find λ_a. The fitted value is $\lambda_a = 159(2)$ nm. In figure 3.37, these fits are compared to the experimental data. We note that both λ_a and λ_b have *increased* over their intermediate field values, consistent with the suggestion that non-locality becomes increasingly important at higher fields.

We now take advantage of the properties of Bravais lattices. At each field, we know where we expect to find a $\{1,1\}$ spot with $\mathbf{q} \parallel \mathbf{b}^*$. Using this information, we initially see that part of the disparity in the $\{1,1\}$ form factors over our field range will be due to the fact that the **q** for the spots with $\mathbf{q} \parallel \mathbf{b}^*$ is *always* larger than those with $\mathbf{q} \parallel \mathbf{a}^*$. On taking the extracted value of λ_a, we use the Clem model to predict the expected field-dependence of the form factor for these spots. These values are

[14] At fields below 7.5 T, we are sensitive to the effects of the FLL structure transition, and thus do not include this data in with the fit.

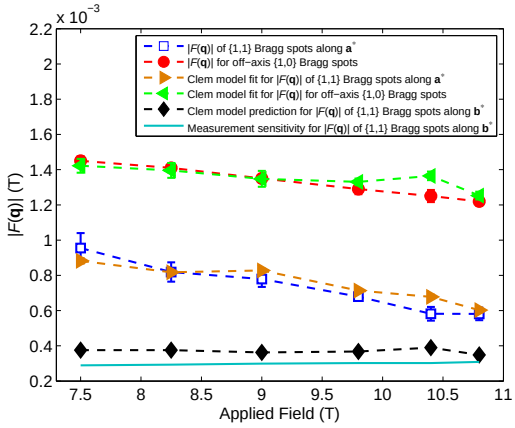

Figure 3.38: A comparison between the experimentally observed $\{1,0\}$ and $\{1,1\}$ form factor data with associated Clem model fits, and the predicted $\{1,1\}$ form factor values for Bragg spots with $\mathbf{q} \parallel \mathbf{b}^*$. These values, predicted on using the Clem model, lie close to the measurement sensitivity across the entire field range. The measurement sensitivity indicated is estimated based on the typical counting statistics used to obtain the $\{1,1\}$ form factor data for the Bragg spots with $\mathbf{q} \parallel \mathbf{a}^*$.

shown in figure 3.38 (filled black diamonds). These predicted values lie very close to our estimate of the measurement sensitivity, which indicates the minimum form factor we might expect to observe under the typically used counting statistics [15]. This indicates that it is not surprising that we do not observe a clear signal from the Bragg spots with $\mathbf{q} \parallel \mathbf{b}^*$. Hence, we can understand the $\{1,1\}$ form factor anisotropy in terms of the Clem model. However, as in the hexagonal phases, this relies on our assumptions being correct. The confirmation of this interpretation will require new, more sensitive measurements that are able to measure the $\{1,1\}$ Bragg spots with $\mathbf{q} \parallel \mathbf{b}^*$.

Our interpretation would also benefit from dedicated theoretical calculations of the internal field distribution, which can make direct predictions for the magnitudes of the Fourier components. The theoretical work of Ichioka et al. (1999) *does* make predictions of the field-dependence of the $\{1,1\}$ form factors for a square

[15] The estimation of the measurement sensitivity is made by rotating the reciprocal lattice to the expected Bragg angle for the $\{1,1\}$ Bragg spot with $\mathbf{q} \parallel \mathbf{b}^*$, and counting just at this angle. The measure of the intensity extracted over a region on the detector corresponding to the expected position and size of the Bragg spot corresponds to a minimum measure of the peak intensity of the rocking-curve. This peak intensity is used to make an estimate of the minimum form factor with its associated error.

FLL stabilised by a $d_{x^2-y^2}$ gap anisotropy. The prediction is that the form factor ratio $F(\mathbf{q}_{\{1,1\}})/F(\mathbf{q}_{\{1,0\}})$ is ∼0.45 at zero field, falls slightly to a minimum value of ∼0.4 at $\sim 0.1H/H_{c2}$, and increases monotonically with field to be ∼0.7 close to H_{c2}. The initial fall of the ratio is consistent with our observations shown in figure 3.36 (b), though there is a clear quantitative disagreement. However, the calculations of Ichioka et al. (1999) were carried out at $T = 0.5T_c$, and later work from the same group at $T = 0.1T_c$ show a large qualitative difference in the form of the field-dependence of the $\{1, 0\}$ form factor between the two temperatures. Numerical calculations of the $\{1, 1\}$ form factors for lower temperatures have not been reported.

Our measurements of $\{1, 1\}$ spots in the rhombic phase cast light on the difficulty in measuring the form factors of the $\{1, 1\}$ spots of the hexagonal phases. Geometrically speaking, for the isotropic hexagonal coordination, $\mathbf{q}_{\{1,1\}}/\mathbf{q}_{\{1,0\}} = \sqrt{3}$, whilst for the isotropic square coordination, $\mathbf{q}_{\{1,1\}}/\mathbf{q}_{\{1,0\}} = \sqrt{2}$. Hence, at lower fields, to first approximation, the **q**-vectors for the $\{1, 1\}$ spots are proportionally larger for the hexagonal structures. Using these predicted **q**-values, and the extracted values for λ obtained in the previous subsection, we use the Clem model to make predictions for the expected form factor values for the $\{1, 1\}$ spots. Again, the difficulty in observing spots for fields above 3 T is consistent with the predicted form factors lying close to the measurement sensitivity.

3.8 Flux line lattice structure and form factor at higher temperatures

3.8.1 Measurements of structure at higher temperatures

We investigated the detailed shape of the FLL at higher temperatures, in order to deduce how the FLL structure phase boundaries might behave as a function of temperature within the $H\|$ **c** phase diagram. Characterising these phase boundaries might also provide extra details regarding the physical mechanism behind the FLL structure transitions, and provide a comparison to the phase diagram of the lightly twinned $YBa_2Cu_3O_7$ sample shown in figure 3.14.

Our preliminary temperature scans indicated the precise shape of the FLL to be remarkably temperature-independent. To investigate this is more detail, at 6.9 T we carried out a temperature-warming scan essentially *along* the high field structure phase boundary. To perform this scan, initially the FLL was prepared at 2 K via an OFC procedure. On warming to the desired temperature, a short field-oscillation was carried out in order to equilibrate the FLL structure. At each temperature, full rocking-curve measurements were carried out in order to obtain the full integrated intensity over all types of spot present.

At 2 K and 6.9 T, figure 3.27 shows we start with a co-existence of both intermediate and high field phases. On increasing the temperature, figure 3.39 shows that both these structures co-exist over the entire range up to 70 K. At temperatures beyond this, although diffracted intensity was visible, we were unable to fit the positions of the Bragg spots reliably. We see in figure 3.39 that the precise shape of the primitive cell for both intermediate (figure 3.39 (a)) and high field (figure 3.39 (b)) structure types is remarkably insensitive to the temperature. In particular, the precise shape of the primitive cell of the intermediate field phase changes only by $\sim 1^\circ$ over the entire temperature range. It is clearly noticeable that the structure only varies with temperature for temperatures above $\sim$50 K. This can be interpreted that the temperature at which the FLL structure is frozen-in (the irreversibility line), in spite of the OFC procedure, is actually at $\sim$50 K, and not at lower temperatures as previously thought.

Figure 3.40 shows the temperature-dependence of the fraction of diffracted intensity associated with each of the two domains. To obtain this fraction at each temperature, for each structure type we calculate the appropriate mean $|F(q)|$ over all the spot types for each structure. The measure of the total diffracted intensity from both structures is found according to $|F_{tot}(q)|^2 = |F_{int}(q)|^2 + |F_{high}(q)|^2$, from which the fraction associated with each structure type is found by dividing its $|F(q)|^2$ by $|F_{tot}(q)|^2$. Such a fraction does not represent the *fraction* of the sample occupied by each domain, unless the scattered intensity of the 'pure' phases each side of the phase boundary is equivalent. We see from figure 3.30 (d) that this is

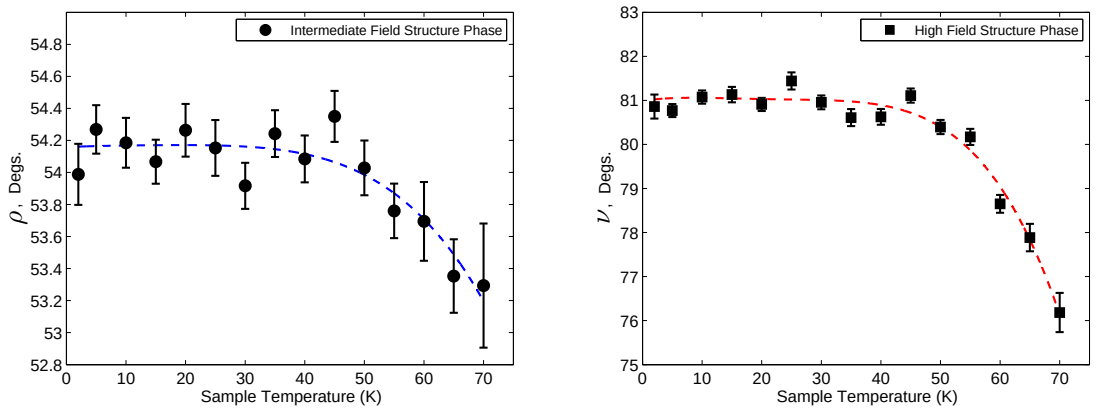

(a) (b)

Figure 3.39: The temperature dependence, with $H \parallel \mathbf{c}$ and at a field of 6.9 T, of the characteristic primitive cell angle (a) ρ for the intermediate field structure phase and (b) ν for the high field structure phase. These angle labels are consistent with those shown in figure 3.27. In each case, the dashed lines are guides to the eye.

not the case, and 6.9 T corresponds to a field slightly deeper into the high field phase. Our comparison also assumes that the intrinsic temperature-dependence of the form factor for both phases has an approximately equivalent form, as large differences could distort our results. Whilst this will not be strictly true, our pure phase measurements shown later in section 3.8.3 (figures 3.43 (a) and 3.44) indicate this is a reasonable assumption. Taking these facts into consideration, figure 3.40 shows that the intensity fraction ascribed to each domain remains essentially temperature-independent. However, within the statistical uncertainty, we cannot rule out a very weak curvature.

Most of our measurements for temperatures above 2 K were carried out using temperature-warming scans. Unfortunately, due to beam time constraints and the large size of the superconducting phase diagram, limited time has been spent investigating hysteretic effects. However, we did carry out some investigations of hysteresis at fields deep within the low and intermediate field phases. The amount of hysteresis was deduced by comparing the Bragg spot intensities obtained from fixed-angle temperature-warming scans to corresponding temperature-cooling scans. In the low field phase at 1 T, a small degree of hysteresis was observed, whilst at 5 T

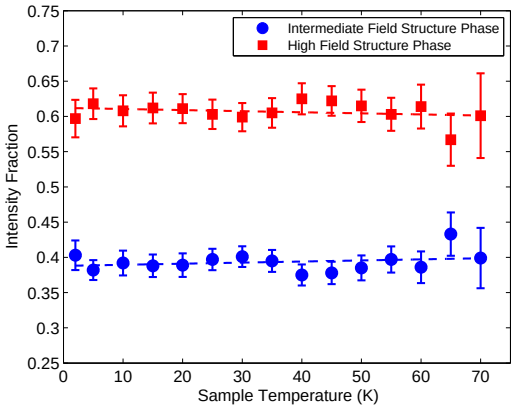

Figure 3.40: A warming scan temperature-dependence of the intensity fraction associated with the intermediate and high field structure types at 6.9 T. The intensity fraction exhibited by each domain is shown as fraction of 1. The dashed lines are linear guides to the eye, indicating the intensity fraction remains essentially temperature-independent.

in the intermediate field phase, there was no difference in spot intensities within the experimental uncertainty. Though not yet fully characterised, our initial results suggest that hysteretic effects will not greatly affect the results presented here. Our measurements of both the detailed FLL structure, and the intensity of each structure at 6.9 T, indicate the high field phase boundary is essentially temperature-independent. However, any variation is unlikely to be larger than the hysteretic field region indicated in figure 3.27. Even though we scanned through the high field hysteretic region, we would expect a phase boundary of stronger curvature to be observable in our temperature-dependent scans. The measurements reported at 6.9 T are currently the only data obtained on using such fine temperature increments. At other fields in the hexagonal phases, coarser temperature scans have been carried out, providing results consistent with a remarkable insensitivity to the temperature.

3.8.2 Flux line lattice structure type phase diagram

The insensitivity of the FLL structure to temperature made the deduction of the structure phase boundary lines for $H \parallel \mathbf{c}$ much simpler. Our method for determin-

ing a phase boundary line is as follows: for a series of fields within the vicinity of the field co-existence region, the same coarse temperature-scan was carried out. At each temperature, full rocking curves were obtained in order to obtain the appropriate mean $|F(q)|$ over all the spot types for each structure. At each temperature, we determine the field at which each FLL structure contributes 50 % of the overall diffracted intensity. Using all of our available information, figure 3.41 shows the FLL structure type phase diagram. We see that, based on the form factor measurements, our estimate of the 2 K transition between the low and intermediate field phases is slightly higher than our initial estimate based on structural measurements. For the upper phase boundary line however, there is good agreement between the transition field determined from form factor and structure measurements. We choose to plot our phase boundary lines as guides to the eye that pass through to the datapoints computed from form factor measurements. We mention that this diagram has only been constructed using warming-scan data. It is the intention of future experiments to learn if hysteretic effects might cause the positions of the phase boundary lines to be slightly different.

Figure 3.41 reveals our phase boundaries to be essentially flat as a function of temperature. However, within the accuracy of our measurements, we are unable to rule out either phase boundary exhibiting a weak curvature at higher temperature. Our phase diagram for $H \parallel \mathbf{c}$ lies in strong contrast to that of the lightly twinned sample shown earlier in figure 3.14. In that sample, the phase boundary exhibits a noticeable upward curvature, indicating the temperature recovers the low field structures which are associated with twin boundary pinning. As the phase boundary for the twinned sample is continuous, we suggest that its field and temperature phase diagram is determined by the balance between the intrinsic $\mathcal{F}_m$, and the $\mathcal{F}_m$ of the $\{110\}$ pinning potential.

Within the theoretical literature, the weak temperature-dependence of our phase boundary lines is also surprising based on what might be expected for High-T_c materials. The terms that introduce anisotropy into the flux line-flux line interactions are predicted to be suppressed with temperature. Within the framework of the qua-

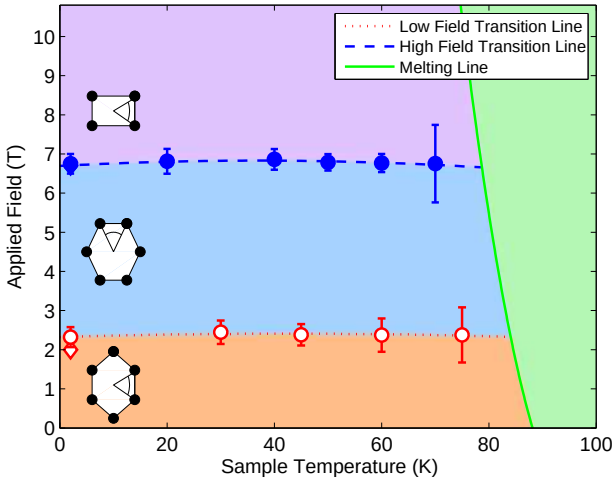

Figure 3.41: The FLL structure type phase diagram for $H \parallel \mathbf{c}$ constructed from measurements of the FLL structure and form factor. The inset schematic diagrams indicate the proposed FLL structure for the relevant region of the superconducting phase diagram. The circle data symbols were obtained from measurements of the FLL form factor. The diamonds correspond to the estimate of the phase boundary as determined from structural measurements. The dotted and dashed lines are determined using just the datapoints determined from the FLL form factor, and provide guide to the eye estimates of the structure phase boundaries. The solid line is the melting line is deduced from data presented by Roulin et al. (1998).

siclassical Eilenberger theory, at higher temperatures the quasiparticle excitation spectrum becomes increasingly isotropic. Hence, any FLL structures stabilised by a d-wave gap anisotropy are expected to become increasingly isotropic, as the quasiparticle excitation spectrum becomes increasingly isotropic. The same is also expected of the various non-local London theories Kogan et al. (1996, 1997a); Affleck et al. (1997); Franz et al. (1997); Amin et al. (2000), as temperature suppresses the influence of non-local effects on the interactions between flux lines. Within the GL theories (Berlinsky et al., 1995; Xu et al., 1996; Shiraishi et al., 1999), the mixed gradient higher-order terms that introduce the anisotropy into the free energy functional *must* be suppressed with temperature, such that an isotropic hexagonal coordination is recovered close to T_{c2}. In fact, our results in figure 3.39 show that the FLL mostly retains the measure of its distortion right up to T_{c2}, supporting the idea that plane and chain states possess a single critical temperature, in agreement with

the proximity effect models (Atkinson, 1999; Atkinson and Sonier, 2008). However, even allowing for this first approximation re-scaling of the isotropic hexagon over the entire phase diagram, from the theoretical perspective, the temperature-independence of the structure phase boundaries is remarkable. We might also suggest that the similar *form* of the structure phase boundaries indicates that similar physics lie behind the FLL structure transitions. This would indicate that the physical mechanism behind both of the structure transitions is due to an increasing influence of non-local effects. However, the deduction as to why the temperature is so uninfluential is currently unexplained.

3.8.3 Temperature-dependence of the form factor

The weak temperature-dependence of the precise FLL structure provided us with the opportunity to record the temperature-dependence of the form factor, without using excessive amounts of beamtime. Typically, carrying out such measurements is a lengthy process. At each temperature, full rocking curves should be carried out to capture the entire integrated intensity for the Bragg spots, and also to accurately determine the associated **q**-vectors. In principle however, the same information can be obtained by counting just at the Bragg angle at each temperature. At this angle, the recorded intensity represents that of the peak of the rocking curve. Assuming the rocking curve width is temperature-independent, this is directly related to the form factor, $|F(q)|$. Our preliminary scans indicated that the assumption of a temperature-independent rocking curve width was reasonable. However, this assumption is checked within our temperature-scans by adopting a compromise approach. While at most temperatures we count at fixed rotation angle, at certain temperatures we perform the full rocking-curve measurements. These measurements check the temperature-independence of the rocking-curve width, and also that the measures of the form factor obtained at fixed angle are consistent with those expected if a full rocking-curve measurement is carried out. We will see that although not perfect, our compromise technique works reasonably well.

Figure 3.42 shows a warming-scan carried out in the low field phase at 0.2 T, an

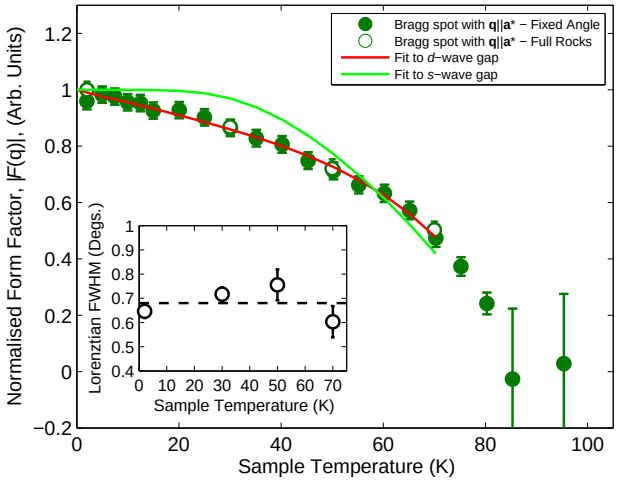

Figure 3.42: The temperature-dependence of the normalised form factor at 0.2 T, for $H \parallel \mathbf{c}$, of a Bragg spot with $\mathbf{q} \parallel \mathbf{a}^*$. The filled symbols show the form factor obtained by measuring the diffracted intensity and $\mathbf{q}$ at fixed rotation angle. The data are normalised by extrapolated zero temperature values. The open symbols show the measure of the form factor obtained using full rocking curve measurements. These data are normalised to the 2 K measurement, which we assume lies close to the value of the form factor at $T = 0$ K. The solid lines indicate the fits to the fixed angle form factor data according to weak-coupling models described in the text. The inset shows the temperature dependence of the FWHM of the Lorentzian lineshapes of these full rocking curve measurements. The dashed line of the inset is the weighted mean of these curve widths.

applied field where we believe the FLL can be described in terms of the Clem model. We only show data for the spot type with $\mathbf{q} \parallel \mathbf{a}^*$, as essentially identical results were obtained for the other spot type. In the main panel of figure 3.42, we compare the measures of the form factor obtained at fixed angle, and those obtained from full rocking curve measurements. At fixed angle, the form factor is found using $|F(\mathbf{q})|^2 \propto I/\mathbf{q}$, where I is the diffracted intensity measured on the detector, and $\mathbf{q}$ is the constant $\mathbf{q}$-value. Above T_c, there is no $\mathbf{q}$ value with which we could technically deduce a form factor value. For the datapoints at 85 K and 90 K, we assume the same $\mathbf{q}$-vector as for lower temperatures, and include these data to indicate the approximate location of T_c. We see that the normalised results obtained using the two different techniques exhibit good agreement. However, the inset shows that the FWHMs of the Lorentzian lineshapes fitted to the rocking-curves of the full rocking

curve data exhibit some scatter about the weighted mean. This introduces an extra error into our fixed angle data shown in the main panel. At each temperature, the calculated error for a fixed angle data point is subsequently the sum of the squares of the fractional errors obtained from I, $\mathbf{q}$, and the mean FWHM of the Lorentzian lineshapes fitted to the rocking-curves of the full rocking-curve measurements. This is also the calculation used for the error bars of the fixed-angle data points of the temperature-scans shown later in figures 3.43 (a) and 3.44.

We previously saw in section 3.6.2 that the low field form factor can be described in terms of the Clem model. In essence, this means that the form factor $|F| \propto gK_1(g)/\lambda_b^2 \propto n_s$ the superfluid density, where the core-correction term $gK_1(g)$ is included, as this term contains the temperature-dependent core-size parameter $\xi_{GL,a}(T)$. For a clean and single band superconductor, we can subsequently compute the superfluid density using

$$n_s(T) \propto \frac{gK_1(g)}{\lambda^2(T)} \propto \left[1 + 2\left\langle \int_0^\infty \mathrm{d}\epsilon \frac{\partial f}{\partial E(\mathbf{k},T)} \right\rangle\right] gK_1(g) \tag{3.6}$$

where, $f = [1 + \exp(-\beta E)]^{-1}$ is the Fermi function, and $E(\mathbf{k},T) = \sqrt{\epsilon^2 + |\Delta_\mathbf{k}(\phi,T)|^2}$ describes the quasiparticle excitation spectrum. Here, ϵ is the single-particle energy as measured from the Fermi energy, and $\mathbf{k}$ is the wave vector. We assume a cylindrical Fermi surface, and that the gap function $\Delta_\mathbf{k}(\phi,T)$ is separable into momentum- and temperature-dependent components according to

$$\Delta_\mathbf{k}(\phi,T) = \Delta_\mathbf{k}(\phi)\Delta(0)\tanh\left(1.74\sqrt{1-\frac{T}{T_c}}\right). \tag{3.7}$$

The temperature-dependent component has a form that is an approximation to the predictions of weak-coupling theory (Tinkham, 1996), the resulting values of which are essentially equivalent to those calculated numerically (Mühlschlegel, 1959). The angularly-dependent component of the gap function is defined $\Delta_\mathbf{k}(\phi) = \sqrt{2}\cos(2\phi)$ for d-wave pairing, or can be simply put equal to 1 for s-wave pairing. The brackets $\langle \ldots \rangle$ indicate an angular average over the Fermi surface. The term g of the core-correction term of the Clem model reduces to $g = \sqrt{2}q_y\xi_{GL,a}(T)$, where q_y is the experimentally determined constant value. We assume an empirical

$(1-(T/T_c)^2)^{-1/2}$ temperature-dependence to the core-size length-scale, and only fit data up to $0.8T_c$ in order to avoid the divergence of the temperature-dependence as $T/T_c \to 1$. The only fitting parameter is $\Delta(0)$, which is the gap magnitude.

In figure 3.42 we show the numerical computation of the superfluid density for the s- and d-wave gap functions. We show the best fits (smallest χ^2) for each, and see that the fit is strongly dependent on the form of $\Delta_{\mathbf{k}}(\phi)$. Our analysis indicates the major part of the condensate can be attributed to a large d-wave gap on a cylindrical Fermi surface, with a gap magnitude of $\Delta_d(0) = 19(1)$ meV. This gap magnitude is comparable to the value of 22.9(1) meV obtained from apparently much more sensitive μSR measurements on $YBa_2Cu_3O_{7-\delta}$ (Khasanov et al., 2007). Thus, assuming the validity of the Clem model, we show the superfluid density as best represented by a large d-wave gap.

However, our single gap analysis is rather basic. In reality, $YBa_2Cu_3O_7$ is a multi-gap material, with an established sub-dominant s-wave component which some attribute to the chain superconductivity, that skews the nodes of the simple d-wave gap (Smilde et al., 2005; Kirtley et al., 2006). We analysed Bragg spots with $\mathbf{q} \parallel \mathbf{a}^*$, which should be more sensitive than the off-axis spots to any effects of the chains. Therefore, we might have expected the temperature-dependences for the off-axis spots to be slightly different. However, as the temperature-dependences of the two spot types are measured to be identical within the error, we are unable to observe any obvious effect of this on our data. If there is any effect, it is therefore rather small, and in order to identify it we require new and more detailed measurements. Similarly, more realistic modelling of our data needs detailed calculations that directly account for the overall Fermi surface anisotropy.

We also mention that one of the proposed tests for the validity of the proximity-effect model is the observation of an inflection point in the superfluid density at low temperatures (Atkinson and Carbotte, 1995; Atkinson, 1999). This inflection point reflects the existence of an s-wave component to the superconducting groundstate, that is quickly suppressed with field and temperature. Our results shown in figure 3.42 show no such inflection point. However, inflection points are seen clearly

in *directly* comparable μSR measurements on detwinned $YBa_2Cu_3O_{7-\delta}$ (Khasanov et al., 2007). The reason for this discrepancy between the results obtained using the two different techniques remains unresolved.

Within the intermediate field phase, we observe most unusual behaviour. The form factor anisotropy between the different spot types at 2 K, is further manifested by anisotropic temperature-dependences. Figure 3.43 (a) shows this clearly from measurements obtained at 5.0 T. For the spots with $\mathbf{q} \parallel \mathbf{b}^*$, we observe the form factor is essentially temperature-independent until $\sim$ 50 K, whereafter the form factor falls linearly. For the off-axis Bragg spots, the low temperature-dependence is slightly more noticeable, but still rather weak, before falling linearly at above 50 K. Figure 3.43 (b) shows that the form factor anisotropy between the different spot types falls away monotonically with increasing temperature.

Within the high field structure phase, due to the lower diffracted intensity, it was not possible to obtain data that were as statistically reliable. For completeness however, in figure 3.44 we show the temperature-dependence of the form factor obtained for the $\{1, 0\}$ spots at 8.25 T. Although less statistically reliable, our results do suggest a similar form of temperature-dependence to that exhibited by the spots with $\mathbf{q} \parallel \mathbf{b}^*$ of the intermediate field structure phase.

Attempting to model the temperature-dependent data of figure 3.43 (a) using equation 3.6 fails for both spot types. Within the framework of the fit, this is due to the increasing size of the core-correction term as a function of temperature, which limits the maximum value the form factor can have, no matter the magnitude of $\Delta(0)$. This means that the essentially flat form factor temperature-dependence at low temperatures cannot be reproduced. The data can be fitted if we postulate that ξ_{GL}, for whatever reason, is temperature-independent. However, now the best fit is achieved by a large s-wave gap, which implies the majority gap on the cylindrical sheet of the model now fully gapped at high fields. We now take a moment to consider this unlikely scenario in more detail.

A mixed $d + s$ character of the gap function in $YBa_2Cu_3O_7$ is well established to be nodal within the plane states at low fields (Smilde et al., 2005; Kirtley et al.,

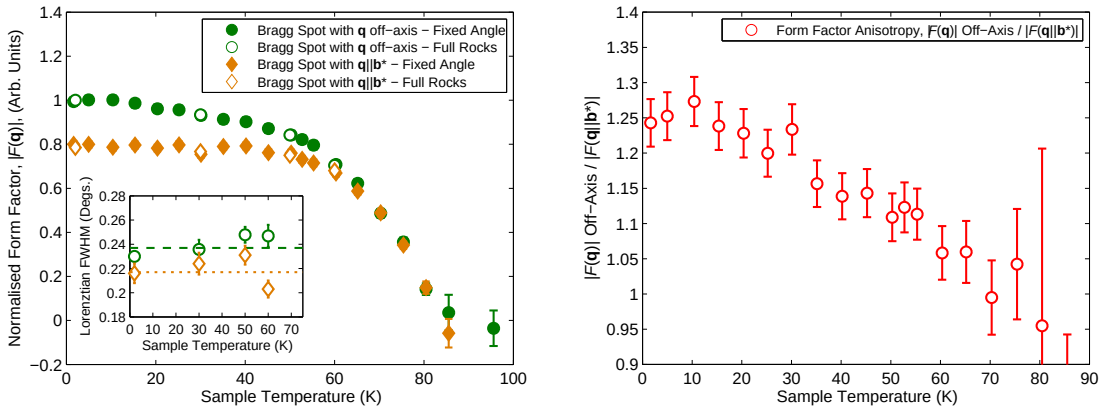

(a) (b)

Figure 3.43: In (a) we show the temperature-dependence of the normalised form factor at 5.0 T, and for $H \parallel \mathbf{c}$, for the inequivalent Bragg spots. Filled symbols show the form factor obtained by measuring the diffracted intensity and q at fixed rotation angle. The open symbols show measurements of the form factor obtained using full rocking curve measurements. The inset shows the temperature-dependence of the FWHM of the Lorentzian lineshapes of the full rocking curve measurements. The symbols correspond to the relevant measurements in the main panel. The dashed lines in the inset are the weighted means of these widths. In (b) we show the temperature-dependence of the ratio between the inequivalent form factors.

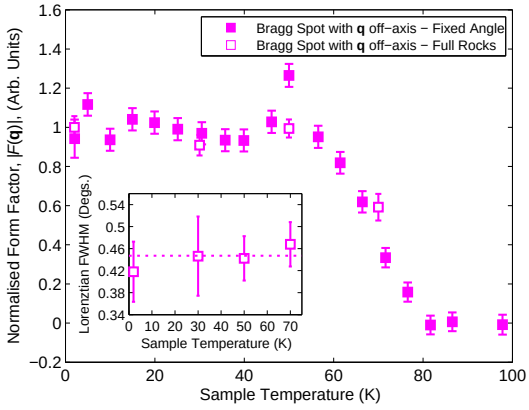

Figure 3.44: The temperature-dependence of the normalised form factor at 8.25 T, and for $H \parallel \mathbf{c}$, for the Bragg spots with **q** off-axis. Filled symbols show the fixed angle measurements of the form factor, whilst open symbols show the measure of the form factor obtained using full rocking curve measurements. The inset shows the temperature-dependence of the FWHM of the Lorentzian lineshapes of the full rocking curve measurements.

2006). Therefore, in the vicinity of the gap nodes, these exist quasiparticle states at arbitrarily low energy close to the Fermi level. It is for this reason the superfluid density shows a well-known approximately linear behaviour at low temperatures, comparable to that which we observe in figure 3.42. At intermediate fields however, if we consider that to a first-approximation that the form factor reflects the superfluid density, our results *are* reminiscent of a fully gapped state. However, this could only be accomplished via the opening of a large energy gap at the nodes. Interestingly, field-induced fully gapped scenarios have long been proposed theoretically (Laughlin, 1998; Franz and Tešanović, 1998; Balatsky, 2000). The prediction is that under a magnetic field, the free energy of the superconductor can be minimised by introducing an imaginary d_{xy} component into a majority $d_{x^2-y^2}$-order parameter. The id_{xy} component forms mainly at the nodes, and the resulting $d_{x^2-y^2} + id_{xy}$ order-parameter is fully gapped. High field tunnelling measurements on overdoped $YBa_2Cu_3O_{7-\delta}$ indicate the realisation of such a scenario, though any gap induced is just between 3-10 % the size of the majority $d_{x^2-y^2}$-order parameter, and is rapidly suppressed with increasing temperature (it disappears by 8.5 K at 6 T) (Elhalel et al., 2007; Leibovitch et al., 2008). The rapid suppression of the minority gap with temperature is also predicted theoretically (Laughlin, 1998; Balatsky, 2000). There is no suggestion in the literature that a *majority* s-wave component emerges as a function of field. This indicates a clear lack of theoretical support for our model fitting, which we attribute to our model being too simplistic.

Figure 3.45 shows the temperature-dependence of the superfluid density, $n_s = (\lambda_{eff}/\lambda_0)^{-2}$, obtained from high-field μSR measurements on $YBa_2Cu_3O_{6.95}$ (Sonier et al., 1999). Whilst, we keep in mind that the parameter λ_{eff} is a product of the data analysis, and represents an average over the plane, we note the similarity of the temperature-dependence for the data at fields comparable to those of our intermediate field phase. Due to the similarity, we tentatively suggest that the physical effects behind both experimental observations are of the same origin. The unusual response was theoretically investigated by Amin et al. (2000). Calculations within their d-wave non-local London model indicates the origin of the suppression of the

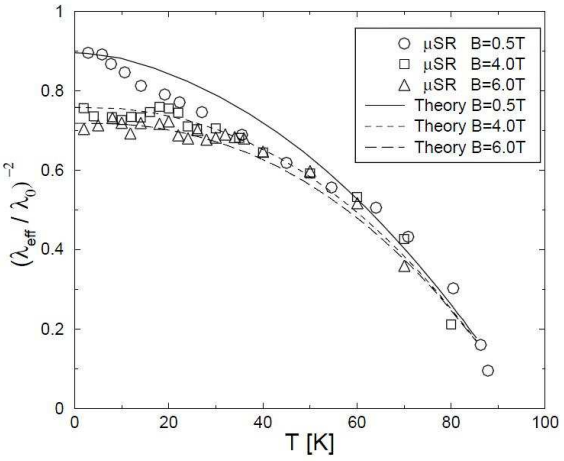

Figure 3.45: The experimental data is that of Sonier et al. (1999), and shows the temperature-dependence of the superfluid density ($= \lambda_{eff}/\lambda_0$) as measured by μSR at high fields. The theoretical fits are calculated according to the d-wave non-local theory of Amin et al. (2000). Figure taken from Amin et al. (2000).

superfluid density is attributable to non-local effects that are more potent due to the nodal form of the gap function. This same effect, as we also mentioned in section 3.6.2, weakens the supercurrent response, thus increasing the measured value of the λ_{eff}. The temperature-dependence of the superfluid density is predicted to deviate from the expected approximately T-linear behaviour, and instead a T^3 dependence is predicted to describe the data below a temperature T^*. Above T^*, quasiparticle states away from the nodes become accessible, the non-local response becomes weaker, and a the linear temperature-dependent behaviour is recovered. The application of the model to the experimental data shown in figure 3.45, indicates this model provides a reasonable description. However, our new SANS measurements at intermediate fields show that the anomalous temperature-dependent response is anisotropic between different types of Bragg spot. Therefore, a theory such as that of Amin et al. (2000) needs to be extended from its current form in order to explain our data.

Whilst the work of Amin et al. (2000) considers how non-local effects might modify the measured value of the penetration depth, we also cannot rule out that the flux line cores exhibit an unexpected temperature-dependence. For example, a

naive way to explain the weak low temperature-dependence of the form factor in the intermediate field phase, would be if the core contracted with increasing *temperature*. This goes against the effect of the core-correction of the Clem model, where ξ_{GL} is ascribed an empirical temperature-dependence. From a more conventional viewpoint, the core-size is expected to fall with decreasing temperatures in clean superconductors according to the Kramer-Pesch effect (Kramer and Pesch, 1974). However, this effect is expected to be suppressed by impurities, implying our weak temperature-dependence of the form factor may reflect an unexpected element in the dirtiness of the superconductivity.

Frustratingly, we can only speculate on the possible physical effects that might need to be considered in order to explain the weakly temperature-dependent behaviour of the FLL form factor. Whilst we focussed on the behaviour in the intermediate field phase, new measurements taken in the rhombic phase, and with improved statistics are needed, in order to obtain a clearer picture of the temperature-dependent behaviour in the upper part of the phase diagram. Most importantly, new theoretical work is required in order to interpret our results.

3.9 Summary

In this chapter we have reported the *first* observations of the *intrinsic* FLL structure in a twin-free sample of $YBa_2Cu_3O_7$. These measurements were made possible by the high quality of the single crystal samples, within which pinning to twin boundaries is nearly entirely suppressed. Our observations with $H \parallel \mathbf{c}$ reveal the existence of three distinct FLL structure types in the field range up to 10.8 T, and temperatures up to $T_{c2}(H)$.

The low field structure is single domain and distorted hexagonal, with nearest neighbours aligned with the real-space **b**-axis. The long-axis of hexagonal distortion is parallel to $\mathbf{a}^*$, consistent with that expected by the in-plane electronic anisotropy. At 2 K, our measurements show that the form factor in this phase is quickly suppressed with field. As a function of temperature, the form factor ex-

hibits a monotonic fall on the approach to T_{c2}. A preferred structural orientation, and the field-induced suppression of the form factor show that even at low fields, local London theory is not strictly satisfied. However, both can be reconciled whilst leaving the FLL structure with a somewhat 'London-like' character. For example, the measure of the distortion of the hexagonal FLL structure can be understood in terms of the effective mass anisotropy, with our low field values being similar to those found by other techniques.We propose that the preferred structural orientation as understandable in terms of a weak non-local effect, whilst the field-induced suppression of the form factor can be accounted for within the framework of the Clem model. A simplistic model also indicates the Clem model can provide a picture for the temperature-dependence of the form factor in this phase.

On increasing the field, we observe the FLL primitive cell to undergo a first-order 90° reorientation transition about the field axis. The overall structure is single-domain and distorted hexagonal, with the long-axis of hexagonal distortion parallel to $\mathbf{a}^*$. It is likely that the physical mechanism behind the transition between the low and intermediate field phases as associated with the increasing prominence of non-local effects associated with either a Fermi surface anisotropy (Kogan et al., 1997a), or the gap anisotropy (Franz et al., 1997). However, we speculate that the different orientations of the FLL are the preferred orientations according to the anisotropies of different Fermi surface sheets. Whether this is the case or not can be resolved with careful theoretical calculations. However, our results clearly indicate there are at least two field-dependent non-local components to the flux line-flux line interactions that compete, and favour orthogonal primitive cell orientations.

Within the intermediate field phase, a noticeable anisotropy emerges between the form factors of different types of Bragg spot. Using the Clem model, we are unable to maintain a consistent description of the form factor at 2 K between the low and intermediate field phases, without introducing extra assumptions. Our analysis leads us to tentatively conclude that we can understand non-local effects as resulting in a correction to our measured value of the apparent penetration depth as measured by SANS. The anisotropy observed at 2 K is further manifested in anisotropic

temperature-dependences of the form factor for different spot types. Now the Clem model is entirely unable to provide a realistic description of the data. Therefore, while we can maintain a picture of the *field*-dependence of the form factor in terms of the Clem model, describing the *temperature*-dependence lies beyond it. To make further progress in understanding our data, dedicated theoretical work is required.

On further increase of the field, the FLL structure undergoes another first-order transition into a rhombic structure phase. Remarkably, the long axis of distortion of the rhombic structure is along $\mathbf{b}^*$, which is orthogonal to the direction of distortion of the hexagonal structures. We see that the structure smoothly evolves with increasing field to approach a square coordination. However, this structure is not quite realised within the currently available field range. The rhombic structure can physically be interpreted as stabilised by the increasing prominence of the predominantly $d_{x^2-y^2}$ gap anisotropy. In this case, the flux line nearest neighbour directions are expected to lie parallel to the nodal directions, indicating the finite aspect ratio of the rectangle overlaying the rhombic structure reveals the existence of a finite admixture to the order parameter. However, the stabilisation of a field-dependent rhombic structure is also consistent with predictions that it is caused by further non-local effects (Kogan et al., 1997a). Unfortunately, $YBa_2Cu_3O_7$ is an example of a material where the predicted orientations of high-field FLL square structures are qualitatively the same, whether stabilised by non-local effects or gap anisotropy. Detailed calculations can help determine the physical mechanism behind the stabilisation of the rhombic phase.

Our measurements of the form factor in the rhombic phase suggest that non-local effects *do* play an increasingly important role at high fields. This was revealed by our investigations of the next nearest order $\{1,1\}$ spots, where we find that these spots are likely to exhibit a clear anisotropy; the spots with $\mathbf{q} \parallel \mathbf{a}^*$ are easily observed, whilst we have not yet clearly observed those with $\mathbf{q} \parallel \mathbf{b}^*$. We attribute this anisotropy to inequivalent lengths of the $\mathbf{q}$-vector, and a penetration depth anisotropy, both of which favour the stronger $\{1,1\}$ spots to be those with $\mathbf{q} \parallel \mathbf{a}^*$. However, new, more targeted, measurements are needed in order to confirm this

interpretation.

Overall, our analysis has shown that understanding many of the results of our experiments requires new theoretical work. It is of interest to understand why the structure phase boundaries are so weakly temperature-dependent, and also the precise role that the multi-band Fermi surface plays on our observations of both the field-dependences of the FLL structure and form factor. Of the theoretical works that are available for consideration, it seems that the vast bulk of our results are broadly describable in terms of field-induced non-locality, where it is possible the potency of non-locality is increased due to the anisotropy of the d-wave gap function. This could explain why non-local effects seem to play an important role at fields as low as $\sim$2 T in this material. In this sense, a distinction between the two anisotropic effects would seem inappropriate, as the symmetry of both is inherently related to that of the Fermi surface.

Field enhanced flux line lattice in $CeCoIn_5$

In this chapter we report SANS studies of the mixed state in the heavy-fermion superconductor $CeCoIn_5$ which reveal new behaviour of the FLL for *any* type-II superconductor. For the first time in a d-wave superconductor, the major part of the FLL structure phase diagram is reported for the case of field parallel to the crystal **c**-axis. Furthermore for this field orientation, we also observe an anomalous field-dependence to the FLL form factor. At low temperatures, the form factor remains essentially constant up to $\approx$ 2 T, before increasing by a factor of four on approaching H_{c2}. The *increase* of the form factor lies beyond predictions based on the Ginzburg-Landau theory, where the form factor is predicted to fall monotonically with increasing field. Instead, the form factor behaviour can be explained by using a modified version of the quasiclassical Eilenberger theory that incorporates a paramagnetic term. Just before H_{c2}, the form factor is observed to fall again which we tentatively associate with a flux line core expansion, whose origin is associated with paramagnetic depairing effects within the cores. We report further studies at higher temperatures, the case of field applied parallel to the plane, and of examinations of the FLL in the same region of phase space as occupied by the Fulde-Ferrell-Larkin-Ovchinnikov (FFLO), or 'Q', phases.

4.1 Introduction to the heavy-fermion superconductor $CeCoIn_5$

Landau introduced the Fermi-liquid theory (Landau, 1957) to address the problem of introducing interactions into the Pauli-Sommerfeld free electron model. In the free-electron model, the interactions are neglected and, bearing in mind that the energy associated with Coulombic repulsion is of the same order as their kinetic energy, it is surprising that the theory describes any properties of free electrons at all. The linchpin of the Fermi-liquid theory is the replacement of interacting fermions by elementary and weakly-interacting quasiparticle excitations. A quasiparticle possesses the same spin, charge and momentum degrees of freedom as the free fermions, but, due to adiabatic interparticle interactions, the excitation cannot be described within a single particle picture. Rather, the excitation describes the combined motion of a subject particle plus its interactions with surrounding particles as the subject particle moves in the material. This behaviour has its origin in the Pauli exclusion principle, and provides a mechanism by which quasiparticles can be scattered from one state to another, though this scattering is far weaker than one might expect from bare Coulomb interactions. The Fermi-liquid theory was successful in providing a phenomenological explanation as to why some experimentally observed properties of metallic systems are similar to the Fermi gas, such as the low temperature linear specific heat, and why other properties differ, such as the T^2 temperature-dependence of the low temperature resistivity. Indeed, the latter relation is commonly used to test a system for Fermi-liquid behaviour.

The physics that surrounds the heavy-fermion materials arises due to these quasiparticle interactions. A most striking manifestation is seen by a renormalisation of the effective carrier mass, showing the interactions to adjust the carrier motion. Typically for heavy-fermion systems, the effective mass is enhanced by a factor of between 50 to 1000 times the free electron mass (Fisk et al., 1988). The increase is experimentally characterised by large Fermi-liquid coefficients, such as those measured in the linear specific heat (Misra, 2008),

$$\frac{C}{T} = \gamma, \qquad \gamma = \frac{V_m k_F k_B^2 m^*}{3\hbar^2} \tag{4.1}$$

where V_m is the molar volume, k_F is the Fermi wave vector and m^* is the effective carrier mass, and in the T^2 term in the temperature-dependent resistivity $\rho(T) - \rho(0) = AT^2$. For normal metals such as copper, the value of γ is $\sim$1 mJ/mol K^2. For heavy-fermion systems, for temperatures below a coherence temperature, T^*, although the $T-$linear behaviour is retained, the *magnitude* of γ increases dramatically. This increase signifies that the system possesses strong correlations.

The first heavy-fermion material to be discovered was $CeAl_3$ (Andres et al., 1975). Below temperatures of 0.2 K, both the linear specific heat term and T^2 term in the resistivity were observed to be enormous at $\gamma = 1620$ mJ/mol K^2, and $A = 35$ $\mu\Omega$ cm/K^2 respectively. Following this were similar observations in $CeCu_2Si_2$, but with the added discovery of superconductivity with a $T_c = 0.5$ K (Steglich et al., 1979). The authors were quick to identify that the large size of the superconducting specific heat anomaly indicated that mass renormalised quasiparticles were involved with the pairing. This, plus the further observation that a slight change in stoichiometry caused the system to order magnetically rather than superconduct (Gegenwart et al., 1998), raises two important points. Firstly, the observations are suggestive that magnetic correlations may play an role in the pairing mechanism. Secondly, the observations show the close proximity in phase space of different quantum ground states in the system. As a natural extension of this, heavy-fermion physics is synonymous with the study of quantum critical phenomena (see section 4.1.3).

Nearly all heavy-fermion systems have a rare-earth Ce, or actinide U, f-electron constituent in their stoichiometry. It is thought that in these materials, the mass renormalisation stems from Kondo-type interactions between the localised f-electrons and the itinerant quasiparticles. The growth of this interaction at low temperatures leads to the slowing of the itinerant quasiparticles, and concomitantly an increase of the band mass. The localised moments also interact with one another, in addition to the itinerant particles. From this viewpoint, it is easy to comprehend why ordered magnetism and superconductivity lie close to one another in the phase diagrams of these materials. Clearly if the superconductivity is mediated by magnetic fluc-

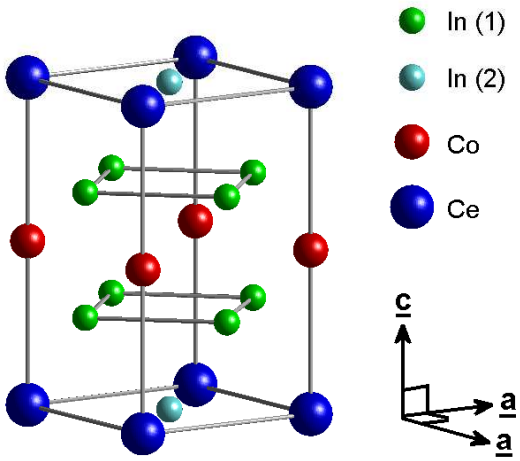

Figure 4.1: The crystal structure of $CeCoIn_5$, shows the existence of two inequivalent In sites. The inset axes define the crystallographic directions. The **a**-axis lattice parameter is 4.614 Å whilst the **c**-axis lattice parameter is 7.552 Å. The density is ~ 8 g.cm^{-3}.

tuations, these will be most pronounced in close proximity to a magnetic ordering instability.

A wide range of experimental studies on the Ce*M*In_5 (*M*=Co,Ir,Rh) family of heavy-fermion compounds have shown this particular group to exhibit a rich variety of exciting physics. The crystal structures of these materials are tetragonal with space group $P4/mmm$, and composed of alternating stacks of $CeIn_3$ and *M*In_2 layers. Figure 4.1 shows the structure for the case of the subject material of this chapter, $CeCoIn_5$.

4.1.1 Superconducting $CeCoIn_5$

$CeCoIn_5$ is one of the more prominent members of the Ce-family of heavy-fermion compounds. It is an ambient pressure superconductor with a zero-field $T_c = 2.3$ K; the highest of any heavy-fermion material. Experimental evidence clearly suggests the order parameter symmetry to have line nodes, as seen for example in observations of power law dependences to both the thermal conductivity ($\kappa \propto T^3$) and heat capacity ($C \propto T^3$) below T_c (Movshovich et al., 2001). The precise detail of

whether the order parameter symmetry is $d_{x^2-y^2}$ or d_{xy} was initially actively discussed in the literature. Measurements made on rotating the field within the basal plane revealed a fourfold oscillation in the thermal conductivity (κ) that was interpreted as being consistent with a $d_{x^2-y^2}$-symmetry (Izawa et al., 2001). However, the fourfold oscillation observed in angularly-dependent specific heat C measurements was observed to be of a sign that favours a d_{xy} gap symmetry (Aoki et al., 2004). The contradictory evidence obtained from the two studies is resolved by the theoretical work of Vorontsov and Vekhter (2006). Within the framework of a microscopic theory, the fourfold oscillation observed in $C(\theta, T, H)$ is predicted to change sign at lower temperatures than those at which the measurements of Aoki et al. (2004) were performed. At low field and temperature, the sign of the fourfold data obtained from the $C(\theta, T, H)$ is reconciled with the $\kappa(\theta, T, H)$ data, thus providing convincing evidence for a $d_{x^2-y^2}$ symmetry of the order parameter.

Measurements of the characteristic length-scales show $CeCoIn_5$ to be a strongly type-II material. Experimental studies of the London penetration depth report values that range from 1900 Å (Ormeno et al., 2002) to 2800 Å (Özcan et al., 2003). Estimates of the coherence length can be derived from the Ginzburg-Landau expression for H_{c2}. We will see in the next section that the low temperature upper critical field is subject to the effects of Pauli-limiting, rendering the usual Ginzburg-Landau expression invalid. However, at higher temperature, these effects are much weaker, and it is possible to make an estimate of the expected value of H_{c2} the zero temperature in the absence of Pauli-limiting. This is obtained from the gradient $\mathrm{d}H_{c2}/\mathrm{d}T|_{T=T_c}$, taken close to the zero-field T_c. Using this approach, the zero-temperature values for the out-of-plane and in-plane upper critical fields are estimated to be $H_{c2\|\mathbf{c}}$ ∼15 T and $H_{c2\|\mathbf{a,b}}$ ∼35 T as determined from magnetisation measurements (Tayama et al., 2002). This yields estimates of the coherence length as $\xi_{a,b} \sim 50$ Å and $\xi_c \sim 30$ Å, thus showing κ to be always at least ~ 40, and the material strongly type-II.

$CeCoIn_5$ is also an unusual example of an extremely clean high-κ superconductor. The electronic mean-free path ℓ, as measured by microwave surface impedance

measurements, is found to to be long at $\sim 4\mu m$ at 400 mK (Ormeno et al., 2002), showing $\ell/\xi \sim 1000$. These observations are also supported by thermal Hall conductivity measurements (Kasahara et al., 2005). The large mean free path, combined with the small Fermi energy and large effective carrier mass, places the material well into the superclean limit ($E_F/\Delta \ll \ell/\xi$).

Finally we note that due to the relative complexity of the Fermi surfaces in heavy-fermion materials, the superconductivity is strongly suspected to exhibit multi-band, and hence multi order-parameter effects. For example, the weight of the f-electron character, that gives rise to heavy-fermion superconductivity, may well vary between different Fermi surface sheets, along with a variation in coupling strength between them (Settai et al., 2007). Evidence for multi-band superconductivity in $CeCoIn_5$ is provided by thermal conductivity measurements at temperatures down to 10 mK (Seyfarth et al., 2008). In this study, in addition to the large d-wave superconducting gap, a second line node gap, associated with a light carrier mass band (Settai et al., 2001) is observed. However, the weight of this small gap is quenched rapidly with field, and it exhibits an extremely small upper critical field of ~ 20 mT, which is approximately equivalent to H_{c1} of the large gap. These observations serve as a reminder of the subtlety of the physics of these materials, and how the signatures of strong correlations will not be manifested equally on all the Fermi surface sheets.

4.1.2 Orbital vs. Pauli Limiting

Heavy-fermion superconductors are good candidates to exhibit the effects of Pauli-limiting because the large effective carrier mass favours higher orbitally-limited critical fields. The clear evidence that $CeCoIn_5$ is a Pauli-limited superconductor, is provided from both magnetisation (Tayama et al., 2002) and heat capacity studies (Bianchi et al., 2002). Some raw isothermal magnetisation curves for fields parallel to the **a**-axis ($H \parallel \mathbf{a}$) that were reported in the magnetisation study of Tayama et al. (2002), are shown in figure 4.2 (a). At high temperature, the field-dependence of the magnetisation varies smoothly between the superconduct-

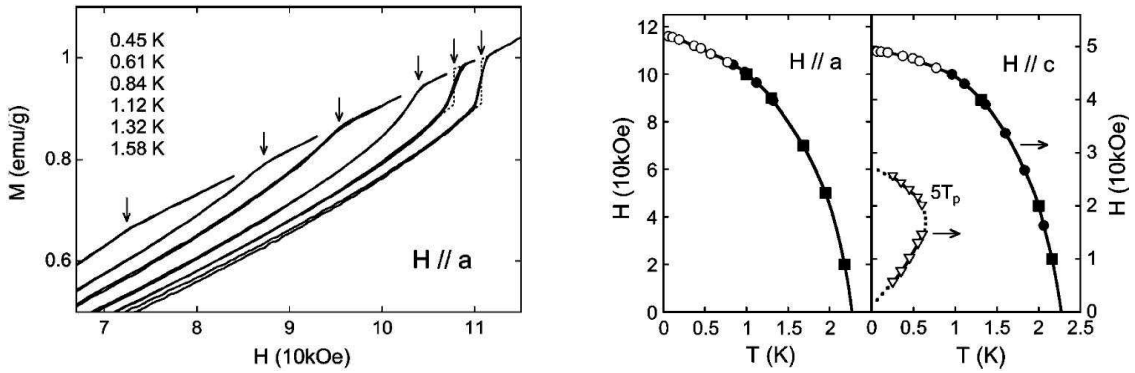

(a) Isothermal magnetisation data for $H \parallel \mathbf{a}$ (b) (H,T) phase space

Figure 4.2: Figure (a) shows some of the isothermal magnetisation data obtained on $CeCoIn_5$ with $H \parallel \mathbf{a}$. The dashed line guide to the eye fits to the low temperature data indicate that the transition into the normal state is discontinuous at low temperature. At higher temperature, the transition between the normal and superconducting states is seen to be continuous. The arrows indicate the position of H_{c2}. Figure (b) shows a summary of the magnetisation data in terms of the position of the H_{c2} boundary in (H,T) phase space for $H \parallel \mathbf{a}$ and $H \parallel \mathbf{a}$. Open (closed) symbols correspond with cases where the transition between the superconducting and normal states is first-(second-)order. The open triangle data of (b) corresponds to those temperatures where a hysteresis peak was observed in the magnetisation data. Figures after Tayama et al. (2002).

ing and normal states, signifying the transition between them as continuous. This is consistent with orbitally-limited behaviour. For low temperatures however, a noticeable kink is discernible at H_{c2}, providing evidence that the transition between the normal and superconducting states is first-order. In figure 4.2 (b), the resulting (H,T) phase diagrams for both principal crystal directions show the field- and temperature-dependence of the H_{c2} boundary, and the nature of the transition between the superconducting and normal states.

Along the two principal crystal directions, the upper critical fields are found to be approximately $H_{c2\parallel\mathbf{c}} \sim 4.95$ T and $H_{c2\parallel\mathbf{a}} \sim 11.6$ T at zero temperature. These values are much lower than the zero temperature orbitally limited critical fields estimated from the gradient $\mathrm{d}H_{c2}/\mathrm{d}T|_{T=T_c}$ reported in the last subsection. The suppression is a direct indication of the increasing prominence of Pauli paramagnetic effects at low temperatures. From the data shown in figure 4.2 (b), we see that the region where the transition between the superconducting and normal states is first-order

is restricted to low temperatures, $T \leq 0.3\, T_c$. Theoretically, in the strong Pauli limit, the first-order boundary extends as high in temperature as 0.56 T_c (Saint-James et al., 1969; Ketterson and Song, 1999). This suggests that orbital effects still play a role in $CeCoIn_5$, which they must do for the FLL to even emerge, though these are superceded for $T \leq 0.3\, T_c$.

4.1.3 Quantum criticality in $CeCoIn_5$

Quantum critical behaviour is commonly associated with the heavy-fermion systems, where different quantum ground states are often found to exist in close proximity. In heavy-fermion systems, the two ground states are typically magnetically ordered and paramagnetic states. The preferred ground state can be obtained by changing the system environment using an appropriate tuning parameter. If, on adjusting the tuning parameter, the system undergoes a quantum phase transition, the system is said to possess a quantum critical point (QCP) at the critical value of the tuning parameter. It is interesting to note that superconductivity is a ground state that is also often found in close proximity to a QCP. Quantum critical behaviour within the vicinity of a QCP is experimentally characterised by a break down of the Fermi-liquid picture of metals, and, as a result, non-Fermi liquid behaviour.

Evidence for non-Fermi liquid behaviour associated with quantum criticality in $CeCoIn_5$ is available from a variety of experimental sources (Petrovic et al., 2001b; Bianchi et al., 2003b; Paglione et al., 2003). Figure 4.3 (a) shows some of the low temperature resistivity data obtained by Bianchi et al. (2003b) with $H \parallel \mathbf{c}$. For fields close to H_{c2}, the resistivity does not follow the T^2 dependence expected from Fermi liquid theory, though this is recovered at higher fields. The clear difference between the Fermi liquid and non-Fermi liquid regimes is seen in the inset to figure 4.3 (a). Using their data, figure 4.3 (b) shows that Bianchi et al. (2003b) were able to construct a phase diagram showing the extremely close proximity of non-Fermi-liquid behaviour to superconductivity. Using a scaling argument, the authors deduced the quantum critical point must be located extremely close to $H_{c2}\,(T = 0)$ of the superconducting phase diagram. As the transition between the normal and super-

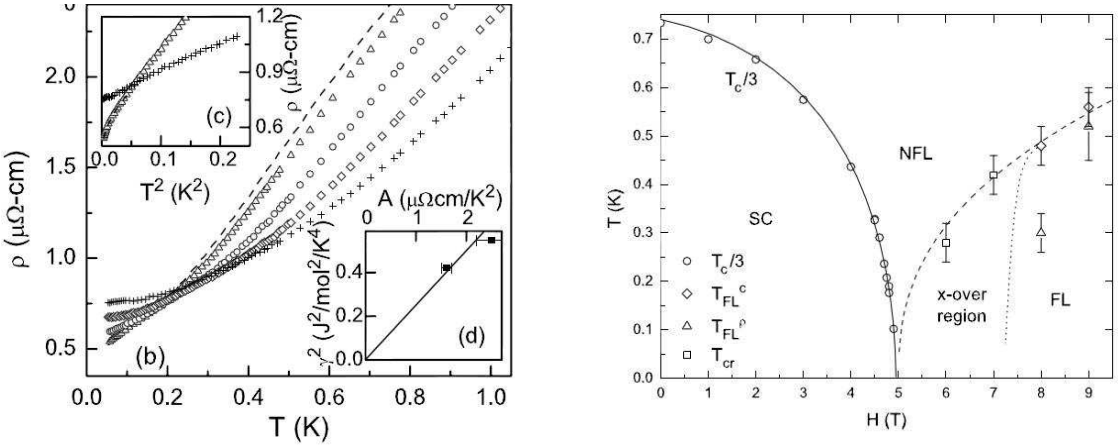

(a) ρ versus T at high field

(b) (T,H) phase space

Figure 4.3: Figure (a) shows resistivity versus temperature data taken on $CeCoIn_5$ with $H \parallel \mathbf{c}$, for fields close to and above H_{c2}. The dashed line corresponds to data at 5.6 T, open triangles data at 6 T, open circles data at 7 T, open diamonds data at 8 T and crosses data at 9 T. The upper left inset shows a closer look at the 6 T and 9 T data plotted as a function of T^2, thus showing the recovery of Fermi liquid behaviour with increasing field. Figure (b) shows the deduced (T,H) phase space extending well beyond the superconducting region. The quantum critical point is deduced to be located extremely close to H_{c2}. Figures after Bianchi et al. (2003b).

conducting states is first-order at zero temperature, this provided evidence against the possibility that the quantum criticality is associated with the superconducting transition. Instead, Bianchi et al. (2003b) suggested their data were consistent with the onset of an antiferromagnetic QCP, even though long-range antiferromagnetic order is not observed within the superconducting state for $H \parallel \mathbf{c}$. This raised the question that the quantum criticality could be 'unconventional' and still related to the superconducting transition. This scenario was later ruled out by resistivity measurements, which showed that as a function of increasing pressure, the locations of the QCP and H_{c2} became displaced in field (Ronning et al., 2006).

The puzzling issue surrounding the location of the magnetically ordered state persists for $H \parallel \mathbf{c}$, though it is possible an answer is provided by the recent neutron scattering study of Kenzelmann et al. (2008). In that study with $H \parallel [1\bar{1}0]$ (discussed in more detail in section 4.1.6) an antiferromagnetic spin density wave is stabilised in the low temperature and high field part of the superconducting phase

diagram. However, rather than the proximity to a QCP providing the energy scale for the stabilisation of the antiferromagnetism, the authors argue this energy scale is made inaccessible by the emergence of superconductivity. Instead, it is the onset of superconductivity that stabilises the magnetism, and in fact, the quantum phase transition is never realised. However, magnetic structure has only been reported for $H \parallel [1\bar{1}0]$, and it remains unclear whether or not a similar phase is stabilised for $H \parallel \mathbf{c}$. It is also unclear the role, if any, that such proximity to magnetism and critical fluctuations might have in the superconducting state. For example, de-Haas van-Alphen measurements in the mixed state (Settai et al., 2001) show the heavy-fermion mass diverging on the approach to the QCP. This could manifest itself in the properties of the FLL. For example, according to the GL theory, and therefore relevant for form factor models derived from GL theory (Appendix D), the GL coherence length (equation 1.23) and the penetration depth (equation 1.26) are sensitive to the effective mass of the carriers.

4.1.4 Band structure in $CeCoIn_5$

The band structures of the f-electron heavy-fermion materials are notoriously complex. They consist of numerous Fermi surfaces and, as mentioned previously, the weight of the f-character can vary markedly between the different sheets. An important question in the study of the Fermi surface of a $4f$-electron material is deciphering the contribution of the f-electrons. Above the coherence temperature, $4f$-electrons are localised and do not contribute to the spectral weight at the Fermi surface. Below this temperature, the $4f$-electrons gradually become itinerant and therefore do contribute a larger spectral weight. Therefore, if certain details of the Fermi surface are temperature-dependent, they can, when compared with an appropriate theoretical model, be used to decipher the role of the $4f$-electrons as a function of temperature.

It is expected that the details of the Fermi surface will reflect the low dimensionality of the crystal structure shown in figure 4.1. As our FLL studies are at low temperatures deep in the Kondo regime, the f-electrons will be itinerant, and con-

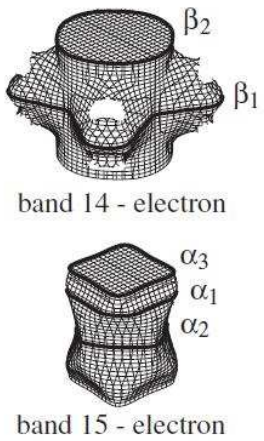

Figure 4.4: The principal Fermi surfaces consistent with the de-Haas van-Alphen experiments of Settai et al. (2001) (as shown in Settai et al. (2007)) and computed within a $4f$-itinerant electron model. The labels in α and β represent the orbits of the cyclotron masses measured in the experiment, with these orbits shown by solid black lines. After Settai et al. (2001, 2007).

tribute at the Fermi surface. Therefore, we consider the results of the early de-Haas van-Alphen (dHvA) study of Settai et al. (2001), as these were recorded at temperatures well below 1 K, and are expected to be most relevant to our studies of the FLL. The major Fermi surfaces deduced from the comparison between the experimental data and theoretical calculations are shown in figure 4.4. Smaller, though more three-dimensional, sheets are not shown.

The good agreement with the $4f$-itinerant band model calculations show the two principal Fermi surfaces to be composed of distorted cylinder-like sheets. This low dimensionality is thought to be derived from the hybridisation between the d electrons of the Co atom and $5p$ electrons of the In atoms. As a consequence, the density of states at the Fermi energy is small, and there are few itinerant electrons in the $CoIn_2$ layer. Since the early dHvA study of Settai et al. (2001), the conclusions about the low dimensional and distorted cylinder shape of the major sheets are in agreement with other experimental (Hall et al., 2001; Koitzsch et al., 2009), and theoretical (Elgazzar et al., 2004) works. The possible effect of the cylindrical Fermi surfaces on the FLL is not easy to decipher due to their distorted shapes. However, some of the cyclotron orbits shown in figure 4.4 clearly trace out a path with a

fourfold symmetry about their respective Fermi surface sheet, though some of these fourfold details are oriented 45° apart.

4.1.5 The Fulde-Ferrell-Larkin-Ovchinnikov phase

Perhaps what has attracted most attention in the research into $CeCoIn_5$ is the genuine possibility that novel superconducting pairing states might exist at low temperatures and high fields. The necessary conditions for such pairing states were considered soon after the BCS theory (Bardeen et al., 1957). Independently, Fulde and Ferrell (1964) and Larkin and Ovchinnikov (1965) (FFLO) predicted that in the presence of a suitably large exchange field, an inhomogeneous superconducting state, in which the pairing state carries a finite momentum $\mathbf{q}$, could be realised. This state is characterised by an order-parameter that changes sign as a function of position in *real space* which is more stable than the usual spatially constant energy gap. This effect arises due to a competition between the superconducting condensation energy and the effect of spin splitting (Zeeman effect) on the electron energy bands. As such, in the FFLO phase, Cooper pairs form between Zeeman split Fermi surface sheets, and possess a finite centre of mass momentum, $(\mathbf{k}\uparrow, -\mathbf{k}+\mathbf{q}\downarrow)$. The condensation energy gain of such a finite momentum pair is less than for the BCS pair, but this is counterbalanced by the reduction in the Zeeman energy of the pair under the applied field.

Although there is no consensus behind the unconventional pairing scheme of the heavy-fermion superconductors, it is informative to compare the FFLO pairing scheme to the conventional BCS scheme $(\mathbf{k}\uparrow, -\mathbf{k}\downarrow)$, as shown in figure 4.5. Due to the finite contribution of $\mathbf{q}$ to FFLO pairing state, the spatial dependence of the order parameter predicted to exist by Fulde and Ferrell is described by

$$\Delta(\mathbf{r}) = \Delta_1 \exp(i\mathbf{q}\cdot\mathbf{r}) \tag{4.2}$$

where the magnitude of the order parameter Δ_1 is homogeneous, but the phase changes sign in real space. Larkin and Ovchinnikov showed this solution to be equivalent in energy with $\Delta(\mathbf{r}) = \Delta_1 \exp(-i\mathbf{q}\cdot\mathbf{r})$, but that this degeneracy can

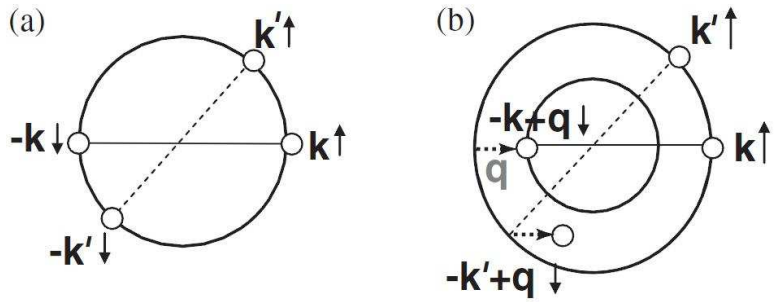

Figure 4.5: A comparison between (a) the BCS pairing state of $(\mathbf{k}\uparrow, -\mathbf{k}\downarrow)$, and (b) the predicted FFLO pairing state $(\mathbf{k}\uparrow, -\mathbf{k}+\mathbf{q}\downarrow)$. In (b), the inner and outer circles, respectively represent the Fermi surfaces of the Zeeman split spin up and spin down Fermi surface sheets. The electron with momentum $\left(-\mathbf{k}^{'}+\mathbf{q}\downarrow\right)$ does not lie on the inner Fermi surface. After Matsuda and Shimahara (2007).

be lifted by forming the linear combination of $\Delta(\mathbf{r}) = \Delta_1 \exp(i\mathbf{q}\cdot\mathbf{r})$ and $\Delta(\mathbf{r}) = \Delta_1 \exp(-i\mathbf{q}\cdot\mathbf{r})$. The resulting gap variation they proposed was

$$\Delta(\mathbf{r}) = \Delta_1 \left(\exp(i\mathbf{q}\cdot\mathbf{r}) + \exp(-i\mathbf{q}\cdot\mathbf{r})\right) = 2\Delta_1 \cos(\mathbf{q}\cdot\mathbf{r}) \tag{4.3}$$

which provides a lower free energy than equation 4.2, when the superconductivity is Pauli-limited. Hence, in the LO regime the amplitude of the order parameter takes on a real-space modulation of periodicity $2\pi/\mathbf{q}$. This implies that, in the LO regime, the superconducting state is characterised by nodal sheets in the bulk of the superconductor, with a propagation direction perpendicular to the planes of the modulation. In the vicinities of these nodal planes where the gap is suppressed, one might expect to find the usual paramagnetic moment induced by the field.

The region of phase space over which an FFLO state is predicted to exist is small, occurring close to H_{c2} and for low temperatures. The precise region is further dependent on the sample type and purity. Due to the strict requirements of the host material, experimental evidence for the realisation of the FFLO phase is scarce. Such a material is expected to be strongly type-II, and possess a large Maki parameter indicating the system to be Pauli-limited. For an s-wave system, theory suggests that $\alpha_M \sim 1.8$ is sufficient to allow the stabilisation of the FFLO state (Gruenberg and Gunther, 1966). In $CeCoIn_5$ estimates of α_M for both $H \parallel \mathbf{c}$ and $H \parallel \mathbf{a}$ are always at least ~ 4, indicating the paramagnetic effects in $CeCoIn_5$ to be sufficiently

large relative to the orbital effects. The material also has to be extremely clean, as the singlet pairing between the Zeeman-split Fermi surfaces is sensitive to impurity scattering. Finally, the stability of the FFLO state is enhanced by a certain degree of Fermi surface anisotropy. This can be inferred from figure 4.5 (b). In a three-dimensional superconductor with a spherical Fermi surface, the pairing **q**-vector is only strictly satisfied at a point on either Fermi surface. If the Fermi surface is two-dimensional and cylindrical this point extends to a line, and if this cylinder is distorted, this optimisation (or nesting) of **q** can enhance the region in momentum space where the pairs can form (Matsuda and Shimahara, 2007). This suggests that low dimensionality and Fermi surface anisotropy favour the FFLO phase. $CeCoIn_5$ satisfies all these requirements listed above, making it a prime candidate for the observation of the FFLO phase.

Experimentally, various thermodynamic studies of $CeCoIn_5$ have provided evidence for the stabilisation of a distinct thermodynamic phase consistent with the expected location of the FFLO phase (Bianchi et al., 2003a; Capan et al., 2004; Martin et al., 2005) (for a full review of these studies, see Matsuda and Shimahara (2007)). Interestingly, the experimental character of the anomalous phases is anisotropic between crystal directions. The region of the superconducting phase diagram where the anomalous phase is stabilised for $H \parallel \mathbf{c}$ is relatively smaller than the corresponding region for either of $H \parallel \mathbf{a}$ or $H \parallel [110]$ (see for example, Bianchi et al. (2003a)). This is in spite of the fact that the Pauli spin susceptibility for $H \parallel \mathbf{c}$ is approximately twice as large than for field in the plane (Tayama et al., 2002). A speculative explanation for this is that the relevant Fermi surface anisotropy for the case of field in the plane allows the formation of a more stable FFLO phase than for field perpendicular (Matsuda and Shimahara, 2007).

The experimental observation of anomalous superconducting phases in $CeCoIn_5$ has led to them being hailed as evidence for a realisation of the FFLO state. However, despite the efforts of microscopic studies, in particular those of nuclear magnetic resonance (NMR), the macroscopic evidence is not supported by an unambiguous microscopic observation.

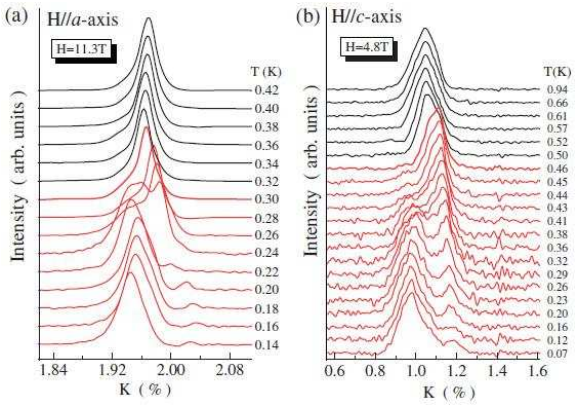

Figure 4.6: ^{115}In-NMR Knight shift spectra as a function of temperature for (a) $H \parallel \mathbf{a}$ and 11.3 T and (b) (a) $H \parallel \mathbf{c}$ and 4.8 T. The black spectra are in the normal state, and the red curves in the superconducting state. The ^{115}In site sample corresponds to In(2) of figure 4.1. After Matsuda and Shimahara (2007) and Kumagai et al. (2006).

As NMR is an extremely powerful tool which is often used to probe the microscopic state of the host material, we take a moment to consider the results of these studies. Figure 4.6 shows ^{115}In-NMR Knight shift spectra taken as a function of decreasing temperature on moving into the proposed FFLO phase. The Knight shift of the resonance frequency arises as a consequence of the paramagnetism of the conduction electrons under the applied field. This paramagnetism induces an 'extra' field at the nuclear site, and the resonance frequency shifts away from the zero field value. On entering the superconducting state, the Knight shift is suppressed as some of the spin polarised electrons take part in the pairing. However, as observed in the NMR spectra taken on $CeCoIn_5$ shown in figure 4.6, a subsidiary peak emerges in the spectra on moving through the superconducting transition, with a frequency similar to that in the normal state. This was taken to be evidence for the existence of normal quasiparticle states, consistent with those that might exist at the FFLO nodal planes. Although these (Kumagai et al., 2006; Matsuda and Shimahara, 2007), and other (Kakuyanagi et al., 2005) NMR studies interpreted their findings as evidence for an FFLO phase, other interpretations of NMR results argue that the anomalous features they see are possibly due to the onset of magnetism (Mitrović et al., 2006; Young et al., 2007). This issue is still unresolved, with Koutroulakis

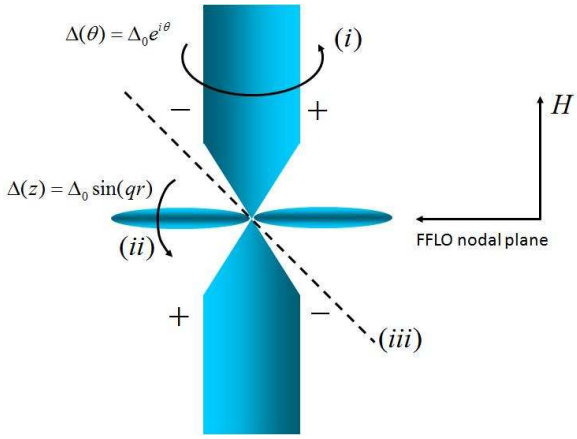

Figure 4.7: A schematic diagram of the spatial distribution of the bound quasiparticle states of a FFLO flux line. The flux line is parallel to the field, and bound quasiparticle states are also induced about the horizontal FFLO nodal plane. Quasiparticles following paths (i) and (ii) will experience a $\pm\pi$ phase change of the order parameter and be bound. Quasiparticles tracing path (iii) will experience a $\pi \pm \pi$ phase change and thus will not be bound. Note that the quasiparticle states within the flux line do not cross the nodal sheet, thus giving the flux line its distinct topological structure.

et al. (2008) offering more recent evidence that their NMR data does not rule out the co-existence of both FFLO and a magnetic phase in the high field and low temperature region of the superconducting phase diagram. To summarise, the NMR studies are inconclusive.

On the other hand, SANS studies of the FLL could offer direct evidence of an inhomogeneous superconducting state through direct imaging of the flux lines. Dedicated theoretical studies (Tachiki et al., 1996; Mizushima et al., 2005; Ichioka et al., 2007) have shown that within the FFLO phase the flux lines should adopt an unusual topology, and local moments are predicted to emerge where the superconducting order parameter is suppressed. In principle, these moments can be probed directly by neutron scattering. In the vicinity of an FFLO flux line, the spatial spectrum of bound quasiparticle states becomes modulated due to a π phase winding around the flux line core, or about a nodal plane of the order parameter. Figure 4.7 shows a schematic diagram of the flux line topology induced by the FFLO state. The quasiparticle trajectories (i) and (ii) will experience a sign change of $\pm\pi$ in

the order parameter on moving to the opposite side of the flux line, or across the FFLO nodal plane respectively. These states are bound due to Andreev reflection. However, quasiparticles following trajectory (iii) will experience a $\pi \pm \pi$ phase shift of the order-parameter on crossing the nodal sheet *and* moving to other side of the flux line, and will be unbound. At the point where a flux line crosses a nodal plane of the order parameter, the lack of bound quasiparticle states is associated with a suppression of the screening currents. Throughout the bulk of the material, this results in a segmentation of the flux lines, with a segmentation period, $\Lambda = 2\pi/\mathbf{q}$. The imaging of the magnetic contrast associated with this modulation period would provide strong microscopic evidence for the existence of an FFLO phase.

4.1.6 The Q-phase

Recently, the question of describing the anomalous superconducting phase in $CeCoIn_5$ took a new twist with the discovery of the so-called 'Q-phase.' In their neutron scattering study, Kenzelmann et al. (2008) searched for magnetic structure in the low temperature and high field portion of the superconducting phase diagram consistent with the region of the proposed FFLO phase. With the field applied along a $[1\bar{1}0]$ direction figure 4.8 (a) shows that magnetic Bragg peaks were observed. The characteristic propagation vector of $\mathbf{Q} = (0.5 + q, 0.5 + q, 0.5)$, where $q \sim 0.06$, showed these peaks to be associated with an amplitude modulated, incommensurate, antiferromagnetic spin density wave. Remarkably, the antiferromagnetism is *only* stabilised within the superconducting phase diagram, being the red region highlighted in figure 4.8 (b). Outside of this phase region, both within the superconducting and normal states, no magnetic Bragg peaks are seen. The authors suggested this observation provided strong evidence that the incommensurate magnetism and superconductivity enjoy a symbiotic relationship in this portion of the phase diagram, in strong contrast to the usually antagonistic nature of magnetic and superconducting ground states. They further discuss how, on decreasing the field from above H_{c2} into the superconducting phase, the onset of the antiferromagnetism is unlikely to be caused by the system undergoing a quantum phase transition as anticipated

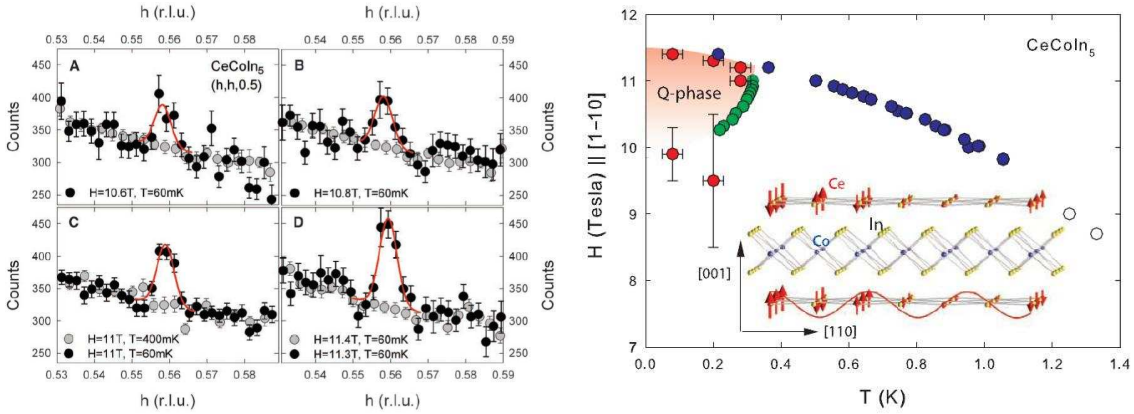

(a) Magnetic Bragg peaks at $q = (h, h, 0.5)$ (b) (H,T) phase space for $H \parallel [1\bar{1}0]$.

Figure 4.8: Figure (a) shows the experimental data of magnetic Bragg peaks observed in the $(h, h, 0.5)$-plane at various fields and temperatures. The propagation vector was observed to be at $\mathbf{Q} = (0.5 + q, 0.5 + q, 0.5)$, where q is found to be $\sim$0.06. Figure (b) is a phase diagram constructed from the neutron scattering data with the region in red corresponding to the phase space where magnetic Bragg peaks are observed. The inset of this figure shows the deduced form of the spin density wave associated with the local Ce^{3+} moments. Both figures after Kenzelmann et al. (2008).

from the associated antiferromagnetic fluctuations observed just above H_{c2}. Instead the antiferromagnetism is stabilised by the opening of the superconducting gap, apparently superceding the effects of quantum criticality.

Using a phenomenological coupling theory, the authors suggest that magnetic and superconducting order parameters could co-exist, preserve symmetry, and conserve momentum if the superconducting gap function, and hence Cooper pairs, carry a finite momentum. Thus, the study of Kenzelmann et al. (2008) provides the first experimental observation of a condensate that carries an intrinsic momentum. A finite momentum to the Cooper pair is consistent with that expected for the FFLO pairing scheme, though that observed by Kenzelmann et al. (2008) comes with an important difference; in the FFLO phase the finite value of the momentum is field-dependent varying as $2\mu_B H/\hbar v_F$. The $\mathbf{q}$ of the pairs in the Q-phase, obtained from the *measured* incommensurability vector of the antiferromagnetism, is observed to be field-independent, suggesting the existence of a new and different pairing channel that is also conducive with the appearance of magnetic order.

It is finally worth noting that the establishment of the Q-phase does not rule out the existence of an unusual FFLO phase. There is also a possibility that the two phases co-exist in a novel fashion. For example, it is not impossible to envisage a scenario where the antiferromagnetism is incipient in the nodal planes of a non-standard FFLO type state, though this question is left to be addressed with further experimental and theoretical work.

4.2 Studies of the flux line lattice in $CeCoIn_5$ and paramagnetic superconductors

Most of the information about the FLL in $CeCoIn_5$ has obtained from SANS studies. The first SANS observations of the FLL were reported by Eskildsen et al. (2003). In that study, with field parallel to the **c**-axis, and at temperatures of 50 mK, a two domain hexagonal FLL structure was observed at low field. Each domain of this structure was observed to possess nearest neighbours oriented along $\{110\}$ directions, and the overall FLL structure exhibits an average fourfold symmetry consistent with that of the underlying crystal. At a field of approximately 0.6 T, the FLL structure was observed to undergo what was likely to be a first-order transition into a square-like phase, which persisted until the highest reported field of 2.0 T. The observed orientation of the square phase was interpreted as consistent with that expected if the structure were stabilised by a $d_{x^2-y^2}$-order parameter anisotropy; that is with nearest neighbours aligned with $\{110\}$ directions. This gave weight in favour of the $d_{x^2-y^2}$-order parameter, being important in the early discussions in the literature on the precise details of the d-wave order-parameter symmetry.

The later study of DeBeer-Schmitt et al. (2006), again with $H \parallel \mathbf{c}$, provided a clearer picture on the details of the field-dependence of the FLL structure. At 0.5 T, figure 4.9 (a) shows the same low-field and two domain hexagonal structure as observed by Eskildsen et al. (2003). The precise shape of the hexagonal structures was found to be only weakly distorted from the isotropic hexagon, with a characteristic opening angle of the primitive cell measured to be $\sim 58^\circ$ at all fields. By 0.55 T however, figure 4.9 (b) shows that the FLL structure actually undergoes a first-order

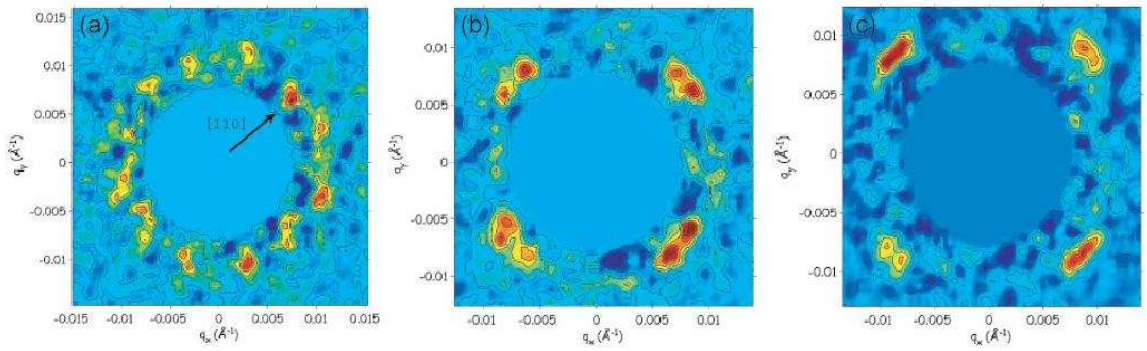

Figure 4.9: FLL diffraction patterns observed in applied fields of (a) 0.5 T, (b) 0.55 T and (c) 0.75 T. All patterns are obtained at a temperature of 50 mK, and with field parallel to the **c**-axis, note the $\{110\}$ direction indicated in (a) is valid for all patterns. After DeBeer-Schmitt et al. (2006).

structure transition and is now composed of two rhombic domains. The aspect ratio of these rhombic domains monotonically decreases with increasing field, until they undergo a second-order phase transition into a stable square structure at an estimated field of 1.1 T. Again, the square structure was observed to persist up to the highest available field of 2.0 T. Therefore, these new measurements revealed that, as function of field at 50 mK, the FLL structure undergoes both a first- and second-order structure transitions within the field range up to 2.0 T (just ~ 40 % of H_{c2}).

An important feature to note about the interpretation of the sequence of FLL structure phase transitions reported in Eskildsen et al. (2003), and DeBeer-Schmitt et al. (2006), is that the authors favoured the scenario where the stabilisation of a square FLL structure was due to the increasing prominence of the order parameter. However, they acknowledge that it is not possible to preclude the possibility that the transition sequence is influenced by non-local effects combined with a Fermi surface anisotropy (Kogan et al., 1997a). In particular, in Eskildsen et al. (2003) a comparison is drawn between the observed results in $CeCoIn_5$, and similar results seen in the borocarbide $ErNi_2B_2C$ (Eskildsen et al., 1997b), where non-local effects are thought to provide a good explanation of the variation in the FLL structure. However for the results obtained on $CeCoIn_5$, the emphasis is placed more on the

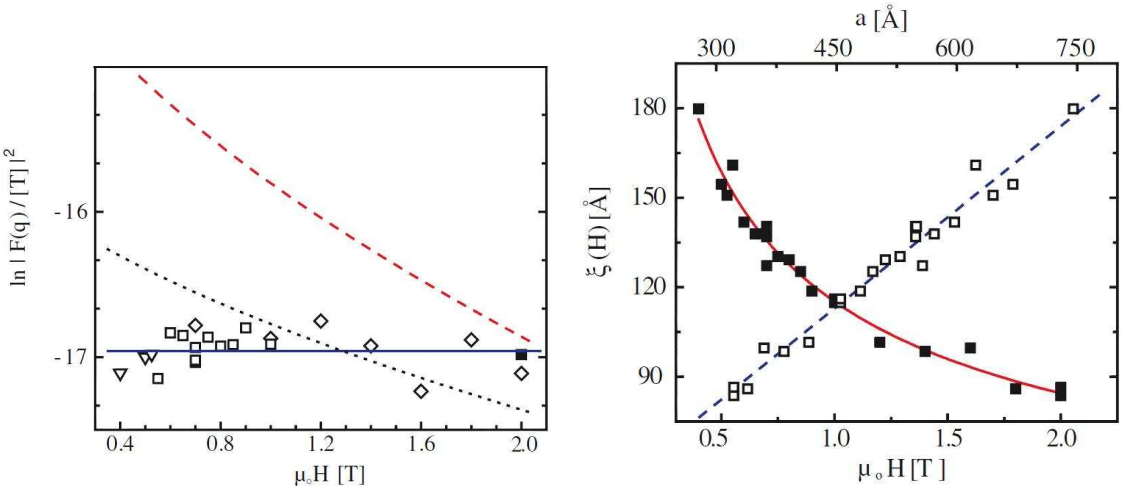

(a) Field-independent form factor

(b) Field-dependent core-size

Figure 4.10: Figure (a) shows a graph of the field-dependence of the flux line lattice form factor, for applied fields up to 2.0 T. The dashed and dotted lines are fits to the Clem model with field-independent fitting parameters. The solid line represents a mean value of the form factor across the entire field range. Figure (b) shows a graph of the deduced field-dependence of the Ginzburg-Landau coherence length ξ, plotted as a function of field (solid squares) and as a function of FLL lattice spacing (open squares), for applied fields up to 2.0 T. The solid line is a guide to the eye, and the dashed line a linear fit of the empty squares. In both figures, all data are obtained at 50 mK and with $H \parallel \mathbf{c}$. Figures after DeBeer-Schmitt et al. (2006).

influence of the order-parameter anisotropy.

The most remarkable result obtained in the study of DeBeer-Schmitt et al. (2006) was the observation that the FLL form factor remains essentially field-independent up to 2.0 T. This field-independence is shown in figure 4.10 (a). An analysis of the form factor data was carried out using the Clem model (Clem, 1975) where the field-dependence of the form factor is described in terms of the characteristic length scales of the penetration depth λ, and a flux line core size parameter ξ_{GL}, which is the Ginzburg-Landau (GL) coherence length. The constant FLL form factor could not be described using the Clem model in the usual sense, that is fitting the data using just single, field-independent, values for both the penetration depth and the core-size parameter. Attempts to fit the data using reasonable and constant values for λ and ξ_{GL} are shown by the dashed and dotted lines in figure 4.10 (a). These provide worse descriptions of the data than a constant form factor. In order

to describe the field-independence of the form factor, the Clem model was generalised somewhat by invoking a field-dependence to the core-size parameter ξ_{GL}. Figure 4.10 (b) shows the extracted field-dependence of ξ obtained by keeping λ constant, and adjusting the value of ξ_{GL} until the resulting form factor matched that observed experimentally. This apparently showed the core-size both contracting with increasing field, and varying linearly with $1/\sqrt{H}$, which is proportional to a, the FLL parameter. The physical mechanism behind a field-induced core contraction was related to theoretical work carried out by Kogan and Zhelezina (2005). Within the framework of their weak-coupling model, a field-induced contraction of the core-size is predicted to occur with increasing field as a consequence of the high cleanliness of the system. The rate of change of ξ_{GL} as a function of a, $\mathrm{d}\xi/\mathrm{d}a$, is predicted to have a value in the range between $0.2/\sqrt{2\pi}$ to $0.4/\sqrt{2\pi}$. The gradient $\mathrm{d}\xi/\mathrm{d}a$ obtained from the linear fit in figure 4.10 (b) is $0.55(2)/\sqrt{2\pi}$, and thus somewhat larger than the proposed theoretical range. In spite of this, the authors concluded that core contraction provided a good description of their data.

However, a possible physical mechanism that may also have played role in maintaining the constant form factor is that of field-induced paramagnetism. As $CeCoIn_5$ is a Pauli-limited superconductor at low temperatures, it might be expected that in the presence of the large Zeeman effect, paramagnetic effects might play a role in the mixed state. Such effects have only been considered comparatively recently, both theoretically (Ichioka and Machida, 2007), and via a combined experimental and theoretical study of the borocarbide superconductor $TmNi_2B_2C$ (DeBeer-Schmitt et al., 2007). The theoretical model developed in both studies is based on extending the usual quasiclassical Eilenberger theory by incorporating an extra term that accounts for the paramagnetism. The resulting model successfully reproduces the similar and anomalous field-dependences of the FLL form factor observed both in $CeCoIn_5$ (DeBeer-Schmitt et al., 2006) and $TmNi_2B_2C$ (DeBeer-Schmitt et al., 2007). Due to the relevance of both studies to the subsequent reports on $CeCoIn_5$, we briefly review them now.

$TmNi_2B_2C$ has a superconducting transition temperature T_c of 11 K, and be-

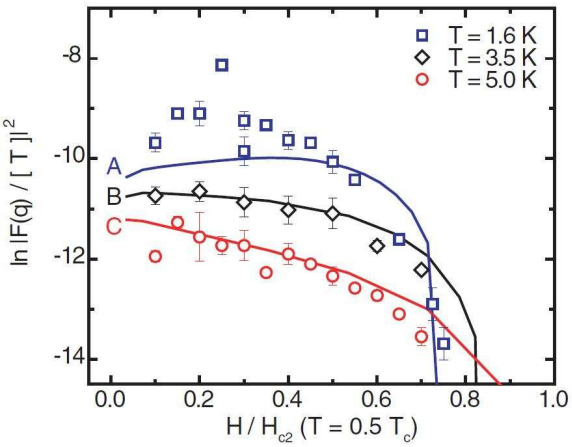

Figure 4.11: The field-dependence of the first-order flux line lattice form factor of $TmNi_2B_2C$ at temperatures of (A) 1.6 K, (B) 3.5 K and (C) 5.0 K. The data are fitted by the predictions of the quasiclassical Eilenberger theory, with different values of the paramagnetism parameter μ appropriate for the different temperatures. After DeBeer-Schmitt et al. (2007).

low 1.5 K, the Tm moments order antiferromagnetically. Above T_N the exchange interaction between the field-induced $4f$ moments of the Tm sub-lattice and the conduction electrons, results in an enhanced Zeeman effect on the conduction electrons and the emergence of enhanced Pauli paramagnetic effects. As a further consequence of the field-induced Tm magnetisation, the superconducting phase diagram is highly unusual (Eskildsen et al., 1998). Starting from low temperature, H_{c2} monotonically falls until T_N, after which H_{c2} rises to a maximum value of 1 T at 5 K, before falling monotonically on the approach to T_c at zero field. To investigate the effect of the paramagnetism on the FLL in $TmNi_2B_2C$, the field-dependence of the first-order FLL form factor was recorded for temperatures of 1.6 K, 3.5 K and 5.0 K (all above T_N). Figure 4.11 shows their resulting field-dependencies. The form factor data clearly shows unusual behaviour. In most other superconductors, the form factor falls monotonically as a function of increasing field. In the paramagnetic phase of $TmNi_2B_2C$ however, the form factor remains robust at low fields, and only falls to zero relatively close to H_{c2}.

Figure 4.11 also shows a comparison of the experimental data with the calculations carried out using the quasiclassical Eilenberger theory. This model, developed

in the reports of DeBeer-Schmitt et al. (2007) and Ichioka and Machida (2007), builds on previous versions of the quasiclassical Eilenberger theory (Ichioka et al., 1999; Nakai et al., 2002) by incorporating the paramagnetism via a Zeeman energy term μB. Here μ is a theoretical parameter which accounts for represents the relative strength of the paramagnetic effect, and which further accounts for the exchange coupling between the Tm moments and the conduction electrons. Within the calculations, a two-dimensional Fermi surface and fourfold symmetric gap function are assumed, along with a square FLL structure. The parameter μ is varied according to the strength of the Tm magnetisation at different temperatures, and takes values of $\mu = 1.71$ at 1.6 K, $\mu = 1.28$ at 3.5 K and $\mu = 0.86$ at 5.0 K. From figure 4.11 we see that a reduction in μ partially corresponds to a change in the low field gradient of the field-dependence of the form factor, which goes from positive to negative with increasing temperature. Clearly, the stronger the paramagnetic effect, and the lower the temperature, the more robust is the low field form factor as a function of field. Moreover, on moving towards the normal state, the form factor at lower temperature plummets more quickly to zero due to the effects of paramagnetic depairing, which are stronger for larger μ.

The physical reason for the robust nature of the low field FLL form factor in $TmNi_2B_2C$ is due to a field-induced accumulation of a paramagnetic moment. This effect is strongest within the flux line cores, as at these regions the order parameter is suppressed from the bulk value, and there exist single quasiparticle states that are subject to the exchange field. The imbalance in the spin population under an applied field results in the emergence of the paramagnetic moment, and an enhanced field distribution $B(\mathbf{r})$. This effect is shown schematically in figure 4.12 which shows the results of calculations that were carried out within the same paramagnetic quasiclassical Eilenberger theory (Ichioka and Machida, 2007). In these calculations, a $d-$wave pairing symmetry is assumed, leading to the fourfold symmetry of the various spatial distributions calculated in the left-hand panels of figure 4.12. The calculations show that the field-induced paramagnetic moment is enhanced exclusively around the flux line core, particularly along the anti-nodal di-

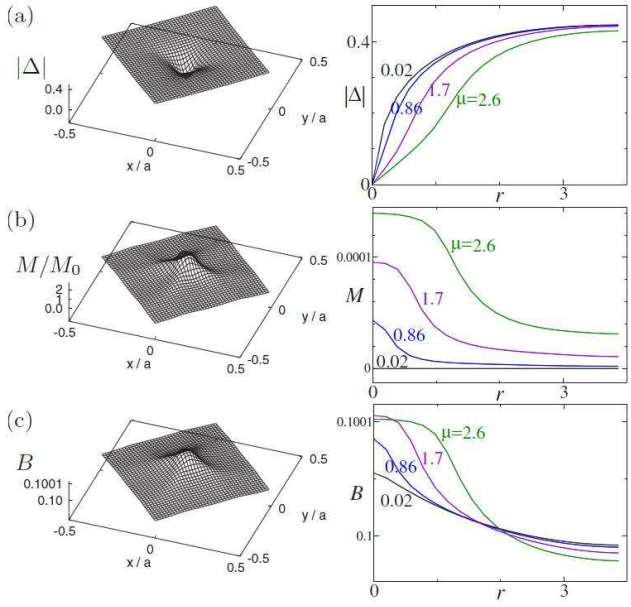

Figure 4.12: Calculations of the spatial distribution of (a) the pair potential $|\Delta|$, (b) the field-induced paramagnetic moment M (**r**), and (c) to overall induction B (**r**) for varying strengths of paramagnetic effects. The left hand panels show these spatial structures in a single unit cell of the FLL, for the case where $\mu = 1.7$. The right panels show cuts along the direction r from the flux line centre to the midpoint between nearest neighbour flux lines, and for $\mu = 0.02$. 0.86, 1.7 and 2.6. The calculations were carried out at $T = 0.1\ T_c$ and $B = 0.1$. After Ichioka and Machida (2007).

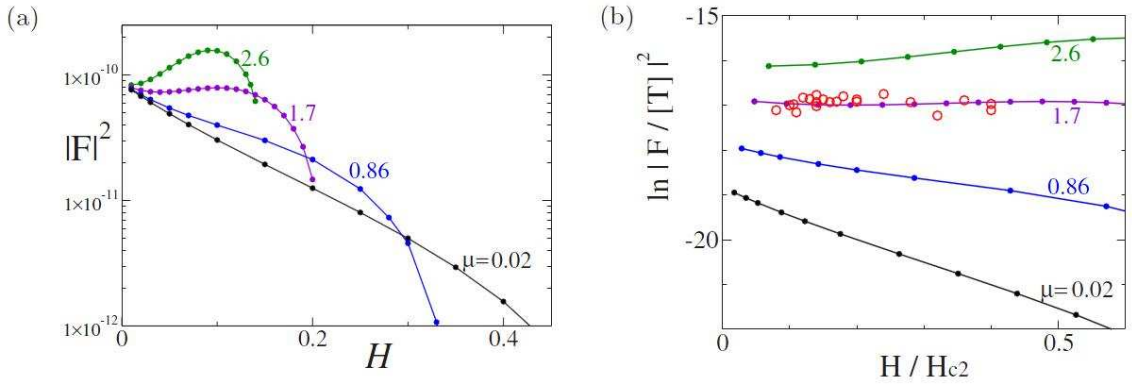

Figure 4.13: In (a) the field-dependence of the first-order FLL form factor is calculated using the model of Ichioka and Machida (2007), at $T = 0.1\ T_c$ and for values of $\mu = 0.02$, 0.86, 1.7 and 2.6. The data are plotted as a function of field parameter H, which is equal to a numerical factor times $H_{c2}(T = 0, \mu = 0)$. In (b) are the same calculations as shown in (a) but normalised to a scale of H/H_{c2} where H_{c2} for each μ corresponds to 5 T. The inset circles are the experimental data of DeBeer-Schmitt et al. (2006) obtained on $CeCoIn_5$, as presented in figure 4.10 (a). After Ichioka and Machida (2007).

rections which correspond to the 'ridge' features visible in figures 4.12 (b) and (c). Figure 4.12 (c) shows that the overall superposition of the induced paramagnetic and conventional diamagnetic contributions leads to a greater internal induction at larger μ, even though figure 4.12 (a) shows the pair potential to become suppressed within the cores, leading to an effectively larger core size. This larger internal induction in the core vicinity helps to maintain the field-contrast, and hence the form factor to higher fields.

The field distributions $B(\mathbf{r})$ for different values of μ are calculated as a function of field, in order to provide a prediction of the field-dependence of the first-order FLL form factor. Although the results of the calculations shown in figure 4.13 were tailored towards explaining the unusual field-dependence of the form factor seen in $CeCoIn_5$ (DeBeer-Schmitt et al., 2006), and as such used appropriate material parameters, they are qualitatively applicable to those results obtained on $TmNi_2B_2C$. Figure 4.13 (a) shows the predicted field-dependence of the form factor as a function of theoretical parameter H, which is related to the field. For a particular value of μ, the value of H where the calculation of the form factor stops corresponds to H_{c2}. It is worth noting that this becomes suppressed with increasing μ. Furthermore, if μ is large enough, the form factor remains finite on reaching H_{c2}, corresponding to a first-order transition between the superconducting and normal states. The important result is that if μ is large enough, the form factor remains constant, and can even rise, as a function of increasing field. This is consistent with the results seen in $CeCoIn_5$ at low field (DeBeer-Schmitt et al., 2006) and in qualitative agreement with the SANS results obtained on $TmNi_2B_2C$ (DeBeer-Schmitt et al., 2007). In the absence of the paramagnetic effect, the monotonic decrease of the form factor with field, as was appropriate for use with $YBa_2Cu_3O_7$ in the last chapter, is recovered. On scaling the parameter H so that all of the calculated curves in figure 4.13 (a) lie on a normalised H/H_{c2} scale (where $H_{c2} = 5$ T, suitable for $CeCoIn_5$ with $H \parallel \mathbf{c}$), Ichioka and Machida find that the low field form factor data first-shown in DeBeer-Schmitt et al. (2006) is well explained if paramagnetic effects play a role, particularly if the paramagnetic parameter $\mu = 1.7$.

A final point to note is that $TmNi_2B_2C$ does not exhibit a Pauli-limited upper critical field, even though paramagnetic effects are induced in the mixed state. The characterisation of the paramagnetic effects induced in $TmNi_2B_2C$ provide a natural comparison with which to compare the possible paramagnetic effects induced in Pauli-limited $CeCoIn_5$.

4.3 Motivation for new SANS studies of the flux line lattice in $CeCoIn_5$

Due to the rich variety of unconventional behaviour exhibited by $CeCoIn_5$, the motivation for further studies in the mixed state is clear. The first SANS studies (Eskildsen et al., 2003; DeBeer-Schmitt et al., 2006) uncovered high field square FLL structures, and the possible effects of an anomalous core-contraction, and field-induced flux line core paramagnetism for $H \parallel \mathbf{c}$. However, the results presented before this thesis were only reported at temperatures of 50 mK, and fields up to 2 T. It is of great interest to understand the field- and temperature-evolution of both the FLL structure and form factor over the rest of the superconducting phase diagram. Recording both will be critical to understanding the mixed-state behaviour, and maintaining a consistent physical interpretation of the observations.

The prospect of carrying out SANS measurements at fields higher than 2 T for $H \parallel \mathbf{c}$ leads to the prospect of observing the FLL within the part of the superconducting phase diagram associated with the proposed FFLO, and possible Q-, phases. It is of great interest to observe if the stabilisation of such phases has an observable influence on the FLL. This is in addition to investigating the possible effects of Pauli paramagnetism and quantum critical behaviour at low temperature.

The natural extension to these studies with $H \parallel \mathbf{c}$ is to apply the field parallel to the plane. With $H \parallel [110]$, the Q-phase has been observed, and the relative size of the region of the superconducting phase diagram associated with the Q-phase (or FFLO phase) is experimentally characterised to be larger (see for example (Bianchi et al., 2003a)). Moreover, the FLL structure and orientation, and the field-dependence of the FLL form factor, are entirely unknown for this field

geometry.

4.4 Sample preparation, characterisation and mounting

Across all the experiments carried out on $CeCoIn_5$, a few different samples of $CeCoIn_5$ have been used. All were co-aligned mosaics of single crystal $CeCoIn_5$, with the single crystals either provided by C. Petrovic, of Brookhaven National Laboratory, USA, or A.D. Bianchi, of Université de Montréal, Canada. Single crystals from each source were not mixed together for any sample, and reasonable agreement was obtained across all samples.

The single crystals from each source were grown in a flux containing excess In (Petrovic et al., 2001b,a). The excess In is combined with stoichiometric volumes of Ce and Co in an alumina crucible, with the crucible encapsulated in an evacuated quartz ampoule. The melt is made at $\sim$1150°C and then cooled via a two stage process. The first stage is an initial rapid cool from $\sim$1150°C to $\sim$750°C whereby the melt is homogenised. The second is a slower cool from$\sim$750°C to $\sim$450°C with the ampoule removed from the oven. During the second cool, the excess In is removed by centrifugation. Each single crystal grows as a platelet, always with large area **c**-faces (of order 1 cm^2) and a thin dimension of order 0.5 mm or less.

Crystal characterisation was carried out by the groups who fabricated the crystals. The $CeCoIn_5$ crystals are of high quality, with typical x-ray studies (powder and single crystal) showing the crystals to be single phase within the resolution of the x-ray technique used. The resistivity ratio reported by Petrovic et al. (2001a) for typical samples is large with values between $\rho(300\ \mathrm{K})/\rho(2\ \mathrm{K}) = 50$ - 80. The zero-field superconducting transition width (according to the 10% - 90% criterion) estimated from Bianchi et al. (2003b) is narrow at $\Delta T_c \leq 0.1$ K. The characterisation indicates the high crystal quality, and the superclean nature of the material.

The preparation of the samples for the SANS measurements was dependent on the field geometry used. Most experiments were carried out in the traditional geometry of field and crystal **c**-axis approximately parallel to the neutron beam. For

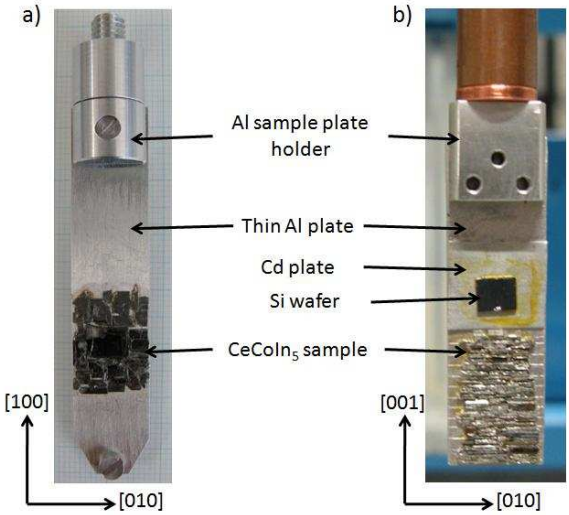

Figure 4.14: Photographs of $CeCoIn_5$ samples used for the SANS experiments reported in this thesis. Each photo shows the samples glued to the sample plate that is attached to the dilution refrigerator (DR). The sample shown in figure (a) is a sample suitable for SANS investigations for $H \parallel \mathbf{c}$. The crystal axes indicate that the **c**-axis lies out of the plane of the page. The sample shown in figure (b) is a sample suitable for SANS investigations for field in the basal plane. The crystals are cut into thin rods before being glued onto the Al plate. The crystal axes indicate that an **a**-axis lies out of the plane of the page. In this picture, the sample holder is already attached to the cold tail of the DR. Photographs courtesy of S. Gerber, PSI.

these experiments, the form of the single crystals as **c**-axis platelets is ideal, as these can be glued on their flat faces to a pure Al plate. Each sample was composed of a mosaic of single crystal platelets co-aligned by eye (using a microscope to observe the prominent (100) edges) about the **c**-axis. The typical mosaicity about the **c**-axis for such a sample was checked using the MORPHEUS instrument at PSI, and found to be $\leq 1.5°$. This lies within the in-plane resolution of the SANS instrument. Although this mosaicity was checked just once for a certain sample, the result can be considered representative of all samples used. Figure 4.14 (a) shows a photograph of a typical mosaic sample used for the $H \parallel \mathbf{c}$ measurements. To maximise the diffracted intensity, a similarly densely packed mosaic is mounted onto another Al plate which is mounted back to back with the plate shown in the photograph. However, care has to be taken not to make the overall thickness of the sample too great. In Appendix B we show the $1/e$ length to be just 0.7 mm for neutrons of

wavelength 5 Å. Therefore, the typical mean thickness of all $H \parallel \mathbf{c}$ samples was low, varying between 0.2 and 0.4 mm.

The preparation of a sample used to observe the FLL with field in the basal plane was a little more involved. In order to use the traditional SANS geometry of field parallel to the neutron beam, the single crystals had to be re-oriented. However, due to the strong neutron absorption, it is not possible to construct a sample simply by mounting single crystal platelets on their sides. Rather, the platelets must be cut into thin rods, with each rod mounted separately on the Al plate such that an **a**-**c** face is flat. An example of one of the samples used in the SANS experiments is shown in figure 4.14 (b). The average thickness of the sample was estimated to be $\sim$0.5 mm. Subsequent characterisation using neutrons showed an in-plane mosaicity similar to that of the $H \parallel \mathbf{c}$ sample.

4.5 High field flux line lattice structure with field parallel to c-axis

Unusually for a d-wave superconductor, as H_{c2} for this field geometry is just 4.95 T, the imaging of the FLL in $CeCoIn_5$ can be carried out over the entire superconducting phase diagram. Here, we describe the field- and temperature-dependence of the FLL structure observed with $H \parallel \mathbf{c}$, at fields and temperatures higher than those previously reported by Eskildsen et al. (2003) and DeBeer-Schmitt et al. (2006). The previous studies revealed the existence of three distinct FLL structure types, which are shown in figure 4.15. For the hexagonal and rhombic phases, the overall FLL structure is composed of two energetically equivalent domains. The observation of multi-domain FLL structures is not unusual in materials where the field is applied along a fourfold symmetry axis. If the symmetry of the crystal is higher than the intrinsic symmetry of a FLL domain, this will force the nucleation of enough lower symmetry FLL domains such that the average symmetry of the multi-domain FLL structure is the same as that of the crystal. Excellent examples of this are discussed in the rigorous studies of the FLL structure in conventional Nb, where a variety of structure types are observed for the case of field parallel to a four-fold symmetry

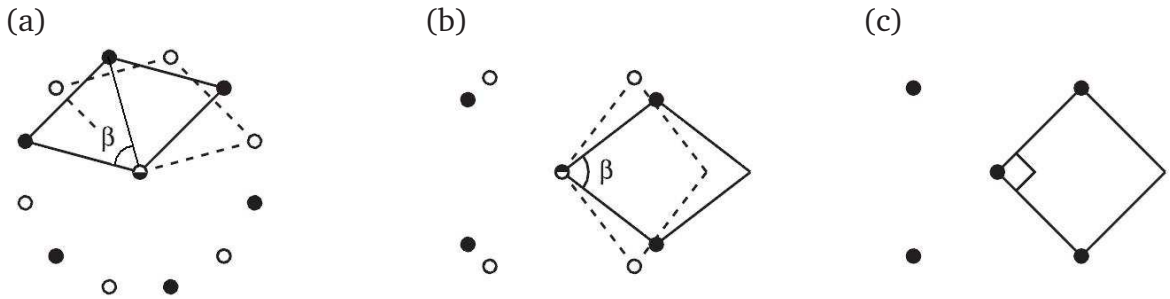

Figure 4.15: Schematic diagrams of the FLL structure types observed in $CeCoIn_5$ for $H \parallel \mathbf{c}$. Starting from low field, the transition sequence on moving towards intermediate fields is (a) hexagonal to (b) rhombic to (c) square. The hexagonal and rhombic FLL structures exhibit two degenerate FLL domains, each distinguished by filled and empty circles. The square phase is single domain. The characteristic opening angle of the primitive cell is indicated by the angle β.

direction (Laver et al., 2006, 2009).

4.5.1 Flux line lattice structure

At the base temperature of 50 mK, after confirming the results of the previous investigations for fields up to 2.0 T, the FLL structure was measured as a function of field right up to H_{c2}. Figure 4.16 shows some examples of new high field diffraction patterns obtained at 50 mK. Figure 4.16 (a) shows the square phase is seen to persist until at least 3.0 T. On increasing the field, figure 4.16 (b) shows that by 4.3 T, the square structure has been replaced by a re-emergent rhombic FLL structure which is qualitatively the same as that seen at low fields; the flux line nearest neighbours lie close, but not parallel to, the $\langle 110 \rangle$ directions. The transition between the two structure phases is likely continuous, being similar to the case for the low field rhombic to square FLL structure transition. On further increase of the field, between the fields of 4.3 T and 4.7 T, a final transition between the rhombic phase and a distorted hexagonal phase like that shown in figure 4.16 (c) takes place. This high field transition is qualitatively similar to that seen between the low field hexagonal and rhombic structure phases; it is likely to be first-order, and the composition and orientations of the FLL structures are the same as indicated in figure 4.15 (a) and (b). We note that as a function of increasing field, the high field transition sequence

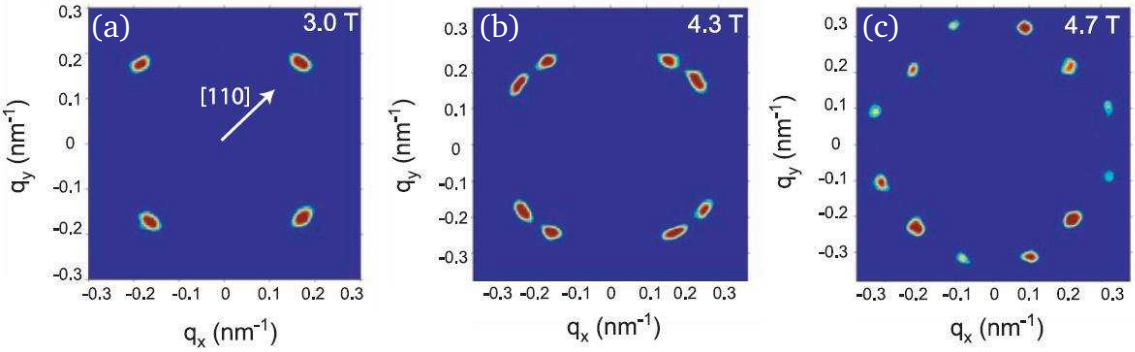

Figure 4.16: Diffraction patterns obtained from the FLL in $CeCoIn_5$ in applied fields of (a) 3.0 T, (b) 4.3 T and (c) 4.7 T. All patterns were obtained at 50 mK and with $H \parallel \mathbf{c}$. The [110] crystallographic direction shown in (a) is valid for all figures.

of square to rhombic to hexagonal, is the precise opposite of the low field transition sequence.

The new results show that although at low temperatures there are four transitions in the FLL structure across the field range, each of these is an example of just one of two transition types. We now determine the location in field of each transition, considering in more detail examples of the structure transitions in the new data at higher fields.

Square to rhombic transition

At low fields, with increasing field the rhombic structure smoothly distorts to undergo a continuous phase transition into a stabilised square structure. By inspection, it is likely that the high field rhombic phase re-emerges continuously from the square phase. We now consider this transition in more detail. Figures 4.17 (a) to (c) show examples of the diffraction data obtained at 50 mK, and over a selection of fields close to the re-entrant transition. In each figure, just the right hand quadrant of reciprocal space was recorded, as this is all that is required in order to re-construct the entire diffraction pattern. At 3.2 T, the single spot aligned with [110] direction indicates the FLL structure to be square. By 3.4 T, figure 4.17 (b) shows this spot to have now broadened slightly azimuthally. At 3.6 T, figure 4.17 (c) shows that the FLL structure is clearly in the rhombic phase, with one each of the

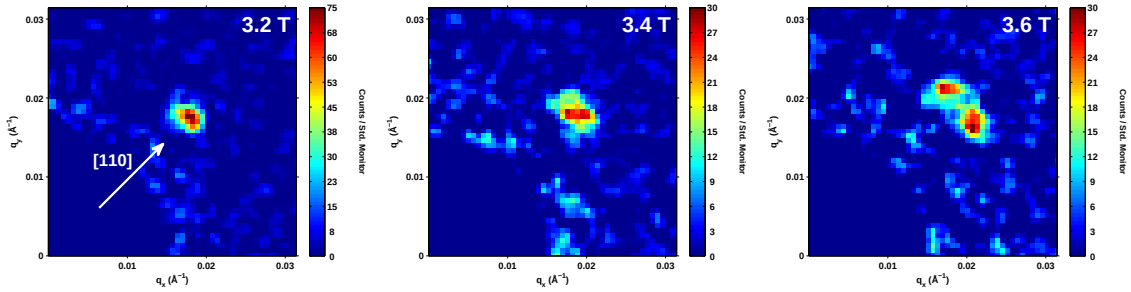

(a) 3.2 T (b) 3.4 T (c) 3.6 T

Figure 4.17: The top right quadrant of reciprocal space of the FLL diffraction patterns recorded in applied fields of (a) 3.2 T, (b) 3.4 T and (c) 3.6 T. The [110] direction indicated in (a) is valid for all the images, the temperature was 50 mK, and $H \parallel \mathbf{c}$. All patterns were collected during the same experiment.

Bragg spots belonging to one of the rhombic domains of the FLL. We see the transition is manifested on the detector by an azimuthal elongation of a square spot that splits into the two spots expected of the rhombic phase. The field at which this process starts is the transition field between the two structure types. However, it is not possible by inspection to determine when this spot broadening starts due to the finite instrumental resolution. For fields *just* above the transition, although the intrinsic FLL structure has changed slightly, any change in Bragg spot shape is within the bounds of the resolution function, and hence unobservable.

We overcome this problem by modelling the field-dependence of the precise spot positions within the rhombic phase, and then extrapolating this dependence back in field to deduce the field at which the spot of the square phase starts to split. To do this, we define an order-parameter δ, which is the angular separation between the direction of the **q**-vector of a Bragg spot in the rhombic structure phase to that of the $[110]$ direction of a Bragg spot in the square structure phase. Figure 4.18 (a) provides a schematic visualisation of this, and shows that all spot angles are defined relative to a vertical coordinate axis.

Adopting a free-energy approach to describe the field-dependence of δ, we define the free energy for a particular FLL configuration F_{FLL} as dependent on the

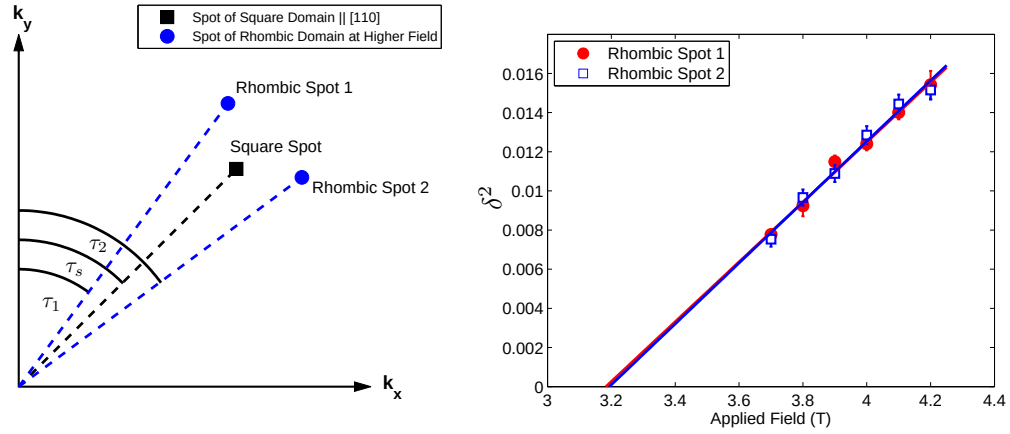

(a) Schematic defining spot angles.

(b) Use of the order parameter method on data obtained at 500 mK.

Figure 4.18: In (a) we define the angles that the Bragg spot **q**-vectors make with respect to a vertical axis. In the rhombic phase these angles are τ_1 and τ_2 for rhombic spot 1 and 2 respectively, whilst in the square phase this angle is τ_s which is parallel to $[110]$. These angles are used to define the order parameter δ^2, see text. In (b) we show an example of the use of the order parameter method (described in the text) on data obtained at 500 mK. The fields where the linear extrapolations intercept the horizontal axis provide estimates of the transition field.

square of δ

$$F_{FLL} = (B_T - B)\,\delta^2 + C\delta^4 \tag{4.4}$$

where B is the induction (=$\mu_0 H$), B_T is the transition field, and C is a field-independent constant. Note by symmetry we only require even power terms of δ. Minimising equation 4.4 leads to

$$\delta^2 = \frac{1}{2C}\,(B - B_T) \tag{4.5}$$

which shows δ^2 to be linear in field, and reveal the transition field B_T when $\delta^2 = 0$. In accordance with figure 4.18 (a), we define $\delta^2 = (\sin\tau_s - \sin\tau_i)^2\,, (i = 1, 2)$ and, for a given temperature, plot the field-dependence of δ^2. An example implementation of the method for data obtained at 500 mK is shown in figure 4.18 (b). For each spot of the rhombic phase, the linear extrapolation in field to $\delta^2 = 0$ yields the field at which the **q**-vector of the spot lies parallel to $[110]$, and the structure is square. The transition field is taken as the mean value of the intercepts with the horizontal axis

for each of the linear fits of the two rhombic spots. The difference between these two values could be considered representative of the error in the analysis method. However, a truer measure of the error is derived from the uncertainty in each of the two linear fits. Therefore, for the case shown in figure 4.18 (b), the transition field $B_T(T = 500 \text{ mK}) = 3.2(1)$ T. Such an analysis method was used to determine the square to rhombic FLL structure transition field for temperatures up to 1125 mK.

This method was also applied in a similar manner to characterise the low field rhombic to square phase boundary. Data obtained in the new experiments allow the deduction of the transition field for temperatures up to 750 mK.

Rhombic to hexagonal transition

In their original discussion on the low field transition between hexagonal and rhombic phases Eskildsen et al. (2003) mentioned that a continuous transition between these two structure types is unlikely. Our observed transition involves not only a change in FLL structure, but also a 45° reorientation of the primitive cell. Such a reorientation cannot be reproduced by smoothly distorting one structure type into the other.

The first-order transition field between the high field rhombic and hexagonal phases is deduced by inspection to be that at which the rhombic and hexagonal phases were observed to coexist. As an example of the implementation of this method, figure 4.19 shows the top right quadrant of reciprocal space obtained for a selection of high fields at 50 mK. Clearly between the fields of 4.3 T and 4.5 T, the structure undergoes a first-order transition between the two phases. At 4.4 T, figure 4.19 (b) shows an essentially continuous streak of diffracted intensity, which encompasses the expected Bragg spot positions for both phases. Here, we suggest that the two structures co-exist at 4.4 T, and likely in the presence of some disorder. By inspection, we declare the transition field $B_T(T = 50 \text{ mK}) = 4.4(1)$ T, with the error derived from the incremental change in field. At higher temperatures, similar inspection of the data yields the rhombic to hexagonal transition field for temperatures up to 1000 mK.

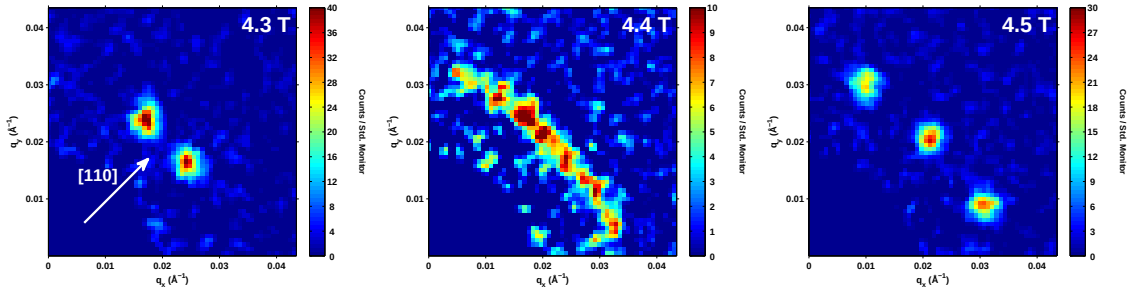

(a) 4.3 T (b) 4.4 T (c) 4.5 T

Figure 4.19: The top right quadrant of reciprocal space of the FLL diffraction patterns recorded in applied fields of (a) 4.3 T, (b) 4.4 T and (c) 4.5 T. The [110] direction indicated in (a) is valid for all the images, the temperature was 50 mK, and $H \parallel \mathbf{c}$. All patterns were collected during the same experiment.

We attempted to carry out the inspection method at low field, in order to deduce the temperature-dependence of the hexagonal to rhombic phase boundary. However, the few measurements that were taken at temperatures above 50 mK suffered from low statistics. After careful consideration of the data, it was concluded that it was not possible to characterise in confidence the hexagonal to rhombic transition field at any higher temperatures beyond that at 50 mK reported in DeBeer-Schmitt et al. (2006).

FLL characteristic angle β as a function of field

The different character of the FLL structure transitions is perhaps clearest on plotting the field-dependence of the primitive cell opening angle β. Using the definition of β for each structure phase as shown in figure 4.15, in figure 4.20 we show the field-dependence of β at 50 mK, and over the entire field range up to H_{c2}. The first-order character of the transitions between rhombic and hexagonal phases is clear, with a discontinuous change in β at the relevant transition field. Similarly, the continuous transition separating the rhombic and square structure phases is evident by the smooth variation of β with field in the rhombic phase on approaching the lock-in square structure phase with $\beta = 90°$. Similar measurements were obtained at higher temperatures, to support the conclusion of the locations of the transition

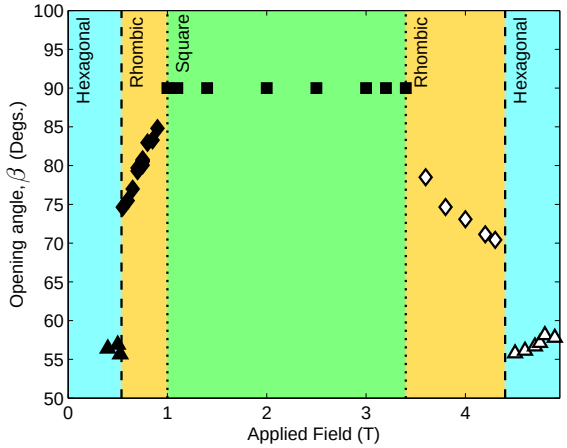

Figure 4.20: The field-dependence of the FLL primitive cell opening angle β, at 50 mK and with $H \parallel \mathbf{c}$. The filled (open) triangles are measurements of the FLL structure in the lower (upper) hexagonal phases. Similarly, the filled (open) diamonds are measurements of the FLL structure in the lower (upper) rhombic phases. Filled squares correspond to measurements in the square phase. Dashed (dotted) lines correspond to first-(second-)order transition boundaries between structure phases. The horizontal axis stops at $H_{c2} = 4.95$ T.

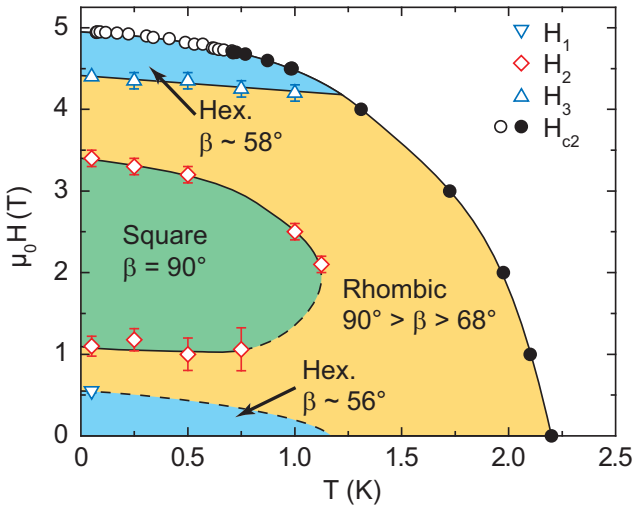

Figure 4.21: The FLL structure phase diagram with $H \parallel \mathbf{c}$. Empty triangles correspond to first-order transition fields between rhombic and hexagonal structure phases. The diamonds correspond to a second-order transition boundary between the rhombic and square structures. The open and filled circles correspond to where the transition between the superconducting and normal states is first- and second-order respectively. These datapoints were deduced from thermodynamic measurements (Bianchi et al., 2003a). The dashed lines correspond to best estimates of structure phase boundaries where a reliable determination was not possible from the data obtained.

fields, and the order of the FLL structure transition.

FLL structure phase diagram

In figure 4.21, we present the deduced FLL structure phase diagram for $H \parallel \mathbf{c}$. Solid lines indicate confidently determined FLL structure phase boundary lines, with dashed lines representing best estimates only based on the available data. This is a little disappointing, as characterising the low field phase boundary lines could provide an interesting comparison to those in the phase diagram of $YBa_2Cu_3O_7$ presented in the previous chapter. At intermediate fields, the estimation of the position of the low field branch of the rhombic to square transition line does not preclude an unexpected field- or temperature-dependence to that indicated in figure 4.21. However, the data do not provide any evidence against either.

In spite of the uncertainty at low fields, the upper portion of the phase diagram is reliably established, the details of which represent genuinely new results for this class of material. The square to rhombic re-entrant transition line is suppressed with temperature, showing the reduced stability of the square phase to both high field and temperature. The phase diagram also shows that the upper field rhombic to hexagonal phase boundary line is only weakly temperature-dependent, suggesting the rhombic to hexagonal transition has a different physical origin to the rhombic to square transition. We note that this uppermost phase boundary line does not intersect H_{c2} at the cross-over temperature between where the superconducting to normal transition is first- or second-order. Although this would suggest that the FLL structure is not determined by proximity to a Pauli limited upper critical field, this is a detail we re-explore in the next subsection.

4.5.2 Discussion of flux line lattice structure

At low field and temperature, the possible physical mechanisms behind the hexagonal to rhombic to square sequence of FLL structure transitions have been discussed previously (Eskildsen et al., 2003; DeBeer-Schmitt et al., 2006). Both of these studies suggested that the transition sequence is explainable in terms of an increasing

prominence of a $d_{x^2-y^2}$ order parameter anisotropy (Ichioka et al., 1999). However, each also acknowledge that such a sequence could be driven by the increasing role of non-local effects (Kogan et al., 1997a). According to the theoretical predictions of Kogan et al. (1997a) (shown in figure 1.3), as a function of increasing field, the primitive cell undergoes a first-order transition from having nearest neighbours at 45° to the crystal axes, to a primitive cell with nearest neighbours aligned parallel with the crystal axes. The second structure then smoothly distorts into a lock-in square phase at high field. This sequence is precisely the same as we observe.

The measurements of these low field structure phases reveal that, for temperatures up to at least 750 mK $(T_c/3)$, the low field rhombic to square transition field is essentially temperature-independent. Similarly, our best estimate of the phase boundary line separating the low field hexagonal and rhombic phases is suggested to be only weakly temperature-dependent. A weak temperature-dependence of a square FLL structure is not what might be naively expected from comparisons to the theoretical predictions for precisely the same reasons as previously mentioned when discussing the weakly temperature-dependent phase boundary lines observed in $YBa_2Cu_3O_7$ presented in the previous chapter. According to the quasiclassical theory, where a square structure is stabilised by the fourfold gap anisotropy (Ichioka et al., 1999) the influence of this anisotropy is expected to become suppressed with temperature. Within the non-local London theory of Kogan et al. (1997a), the non-local correction terms which describe the stabilisation of the square FLL due to non-local effects are predicted by a factor of approximately 2 between low temperatures and T_c. Hence, we expect more isotropic FLL structures to be recovered on increasing the temperature. On consideration of these points, we note that we suspect these effects to be more noticeable at temperatures higher than $(T_c/3)$. Re-investigating the low field structure transition boundaries shown in figure 4.21 could cast some light on the role of thermal fluctuations on the low field transitions.

At high field and low temperature, the re-entrant sequence of transitions was unexpected, and reflects a *field*-induced suppression of the stabilising anisotropy of the square phase. At this stage, we rule out a possible role for field-induced

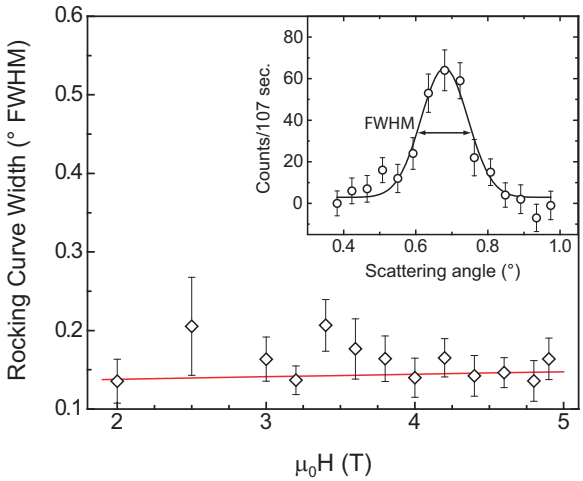

Figure 4.22: The field-dependence of the rocking curve width at 50 mK, and $H \parallel \mathbf{c}$. The inset indicates the definition of the FWHM of the gaussian lineshape fitted to the rocking curves. In the main panel, the field-dependence of this measured quantity is compared to an estimate of the instrumental resolution showed by the red line.

FLL disorder. Across all experiments carried out with $H \parallel \mathbf{c}$, the rocking-curve widths lie close to, or at, that of the instrument. Figure 4.22 shows an example of the field-dependence of the rocking curve FWHM at 50 mK, for a set of rocking curves obtained under identical experimental conditions. Discounting any effects of FLL disorder, we now consider the available theoretical predictions for the FLL structure in the upper half of the phase diagram. The quasiclassical Eilenberger theory of Nakai et al. (2002) details a re-entrant square to rhombic transition at high field, which derives from a close balance between the competing anisotropies of the Fermi surface and the gap function. However, for reasonable values of the various anisotropy parameters, the resulting FLL structure phase diagram predicts the emergence of a second square phase at high field, which clearly does not resemble the behaviour seen in $CeCoIn_5$. A high field re-entrant rhombic phase is also predicted to emerge as a consequence of strong thermal fluctuations (Gurevich and Kogan, 2001). In this scenario, the fluctuations weaken the stabilising anisotropy at high field, which in this case is due to non-local effects. This model is also deemed unsuitable to explain our superconducting phase diagram, as the effects of thermal fluctuations at high fields are likely only applicable very close to H_{c2}. Furthermore,

whilst it is possible that such fluctuations play a role in suppressing the square phase at intermediate field and at higher temperature, at high field and low temperature our square FLL structure phase is suppressed well short of H_{c2}.

A more promising theoretical explanation for our observed high field transition sequence has recently been proposed by Hiasa and Ikeda (2008). Using a Ginzburg-Landau model, the authors are able to qualitatively reproduce the main features at high field of the experimentally observed FLL structure phase diagram. Although the model is not expected to be numerically accurate regarding reproducing the FLL structure phase diagram precisely, it is reasonable to suggest that the model will reflect the physics by which a square phase is suppressed with field. The calculated structure phase diagram is shown in figure 4.23. At low temperatures, the re-entrance of the rhombic phase with increasing field is attributed to paramagnetic depairing in the flux line cores. As a result of the depairing, the stabilising anisotropy of the square phase, which in the model is due to the fourfold core anisotropy induced by the gap function anisotropy, is suppressed with increasing field.

The positive slope of the upper branch of the square to rhombic phase boundary suggests the paramagnetic depairing effect to be suppressed with temperature. This is in contrast to the experimentally observed negative slope. The authors suggest that critical thermal fluctuations could induce a reduction in the mean free path ℓ, which brings the slope of the upper branch of the thick red curve in figure 4.23 slightly more in to agreement with the experimental data. This correction is comparatively weak however, leading the authors to suggest that a further additional, and currently unknown, correction is needed. Aside from this detail, the phase diagram of figure 4.23 captures many of the features of the phase diagram shown in figure 4.21. Furthermore, by mixing in a weak fourfold Fermi surface anisotropy that competes with that of the order parameter, the model also predicts the stabilisation of an upper hexagonal phase of correct orientation close to H_{c2} and at low temperature. This Fermi surface anisotropy further results in the stabilisation of the same hexagonal phase at low fields (not shown in figure 4.23). Therefore it

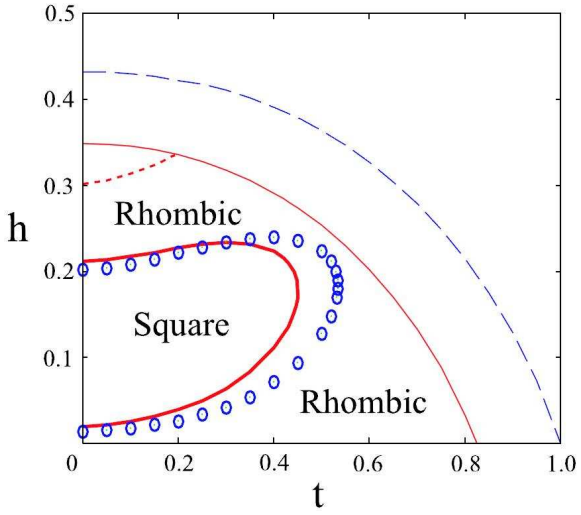

Figure 4.23: The high FLL structure phase diagram calculated within the Ginzburg-Landau theory of Hiasa and Ikeda (2008). For all calculations, $\alpha_M = 2.8$. The blue circles and dashed line respectively represent the lock-in phase boundary of the square FLL structure phase, and H_{c2}, for the case for $\ell \to \infty$. The thick and thin red solid lines respectively represent the same boundaries but now with $\ell = 14.5\xi_0$. In addition, the region at low temperatures and high field between the red dashed and solid lines hosts a hexagonal structure of orientation consistent to that shown in figure 4.15 (a).

seems that a reasonable physical explanation for the qualitative features of the entire structure phase diagram is derivable from the GL model where the anisotropies of the order parameter and Fermi surface compete. However, the potency of the Fermi surface anisotropy is relatively weak. It only provides the dominant structural $\mathcal{F}_m$ either at low field where the influence of the flux line core is too weak, or at high fields, where the order parameter anisotropy is suppressed by paramagnetic depairing.

Although unpublished, recent calculations made using the quasiclassical Eilenberger theory Ichioka and Machida (2009) also support the conclusion that paramagnetic depairing effects within the flux line cores destabilise the square structure. This high field depairing results in the suppression of the core anisotropy induced by the order-parameter, leading to the re-entrance of the rhombic and hexagonal FLL phases, and more isotropic FLL interactions. It is further possible that high field depairing may explain the qualitatively similar sequence of FLL structure phase

transitions seen in $TmNi_2B_2C$ (Eskildsen et al., 1998).

4.6 Field enhanced flux line lattice with field parallel to c-axis

In this subsection, we show that the ability to characterise the major part of the FLL structure phase diagram for fields close to H_{c2} stems from a highly anomalous field-dependence of the FLL form factor. Already the study of DeBeer-Schmitt et al. (2006) revealed an unusual behaviour of the form factor for fields up to 2.0 T, and at 50 mK. Here, we extend these low field measurements by measuring $|F(q)|^2$ for fields right up to H_{c2}, and carry out further measurements at higher temperatures. We will see that the field-dependence of the form factor observed in $CeCoIn_5$ behaves in stark contrast to the predictions of phenomenological theory.

4.6.1 Field- and temperature-dependence of the flux line lattice form factor

The calculation of the form factor $|F(q)|$ for an individual Bragg spot was carried out in accordance with the details laid out in Appendix A. For the hexagonal and rhombic structure phases, there are two domains that occupy the sample volume. For measurements of Bragg spots in these two phases, the overall form factor sums the contributions due to each domain according to $|F_{tot}(q)|^2 = |F_{dom1}(q)|^2 + |F_{dom2}(q)|^2$, where, for example, $|F_{dom1}(q)|^2$ is the mean value of $|F(q)|^2$ for all the spots of the domain.

An extra detail that emerges from analysing the form factor of the high field hexagonal phase is the emergence of a small, but clear, anisotropy in the value of $|F(q)|^2$ between the different types of Bragg spot. Figure 4.24 (a) provides a definition of the two inequivalent spot types of this structure. For a certain domain, two of the spots have $\mathbf{q} \parallel$ [110] whilst the $\mathbf{q}$-vectors of the other four spots lie away from these directions. Our analysis reveals that, over the field range, the value of $|F(\mathbf{q} \parallel [110])|^2$ is a factor of 1.20(3) larger than the value of $|F(\mathbf{q}$ off-$[110])|^2$. Figure 4.24 (b) further shows that this anisotropy is essentially field-independent, and measurements at higher temperatures showed this anisotropy to be also temperature-independent. This anisotropy is not what might

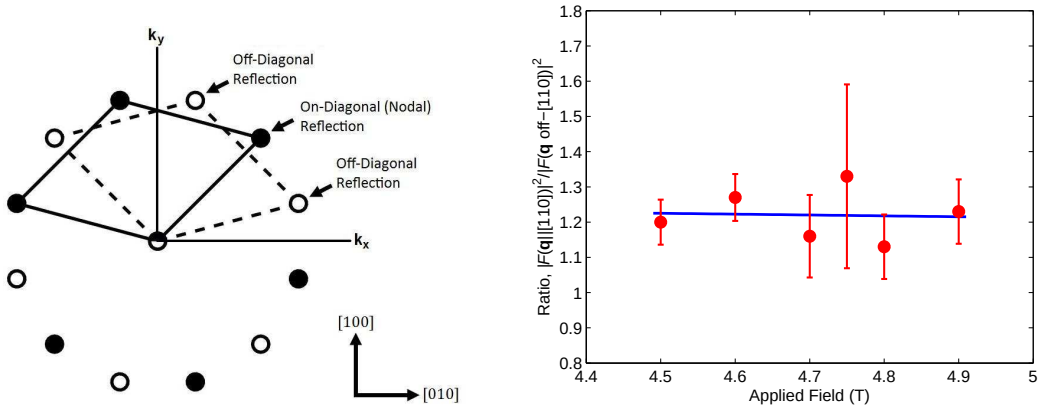

(a) (b)

Figure 4.24: In (a) we show a schematic describing the inequivalent Bragg spots of the upper hexagonal phase. In (b) we plot the field-dependence of the form factor ratio $|F(\mathbf{q} \parallel [110])|^2 / |F(\mathbf{q} \text{ off-}[110])|^2$ between these different spot types. The blue line is a linear fit to the data, showing the anisotropy to be essentially field-independent.

be naively expected for a $d_{x^2-y^2}$ gap function, as the gap is smaller along the $\{110\}$ directions and we would expect a weaker supercurrent response. In the absence of an explanation for such an anisotropy in the literature, we speculate that the weaker field-modulation along the $\{110\}$ directions could be invoked by Fermi surface effects, possibly in the form of a non-local correction. It is also possible an explanation for the anisotropy lies with the different lengths of $\mathbf{q}$-vector of the different types of spot. To account for the anisotropy, the computation of the overall form factor in the upper hexagonal phase is a mean of the contributions for all six spots. In cases where not all spots were measured equally, a weighted mean was formed, which allows for this anisotropy.

The overall field-dependence of the form factor at 50 mK is shown in figure 4.25. Very few new measurements of the form factor were performed at low field, as these measurements had been carried out previously in the study of DeBeer-Schmitt et al. (2006). Correspondingly, it is not possible to ascribe a field-dependence to the low field data beyond that previously reported. Rather, these datapoints can be considered as consistent with the previous work. Instead, we concentrated on higher field measurements, where figure 4.25 shows we observe most unusual behaviour.

On increasing the field above 2 T, the form factor *increases* markedly up to a peak value at high field. On the approach to H_{c2}, the form factor is observed to fall again slightly from this peak value, whereafter it falls sharply to zero on passing through H_{c2}. The latter behaviour is consistent with the experimentally observed (Tayama et al., 2002; Bianchi et al., 2002), and theoretically predicted (Chandrasekhar, 1962; Clogston, 1962), first-order transition between the superconducting and normal states that arises due to Pauli-limiting.

Figure 4.25 also indicates that there is no obvious signature of the sequence of FLL structure transitions in the form factor data, although the apparent peak value of the form factor coincides with the location in field of the upper rhombic to hexagonal transition field. Despite this coincidence, it seems unlikely that the peak in the form factor is correlated to the structure transition. Measurements at higher temperature shown in figure 4.26 indicate that even though the form factor initially rises with field for all temperatures up to 1250 mK, the peak position of the form factor becomes suppressed with field. Simple inspection shows the variation in temperature of both the uppermost phase boundary line and the peak in the form factor to be uncorrelated, exemplified by the fact that there is no upper hexagonal phase at a temperature of 1250 mK. Therefore, we do not associate any direct changes in FLL structure with details in the field-dependence of the form factor.

At low fields, we see that the form factor data shown in figure 4.25 are essentially temperature-independent. The distinction between the form factor behaviour at different temperatures only becomes apparent on moving to higher fields, where the increase of the form factor at high fields is progressively suppressed with temperature. This suppression is further accompanied by a gradual crossover to more conventional behaviour of the transition between the superconducting and normal states. On increasing the temperature up to 500 mK, the sharp fall of the form factor becomes increasingly less severe on moving through H_{c2}. By 750 mK, the form factor falls monotonically to essentially zero at H_{c2}, consistent with expectations from the thermodynamic measurements (Bianchi et al., 2003a). At this temperature, the FLL behaviour has just crossed over into the regime where the

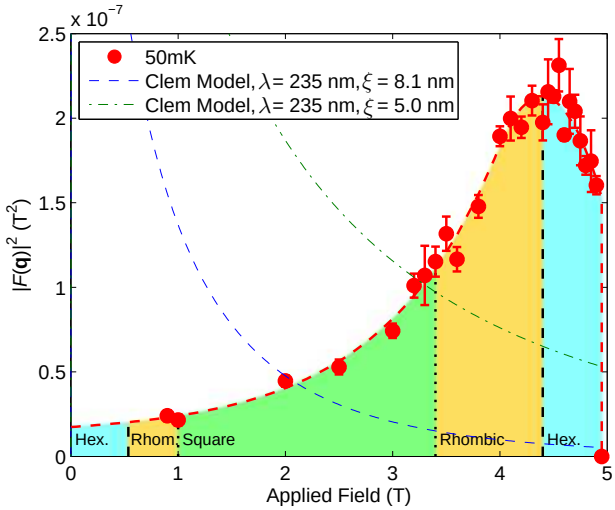

Figure 4.25: The field-dependence of the first-order FLL form factor in $CeCoIn_5$, at 50 mK and for $H \parallel \mathbf{c}$. The red dashed line is a guide to the eye. The blue dashed and green dashed dot lines are representative of the field-dependence of the form factor expected according to the Clem model with reasonable fitting parameters. The shaded portions indicate field regions occupied by the FLL structure as a function of field, with the black dashed and dotted lines respectively representing the first- and second-order FLL structure transition boundaries. The point where the form factor falls to zero represents H_{c2}, and is taken from thermodynamic measurements (Bianchi et al., 2003a).

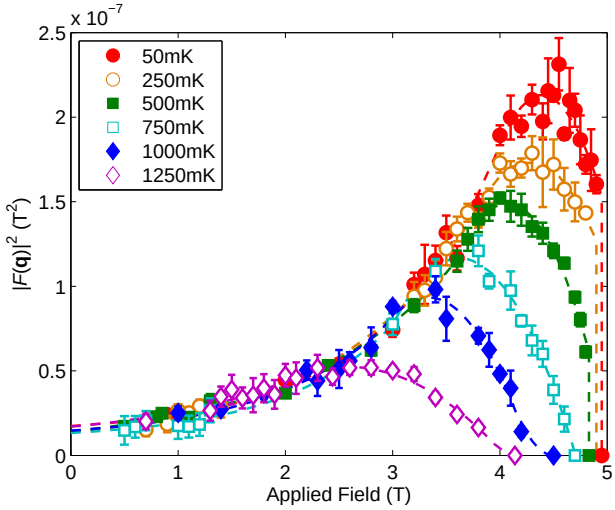

Figure 4.26: The field- and temperature-dependence of the first-order flux line lattice form factor $|F(\mathbf{q})|^2$ over the range of temperatures indicated. The dashed lines are guides to the eye at each temperature. The points where the form factor falls to zero represent H_{c2}, and are taken from thermodynamic measurements (Bianchi et al., 2003a).

superconductivity begins to be dominated by orbital effects, and thus supercedes the Pauli-paramagnetism that gave rise to the first-order transition at H_{c2}. At higher temperatures still, the crossover to a conventional regime is clearer, although the form factor still shows unusual behaviour by initially rising with field. However, the suppression of this rise, and the more gradual fall with field towards zero form factor, suggests increasingly conventional behaviour is recovered at higher temperatures.

In figure 4.27 (a) we present the temperature-dependence of the diffracted intensity obtained in applied field fields of 4.60 T, 4.85 T and 4.90 T. Across all temperatures and fields, the FLL structure is hexagonal and remains essentially constant. Therefore, this allowed the collection of the diffracted intensity at the peak of the rocking curve for a Bragg spot whose **q**-vector is aligned parallel to a $\langle 110 \rangle$ direction. As the rocking curve widths are essentially resolution limited, the resulting measure of the diffracted intensity is proportional to the integrated intensity of a full rocking curve, and hence proportional to the form factor. The temperature-dependent data shown in figure 4.27 reveal that the crossover between the regimes where H_{c2} is first- and second-order is also sensitive to the field. The different behaviour of the results collected at 4.60 T and those at 4.85 T and 4.90 T is clear. On moving through T_{c2}, the intensity of the higher two fields drops in a discontinuous manner, indicating the first-order nature of the transition into the normal state. The data at 4.60 T falls monotonically as a function of temperature, tending parabolically towards zero on passing through T_{c2}. This suggests the superconductivity is orbitally-limited at H_{c2} for the lowest field. However, the intensity scale of figure 4.27 (a) serves as a reminder that the larger diffracted intensity (and hence form factor) is associated with the field of 4.60 T, indicating that the effects of Pauli-limiting are important at all fields.

In figure 4.27 (b) we show the same data as in figure 4.27 (a) but on normalised intensity and temperature scales. The intensity is normalised at each field by extrapolating the intensity data shown in figure 4.27 (a) down to zero temperature. The temperature is normalised to the expected critical temperature $T_{c2}(H)$ as de-

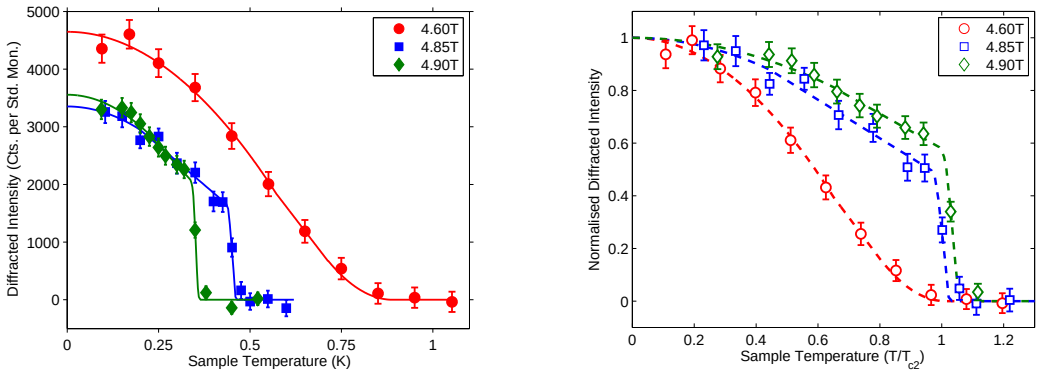

(a) (b)

Figure 4.27: In (a) we show the temperature-dependence of the diffracted intensity at the peak of the rocking curve for a Bragg spot whose **q**-vector lies parallel to $\langle 110 \rangle$. This is performed at fields of 4.60 T, 4.85 T and 4.90 T. The solid lines are guides to the eye. In (b) we show the same data as in (a), but with the intensity normalised to the extrapolated intensity at zero temperature, and the temperature normalised to the critical temperature for the relevant field. The dashed lines are guides to the eye.

duced from thermodynamic measurements (Bianchi et al., 2003a). The graph in figure 4.27 (b) serves to amplify the sharpness of the drop in diffracted intensity on moving into the normal state at the two higher fields. The drop is also seen to sharpen up slightly more at the highest field, as might be expected. We also see that for the two highest fields, the diffracted intensity remains finite at precisely $T/T_c = 1$. This likely indicates the presence of some hysteresis, or slightly different behaviour of the crystals in the mosaic. Such behaviour is unsurprising however, as the temperature-scans at such highest fields are essentially parallel to the H_{c2} phase boundary, and the transition into the normal state is first-order. Although this irreversible behaviour was not characterised experimentally any further, it does not detract from the clearly different nature of the superconducting to normal transition between 4.60 T and the two higher fields investigated.

4.6.2 Discussion of field-enhancement of the flux line lattice form factor

Although the previous study of DeBeer-Schmitt et al. (2006) indicated that the field-dependence of the form factor was anomalous at low fields, our new measurements

for fields up to H_{c2}, and temperatures up to $T_c/2$ show this departure to be more spectacular than might have been expected from the previous measurements. In figure 4.25 we show this explicitly, where we include the predicted field-dependence of the form factor according to the Clem model (equation 1.43). For the two curves shown, we use the values for λ and ξ as used by DeBeer-Schmitt et al. (2006); for both curves a mean literature value of $\lambda = 235$ nm is used, and estimates of ξ in each case are based on H_{c2}^{Orb} so that $\xi = 5.0$ nm and H_{c2}^{P} so that $\xi = 8.1$ nm. Clearly the Ginzburg-Landau model provides a poor description of the data, as for all fields the FLL form factor is predicted to *fall* monotonically with field.

The previous approach of DeBeer-Schmitt et al. (2006) was to generalise the Clem model by ascribing a field-dependence to the core-size length scale ξ_{GL}. We saw in section 4.2, that the field-independence of the form factor for fields up to 2.0 T could be explained by a field-induced reduction of ξ. For sake of comparison, we re-apply the approach here, and extend it up to H_{c2}, even though the approximation provided by the Clem model will be rigorously inadequate. We would also expect λ to be field-dependent across the field range, however, without the knowledge of what this field-dependence might be, we hold λ constant at 235 nm. Therefore, using a constant λ, we adjust the value of ξ so the form factor predicted by the Clem model matches that observed experimentally.

Figure 4.28 (a) shows the resulting field-dependence of ξ at 50 mK on application of the generalised Clem model. The data indicate that for a core-contraction to explain the field enhancement of the form factor, the core-size must contract by a factor of ~ 6 between the fields of 1.0 T and $\sim$ 4.4 T, the approximate field at which the core-size is a minimum. For higher fields than this, the core-size expands slightly, which it must do in order to reproduce the form factor fall just below H_{c2}. In figure 4.28 (b) we plot the extracted value of ξ versus the FLL parameter a, which itself is extracted from the **q**-vector. For the data in this figure, the bulk of the data is reasonably well represented by the indicated linear fit. This linear fit only extends up to the field of maximum form factor. For the data at higher fields (and smaller FLL parameter), the core-size expands slightly, thus deviating

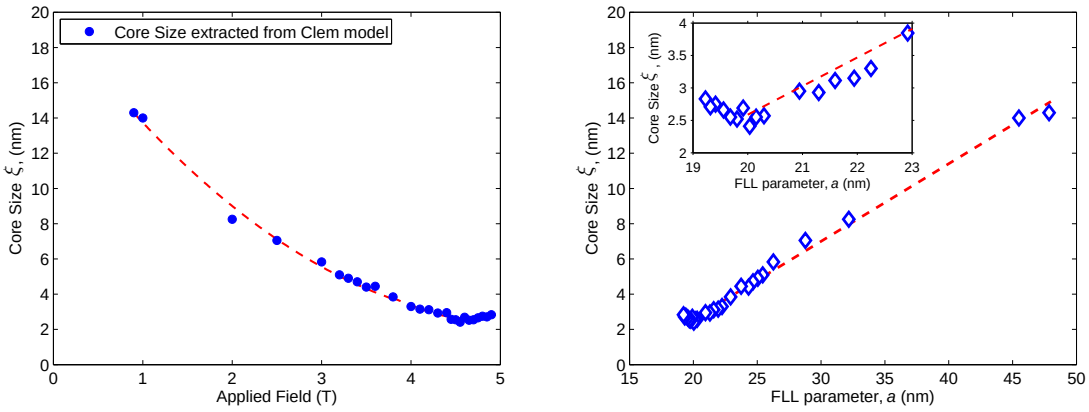

(a) (b)

Figure 4.28: In (a) we examine the field-dependence of the core-size parameter ξ. The value for ξ is found from the Clem model, and is the Ginzburg-Landau coherence length. The red dashed line is a guide to the eye. In (b) we subsequently plot the variation of ξ versus the lattice parameter, which is found from **q**. The bulk of the data are well represented by the linear fit indicated by the red dashed line. This fit is not extended through the entire dataset, as the inset shows that for the data at smallest lattice parameters, ξ increases for decreasing lattice parameter. The linear fit extends up the value of a which corresponds to the peak in the form factor.

from this linear tendency. The core-expansion is shown more clearly in the inset of figure 4.28 (b).

In the previous study of DeBeer-Schmitt et al. (2006), the ξ versus a data were well fitted linearly with a gradient $\mathrm{d}\xi/\mathrm{d}a = 0.55(2)/\sqrt{2\pi}$. The corresponding gradient of the red dashed line shown in figure 4.28 (b) is twice as large at $1.10(4)/\sqrt{2\pi}$. The size of this gradient is in strong disagreement with the predictions of Kogan and Zhelezina (2005). Their model is used to predict the expected contraction of the core-size at low temperature and in the clean limit. The core is predicted to contract with field, but by a factor of $\sim$ 50 % across the field range from 0.2 H/H_{c2} up to H_{c2}. The resulting gradient $\mathrm{d}\xi/\mathrm{d}a$ is expected to have a value in the range between 0.2 - $0.4/\sqrt{2\pi}$, and is therefore too shallow to describe our data. This essentially means that the flux line cores do not contract fast enough with increasing field to explain the form factor increase. Expressed another way, within the theory the ratio ξ/a always *increases* as a function of field over the entire field range. For

core-contraction alone to explain the observed enhancement of the form factor, ξ/a has to *fall* as function of increasing field. Similar conclusions are drawn from the numerical calculations of Ichioka et al. (1999). In these calculations at $T = 0.5T_c$, the flux line cores are also predicted to contract with increasing field, but by only ~ 50 % across the entire field range. If we consider the BCS coherence length, $\xi_{BCS} = \hbar v_F/\pi\Delta_0$, on ascribing a field-dependence to ξ_{BCS}, then either v_F decreases with field, or Δ_0 increases. The former is unlikely; a reduced v_F corresponds to an increase in the effective mass, and thus also in λ. Similarly, an enhancement of Δ_0 is also unlikely, as this would need to be rather large to explain our results. Therefore, based on the available literature, and simple arguments, it seems very unlikely that flux line core contraction alone can explain the observed increase of the form factor.

A more likely explanation for the increase of the form factor is found within the quasiclassical Eilenberger theory with the inclusion of the paramagnetic effect (Ichioka and Machida, 2007). In figure 4.13 (a) we see the predictions for the field-dependence of the form factor for various strengths of paramagnetic effect. An increased strength of the effect is denoted by a larger value of μ. We firstly note from figure 4.13 (a) that when the paramagnetic effect is strong enough, the form factor remains finite on reaching H_{c2}. As this is qualitatively similar our observations at low temperature, this immediately suggests that field-induced core paramagnetism is likely to play a role in the mixed state in CeCoIn$_5$.

Based on the previous measurements up to 2.0 T (DeBeer-Schmitt et al., 2006), Ichioka and Machida (2007) indicate that the most appropriate value of the theoretical parameter μ which describes the form factor data is 1.7 (see figure 4.13 (a)). However, according to the predictions made using the theory, this value of μ is not large enough to cause the increase in the form factor that we observe experimentally. We also note that according to these calculations, the flux line cores are not predicted to contract at any field (Ichioka and Machida, 2009). Instead, the increase in the form factor is generated by a larger paramagnetic effect, when $\mu = 2.6$. Hence, it is important to consider the most appropriate value of μ which

may describe our data. We now show the relationship between the parameter μ, and the Maki parameter α_M, the latter of which is related to the material properties of $CeCoIn_5$. To do so, we note that within the literature, there are at least three ways of describing the strength of the Pauli paramagnetic effect; the Maki parameter introduced in section 1.6, α_{para} introduced by Adachi et al. (2005),

$$\alpha_{para} = \frac{\mu_B H_{c2}^{Orb}}{2\pi k_B T_c} \tag{4.6}$$

and the paramagnetism parameter μ which is introduced within the Eilenberger theory (Ichioka and Machida, 2007),

$$\mu = \frac{\mu_B B_0}{\pi k_B T_c} \tag{4.7}$$

where B_0 is a scaling parameter related to B_{c2}, and refers to the field-scale used by Ichioka and Machida (2007). The parameter H_{c2}^{Orb} of equation 4.6 is equal to 0.561 of the Eilenberger unit B_0 shown in equation 4.7. If we divide α_{para} by μ, we obtain

$$\frac{\alpha_{para}}{\mu} = \frac{H_{c2}^{Orb}}{2B_0} \sim 0.28. \tag{4.8}$$

By substitution of equation 1.61 into equation 4.6 and re-arranging, we find $\alpha_M \sim 7.12\ \alpha_{para}$, and therefore using this result in combination with equation 4.8 we obtain

$$\mu = \frac{\alpha_M}{1.99}. \tag{4.9}$$

Therefore, we see that μ is sensitive to the values of the Pauli- and orbitally-limited upper critical fields. Within the literature, estimates for the latter are somewhat variable, such that μ could vary between a range of values. The previously suggested value for μ of 1.7 implies that $H_{c2}^{Orb} \sim$11.8 T. This estimate for H_{c2}^{Orb} differs from, for example, the estimate of Tayama et al. (2002) of $\sim$ 15 T, which yields a value for μ of 2.15. Therefore, it seems reasonable to suggest that, based on the available estimates of H_{c2}^{Orb}, μ may actually be larger than the value of 1.7 previously used to describe the observations of DeBeer-Schmitt et al. (2006). A larger value of μ fits in with the requirement of the quasiclassical theory to cause the increase in the form factor that we observe experimentally. However, even within

the range of acceptable μ values, the form factor is not predicted to increase by the amount shown in figure 4.25. Hence, whilst there is a qualitative agreement between our low temperature form factor data and the predictions of Ichioka and Machida (2007), even for a realistic range of μ values, a quantitative agreement is lacking.

We now consider possible reasons for this discrepancy. A possible physical effect not accounted for within the theory of Ichioka and Machida (2007) is the non-Fermi liquid behaviour associated with the QCP located near H_{c2}. The theory inherently assumes Fermi liquid behaviour, but anomalous behaviour in the fermionic properties could exert an influence on the FLL. The onset of non-Fermi liquid behaviour within the mixed state is indicated by a divergence of m^* on the approach to H_{c2} (Settai et al., 2001; Bianchi et al., 2003b). A divergent heavy-fermion mass might be expected to lead to an enhancement of the paramagnetism parameter μ (by crudely considering $\mu \propto B_{c2}^{Orb}$, where $B_{c2}^{Orb} \propto (m^*)^2$). However, we might then expect the core-size to contract. Both of these effects would be expected to maintain, or increase the form factor at higher fields. These arguments are speculative, and not supported theoretically. However, if a divergent heavy-fermion mass is a contributory factor to the increase of the form factor, then a certain degree of generalisation of the theory of Ichioka and Machida (2007) is required. Based on the arguments above, a divergent m^* would cause the parameter μ to be field-dependent, leading it to increase on the approach to H_{c2}.

Ichioka and Machida (2009) have recently investigated modifications to their calculations presented in Ichioka and Machida (2007), in order to address the discrepancy between the theory and experiment. They re-calculated the expected field-dependence of the form factor as a function of parameter μ, but considered an isotropic and three-dimensional Fermi surface instead of a purely two-dimensional Fermi surface. The results of the calculations are shown in figure 4.29.

We see that for progressively larger values of μ, the qualitative form of the field-dependence of the form factor approaches that of our experimental observations. This is particularly the case for μ =5, where the size of the fall of the form factor

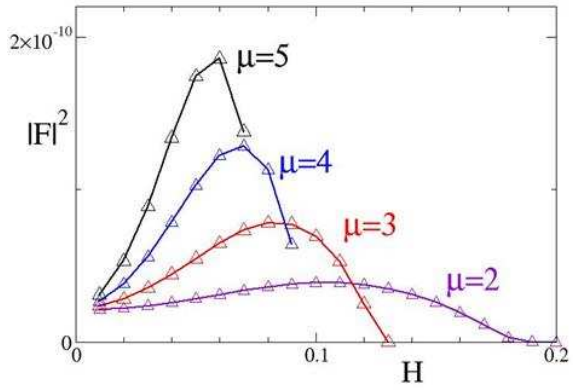

Figure 4.29: The calculated predictions of the field-dependence of the first-order form factor for increasingly large values of μ. The Fermi surface is three dimensional and isotropic, the order-parameter is $d_{x^2-y^2}$, κ =89, $T = 0.2T_c$ and the FLL structure is hexagonal. After Ichioka and Machida (2009).

close to H_{c2} is in better agreement with our experimental data, over the somewhat larger high field fall predicted for when $\mu = 2.6$ figure 4.13 (a). Therefore, it seems necessary to introduce a certain amount of three-dimensionality to the Fermi surface in these calculations, even though the Fermi surface of $CeCoIn_5$ is known to be quasi two-dimensional. This is indicated more clearly in figure 4.30 (a), which show calculations of the predicted field-dependence of the form factor at $\mu = 5$. The figure indicates the calculations for the three-dimensional Fermi surface to be closer to the experimental observations than for the two-dimensional Fermi surface. Indeed, for such a high μ in the two-dimensional case, the slight fall of the form factor just below H_{c2} is not reproduced.

Figure 4.30 (b) provides further support for a larger μ value and three-dimensional Fermi surface, by calculating the field-dependence of the form factor under such conditions, but at higher temperatures. The qualitative agreement with the experimental data is good; even at 0.5 T_c the form factor initially rises due to the Pauli paramagnetism before being suppressed at higher fields, consistent with our observations. We also see the field at which the form factor peaks is also suppressed with increasing temperature, and that the form factor exhibits increasingly conventional behaviour by falling monotonically to zero on the approach to H_{c2}.

Whilst it seems plausible that a more three-dimensional Fermi surface needs to

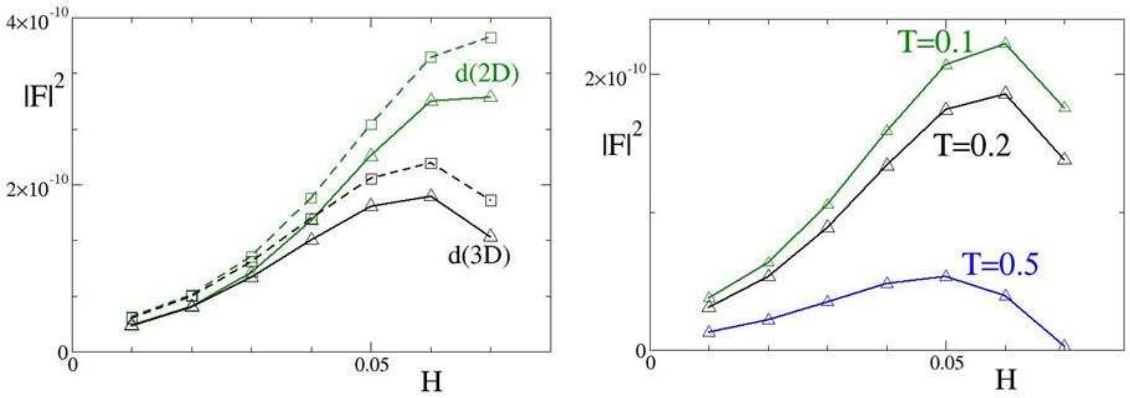

(a) (b)

Figure 4.30: The predicted field-dependence of the first-order FLL form factor for μ =5, a $d_{x^2-y^2}$ order parameter, and κ =89 for (a) both three- and two-dimensional Fermi surfaces at $T = 0.2T_c$, and (b) for a three-dimensional Fermi surface, and also as a function of temperature. For both figures, triangle symbols indicate the FLL structure to be hexagonal, and square symbols indicate the FLL to be square. After Ichioka and Machida (2009).

be included within the calculations, we should consider what would physically allow the value of μ to take on larger values. We showed earlier that μ is essentially determined by the experimentally determined value of H_{c2}^{P}, and an *estimated* value of H_{c2}^{Orb}. As H_{c2}^{Orb} is only estimated from the gradient $\mathrm{d}H_{c2}/\mathrm{d}T|_{T=T_c}$, we suggest that the value of H_{c2}^{Orb} deduced from measurements close to T_c might not accurately reflect the value of H_{c2}^{Orb} at much lower temperatures. If non-Fermi liquid behaviour is important at low temperatures and high field *within* the mixed state, the usual method of finding H_{c2}^{Orb} from the gradient $\mathrm{d}H_{c2}/\mathrm{d}T|_{T=T_c}$ may not be valid. A divergent heavy-fermion mass could enhance H_{c2}^{Orb} beyond a value previously anticipated, essentially amounting to allow μ to be field-dependent such that it increases on approaching H_{c2}. Experimentally, heat capacity measurements observe a field-dependence to the low energy density of normal states (Ikeda et al., 2001) such that it increases on the approach to H_{c2}, in support for the necessity of allowing μ to be field-dependent.

4.6.3 Fall of the flux line lattice form factor just below H_{c2}

Previously, we introduced the field- and temperature-dependence of the FLL form factor for $H \parallel \mathbf{c}$. For all temperatures, and for fields below H_{c2}, the magnitude of the form factor is suppressed from a peak value on moving to the highest fields. It remains of interest to address the physical origin of the fall of the form factor from the peak value.

Initially, it was suggested in Bianchi et al. (2008) that at 50 mK, the fall might reflect the onset of an FFLO-type state, where theory predicts the flux lines to adopt a modulated topology (Tachiki et al., 1996; Mizushima et al., 2005; Ichioka et al., 2007). In this scenario, the form factor of the FLL Bragg peak is expected to be lower due to the reduced field contrast at the nodal points of the flux lines. A simple argument in favour of this would be to expect the temperature-dependence of the field at which the form factor peaks to be correlated with that of the FFLO phase boundary. In figure 4.31 we plot this temperature-dependence, and clearly see no correlation with any major feature within the superconducting phase diagram. Although we cannot rule out a contribution to the fall of the form factor at low temperatures, it seems unlikely that a the onset of an FFLO, or Q-phase, is the dominant physical mechanism behind the high field fall of the form factor.

The calculations of Ichioka and Machida (2009) within the quasiclassical Eilenberger are able reproduce the high field fall of the form factor, apparently in the absence of an FFLO state. We therefore look more closely at the theory in order to identify the physical mechanism behind the fall. For large μ values, and a two-dimensional Fermi surface, the authors are able to identify the contributions to the overall internal magnetisation. These components are the usual diamagnetic contribution associated with the screening currents, and the field-induced core magnetisation. Whilst the neutron is sensitive to the net magnetisation, the theoretical work is able to identify the contribution due to each. Figure 4.32 shows that the diamagnetic contribution to the overall field contrast falls away with increasing field in the manner expected for conventional materials. However, the field-dependence

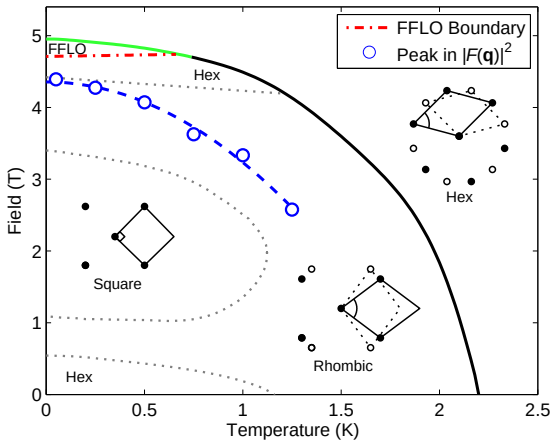

Figure 4.31: FLL structure phase diagram for $CeCoIn_5$ with $H \parallel \mathbf{c}$. Phase boundaries separating regions of different FLL structure are shown by gray dotted lines. The inset diagrams show the three FLL configurations, where a [100] direction is vertical, and first-order Bragg spots belonging to different FLL domains are denoted by open and filled circles respectively. The green and black solid lines show where the superconducting to normal state transition is first- and second-order respectively. The open blue circles show the temperature evolution of the maximum of the form factor ($|F(\mathbf{q})|^2$), with the blue dashed line being a guide to the eye. The error bars of the data points are comparable in size to the data symbol. The area enclosed by the green solid and red dash-dot lines provide an estimate of the region occupied by the FFLO phase, as deduced from other studies (Bianchi et al., 2003a; Kumagai et al., 2006).

of the core magnetisation rises markedly with field, and is the dominant component of the overall magnetisation at high fields. However, even at the highest fields, this component begins to fall, and it seems that the fall in the form factor is correlated to this reduction in core magnetisation. Therefore, it is clearly of interest to look in more detail at the field evolution of the spatial distribution of the field-induced core magnetisation. In figure 4.33 (a), we show calculated spatial structure of the core magnetisation $M(\mathbf{r})$ as function of the applied field. At low fields, the spatial extent of the core magnetisation is unimportant. However, at higher fields, and particularly close to the upper critical field, the spatial distribution becomes significantly broader. This means that the paramagnetic flux line cores are predicted to expand, and at the highest fields they start to overlap. Figure 4.33 (b) also shows the spatial increase of core magnetisation is also reflected by an increase in the spatial extent

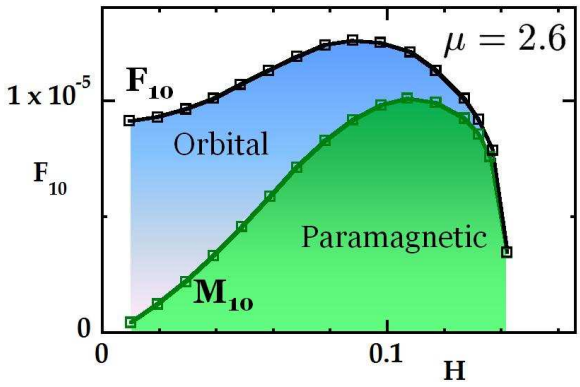

Figure 4.32: The field-dependence of the form factor for $\mu = 2.6$, $T = 0.1T_c$, $\kappa = 89$, a square FLL structure and a two-dimensional Fermi surface. The coloured regions indicate the relative contribution to the overall internal magnetisation arising due to the field-induced flux line core paramagnetism (green) and the orbital contribution that arises due to the screening currents (blue). After Ichioka and Machida (2009).

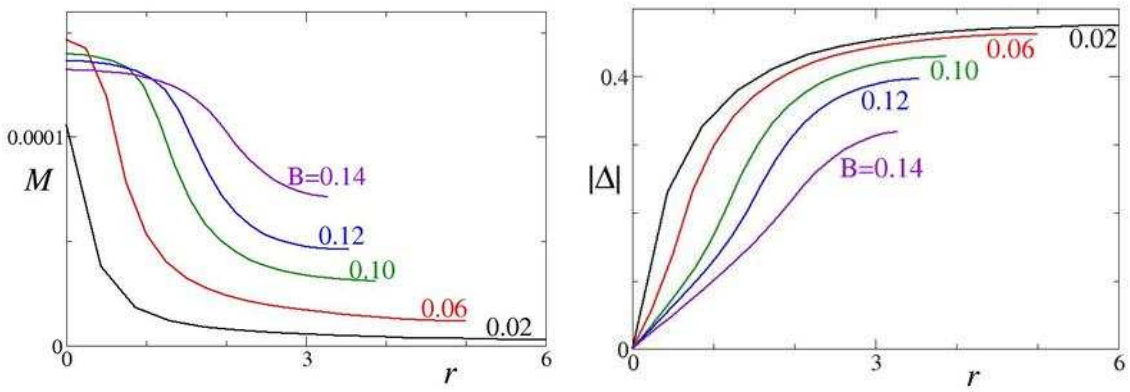

(a) (b)

Figure 4.33: Numerical calculations of the field-dependence of the spatial distributions of (a) the core-induced paramagnetic moment $M(\mathbf{r})$, and (b) the amplitude of the pair potential $|\Delta(\mathbf{r})|$. For both figures, r is the distance away from the flux line core in the direction of the nearest neighbour flux line of a square FLL. Where the line stops corresponds to half the distance between nearest neighbours. The calculations consider the case where $\mu = 2.6$, $T = 0.1T_c$, $\kappa = 89$, and the Fermi surface is two-dimensional. Figures after Ichioka and Machida (2009).

of $|\Delta(\mathbf{r})|$. Noticeably, $|\Delta(\mathbf{r})|$ is also more strongly suppressed at higher fields, which indicates the importance of paramagnetic depairing within the cores. Overall, these effects at the highest fields are due to an expanding of the flux line cores, and the reduction in the FLL form factor close to H_{c2} is due to a reduced spatial confinement of the field induced core magnetisation.

Measurements of higher-order Bragg spots

To provide experimental evidence for such a core expansion, we carried out systematic measurements of the field-dependence of the $\{1,1\}$ form factors at ~ 60 mK. It is suspected that the influence of a high field core expansion will manifest more strongly in the higher-order spots. To understand this proposal, consider the simple phenomenological model of Yaouanc et al. (1997). This model directly relates the form factor to a measure of the core-size via the insertion of a core-correction term, such as $\exp(-\mathbf{q}\rho_c)$ or $\exp(-(\mathbf{q}\rho_c)^2)$, into the numerator of the simple London model (see Appendix D). Here $\mathbf{q}$ is the $\mathbf{q}$-vector, and ρ_c denotes the measure of the core-size (often denoted as ξ). Any constants in the exponential have been absorbed into ρ_c. This is perhaps the simplest model where the measured form factor can be written as $F(\mathbf{q}) \sim \exp(-\mathbf{q}\rho_c)$. According to this simple model, we can plot $\ln F$ versus $\mathbf{q}$, and we see that $\mathrm{d}(\ln F)/\mathrm{d}\mathbf{q}$ will be linear with a gradient of magnitude ρ_c. By carrying out such an analysis over a range of fields, we obtain a field-dependence of the measure of the core-size. Although such a simple model will likely be inaccurate, our discussion highlights the principle that we expect the rate at which the form factor falls with $\mathbf{q}$ to be dependent on the core-size.

A systematic set of measurements were carried out, whereby the first-order form factor was recorded in the same manner as previously, but whereby we also measured as many types of $\{1,1\}$ spots as possible. In order to understand our analysis, in figure 4.34 we show schematic diagrams of the three different FLL structure types. In the figure, we indicate the $\{1,0\}$ and $\{1,1\}$ Bragg spots for each structure type, and also the different types of $\mathbf{q}$-vector. We only carried out measurements at fields corresponding to the upper three phases of the structure phase diagram, and

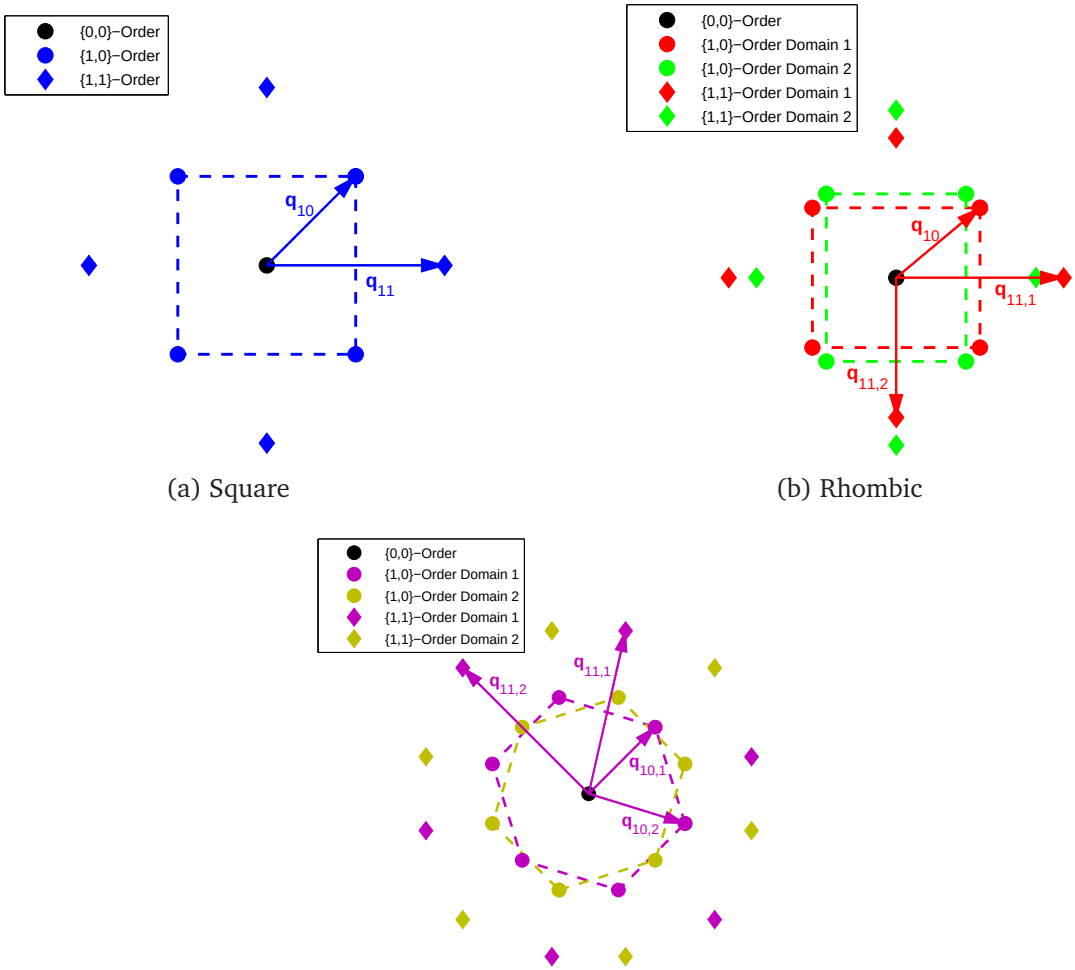

(a) Square

(b) Rhombic

(c) Hexagonal

Figure 4.34: Schematic diagrams indicating the positions in reciprocal space of the $\{1,1\}$ Bragg spots with respect to the $\{1,0\}$ Bragg spots, for (a) the square FLL structure, (b) the rhombic FLL structure, and (c) the hexagonal FLL structure. In each case, the dashed lines indicate the FLL structure deduced from the first-order spots, and the arrows indicate the types of **q**-vector for both the $\{1,0\}$ and the $\{1,1\}$ Bragg spots for a single domain. For clarity, in (b) and (c) we only present **q**-vectors for a single domain of the two that are present.

have not yet observed $\{2,0\}$ Bragg spots at any field.

Analysing the $\{1,1\}$ Bragg spots of a square structure is simple, and is carried out in the same way as for the $\{1,0\}$ spots. In the rhombic phase, within a single domain there are two types of $\{1,1\}$ spot with noticeably different **q**-vectors. For each domain, we obtain the $\left|F\left(\mathbf{q}_{11,1}\right)\right|^2$ and $\left|F\left(\mathbf{q}_{11,2}\right)\right|^2$ form factors by respectively taking the mean of the form factors for the $\mathbf{q}_{11,1}$ and $\mathbf{q}_{11,2}$ spots. We then sum the contributions from the two domains to obtain the overall $\{1,1\}$ form factor for each type of **q**-vector. For example, for the $\mathbf{q}_{11,1}$ type of spot, the overall form factor is found using $\left|F_{tot}\left(\mathbf{q}_{11,1}\right)\right|^2 = \left|F_{dom1}\left(\mathbf{q}_{11,1}\right)\right|^2 + \left|F_{dom2}\left(\mathbf{q}_{11,1}\right)\right|^2$.

Within the upper hexagonal phase, the situation is more complicated because for each domain there are strictly two different types of **q**-vectors for both the $\{1,0\}$ and $\{1,1\}$ spots (see figure 4.34 (c)) and unfortunately, until now, it has not been possible to measure the form factors of all the different spot types, at all fields. At no fields at all did we observe the form factor for the spots of type $\mathbf{q}_{11,2}$, and at most fields in this phase, only spots of type $\mathbf{q}_{10,2}$ and $\mathbf{q}_{11,1}$ were measured. The signal associated with the spots of type $\mathbf{q}_{11,1}$ was extremely weak, which meant we were only able to obtain a measure of the form factor by counting at the Bragg angle. The inability to measure full rocking-curves introduces a larger degree of uncertainty into our results. To present the **q**-dependence of the form factor for each spot type, we follow the approach adopted in the rhombic phase. That is, within each domain, we find the mean form factor value for the spot type, and then sum the contributions for that spot type from the two domains.

In figure 4.35 (a) we show form factor versus **q** over the investigated field range. We have normalised *all* the form factors such that the $\{1,0\}$ form factors shown in figure 4.35 (a) fall on the guide to the eye shown in figure 4.25. To find the best description of the data at each field, we can only consider the data at fields within the rhombic phase, as here there are more than two datapoints. After careful consideration, we find a simple linear fit on the linear-linear scale provides a better description of the data than an exponential form. Subsequently, at all other fields with just two datapoints, we apply a linear fit. In figure 4.35 (b), we show the

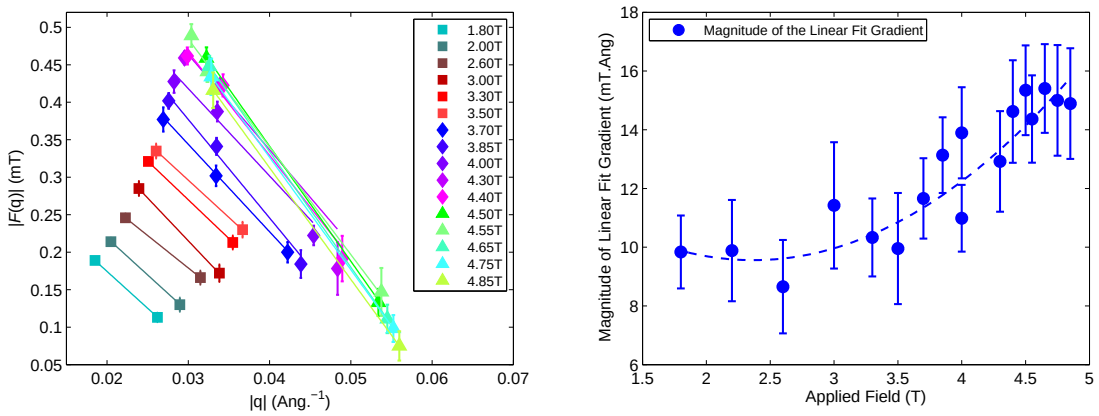

(a) (b)

Figure 4.35: In (a) we show all the form factors obtained at various fields and at ~ 60 mK, and plot them versus **q** on a linear scale. At all fields, when appropriate we fit the data linearly. Otherwise we apply the linear fit. Square symbols, diamond symbols and triangle symbols indicate data taken in the square, rhombic and hexagonal structure phases respectively. In (b) we show the field-dependence of the magnitude of the gradient of the linear relation that was fitted/applied to the data shown in (a).

field-dependence of the *magnitude* of the linear gradient $|\mathrm{d}F/\mathrm{d}\mathbf{q}|$, as obtained from the data shown in figure 4.35 (a). We see that the magnitude of the slope becomes progressively steeper on the approach to H_{c2}. However, this gradient has units of [Field][Length], and cannot be taken as a measure of the core-size. However, now we reach the problem of the next step in the analysis, as it is unclear how to manipulate the data in order to extract a measure of the core-size.

The quasiclassical Eilenberger theory can be used to directly calculate the expected form factors for both the $\{1,0\}$ and $\{1,1\}$ spot types. We then compare the predicted form factors for the $\{1,0\}$ and $\{1,1\}$ Bragg spots in the presence of the core expansion at high fields, and see how the resulting **q**-dependence of the form factor compares to the experimental data. At the time of writing, the first calculations have recently been carried out by M. Ichioka of Okayama University, Japan. Under the conditions of $T = 0.1T_c$, $\kappa = 89$ and for the case of $\mu = 2.6$, he calculates the $\{1,0\}$ and $\{1,1\}$ form factors for a square structure at all fields. The results of the calculations lie in stark contrast to our experimental data, with $|\mathrm{d}F/\mathrm{d}\mathbf{q}|$ *falling*

monotonically with field. However, the calculations neglect the experimentally observed changes in FLL structure, which may contribute to change in the behaviour of $|\mathrm{d}F/\mathrm{d}\mathbf{q}|$ with field. In spite of this however, the initial calculations do not look so promising.

In order to be able to treat our data more quantitatively, an alternative approach might be to find a form of phenomenological model for the form factor that provides the best approximation to the numerical calculations. Such a model would allow us to extract a core-size length-scale from our data, whilst maintaining consistency with the microscopic calculations. The simplest models that are easiest to use are those of Yaouanc et al. (1997) introduced earlier, where the core-size is contained within an exponential term with an argument dependent on the product of $\mathbf{q}$ and ρ_c. At the time of writing, Ichioka and Machida (2009) have recently investigated the quality of the approximation to the quasiclassical theory on using the exponential terms proposed by Yaouanc et al. (1997). Unsurprisingly, the quality of the approximation is sensitive to the form of the term used, and other parameters such as the temperature. Therefore, it remains unclear which model is the more appropriate. Indeed, these exponential relationships are not obviously compatible with our data, where we find that the form factor and $\mathbf{q}$ enjoy a *linear* relationship on a linear-linear scale. However, we cannot rule out that a more complicated phenomenological term could describe our data. Finding the best form of phenomenological expression involves making quantitative comparisons between the predictions based on using the phenomenological model and the quasiclassical calculations for constant parameters. The form of any cut-off *must* depend on $\mathbf{q}$ and ξ, though a knowledge of precisely *how* the form factor will depend on both parameters, should allow us to determine whether or not we observe a core expansion at high fields.

4.7 Measurements with field in the basal plane

Here, we outline the main observations of our SANS studies with field in the plane. Only a limited number of experiments have been carried out for this field geometry during the time of this thesis, leaving the physical picture incomplete and the focus of future experimental work. However, here we introduce the main observations, and draw comparison with the rather more detailed studies carried out for $H \parallel \mathbf{c}$.

4.7.1 Flux line lattice structure with field in the plane

Field parallel to the a-axis, $H \parallel \mathbf{a}$

With $H \parallel \mathbf{a}$, and at $\sim$ 70 mK [16], the FLL structure type remains constant over the entire investigated range in field between 2.0 T and 10.9 T. Figure 4.36 shows an example of this FLL structure, in a diffraction pattern obtained in an applied field of 8.0 T, but at $\sim$ 85 mK. The diffraction pattern shows the FLL structure to be composed of a distorted single hexagonal domain aligned with the atomic lattice. The hexagonal structure is strongly elongated along the $\mathbf{c}^*$ direction, and this is indicative of the underlying crystal anisotropy. The Bragg spots whose $\mathbf{q}$-vectors lie parallel to $\mathbf{c}^*$ are extremely weak and barely visible in the figure. The simple explanation for this can be derived from equation 2.20, where the diffracted intensity for Bragg spots at larger $\mathbf{q}$ is lower.

Although the structure type remains constant for this field geometry, there appears to be a slight field-dependence to the precise shape of the hexagonal structure. In figure 4.37 we show the field-dependence of the anisotropy parameter η at $\sim$ 70 mK, where η is deduced from the primitive cell angle ϕ indicated in figure 4.36 [17]. Within anisotropic London theory, η is equivalent to the penetration depth anisotropy. Although this simple relation is likely invalid for the measurements reported here, the characterisation of the distortion is at least reflecting the Fermi surface anisotropy. Interestingly, it appears that on moving from low to

[16] For these experiments with field in the plane, the base temperature provided by the DR was slightly higher than for $H \parallel \mathbf{c}$.

[17] The method for extracting η from the primitive cell angle is described in Appendix C.

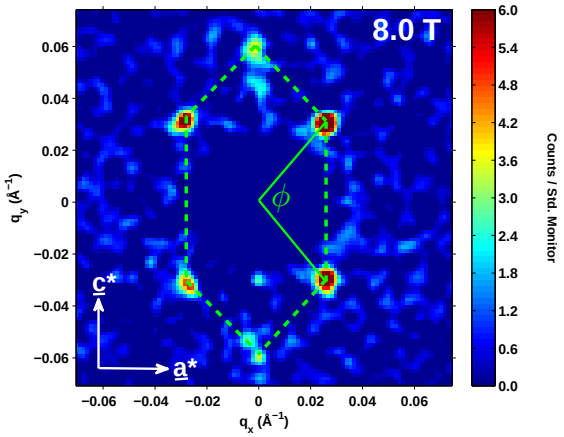

Figure 4.36: The FLL diffraction pattern obtained in $CeCoIn_5$ for $H \parallel \mathbf{a}$, at a field of 8.0 T and temperature of 85 mK. The dashed green hexagon indicates the overall FLL structure, which characteristic angle ϕ.

higher fields, the FLL structure becomes slightly more isotropic. However, on moving toward the highest fields, in particular, on crossing the possible FFLO/Q-phase boundary line, the structure becomes more distorted again. This excludes the point at the highest investigated field of 10.9 T, which does not agree with the general trend.

Further possible evidence for anomalous behaviour at high field is provided by the details of the FLL quality. Figure 4.38 (a) shows the field-dependence of the FWHM of the Gaussian lineshape that is fitted to the rocking curves of the Bragg spots. We cannot deduce much from the field-dependence of the rocking-curve width for spots with $\mathbf{q} \parallel \mathbf{c}^*$. However, the rocking-curves widths for the off-axis spots lie close to the instrumental resolution until the highest fields, whereafter the FWHM noticeably broadens on the approach to H_{c2}. This is in contrast to the case for $H \parallel \mathbf{c}$, where the rocking curve FWHM remained close to the instrument resolution across the entire field range. Figure 4.38 (b) shows the field-dependence of the Bragg spot azimuthal FWHM spread. Interestingly, the field-dependence of the azimuthal spread indicates worsening orientational order as a function of increasing field, again with the quality deteriorating more rapidly at the highest fields.

Although $CeCoIn_5$ is a superclean material, we cannot rule out that the deteri-

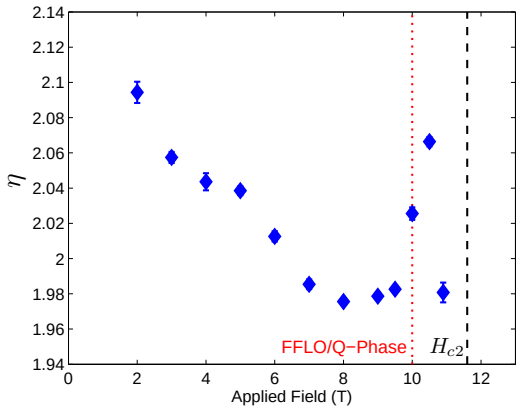

Figure 4.37: The field-dependence of the anisotropy parameter η for the distorted hexagonal FLL structure with $H \parallel \mathbf{a}$, and a temperature of $\sim$70 mK. The black dashed line represents H_{c2}, and the red dotted line the estimated location of the FFLO/Q-phase boundary. Both of these boundaries are deduced from the study of Bianchi et al. (2003a).

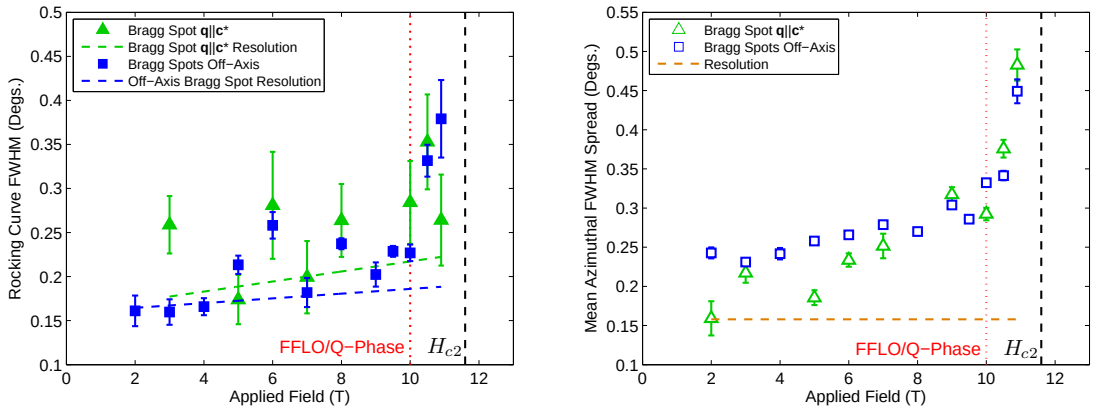

(a) (b)

Figure 4.38: Investigations of the field-dependence of the FLL quality in $CeCoIn_5$ for $H \parallel \mathbf{a}$. In (a) we show field-dependence the Bragg spot gaussian FWHM of the rocking curve for the Bragg spots with $\mathbf{q} \parallel \mathbf{c}^*$ (filled green triangles) and the off-axis Bragg spots (filled blue squares). The estimated resolution for these two types of Bragg spot are indicated by the green and blue dashed lines respectively. In (b) we show the field-dependence of the the Bragg spot azimuthal FWHM, with the Bragg spots with $\mathbf{q} \parallel \mathbf{c}^*$ indicated by open green triangles, and the off-axis Bragg spots indicated by the open blue squares. The estimated resolution indicated by the orange dashed line is common for both spot types. In both figures, the black dashed line represents H_{c2}, and the red dotted line the estimated location of the FFLO/Q-phase boundary. Both boundaries are deduced from Bianchi et al. (2003a).

oration in the FLL quality is due to pinning of the FLL to crystal imperfections and inhomogeneities. It is interesting that the field at which the rate of FLL deterioration increases is approximately correlated with the proposed onset of the FFLO, or Q-phase, state. This may be coincident, but an enthusiastic interpretation would be to associate the deterioration in FLL quality with the onset of such a state. In the FFLO scenario for example, the order parameter is suppressed in the planes at the point where Δ changes sign. These planes might provide an unexpected source of flux line pinning which gives rise to the reduction in the order of the FLL.

However, an important test yet to be made for the $H \parallel \mathbf{a}$ geometry is whether the FLL order is sensitive to field oscillations, as was the case for $YBa_2Cu_3O_7$ at low fields in the last chapter. For all measurements carried out for $H \parallel \mathbf{a}$, no field oscillations were applied. Investigating the effect of field oscillations on the FLL quality might reveal whether pinning does play a role at unexpectedly high field. Furthermore, measurements at higher temperatures than $\sim$70 mK have not been carried out for in this field geometry, so it remains unknown how the FLL structure varies as a function of temperature. It would be of interest to look more closely at the FLL order in the high-field region of the phase diagram, to see if the onset of FLL disorder correlates with the FFLO/Q-phase boundary as functions of both field and temperature.

Field parallel to [110], $H \parallel$ [110]

For the case of $H \parallel$ [110] and at a temperature of 85 mK, similarly distorted single domain hexagonal structures are observed as for the case of $H \parallel \mathbf{a}$. Example diffraction patterns are shown in figure 4.39. At fields of 7.5 T and below for this field geometry, the orientation of the hexagonal structure is of the same type as for the case of $H \parallel \mathbf{a}$. However, by 9.5 T, the primitive cell has undergone a field-driven 90° re-orientation transition. The nature of the transition is most likely first-order; as a function of field on moving between the transition there is no clear smooth variation of the spot shape or position that would suggest a continuous transition. More tellingly, there is relatively large hysteretic field region where the precise details of

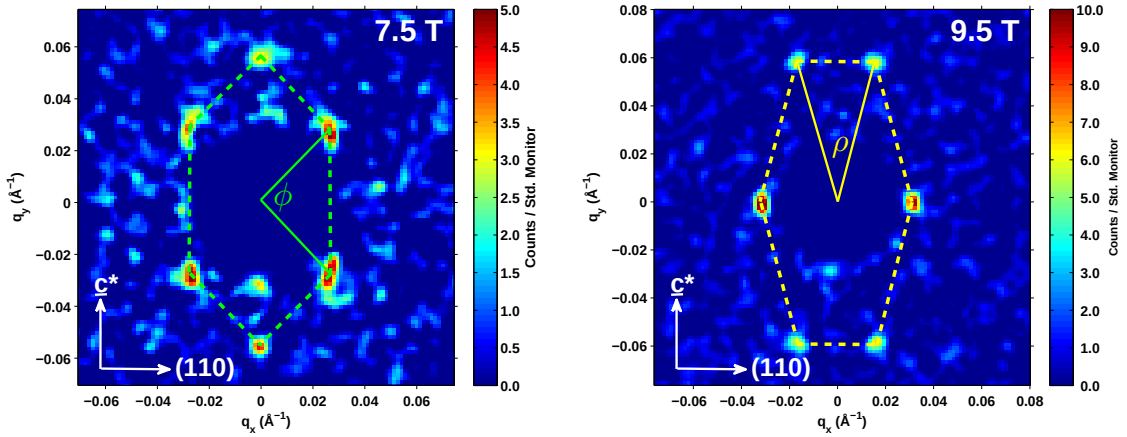

(a) 7.5 T

(b) 9.5 T

Figure 4.39: The FLL diffraction patterns obtained in $CeCoIn_5$ for $H \parallel [110]$, at a temperature of 85 mK, and applied fields of (a) 7.5 T and (b) 9.5 T. The dashed line patterns indicate the overall FLL structure, with characteristic angles of (a) ϕ and (b) ρ.

the FLL structure are unclear.

Figure 4.40 shows the accumulated, and provisional, FLL structure phase diagram for this field geometry. Measurements in this field geometry were carried out for fields up to 10.7 T, and a selection of higher temperatures in order to elucidate the details of the FLL structure transition phase boundary line. However, stymied by the hysteresis around the transition, it was not possible to confidently deduce even the precise transition field at base temperature, let alone how it evolves at higher temperatures. From figure 4.40 we can infer that the hysteretic region at base temperature could be as wide as $\sim$1 T in field, allowing us to estimate the transition field to be 8.1(5) T. For this field geometry, although a series of measurements were carried out over a range of fields and temperatures, due to the weak signal a systematic investigation of the FLL quality has not possible up to present.

4.7.2 Discussion of flux line lattice structure transition with field parallel to [110]

When the field is applied in the basal plane, it seems that the resulting FLL structure phase diagrams are comparatively featureless when compared to those obtained for

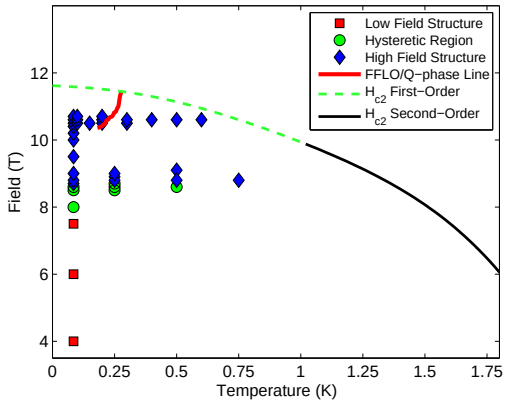

Figure 4.40: The incomplete FLL structure phase diagram for the case of $H \parallel [110]$. The dashed green and solid black lines correspond to where the transition between the superconducting and normal states is first- and second-order respectively. The thick red line indicates the proposed FFLO/Q-phase boundary, with the data taken from the study of Bianchi et al. (2003a). The positions of the symbols within the superconducting phase diagram correspond to where measurements of the FLL structure have been made up to now. Red filled squares indicate the identification of the low field structure (figure 4.39 (a)), blue filled diamonds the location of the high field structure(figure 4.39 (b)), and green filled circles indicate measurements within the hysteretic region, where there is uncertainty as to the precise structure.

$H \parallel \mathbf{c}$. This indicates the importance of the order-parameter anisotropy in understanding the results for a given field geometry. Of the in-plane results, it is of interest to understand why there is a field-driven FLL structure transition when $H \parallel [110]$, but no structure transition for $H \parallel \mathbf{a}$. Figure 4.40 shows the FLL structure transition field not to be correlated with the FFLO/Q-phase boundary. Furthermore, many measurements in and around the vicinity of the FFLO/Q-phase seemingly do not indicate a dependence of the FLL structure type on a novel type of superconducting state.

The transition that we observe is a re-orientation transition that is qualitatively the same as that seen between the low and intermediate field phases of $YBa_2Cu_3O_7$. In that material, we attributed the transition to non-local effects. In the face of a similar comparison, a similar explanation could be offered for $CeCoIn_5$. However, we note that for $H \parallel \mathbf{a}$, the field is parallel to an antinode of the $d_{x^2-y^2}$ order parameter. For $H \parallel [110]$, the field is parallel to a node. From this point of view, the

FLL structure transition could be associated with d-wave effects. Preliminary calculations using the quasiclassical Eilenberger theory have been carried out (Ichioka and Machida, 2009), in order to test if there is a dependence on the direction the field is applied relative to the node or antinode. At the time of writing, the results of numerical calculations were inconclusive. At high field, the free energy minimum $\mathcal{F}_m$, of the FLL structure for $H \parallel \mathbf{a}$ is associated with the structure shown in figure 4.36. However, the calculations predict the 90° re-orientation transition to occur as a function of decreasing field for this field direction. For $H \parallel [110]$, across the entire field range the orientational $\mathcal{F}_m$ is associated with a FLL structure like that shown in figure 4.39 (b), and there is no transition predicted as a function of field. We might take these results as indicating that FLL structure does not depend on the direction of applied field relative to the $d_{x^2-y^2}$ order parameter. However, the calculations did not account for the observed distorted shape of the FLL, or compare the calculated $\mathcal{F}_m$ of FLL structures whose shapes are determined by the order parameter and Fermi surface anisotropy. Such theoretical work is on-going.

4.7.3 Field-dependence of the form factor with field in the plane

With the field in the plane, we are sensitive to the out-of-plane penetration depth, and the in-plane susceptibility. The latter will be important, as at high field the quasiclassical calculations show the core magnetisation is the largest component of the internal magnetisation, and hence form factor. Tayama et al. (2002) have measured the anisotropy in the susceptibility χ_c/χ_{ab} to be ~ 2. Therefore, we expect the form factor to be weaker for fields for field in the basal plane.

With $H \parallel \mathbf{a}$, we were able to carry out a systematic investigation of the field-dependence of the FLL form factor. Before presenting these results, we address the question of whether there exists a form factor anisotropy between the different spot types of the distorted hexagonal FLL structure. For perpendicular fields, there existed a clear anisotropy between the different spot types in the high field hexagonal structure phase. For the only FLL structure type we observe for $H \parallel \mathbf{a}$, the spots are associated with two different directions, those with $\mathbf{q} \parallel \mathbf{c}^*$, and those with $\mathbf{q} \nparallel \mathbf{c}^*$. An

investigation of the FLL form factors of the different spot types showed the error-weighted ratio of $|F(\mathbf{q} \parallel \mathbf{c}^*)|^2$ to $|F(\mathbf{q} \nparallel \mathbf{c}^*)|^2$ to be 1.02(8) across the entire field range. Hence we conclude that within the sensitivity of the measurements, there is no form factor anisotropy between the different spot types of the hexagonal structure. Therefore, the overall form factor at a certain field is calculated according to an error-weighted mean of all available spots.

The resulting field-dependence of the first-order FLL form factor at ~ 70 mK is presented in figure 4.41. Similar to the low temperature data obtained for $H \parallel \mathbf{c}$, the form factor increases with field. Again, after the form factor has risen to a peak value, it falls on the approach to H_{c2}. Unfortunately, measurements at fields closer to H_{c2} than 10.9 T were not possible, due to the limitations of the available magnetic field. However, the similarity of the overall field-dependence with the corresponding $H \parallel \mathbf{c}$ measurements suggests that the two field-dependences can be explained within a similar physical framework.

Up until the time of writing, very few measurements of the FLL form factor with $H \parallel [110]$ have been carried out. The measurements presented in figure 4.40 were more concerned with observing the FLL structure, and values of the form factor cannot be obtained from these measurements. For this reason, and as nothing systematic can be gleaned from the few datapoints we have, we await future experimental work to obtain the more complete picture for this particular field direction.

4.7.4 Discussion of field-dependence of form factor with field parallel to a

On comparing the low temperature field-dependences of the form factor for $H \parallel \mathbf{c}$ and $H \parallel \mathbf{a}$ we see qualitatively similar behaviour between the two. The most noticeable difference between the two field directions is the form factor magnitude. This is emphasised in figure 4.42 where we plot the field-dependence of the first-order form factor for both field directions on a normalised field-scale. It is remarkable to see that the difference in form factor magnitude between the two directions is essentially constant over the normalised field-range, being approximately a factor of 8 in $|F(\mathbf{q})|^2$.

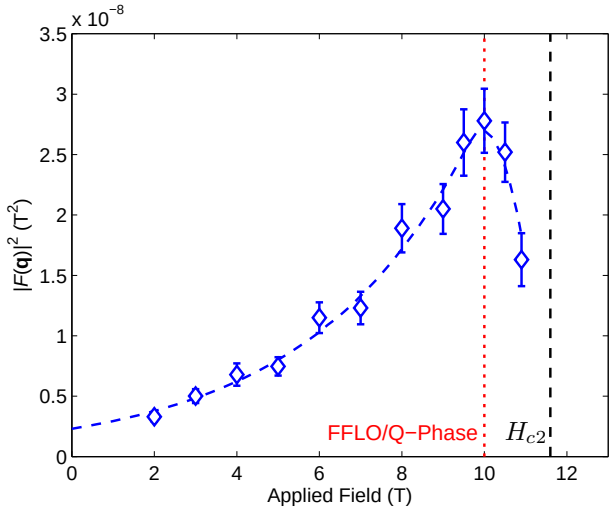

Figure 4.41: The field-dependence of the first-order FLL form factor for the case of $H \parallel \mathbf{a}$, and at a temperature of $\sim$ 70 mK. The dashed blue line is a guide to the eye fit of the data. The black dashed line represents H_{c2}, and the red dotted line the estimated location of the FFLO/Q-phase boundary. Both boundaries are deduced from Bianchi et al. (2003a).

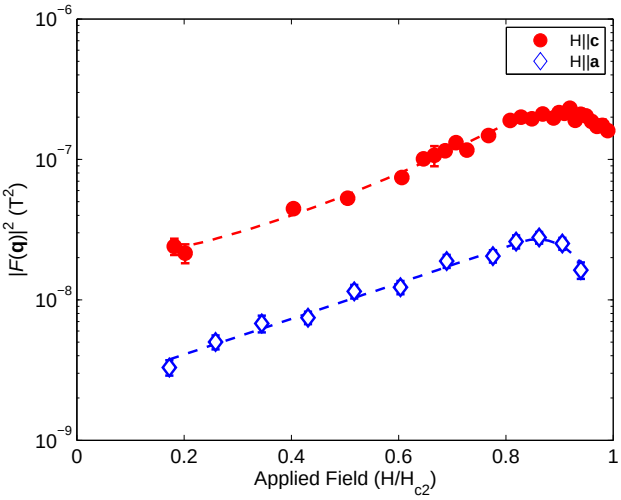

Figure 4.42: A comparison between the field-dependence of the first-order FLL form factor for the cases of $H \parallel \mathbf{c}$ at $\sim$ 50 mK and $H \parallel \mathbf{a}$ at $\sim$ 70 mK. The vertical scale is logarithmic, and the horizontal scale is field normalised to H_{c2}. The dashed line are guides to the eye for the data.

Initially we can ascribe the difference in magnitude to the anisotropy in the susceptibility (Tayama et al., 2002). Between the principal crystal directions and at low temperature, this anisotropy is approximately a factor of 2. We would expect the contribution of the field-induced core moment to the FLL form factor to dominate at high fields, and to be less important at low field. Therefore, if the susceptibility anisotropy is the sole cause for the anisotropy in the form factor ratio, we might also expect this ratio to vary as a function of normalised field. At high field, we would expect the anisotropy to be accountable in terms of the anisotropy in the susceptibility. At lower field, we might expect another anisotropy to manifest, such as that possibly associated with the penetration depth. The field-dependent ratio of the form factor for $H \parallel \mathbf{a}$ and $H \parallel \mathbf{c}$ is observed to remain approximately constant as a function of normalised field. Therefore, accounting for the difference in the susceptibility alone is insufficient to provide a sole explanation for the approximately field-independent factor of 8 difference in $|F(\mathbf{q})|^2$. Our results still suggest that for all fields and field directions the form factor behaviour is dominated by paramagnetic effects, and that they can be understood qualitatively in terms of the quasiclassical Eilenberger theory (Ichioka and Machida, 2007). However, it is also necessary to invoke other currently unaccounted for physical effects which may also be anisotropic.

We see from figure 4.42 that at the highest fields, there is possibly a deviation between the form of the two field-dependencies. For $H \parallel \mathbf{a}$, the field at which the form factor peaks is a lower fraction of H_{c2} than for $H \parallel \mathbf{c}$, and the form factor fall at the highest fields is also proportionally larger. This suggests that the physical mechanism that gives rise to this detrimental effect on the high field form factor behaves differently under parallel fields, or again, an enthusiastic interpretation would be that the additional effect of the onset of an FLLO/Q-phase state may be manifesting on the FLL. However, further experimental work is required, particularly with $H \parallel [110]$, where relatively few measurements have been carried out. Only then can reliable comparisons be drawn with the detailed picture of $H \parallel \mathbf{c}$, and the results of theoretical calculations.

4.8 Search for the Larkin-Ovchinnikov flux line modulation

Here, we briefly outline the results of SANS investigations within the low temperature and high field region of the superconducting phase diagram, where the FFLO/Q-phase state is predicted to be stabilised. In the Larkin-Ovchinnikov (LO) scenario of FFLO, due to the oscillatory nature of the order parameter amplitude in real-space, the flux lines are proposed to adopt a modulated topology (Tachiki et al., 1996; Mizushima et al., 2005; Ichioka et al., 2007). In principle, the periodicity associated with the inhomogeneous state can be probed via SANS measurements.

The calculations of Ichioka et al. (2007) suggest that the FFLO modulation reflected in both the modulation of the flux line, and by the paramagnetic moment that accumulates within the FFLO nodal plane, are able to provide sufficient field contrast for detection by SANS. The prediction is that Bragg spots associated with the field contrast modulation are observed as 'satellites' of the usual Bragg spots associated with the FLL configuration. In the traditional SANS geometry with field parallel to the neutron beam, these satellites are expected to lie out of the plane of the two dimensional reciprocal FLL. In order to observe this scattering and bring a Bragg satellite onto the diffraction condition, it is necessary to rotate the reciprocal lattice by large angles. Then the observation of the FFLO modulation is seen in the form of subsidiary peaks of the rocking-curve, in addition to the usual Bragg peak associated with the FLL.

A more appealing way to visualise the predicted Bragg satellites directly on the detector is to adopt the field-perpendicular experimental geometry. In this situation, the cryomagnet is rotated by 90° with respect to the neutron beam, and the scattering associated with both the first-order spots of the FLL, and the FFLO modulation, can be observed on the detector simultaneously. Figure 4.43 indicates what the possible diffraction pattern might look like once summed over all rocking angles.

One of the great hindrances of the search for the FFLO modulation is the predicted weakness of the FFLO satellites. In the work of Ichioka et al. (2007), even the closest satellites to the FLL Bragg peak are predicted to be an order of magnitude

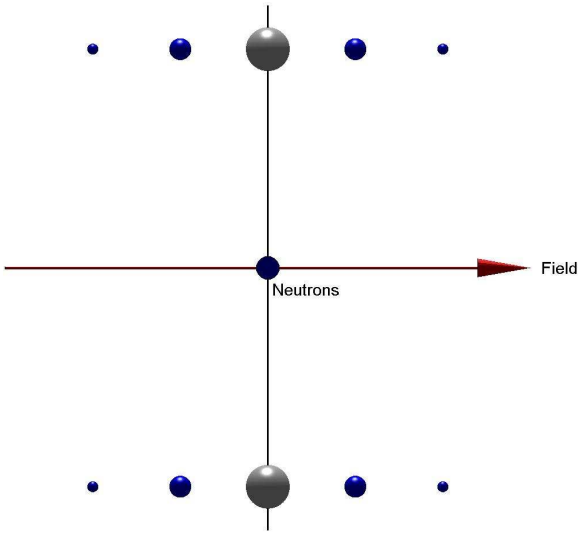

Figure 4.43: A schematic diagram of the expected diffraction pattern obtained from Bragg scattering due to a FLL with FFLO modulation. The diagram indicates the field perpendicular experimental geometry; the neutron beam (shown into the page) is shown as perpendicular to the applied field. The resulting scattering is therefore above and below the horizontal plane. The large grey spots represent the Bragg spots associated with the FLL. The small blue spheres indicate the expected Bragg 'satellites' associated with a FFLO modulation. The smaller size of the Bragg satellites indicates that they are expected to be weaker than the FLL Bragg spot.

weaker in $|F(\mathbf{q})|^2$. This gets progressively weaker for larger $\mathbf{q}$-vectors associated with the FFLO modulations, as indicated in figure 4.43. Perhaps as a consequence of this, and despite concerted efforts both in the perpendicular field geometry and the traditional SANS geometry, no evidence for a FFLO modulation satellite has been observed for $H \parallel \mathbf{c}$ or field in the plane. In the presence of a null result, we conclude that the signal due to the modulation is weaker than expected. It is also possible that the LO interpretation of the FFLO phase is not realised. In this case, the novel phase seen in this material would be solely associated with the Q-phase, even if such a phase has not yet been observed for all field configurations.

4.9 Summary

In this chapter, we have reported SANS studies of the FLL in $CeCoIn_5$, a material with a ground state that exhibits both d-wave superconductivity and strong paramagnetism. Our observations indicate that both of these properties are influ-

ential on the observed FLL structure with $H \parallel \mathbf{c}$. The physical mechanisms behind the low field hexagonal to rhombic to square sequence of FLL structure transitions can be considered in same terms as those for the structure transition sequence of $YBa_2Cu_3O_7$; namely as caused by the increasing prominence with field of non-local effects in combination with a Fermi surface anisotropy, or due to the increasing prominence of the $d_{x^2-y^2}$ order-parameter anisotropy. At higher field, the re-entrant transition sequence of square to rhombic to hexagonal represents a field-induced suppression of the in-plane anisotropy that stabilised the square FLL structure observed at intermediate field. Dedicated theoretical work (Hiasa and Ikeda, 2008; Ichioka and Machida, 2009) indicates that the suppressed anisotropy is that associated with the flux line core, which itself reflects the spatial anisotropy of the $d_{x^2-y^2}$ order-parameter. Thus the calculations indicate that the square structure phase can be understood as stabilised due to the influence of the gap anisotropy. The physical reason for the suppression of the fourfold core anisotropy is due to paramagnetic depairing at high field; an effect that is strongest within the vicinities of the flux line cores. Similarly, increasing the temperature results in the suppression of the square FLL structure, as expected if such a structure stabilised by the anisotropy of the $d_{x^2-y^2}$ order-parameter.

Field-induced core paramagnetism also plays a crucial role in understanding the behaviour of the FLL form factor. As a function of increasing field, and for temperatures up to $T_c/2$, the form factor is observed to *increase*. This is in contrast to predictions made using phenomenological theories, which predict the form factor to fall monotonically as a function of field. Our results are in qualitative agreement with the predictions made using a version of the quasiclassical Eilenberger theory that accounts for a paramagnetic effect (Ichioka and Machida, 2007, 2009). The calculations suggest that the increase of the FLL form factor is due to an increasing contribution of a field-induced core magnetisation to the overall internal magnetisation. This core-component is field-dependent, and increases as a function of field, which directly results in the observed increase of the FLL form factor.

For temperatures below 750 mK, we observe the form factor to rise to a peak

value, and then fall slightly on the approach to H_{c2}. At H_{c2}, the form factor falls sharply to zero, which is consistent with the expected first-order transition between the superconducting and normal states observed in thermodynamic studies (Tayama et al., 2002; Bianchi et al., 2002). With increasing temperature, the peak in the form factor is suppressed in both magnitude and field, and by 750 mK, the form factor falls monotonically to zero on approaching H_{c2}. This indicates that the superconductivity is orbitally-limited at H_{c2}, and that more conventional FLL behaviour is recovered at higher temperatures. However, an initial field-induced increase of the form factor for all temperatures investigated up to $\sim T_c/2$, indicating that the effects of field-induced core paramagnetism remain important over this entire temperature range.

At low temperature, we tried to understand the physical reason for the form factor fall just below H_{c2}. According to the predictions of numerical calculations (Ichioka and Machida, 2009), the reduction in the form factor is due to a high field expansion of the flux line cores. This occurs due to paramagnetic depairing within the flux line cores, which causes an increase in their spatial extent, and hence that of the core magnetisation. The experimental verification of this core expansion has proved challenging. A systematic set of SANS measurements was carried out in order to record the field-dependence of both $\{1,0\}$ and $\{1,1\}$ spots. On analysing the **q**-dependence of the form factors at each field, we find that the field-dependence of $|\mathrm{d}F/\mathrm{d}\mathbf{q}|$ increases smoothly with field. However, the predictions made according to the quasiclassical Eilenberger theory disagree with our observations, and predict $|\mathrm{d}F/\mathrm{d}\mathbf{q}|$ to fall monotonically with field. This disagreement currently remains unresolved, and remains an outstanding challenge for explaining our observations of the mixed state of $CeCoIn_5$ with $H \parallel \mathbf{c}$. In order to extract a measure of the core-size directly from the data, we propose it is necessary to develop a new form of phenomenological model that makes the best approximation to predictions made using the Eilenberger theory. We hope this will allow us to analyse our data quantitatively whilst remaining consistent with the more detailed calculations.

We also presented limited measurements with field in the basal plane. At low

temperatures, and for $H \parallel \mathbf{a}$, the FLL structure type is single domain and distorted hexagonal, with the long-axis of the distortion parallel to $\mathbf{c}^*$. This structure type remains unchanged as a function of field at base temperature. The same structure is observed at low field and temperature for $H \parallel [110]$, but at ~ 8 T a first-order 90° reorientation transition occurs into a similarly distorted single domain hexagonal structure. There are currently no physical explanations for the mechanism behind such a structure transition, or as to why a transition is observed for $H \parallel [110]$, whilst not for $H \parallel \mathbf{a}$. However, we speculate that this anisotropic behaviour is associated with the orientation that the field makes relative to a node, or antinode, of the $d_{x^2-y^2}$ order parameter. We also note that the structure transition field for $H \parallel [110]$ is uncorrelated with the proposed FFLO, or Q-phase boundary lines reported by other experiments. We examined the FLL at fields and temperature within the proposed FFLO/Q-phase in this field geometry, as well as for $H \parallel \mathbf{c}$, though do not observe any clear indication of an effect on the FLL due to the stabilisation of a novel phase.

The field-dependence of the form factor was reported at low temperature for $H \parallel \mathbf{a}$. The form factor exhibits qualitatively similar behaviour as for $H \parallel \mathbf{c}$; field-induced paramagnetic effects cause the form factor to increase to a peak value, before falling on the approach to H_{c2}. As a function of normalised field, the ratio in $|F(\mathbf{q})|^2$ between the two directions remains approximately constant at ∼8, with the larger form factor associated with that for $H \parallel \mathbf{c}$. This is in qualitative agreement with that expected from the anisotropy in the susceptibility (Tayama et al., 2002), though this anisotropy is too small to provide the sole explanation for the difference. Understanding this form factor anisotropy is left for future work.

Concluding Remarks and Outlook

In this thesis we have utilised the small-angle neutron scattering technique to present new observations of the FLL in the High-T_c superconductor $YBa_2Cu_3O_7$, and the heavy-fermion superconductor $CeCoIn_5$. Whilst belonging to different classes of material, they share some common characteristics. For both materials, certain properties can be changed on doping; reducing the oxygen content of $YBa_2Cu_3O_{7-\delta}$ leads to the emergence of antiferromagnetic correlations, whilst in $CeCoIn_5$, long-range antiferromagnetic order is known to be established under the extreme conditions of high field and low temperature. The close proximity of magnetism and superconductivity in both systems indicate that certain electronic states, the d-electron states in $YBa_2Cu_3O_{7-\delta}$ and the f-electron states in $CeCoIn_5$, are responsible for both phenomena in each material. Each material also possesses a quasi two-dimensional crystal structure, which has been suggested to suppress antiferromagnetic fluctuations such that the superconductivity can emerge. Our studies reveal new manifestations of the unconventional superconducting state on the FLL within both materials.

Our measurements on $YBa_2Cu_3O_7$ were carried out on sufficiently twin-free samples that the pinning to twin boundaries was largely suppressed. This allowed the observation of the intrinsic FLL structure with $H \parallel \mathbf{c}$ for the first time. We observed three distinct FLL structure phases, all separated from one another by first-order phase transitions. Both the low field transition between distorted hexagonal phases, and the high field transition between distorted hexagonal and rhombic phases, can be understood as being caused by the increasing importance with field of non-local

effects on the flux line-flux line interactions. Whilst this is likely the case for our low field transition, our measurements cannot unequivocally rule out that the high-field transition is caused solely by an increasing prominence of the gap anisotropy. To possibly address this issue, we suggest that future experiment might investigate the FLL with the field applied at an angle to the **c**-axis. If our high field rhombic structure is stabilised by the gap anisotropy, then rotating the field about either crystal axis will move the in-plane anisotropy out of the field direction, and result in an increase of the transition field into the rhombic phase. However, if the transition is caused by non-local effects, and the chain states play a role in this, we would expect the observed effect on the transition field to be dependent on whether the field is rotated about **a**, or **b**. This is a measurement that is planned for the near future. On this theme, it would also be of great interest to investigate the effect on the FLL of causing wholesale changes to the Fermi surface by systematically changing the oxygen doping. This would allow us to observe the interplay between the FLL and established spin/charge correlations. Measurements at higher magnetic fields are also clearly of interest, with investigations up to 17 T a genuine possibility within the very near future.

The ability to observe the intrinsic FLL structures in the twin-free sample allowed us to measure the field- and temperature-dependence of the FLL form factor. A basic understanding of the form factor in the low field structure phase can be obtained using the Clem model. However, at higher fields it is necessary to invoke corrections to, and assumptions of, the characteristic length-scales in order to maintain some form of understanding of the field-dependent form factor data. However, there are no obvious corrections we can introduce in order for us to understand our temperature-dependent data at higher fields. The understanding of these data awaits the results of careful and dedicated calculations.

The benefit of dedicated theoretical work is no clearer than for the case of understanding our observations of the FLL in the heavy-fermion superconductor $CeCoIn_5$. This material revealed an exciting mix of unconventional superconductivity and paramagnetic effects, which resulted in us observing new FLL physics. Initially, we

were able to record the major part of a rich FLL structure phase diagram for $H \parallel \mathbf{c}$. At high fields, we observe a square to rhombic to hexagonal transition sequence, which reflects a suppression of the fourfold core anisotropy which stabilises the square phase at intermediate fields. This core anisotropy is suppressed by paramagnetic depairing effects that originate from within the flux line cores. Field-induced flux line core paramagnetism also results in the field-induced amplification of the FLL form factor, the observation of which lies in stark contrast to the predicted monotonic decrease with field according to the conventional theories. A satisfactory explanation for our observations is only provided on harnessing the power of a version of the quasiclassical Eilenberger theory that accounts for a paramagnetic effect.

Our measurements at temperatures between 50 mK and 1250 mK detail the balance between conventional orbital-limiting behaviour, and Pauli-limited behaviour in this material. At low temperatures, the form factor increases with field, and the superconductivity is Pauli-limited as evidenced by the sharp fall of the form factor close to H_{c2}. However, the size of the form factor increase, and the field at which the form factor peaks, are both suppressed by increasing temperature. By 750 mK, the superconducting to normal transition is continuous, as expected for orbitally-limited superconductivity, and increasingly conventional behaviour is recovered as a function of increasing temperature. However, for *all* temperatures up to 1250 mK, the Pauli paramagnetic effects remain important, as evidenced by the initial increase in the form factor as a function of field. At low temperatures, and on the approach to H_{c2}, the form factor falls with field slightly from its peak value. Within the framework of the quasiclassical Eilenberger theory, this is ascribed to a high field expansion of the flux line cores. We attempted to provide evidence for this core-expansion via measurements of both first- and next-order diffraction spots. In principle, we believe the information is contained within the data, though the next step in the analysis is not forthcoming at the time of writing.

With the field applied within the basal plane, our currently limited set of measurements reveal a comparatively featureless FLL structure phase diagram when

compared with that obtained for $H \parallel \mathbf{c}$. However, for $H \parallel \mathbf{a}$ we observe a qualitatively similar form to the field-dependence of the form factor at low temperatures, thus indicating that Pauli paramagnetic effects will also seem to dominate the behaviour of the FLL in this field geometry. The focus of future experimental work on this material is to further characterise the FLL for field in the plane, in particular for $H \parallel [110]$. For this direction, the picture is rather incomplete. The new measurements will include the field-dependence form factor, to see if there is any difference in the field-dependence between the in-plane orientations. Subsequently, these measurements would indicate if paramagnetic effects might be sensitive to whether the field is applied parallel, or antiparallel, to a node of the d-wave order-parameter.

From the broader perspective of the FLL in heavy-fermion systems, it would be of further interest to carry out SANS measurements on other members of the Ce*M*In_5 family, in particular CeIrIn_5. CeCoIn_5 and CeIrIn_5 exhibit similar crystal structures and Fermi surface properties, yet the T_c of CeIrIn_5 is just 0.4 K. Therefore, it would be interesting to understand whether the FLL of CeIrIn_5 reflects the difference in T_c, and also whether the remarkable behaviour exhibited by CeCoIn_5 is observable in similar materials.

Appendix A - Experimental Details

A.1 A rocking-curve measurement

As in any diffraction experiment, the key information obtained from SANS measurements on the FLL is obtained by carrying out rocking curve measurements. For the SANS measurements reported in this thesis, this involves rotating a reciprocal lattice vector through the Bragg condition at the detector, and recording the diffracted intensity as a function of rotation angle. To do this involves careful alignment of the sample with respect to the field and neutron beam, and then rotation of the reciprocal lattice.

To perform a rocking curve measurement, the experimenter chooses a series of angles about which to rotate the reciprocal lattice and measure the diffracted intensity, which typically has the expected Bragg angle at the midpoint. Ideally the angular range should take into account the anticipated angular width of the rocking curve as might be expected from resolution considerations, and be wide enough so that at the widest scanned angles the observed intensity falls to the background level.

In SANS experiments, there are two complementary activities that are carried out on recording the rocking curve of a Bragg spot. The first is to perform background measurements with no FLL established in the sample (above $T_c(H)$, or after zero-field cooling). These are then subtracted from foreground measurements where the FLL is present, leaving just the diffracted signal from the FLL. Background measurements should ideally be performed over the same angular range as the foreground measurements, especially if there is angularly dependent background scattering. All of the diffraction patterns presented in this thesis have had

background measurements (either at $T > T_c$ or after zero-field cooling) subtracted from the field-cooled foreground measurements. The second complementary activity is essential, and it is to record the intensity and position of the un-diffracted beam. This intensity is important as it provides a measure of the incident flux of the neutrons on the sample, and is subsequently used to calculate FLL form factors. The position of the un-diffracted beam defines the origin of reciprocal space. From this point, the magnitude of the reciprocal space wavevectors for the Bragg spots are calculated. Obtaining the full rocking curves, allows the deduction of the precise positions of the Bragg spots and subsequently the size of the reciprocal lattice vector. This is all that is needed in order to extract the FLL form factor.

A.2 Data analysis using GRASP

For the results presented in this thesis, the major part of the basic data analysis has been carried out using the GRASP software developed by C.D. Dewhurst at the ILL [18]. The software is developed within a Matlab® environment, and as such is adept at handling the two-dimensional and pixelated multidetector data recorded by the SANS instrument.

The user interface includes a pane that allows a view of the distribution of the diffracted intensity across the multidetector at a certain rotation angle of the reciprocal lattice. It is also possible to sum the measurements at many rotation angles together into just one image, providing a picture of the diffracted intensity over an entire rocking curve. By similarly summing over multiple rocking curves, it is possible to deduce the FLL coordination by showing all of the first-order Bragg spots in just one image. An example of this is shown in figure A.1. In the viewing window of the front panel, we see some SANS foreground data summed over numerous rocking curves. The corresponding background data is subtracted. Statistical noise that occurs close to the beam stop is masked, and the data have been smoothed by a 2×2 pixel gaussian envelope that is smaller than the instrumental resolution [19].

[18] At the time of writing, the software is freely available from the internet at *http://www.ill.eu/instruments-support/instruments-groups/groups/lss/grasp/home/*.

[19] Note, that any smoothing treatment to the image observed in the front-end of the software is purely a visual effect. It does not influence the data analysis within the software routines.

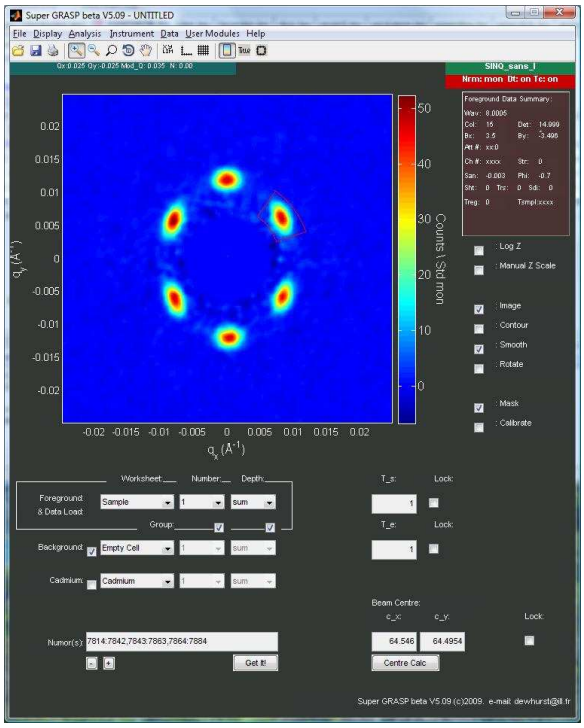

Figure A.1: Image capture of the front-end of the GRASP software (version 5.09). SANS data over multiple rocking curves is loaded, showing all the first-order Bragg spots in a single image. A sector box is defined on the detector over area occupied by the upper right Bragg spot.

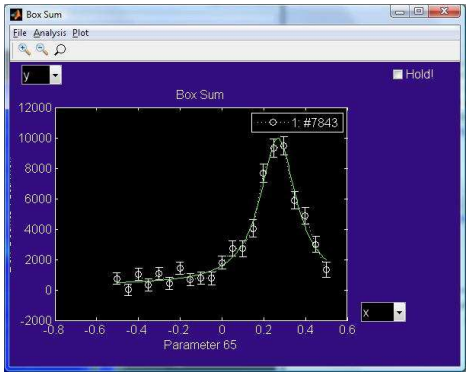

Figure A.2: Image capture of a rocking curve plot output by the GRASP software, and fit with a suitable lineshape function. The horizontal axis is in units of degrees of rotation angle of the reciprocal lattice about the vertical axis, where zero corresponds to the straight through position. The vertical axis is in units of total counts within the sector box per standard monitor.

In figure A.1 we have also defined a sector box on the detector to lie over the region occupied by the upper right Bragg reflection. This box defines an area of pixels, and it is over this region on the detector that the rocking curve is obtained in order to calculate the integrated intensity for the Bragg reflection. At each angle of the rocking curve, the program sums the pixel counts within the box, and presents a graph of the angular dependence of the summed box intensity. The output rocking curve for the sector box shown in figure A.1 is shown in figure A.2. To obtain the *raw* integrated intensity $I_{raw}(\mathbf{G}_{h,k})$, the curve is fitted with a suitable lineshape function and the area between the curve and the background level is integrated.

The raw measure of the integrated intensity can be used to calculate the FLL form factor $|F(\mathbf{G}_{h,k})|^2$. In order to to do this, we initially re-arrange equation 2.20 to show the relationship between the form factor, the reciprocal lattice vector $\mathbf{G}_{h,k}$, and the *intrinsic* integrated intensity $I_{int}(\mathbf{G}_{h,k})$.

$$I_{int}(\mathbf{G}_{h,k})\cos(\zeta) = 2\pi V \phi_n \left(\frac{\gamma}{4}\right)^2 \frac{\lambda_n^2}{\Phi_0^2 \mathbf{G}_{h,k}} |F(\mathbf{G}_{h,k})|^2, \tag{A.1}$$

We remind ourselves that V is the sample volume, ϕ_n is the incident neutron flux, γ is a constant equal to 1.91, λ_n is the neutron wavelength, and Φ_0 is the flux quantum $h/2e$. The term $\cos(\zeta)$ is the Lorentz correction factor, which corrects the raw integrated intensity $I_{raw}(\mathbf{G}_{h,k})$ to the intrinsic integrated intensity expected if the reciprocal lattice were to cut through the Ewald sphere directly, $I_{int}(\mathbf{G}_{h,k})$. This correction factor requires determining the angle ζ that the reciprocal lattice vector makes relative to the direction normal to the rotation axis of the reciprocal lattice. Of course, for the case where the reciprocal lattice vector *does* cut through the Ewald sphere directly, $\zeta = 0$, and $I_{raw}(\mathbf{G}_{h,k}) = I_{int}(\mathbf{G}_{h,k})$. In general however, it is necessary to accurately determine ζ, and make the Lorentz factor correction. To do this, we initially use the rocking-curve to identify the most statistically relevant data. For example, from figure A.2, we would choose to load the data taken at the two or three measurement angles that gives the largest intensity. At these few measurement angles, the position of the Bragg spot as measured on the detector is most likely to represent its true position in reciprocal space. Using these few measurements summed into one foreground image, the Bragg spot position is

fitted using a two-dimensional gaussian function that returns the the centre of mass position of the spot in terms of x and y pixel coordinates. These coordinates can be compared to those of the direct beam measurement in order to deduce the angle that the Bragg spot makes to relative to the rotation axis. By comparing the pixel positions of both the Bragg spot under question and the direct beam, the magnitude of the reciprocal lattice vector $\mathbf{G}_{h,k}$ can be calculated with a knowledge of the sample-to-detector distance and the pixel size. Therefore, with the the knowledge of both the intrinsic integrated intensity, and the magnitude of $\mathbf{G}_{h,k}$, the FLL form factor for a certain Bragg spot can be obtained.

Appendix B - Neutron absorption by $YBa_2Cu_3O_7$ and $CeCoIn_5$

B.1 Calculating the 1/e length for $YBa_2Cu_3O_7$ and $CeCoIn_5$

In this appendix we determine the neutron absorption of the materials studied in this thesis, $YBa_2Cu_3O_7$ and $CeCoIn_5$. This is characterised by the 1/e length, which corresponds to the thickness of material that attenuates the neutron beam by such this factor at a given wavelength. The 1/e length is calculated according to

$$1/e = \frac{1}{\sum_{coh} + \sum_{inc} + \sum_{abs}} \tag{B.1}$$

where $\sum_{coh}$, $\sum_{inc}$ and $\sum_{abs}$ are respectively the macroscopic coherent, incoherent and absorption scattering cross-sections per unit volume. Each of these macroscopic cross-sections can be calculated by summing over the contributions to each from the stable isotopes of each element. Tabulated values for the elemental microscopic cross-sections can be obtained from those reported in Neutron News (1992) [20]. In table B.1, we list the microscopic neutron scattering cross-sections for each of the constituent elements of $YBa_2Cu_3O_7$ and $CeCoIn_5$. Taking the example of calculating the macroscopic absorption cross-section,

$$\sum_{abs} = N \sum_{j} p_j n_j \sigma_{abs,j} \tag{B.2}$$

where the sum in j represents the sum over all the stable isotopes, p_j is the natural abundance of the isotope as a fraction of 1, n_j is the number of times this atom

[20] These tabulations are freely available on the internet at the National Institute for Standards and Technology (NIST) website: *http://www.ncnr.nist.gov/resources/n-lengths/*

Element	A	Z	Natural Abundance (%)	σ_{coh} (barns)	σ_{inc} (barns)	σ_{abs} (barns)
Y	39	89	100	7.55	0.15	1.28
Ba	56	130	0.11	1.6	0	30.0(5)
		132	0.1	7.6	0	7
		134	2.42	4.08	0	2.0(1.6)
		135	6.59	2.74	0.5	5.8
		136	7.85	3.03	0	0.68
		137	11.23	5.86	0.5	3.6
		138	71.7	2.94	0	0.27
Cu	29	63	69.17	5.2	0.006	4.5
		65	30.83	14.1	0.4	2.17
O	8	16	99.762	4.232	0	0.0001
		17	0.038	4.2	0.004	0.236
		18	0.2	4.29	0	0.00016
Ce	58	136	0.19	4.23	0	7.3(1.5)
		138	0.25	5.64	0	1.1
		140	88.48	2.94	0	0.57
		142	11.08	2.84	0	0.95
Co	27	59	100	0.779	4.8	37.18
In	49	113	4.3	3.65	0.000037	12.0(1.1)
		115	95.7	2.02	0.55	202(2)

Table B.1: Neutron absorption cross-sections for the stable isotopes of the elemental constituents of $YBa_2Cu_3O_7$ and $CeCoIn_5$. The absorption cross-sections were measured with neutrons of wavelength 1.8 Å, and the data were obtained from an article in Neutron News (1992).

appears in the unit cell, (e.g. when including either of the In isotopes of $CeCoIn_5$, $n_j = 5$), and $\sigma_{abs,j}$ is the microscopic absorption cross-section of the isotope. Finally, N is the number density $= \rho N_A/m_{mol}$. Here, ρ is the overall molecular density, N_A is Avogadro's number and m_{mol} is the molecular mass. The macroscopic cross-section can be normalised to units of inverse length by dividing by 1 barn (1.10^{-24} cm^2). Correctly summing the coherent, incoherent and absorption cross-sections allows the estimation of the 1/e length. Note all values in table B.1 are valid for a neutron wavelength of 1.8 Å. To estimate the overall 1/e length at different wavelength λ_n, just the macrosopic absorption cross-section is multiplied by a factor $\lambda_n/1.8$. The macroscopic coherent and incoherent scattering lengths are not dependent on λ_n.

Taking the example of $CeCoIn_5$, with $m_{mol} = 774$ g and $\rho \sim 6$ g.cm^{-3}, the 1/e length is ~ 0.7 mm at $\lambda_n = 5$ Å. This short length can be attributed to the strong absorption of In, leading to the necessity for thin samples in the SANS experiments. On the other hand, $YBa_2Cu_3O_7$ with $m_{mol} = 668$ g and $\rho \sim 5$ g.cm^{-3} has a 1/e length of ~ 2.0 cm at $\lambda_n = 5$ Å. Therefore, absorption is not an issue for the 0.35 mm thick samples used for the measurements in this thesis.

Appendix C - The measure of distortion of hexagonal FLL structures

In this Appendix, we provide a geometrical derivation of the relationship between a FLL primitive cell opening angle, and the axial ratio of the ellipse that overlays the Bragg spot distribution of a hexagonal FLL structure. This method of analysis was found to give values of the elliptical axial ratio η, which were found to be reproducible and accurate.

C.1 General geometrical construction

Our method takes advantage of the properties of Bravais lattices, and the subsequent observation that positions of three first-order Bragg spots can *always* be overlaid by an ellipse. Figure C.1 (a) schematically shows an isotropic and hexagonal FLL, whose distribution of Bragg spots may be overlaid by an ellipse of axial ratio 1, i.e. a circle. Note that to keep a degree of generality, the coordinate axes have been chosen so that the hexagonal structure is of arbitrarily oriented with respect to them. However, we are free to choose a coordinate axis that is parallel to the direction of distortion of the distorted hexagonal structures. Figure C.1 (b) shows the result of a London-like scale transformation on the isotropic lattice, so that the isotropic hexagonal FLL distorts by $\sqrt{\eta}$ along the $\mathbf{k}_y$ direction, and by $1/\sqrt{\eta}$ along the $\mathbf{k}_x$ direction. This results in the Bragg spots lying on an ellipse.

In reference to figure C.1, it is straightforward to show that on distorting the

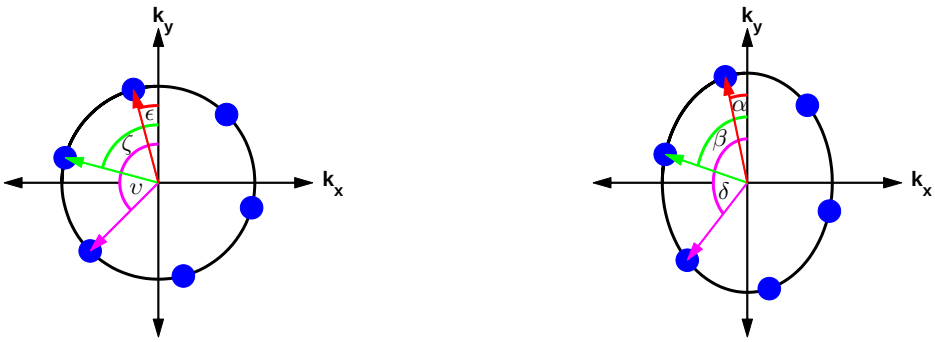

(a) Isotropic hexagonal FLL (b) Distorted hexagonal FLL

Figure C.1: In (a) we show an isotropic hexagonal FLL structure of arbitrary orientation with respect to the coordinate axes. In (b) the isotropic hexagonal structure of (a) is distorted along $\mathbf{k}_y$ such that the distribution is elliptical. In both cases, filled blue circles represent Bragg spots, and the indicated angles are measured with respect to the positive $\mathbf{k}_y$ direction i.e. a long axis of the direction of elliptical distortion. The angles shown in (a) are analogous to those shown in (b), but different in magnitude due to the distortion.

isotropic circular arrangement of Bragg spots

$$\tan\epsilon = \eta\,\tan\alpha \tag{C.1}$$

where ϵ and α are the angles defined in figures C.1 (a) and (b) respectively, whilst η is the elliptical axial ratio defined earlier. Note for a given value of η, the same relation between ϵ and α as shown in equation C.1 exists between ζ and β, and υ and δ. It is clear that

$$\tan\left(\zeta - \epsilon\right) = \tan 60^\circ = \sqrt{3}. \tag{C.2}$$

Hence using equations C.1 and C.2, and using trigonometry, we obtain

$$\frac{\tan\zeta - \tan\epsilon}{1 + \tan\zeta\,\tan\epsilon} = \tan 60^\circ = \sqrt{3} = \frac{\eta\,\tan\beta - \eta\,\tan\alpha}{1 + \eta^2\,\tan\beta\,\tan\alpha}. \tag{C.3}$$

Re-arranging the right hand side of equation C.3 yields

$$\sqrt{3}\,\eta^2\,\tan\beta\,\tan\alpha - \eta\,\left(\tan\beta - \tan\alpha\right) + \sqrt{3} = 0 \tag{C.4}$$

and solving equation C.4 gives

$$\eta = \frac{\left(\tan\beta - \tan\alpha\right) \pm \sqrt{\left(\tan\beta - \tan\alpha\right)^2 - 12\tan\alpha\,\tan\beta}}{2\sqrt{3}\tan\alpha\,\tan\beta}. \tag{C.5}$$

Note that in equation C.5, the way we have constructed the situation will force us to choose the negative sign.

For completeness, it is worth considering the possible choices of angles α and β to use with equation C.5. The equation will diverge as either of α or β tend to zero. Therefore, for hexagonal FLL structures arbitrarily oriented with respect to the coordinate axis, the value of η will remain finite. However, the sensitivity of the value of η to variations in α are large when α is close to zero (for example, as shown in figure C.1 (b)). An investigation of equation C.5 shows that values of η which are less sensitive to experimental error can be obtained by choosing angles that approximately bisect an axis of high symmetry. So choosing the example of the ellipse in figure C.1 (b), one would choose to respectively replace α and β in equation C.5 with β and δ as defined in the figure. For any arbitrarily oriented arrangement of Bragg spots, a judicious choice of angles based on the approximate bisection of a high symmetry axis is required to gain the most reliable value of η.

C.2 Special cases of hexagonal FLL structure orientation

In this thesis, FLL structures are reported where the hexagonal distribution of the Bragg spots is *not* arbitrary with respect to the coordinate axes. In these situations, Bragg spots are aligned both with the coordinate axes, which themselves are defined by the reciprocal atomic lattice, and the major or minor axis of the ellipse that overlays their distribution. Figure C.2 shows examples of two distorted hexagonal structures with nearest neighbours aligned with the real space x-axis (figure C.2 (a)) and the real-space y-axis (figure C.2 (b)). For the case shown in figure C.2 (a), the axial ratio of the ellipse that overlays the Bragg spots can be obtained by respectively substituting the defined values of the angles μ and ι for the angles α and β of equation C.5. However, using the general equation for an ellipse, it can be shown that

$$\eta = \frac{\sqrt{3}}{\tan\mu} \tag{C.6}$$

where μ is as defined in figure C.2 (a). The numerical value obtained using equation C.6 is exactly the same as obtained on using equation C.5. Similarly for obtain-

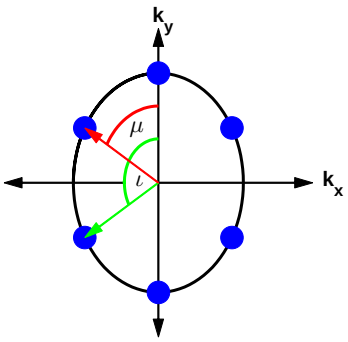

(a) Flux line nearest neighbours along the real-space x direction

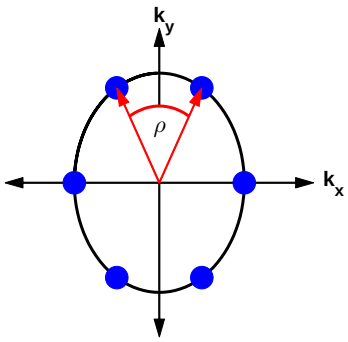

(b) Flux line nearest neighbours along the real-space y direction

Figure C.2: Schematic diagrams of distorted hexagonal FLL structures with nearest neighbours aligned with (a) the real-space x-axis and (b) the real-space y-axis. In these cases, the direction of nearest neighbour alignment also corresponds to either a major or minor axis of the elliptical distortion.

ing a value of η for the FLL structure depicted in figure C.2 (b), equation C.5 can be used, where $-\rho/2$ and $\rho/2$ would be substituted in for α and β respectively. However, again using simple geometrical rules, precisely the same answer is obtained using equation C.7, where ρ is as defined in figure C.2 (b).

$$\eta = \frac{1}{\sqrt{3}\tan\left(\frac{\rho}{2}\right)} \tag{C.7}$$

Appendix D - Finding a suitable phenomenological model for the form factor

In chapter 3, we present our analysis of the field-dependence of the FLL form factor at 2 K, in $YBa_2Cu_3O_7$. The type of phenomenological model that we should use to analyse our data, based on those available, is not immediately obvious. Here we present and briefly discuss the models that are most commonly used to describe form factor data deep within the mixed state (see for example, (Cubitt et al., 2007; Densmore et al., 2009; Eskildsen et al., 2009)). The simplest model is the uniaxial London model, where the form factor is related to the London penetration depth λ_L, the magnitude of the scattering vector q and the mean induction within the sample $\langle B \rangle$.

$$F(q) = \frac{\langle B \rangle}{1 + q^2 \lambda_L^2} \tag{D.1}$$

However, this simple relation implies the existence of the unphysical effect of a logarithmic divergence of the field at the flux line axis.

Clem (1975) proposed a model which accounts for the effect of the flux line cores on the magnitude of the measured form factor. The model was first introduced in section 1.2.2, and incorporates a variational core length-scale parameter ξ_ν into the Ginzburg-Landau theory. Here, we re-state the final result valid for high-κ materials and for fields along an axis of four-fold symmetry.

$$F(q) = \langle B \rangle \frac{g K_1(g)}{(1 + q^2 \lambda^2)}, \qquad g = \frac{\xi_\nu}{\lambda} \left(1 + q^2 \lambda^2\right)^{-1/2} \tag{D.2}$$

Here $\xi_\nu = \sqrt{2}\xi_{GL}$, the Ginzburg-Landau coherence length. In the limit of $\kappa \to \infty$ and $B \to 0$, the London model of equation D.1 is recovered. Even though the Clem model was originally developed for s-wave materials, calculations of first-order form factors within the quasiclassical Eilenberger theory show no large effect between s- and d-wave pairing symmetries, and no large difference between hexagonal and square FLL structures (Ichioka et al., 1999). Therefore we assume these details to not be important over our field range.

Later, Hao and Clem (1991) attempted to improve the accuracy of the model at lower temperature by letting ξ_ν be field-dependent according to

$$\xi_\nu = \xi_{GL}\left(\sqrt{2} - \frac{0.75}{\kappa}\right)\left(1 + b^4\right)^{1/2}\left[1 - 2b\left(1 - b\right)^2\right]^{1/2} \tag{D.3}$$

where $b = B/B_{c2}$. In the limit of high-κ and $b \to 0$, $\xi_\nu \sim \sqrt{2}\xi_{GL}$ as expected for the Clem model. A second correction term which originates from a suppression of the superfluid density is $f_\infty^2 = 1 - b^4$. This term factors into the numerator of the expression for $F(q)$. The model that incorporates these two corrections into the Clem model is called the Hao-Clem (HC) model.

The form of the Clem model is essentially the simple London model, with a $gK_1(g)$ term that accounts for the effect of the flux line cores. According to Yaouanc et al. (1997), the term $gK_1(g)$ can be approximated for all g either by a term, $\exp\left(-\sqrt{2}\xi_{GL}q\right)$, or by, $\exp\left(-2\xi_{GL}^2q^2\right)$. As further comparison, we also consider the proposed form of the core correction term according to Brandt, $\exp\left(-0.25\xi_{GL}^2q^2\right)$, which was deduced from his solutions of the GL equations close to T_{c2} (Brandt, 1972).

In figure D.1 we compare the predictions for the field-dependence of the form factor according to the various models. Firstly, we see the necessity of considering the core-correction term; the pure London model (black dotted line) predicts the form factor to be field-independent, so this simple model is inappropriate for describing the data shown in figure 3.30. We further see that the approximations to the Clem model according to Yaouanc et al. (1997), and the form proposed by Brandt (1972), result in predictions that are in poor agreement with the Clem and HC models. Therefore, as there is nothing to be gained by making these ap-

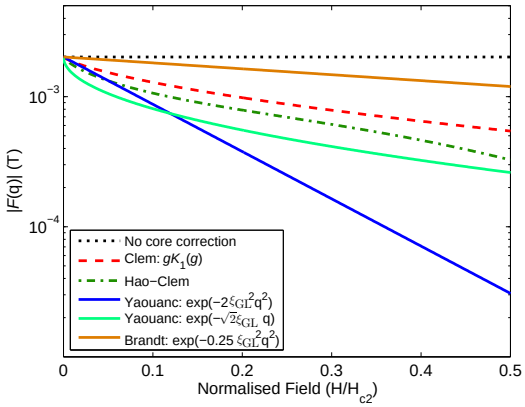

Figure D.1: The field-dependence of the form factor $|F(q)|$ calculated using the various models described in the text. For all calculations, material parameters appropriate for $YBa_2Cu_3O_7$ are used; λ_L =150 nm (Basov et al., 1995), ξ_{GL} =1.81 nm such that H_{c2} =100 T. We assume an isotropic hexagonal FLL structure.

proximations, we do not make further use of them here. The question remains however as to which of the Clem or HC models is the most appropriate. In general, we note that Ginzburg-Landau models are only strictly applicable close to T_{c2}, and therefore not applicable for our FLL experiments which are carried out deep within the mixed state. The models proposed by Clem (1975) and Hao and Clem (1991) attempt to extend this range of validity over a larger field range, which ultimately represents an approximation to the predictions of more detailed calculations. The quality of these approximations has been somewhat examined by Brandt (1997, 2003). In his work he numerically solves the GL equations in order to calculate the magnetisation and internal field distribution. In principle, the results obtained are valid for *any* field at high-κ (Brandt, 1997). In his later work, Brandt (2003) shows that, over our field range, the HC model provides a poorer approximation to the exact solutions of the GL model, with the Clem model recommended as being more appropriate. Therefore, we proceed with attempting to model our form factor data in Chapter 3 using the Clem model.

Appendix E - Publications

Publications arising from work in this thesis

A.D. Bianchi, M. Kenzelmann, L. DeBeer-Schmitt, **J.S. White**, E.M. Forgan *et al., "Superconducting Vortices in $CeCoIn_5$: Toward the Pauli-Limiting Field"* Science **319**, 177 (2008).

J.S. White, V. Hinkov, R.W. Heslop, R.J. Lycett, E.M. Forgan *et al., "Fermi Surface and Order Parameter Driven Vortex Lattice Structure Transitions in Twin-Free $YBa_2Cu_3O_7$"* Phys. Rev. Lett. **102**, 097001 (2009).

J.S. White, P. Das, M.R. Eskildsen, L. DeBeer-Schmitt, E.M. Forgan *et al., "Observations of Pauli Paramagnetic Effects on the Flux Line Lattice in $CeCoIn_5$"* (In preparation).

Other publications arising during the thesis period

R. Cubitt, **J.S. White** *et al., "Small-angle neutron scattering measurements of the vortex lattice in CaC_6"* Phys. Rev. B **75**, 140516(R) (2007).

J.S. White, E.M. Forgan *et al., "Finite gap behaviour in the superconductivity of the infinite layer n-doped high-T_c superconductor $Sr_{0.9}La_{0.1}CuO_2$"* J. Phys.: Condens. Matter **20**, 104237 (2008).

J.S. White, S.P. Brown, E.M. Forgan *et al., "Observations of the configuration of the high-field vortex lattice in $YBa_2Cu_3O_7$: Dependence upon temperature and angle of applied field"* Phys. Rev. B **78**, 174513 (2008).

D.S. Inosov, T. Shapoval, V. Neu, U. Wolff, **J.S. White** *et al., "Symmetry and disorder of the vitreous vortex lattice pointing to unusually strong flux pinning in an overdoped $BaFe_{2-x}Co_xAs_2$ superconductor"* (Submitted to Supercond. Sci. Technol. (2009)).

Bibliography

Abrikosov, A. A. (1957). *On the magnetic properties of superconductors of the second group*. *Soviet Physics JETP*, 5:1174.

Adachi, H., Ichioka, M., and Machida, K. (2005). *Mixed-State Thermodynamics of Superconductors with Moderately Large Paramagnetic Effects*. *J. Phys. Soc. Jpn.*, 74:2181.

Affleck, I., Franz, M., and Sharifzadeh Amin, M. H. (1997). *Generalized London free energy for high-T_c vortex lattices*. *Phys. Rev. B*, 55:R704.

Ager, C., Ogrin, F. Y., Lee, S. L., Aegerter, C. M., Romer, S., Keller, H., Savić, I. M., Lloyd, S. H., Johnson, S. J., Forgan, E. M., Riseman, T., Kealey, P. G., Tajima, S., and Rykov, A. (2000). *Angular-dependent muon-spin rotation and torque magnetometry on the mixed state of the high-temperature superconductor $YBa_2Cu_3O_{7-\delta}$. Phys. Rev. B*, 62:3528.

Amin, M. H. S., Affleck, I., and Franz, M. (1998). *Low-temperature behavior of the vortex lattice in unconventional superconductors*. *Phys. Rev. B*, 58:5848.

Amin, M. H. S., Franz, M., and Affleck, I. (2000). *Effective Penetration Depth in the Vortex State of a D-Wave Superconductor*. *Phys. Rev. Lett.*, 84:5864.

Andersen, N. H., von Zimmermann, M., Frello, T., Käll, M., Mønster, D., Lindgård, P. A., Madsen, J., Niemöller, T., Poulsen, H. F., Schmidt, O., Schneider, J. R., Wolf, T., Dosanjh, P., Liang, R., and Hardy, W. N. (1999). *Superstructure formation and the structural phase diagram of $YBa_2Cu_3O_{6+x}$*. *Physica C*, 317:259.

Andersen, O. K., Liechtenstein, A. I., Jepsen, O., and Paulsen, F. (1995). *LDA ENERGY BANDS, LOW-ENERGY HAMILTONIANS, t', t", $t_\perp$ (k), and $J_\perp$*. *J. Phys. Chem. Solids*, 56:1573.

Andres, K., Graebner, J. E., and Ott, H. R. (1975). *$4f$-Virtual-Bound-State Formation in $CeAl_3$ at Low Temperatures*. *Phys. Rev. Lett.*, 35:1779.

Annett, J. F. (2004). *Superconductivity, Superfluids and Condensates*. Oxford, 1st edition.

Aoki, H., Sakakibara, T., Shishido, H., Settai, R., Onuki, Y., Miranović, P., and Machida, K. (2004). *Field-angle dependence of the zero-energy density of states in the unconventional heavy-fermion superconductor $CeCoIn_5$*. *J. Phys.: Condens. Matter*, 16:L13.

Atkinson, W. A. (1999). *Disorder and chain superconductivity in $YBa_2Cu_3O_{7-\delta}$*. *Phys. Rev. B*, 59:3377.

Atkinson, W. A. and Carbotte, J. P. (1995). *Effect of proximity coupling of chains and planes of the penetration-depth anisotropy in $YBa_2Cu_3O_7$*. *Phys. Rev. B*, 52:10601.

Atkinson, W. A. and Sonier, J. E. (2008). *Role of CuO chains in vortex core structure in $YBa_2Cu_3O_{7-\delta}$*. *Phys. Rev. B*, 77:024514.

Balatsky, A. V. (2000). *Field-induced $d_{x^2-y^2} + id_{xy}$ state and marginal stability of high-T_c superconductors*. *Phys. Rev. B*, 61:6940.

Bardeen, J., Cooper, L. N., and Schrieffer, J. R. (1957). *Microscopic Theory of Superconductivity*. *Phys. Rev.*, 106:162.

Bardeen, J., Kümmel, R., Jacobs, A. E., and Tewordt, L. (1969). *Structure of Vortex Lines in Pure Superconductors*. *Phys. Rev.*, 187:556.

Basov, D. N., Liang, R., Bonn, D. A., Hardy, W. N., Dabrowski, B., Quijada, M., Tanner, D. B., Rice, J. P., Ginsberg, D. M., and Timusk, T. (1995). *In-Plane Anisotropy of the Penetration Depth in $YBa_2Cu_3O_{7-x}$ and $YBa_2Cu_4O_8$ Superconductors*. *Phys. Rev. Lett.*, 74:598.

Basov, D. N. and Timusk, T. (2005). *Electrodynamics of high-T_c superconductors*. *Rev. Mod. Phys.*, 77:721.

Bednorz, J. G. and Müller, K. A. (1986). *Possible High-T_c Superoconductivity in the Ba La Cu O System*. *Z. Phys. B*, 64:189.

Berlinsky, A. J., Fetter, A. L., Franz, M., Kallin, C., and Soininen, P. I. (1995). *Ginzburg-Landau Theory of Vortices in d-Wave Superconductors*. *Phys. Rev. Lett.*, 75:2200.

Bianchi, A., Movshovich, R., Capan, C., Pagliuso, P. G., and Sarrao, J. L. (2003a). *Possible Fulde-Ferrell-Larkin-Ovchinnikov Superconducting State in $CeCoIn_5$*. *Phys. Rev. Lett.*, 91:187004.

Bianchi, A., Movshovich, R., Oeschler, N., Gegenwart, P., Steglich, F., Thompson, J. D., Pagliuso, P. G., and Sarrao, J. L. (2002). *First-Order Superconducting Phase Transition in $CeCoIn_5$*. *Phys. Rev. Lett.*, 89:137002.

Bianchi, A., Movshovich, R., Vekhter, I., Pagliuso, P. G., and Sarrao, J. L. (2003b). *Avoided Antiferromagnetic Order and Quantum Critical Point in $CeCoIn_5$*. *Phys. Rev. Lett.*, 91:257001.

Bianchi, A. D., Kenzelmann, M., DeBeer-Schmitt, L., White, J. S., Forgan, E. M., Mesot, J., Zolliker, M., Kohlbrecher, J., Movshovich, R., Bauer, E. D., Sarrao, J. L., Fisk, Z., Petrovic, C., and Eskildsen, M. R. (2008). *Superconducting Vortices in $CeCoIn_5$: Toward the Pauli-Limiting Field*. *Science*, 319:177.

Bobowski, J. S., Turner, P. J., Harris, R., Liang, R., Bonn, D. A., and Hardy, W. N. (2007). *Oxygen chain disorder as a weak-limit scatterer in $YBa_2Cu_3O_{6.50}$*. *Physica C*, 460:914.

Bowell, C. (2008). *Studies of the Vortex Lattice Using Complementary Small Angle Neutron Scattering and Heat Capacity Measurements*. PhD thesis, University of Birmingham.

Brandt, E. H. (1972). *GINSBURG-LANDAU THEORY OF VORTEX LATTICE IN TYPE-II SUPERCONDUCTORS FOR ALL VALUES OF CHI AND BETA*. *Phys. Status Solidi*, 51:345.

Brandt, E. H. (1995). *The flux-line lattice in superonductors*. *Rep. Prog. Phys.*, 58:1465.

Brandt, E. H. (1997). *Precision Ginzburg-Landau Solution of Ideal Vortex Lattices for Any Induction and Symmetry*. *Phys. Rev. Lett.*, 78:2208.

Brandt, E. H. (2003). *Properties of the ideal Ginzburg-Landau vortex lattice*. *Phys. Rev. B*, 68:054506.

Brown, S. P. (2005). *High-field SANS studies of the vortex lattice in YBCO*. PhD thesis, University of Birmingham.

Brown, S. P., Charalambous, D., Jones, E. C., Forgan, E. M., Kealey, P. G., Erb, A., and Kohlbrecher, J. (2004). *Triangular to Square Flux Lattice Phase Transition in $YBa_2Cu_3O_7$*. *Phys. Rev. Lett.*, 92:067004.

Campbell, L. J., Doria, M. M., and Kogan, V. G. (1988). *Vortex lattice structures in uniaxial superconductors*. *Phys. Rev. B*, 38:2439.

Capan, C., Bianchi, A., Movshovich, R., Christianson, A. D., Malinowski, A., Hundley, M. F., Lacerda, A., Pagliuso, P. G., and Sarrao, J. L. (2004). *Anisotropy of thermal conductivity and possible signature of the Fulde-Ferrell-Larkin-Ovchinnikov state in $CeCoIn_5$*. *Phys. Rev. B*, 70:134513.

Caroli, C., de Gennes, P. G., and Matricon, J. (1964). *BOUND FERMION STATES ON A VORTEX LINE IN A TYPE-II SUPERCONDUCTOR*. *Phys. Lett.*, 9:307.

Chandrasekhar, B. S. (1962). *A note on the maximum critical field of high field superconductors*. *Appl. Phys. Lett.*, 1:7.

Clem, J. R. (1975). *Simple Model for the Vortex Core in a Type-II Superconductor*. *J. Low Temp. Phys.*, 18:427.

Clogston, A. M. (1962). *Upper limit for the critical field in hard superconductors*. *Phys. Rev. Lett.*, 9:266.

Cooper, L. N. (1956). *Bound Electron Pairs in a Degenerate Fermi Gas*. *Phys. Rev.*, 104:1189.

Cubitt, R., Eskildsen, M. R., Dewhurst, C. D., Jun, J., Kazakov, S. M., and Karpinski, J. (2003). *Effects of Two-Band Superconductivity on the Flux-Line Lattice in Magnesium Diboride*. *Phys. Rev. Lett.*, 91:047002.

Cubitt, R., Forgan, E. M., Paul, D. M., Lee, S. L., Abell, J. S., Mook, H., and Timmins, P. A. (1992). *Neutron diffraction by the flux lattice in high-T_c superconductors*. *Physica B*, 180:377.

Cubitt, R., White, J. S., Laver, M., Eskildsen, M. R., Dewhurst, C. D., Paul, D. M., Crichton, A. J., Ellerby, M., Howard, C., Kurban, Z., and Norris, F. (2007). *Small-angle neutron scattering measurements of the vortex lattice in CaC_6*. *Phys. Rev. B*, 75:140516(R).

Daemen, L. L., Campbell, L. J., and Kogan, V. G. (1992). *Flux-line lattice in uniaxial superconductors at low magnetic inductions*. *Phys. Rev. B*, 46:3631.

Damascelli, A., Hussain, Z., and Shen, Z.-X. (2003). *Angle-resolved photoemission studies of the cuprate superconductors*. *Rev. Mod. Phys.*, 75:473.

de Gennes, P. G. (1989). *Superconductivity of Metals and Alloys*. Addison-Wesley, 2nd edition.

DeBeer-Schmitt, L., Dewhurst, C. D., Hoogenboom, B. W., Petrovic, C., and Eskildsen, M. R. (2006). *Field Dependent Coherence Length in the Superclean, High-κ Superconductor $CeCoIn_5$*. *Phys. Rev. Lett.*, 97:127001.

DeBeer-Schmitt, L., Eskildsen, M. R., Ichioka, M., Machida, K., Jenkins, N., Dewhurst, C. D., Abrahamsen, A. B., Bud'ko, S. L., and Canfield, P. C. (2007). *Pauli Paramagnetic Effects on Vortices in Superconducting $TmNi_2B_2C$*. *Phys. Rev. Lett.*, 99:167001.

Densmore, J. M., Das, P., Rovira, K., Blasius, T. D., DeBeer-Schmitt, L., Jenkins, N., Paul, D. M., Dewhurst, C. D., Bud'ko, S. L., Canfield, P. C., and Eskildsen, M. R. (2009). *Small-angle neutron scattering study of the vortex lattice in superconducting $LuNi_2B_2C$*. *Phys. Rev. B*, 79:174522.

Dewhurst, C. D., Levett, S. J., Cubitt, R., and Paul, D. M. (2006). *unpublished*.

Dolan, G. J., Chandrashekhar, G. V., Dinger, T. R., Feild, C., and Holtzberg, F. (1989a). *Vortex Structure in $YBa_2Cu_3O_7$ and Evidence for Intrinsic Pinning*. *Phys. Rev. Lett.*, 62:827.

Dolan, G. J., Holtzberg, F., Feild, C., and Dinger, T. R. (1989b). *Anisotropic vortex structure in $Y_1Ba_2Cu_3O_7$*. *Phys. Rev. Lett.*, 62:2184.

Eilenberger, G. (1968). *Transformation of Gorkov's Equation for Type-II Superconductors into Transport-Like Equations*. *Z. Phys.*, 214:195.

Elfimov, I. S., Sawatzky, G. A., and Damascelli, A. (2008). *Theory of Fermi-surface pockets and correlation effects in underdoped $YBa_2Cu_3O_{6.5}$*. *Phys. Rev. B*, 77:060504(R).

Elgazzar, S., Opahle, I., Hayn, R., and Oppeneer, P. M. (2004). *Calculated de Haas-van Alphen quantities of $CeMIn_5$ (M=Co, Rh, and Ir) compounds*. *Phys. Rev. B*, 69:214510.

Elhalel, G., Beck, R., Leibovitch, G., and Deutscher, G. (2007). *Transition from a Mixed to a Pure d-Wave Symmetry in Superconducting Optimally Doped $YBa_2Cu_3O_{7-x}$ Thin Films Under Applied Fields*. *Phys. Rev. Lett.*, 98:137002.

Erb, A., Manuel, A. A., Dhalle, M., Marti, F., Genoud, J. Y., Revaz, B., Junod, A., Vasumathi, D., Ishibashi, S., Shukla, A., Walker, E., Fischer, Ø., Flükiger, R., Pozzi, R., Mali, M., and Brinkmann, D. (1999). *Experimental evidence for fast cluster formation of chain oxygen vacancies in $YBa_2Cu_3O_{7-\delta}$ as the origin of the fishtail anomaly*. *Solid State Commun.*, 112:245.

Erb, A., Walker, E., and Flükiger, R. (1996). *The use of $BaZrO_3$ crucibles in crystal growth of the high-T_c superconductors Progress in crystal growth as well as in sample quality*. *Physica C*, 258:9.

Eskildsen, M. R. (1998). *Small Angle Neutron Scattering Studies of the Flux Line Lattices in the Borocarbide Superconductors*. PhD thesis, Risø National Laboratory.

Eskildsen, M. R., Dewhurst, C. D., Hoogenboom, B. W., Petrovic, C., and Canfield, P. C. (2003). *Hexagonal and Square Flux Line Lattices in $CeCoIn_5$*. *Phys. Rev. Lett.*, 90:187001.

Eskildsen, M. R., Gammel, P. L., Barber, B. P., Ramirez, A. P., Bishop, D. J., Andersen, N. H., Mortensen, K., Bolle, C. A., Lieber, C. M., and Canfield, P. C. (1997a). *Structural Stability of the Square Flux Line Lattice in YNi_2B_2C and $LuNi_2B_2C$ Studied with Small Angle Neutron Scattering*. *Phys. Rev. Lett.*, 79:487.

Eskildsen, M. R., Gammel, P. L., Barber, B. P., Yaron, U., Ramirez, A. P., Huse, D. A., Bishop, D. J., Bolle, C., Lieber, C. M., Oxx, S., Sridhar, S., Andersen, N. H., Mortensen, K., and Canfield, P. C. (1997b). *Observation of a Field-Driven Structural Phase Transition in the Flux Line Lattice in $ErNi_2B_2C$*. *Phys. Rev. Lett.*, 78:1968.

Eskildsen, M. R., Harada, K., Gammel, P. L., Abrahamsen, A. B., Andersen, N. H., Ernst, G., Ramirez, A. P., Bishop, D. J., Mortensen, K., Naugle, D. G., Rathnayaka, K. D. D., and Canfield, P. C. (1998). *Intertwined symmetry of the magnetic modulation and the flux-line lattice in the superconducting state of $TmNi_2B_2C$*. *Nature (London)*, 393:242.

Eskildsen, M. R., Vinnikov, L. Y., Blasius, T. D., Veshchunov, I. S., Artemova, T. M., Densmore, J. M., Dewhurst, C. D., Ni, N., Kreyssig, A., Bud'ko, S. L., Canfield,

P. C., and Goldman, A. I. (2009). *Vortices in superconducting Ba($Fe_{0.93}Co_{0.07}$)$_2As_2$ studied via small-angle neutron scattering and Bitter decoration*. *Phys. Rev. B*, 79:100501(R).

Fisk, Z., Hess, D. W., Pethick, C. J., Pines, D., Smith, J. L., Thompson, J. D., and Willis, J. O. (1988). *Heavy-Electron Metals: New Highly Correlated States of Matter*. *Science*, 239:33.

Forgan, E. M. and Lee, S. L. (1995). *Comment on "Vortex Lattice Symmetry and Electronic Structure in $YBa_2Cu_3O_7$"*. *Phys. Rev. Lett.*, 75:1422.

Forgan, E. M., Levett, S. J., Kealey, P. G., Cubitt, R., Dewhurst, C. D., and Fort, D. (2002). *Intrinsic Behavior of Flux Lines in Pure Niobium near the Upper Critical Field*. *Phys. Rev. Lett.*, 88:167003.

Forgan, E. M., Paul, D. M., Mook, H. A., Timmins, P. A., Keller, H., Sutton, S., and Abell, J. S. (1990). *Observation by neutron diffraction of the magnetic flux lattice in single-crystal $YBa_2Cu_3O_{7-\delta}$*. *Nature (London)*, 343:735.

Franz, M., Affleck, I., and Amin, M. H. S. (1997). *Theory of Equilibrium Flux Lattices in Unconventional Superconductors*. *Phys. Rev. Lett.*, 79:1555.

Franz, M., Kallin, C., Soininen, P. I., Berlinsky, A. J., and Fetter, A. L. (1996). *Vortex state in a d-wave superconductor*. *Phys. Rev. B*, 53:5795.

Franz, M. and Tešanović, Z. (1998). *Self-Consistent Electronic Structure of a $d_{x^2-y_2}$ and a $d_{x^2-y_2} + id_{xy}$ Vortex*. *Phys. Rev. Lett.*, 80:4763.

Fröhlich, H. (1950). *Theory of the Superconducting State. I. The Ground State at the Absolute Zero of Temperature*. *Phys. Rev.*, 79:845.

Fulde, P. and Ferrell, R. A. (1964). *Superconductivity in a Strong Spin-Exchange Field*. *Phys. Rev.*, 135:A550.

Gammel, P. L., Bishop, D. J., Dolan, G. J., Kwo, J. R., Murray, C. A., Schneemeyer, L. F., and Waszczak, J. V. (1987). *Observation of Hexagonally Correlated Flux Quanta In $YBa_2Cu_3O_7$*. *Phys. Rev. Lett.*, 59:2592.

Gegenwart, P., Langhammer, C., Geibel, C., Helfrich, R., Lang, M., Sparn, G., Steglich, F., Horn, R., Donnevert, L., Link, A., and Assmus, W. (1998). *Breakup of Heavy Fermions on the Brink of "Phase A" in $CeCu_2Si_2$*. *Phys. Rev. Lett.*, 81:1501.

Gilardi, R., Mesot, J., Drew, A., Divakar, U., Lee, S. L., Forgan, E. M., Zaharko, O., Conder, K., Aswal, V. K., Dewhurst, C. D., Cubitt, R., Momono, N., and Oda, M. (2002). *Direct Evidence for an Intrinsic Square Vortex Lattice in the Overdoped High-Tc Superconductor $La_{1.83}Sr_{0.17}CuO_{4+\delta}$*. *Phys. Rev. Lett.*, 88:217003.

Gor'kov, L. P. (1958). *On the energy spectrum of superconductors*. *Sov. Phys. JEPT*, 7:505.

Grévin, B., Berthier, Y., and Collin, G. (2000). *In-Plane Charge Modulation below T_c and Charge-Density-Wave Correlations in the Chain Layer in $YBa_2Cu_3O_7$*. *Phys. Rev. Lett.*, 85:1310.

Gruenberg, L. W. and Gunther, L. (1966). *Fulde-Ferrell Effect in Type-II Superconductors*. *Phys. Rev. Lett.*, 16:996.

Gurevich, A. and Kogan, V. G. (2001). *Effect of Fluctuations on Vortex Lattice Structural Transitions in Superconductors*. *Phys. Rev. Lett.*, 87:177009.

Hall, D., Palm, E. C., Murphy, T. P., Tozer, S. W., Fisk, Z., Alver, U., Goodrich, R. G., Sarrao, J. L., Pagliuso, P. G., and Ebihara, T. (2001). *Fermi surface of the heavy-fermion superconductor $CeCoIn_5$: The de Haasvan Alphen effect in the normal state*. *Phys. Rev. B*, 64:212508.

Hao, Z. and Clem, J. R. (1991). *Reversible magnetization and torques in anisotropic high-κ type-II superconductors*. *Phys. Rev. B*, 43:7622.

Hardy, W. N., Bonn, D. A., Morgan, D. C., Liang, R., and Zhang, K. (1993). *Precision measurements of the temperature dependence of λ in $YBa_2Cu_3O_{6.95}$: Strong evidence for nodes in the gap function*. *Phys. Rev. Lett.*, 70:3999.

Hiasa, N. and Ikeda, R. (2008). *Instability of Square Vortex Lattice in d-Wave Superconductors is due to Paramagnetic Depairing*. *Phys. Rev. Lett.*, 101:027001.

Hinkov, V., Pailhès, S., Bourges, P., Sidis, Y., Ivanov, A., Kulakov, A., Lin, C. T., Chen, D. P., Bernhard, C., and Keimer, B. (2004). *Two-dimensional geometry of spin excitations in the high-transition-temperature superconductor $YBa_2Cu_3O_{6+x}$*. *Nature (London)*, 430:650.

Hoffman, J. E., Hudson, E. W., Lang, K. M., Madhavan, V., Eisaki, H., Uchida, S., and Davis, J. C. (2002). *A Four Unit Cell Periodic Pattern of Quasi-Particle States Surrounding Vortex Cores in $Bi_2Sr_2CaCu_2O_{8+\delta}$*. *Science*, 295:466.

Hossain, M. A., Mottershead, J. D. F., Fournier, D., Bostwick, A., McChesney, J. L., Rotenberg, E., Liang, R., Hardy, W. N., Sawatzky, G. A., Elfimov, I. S., Bonn, D. A., and Damascelli, A. (2008). *In situ doping control of the surface of high-temperature superconductors*. *Nat. Phys.*, 4:527.

Huxley, A., Rodière, P., Paul, D. M., van Dijk, N., Cubitt, R., and Flouquet, J. (2000). *Realignment of the flux-line lattice by a change in the symmetry of superconductivity in UPt_3*. *Nature (London)*, 406:160.

Ichioka, M., Adachi, H., Mizushima, T., and Machida, K. (2007). *Vortex state in a Fulde-Ferrell-Larkin-Ovchinnikov superconductor based on quasiclassical theory*. *Phys. Rev. B*, 76:014503.

Ichioka, M., Hasegawa, A., and Machida, K. (1999). *Field dependence of the vortex structure in d-wave and s-wave superconductors*. *Phys. Rev. B*, 59:8902.

Ichioka, M., Hayashi, N., Enomoto, N., and Machida, K. (1996). *Vortex structure in d-wave superconductors*. *Phys. Rev. B*, 53:15316.

Ichioka, M. and Machida, K. (2007). *Vortex states in superconductors with strong Pauli-paramagnetic effect*. *Phys. Rev. B*, 76:064502.

Ichioka, M. and Machida, K. (2009). *private communication*.

Ikeda, S., Shishido, H., Nakashima, M., Settai, R., Aoki, D., Haga, Y., Harima, H., Aoki, Y., Namiki, T., Sato, H., and Onuki, Y. (2001). *Unconventional Superconductivity in CeCoIn5 Studied by the Specific Heat and Magnetization Measurements*. *J. Phys. Soc. Jpn.*, 70:2248.

Imry, Y. and Wortis, M. (1979). *Influence of quenched impurities on first-order phase transitions*. *Phys. Rev. B*, 19:3580.

Ito, T., Takagi, H., Ishibashi, S., Ido, T., and Uchida, S. (1991). *Normal-state conductivity between CuO_2 planes in copper oxide superconductors*. *Nature (London)*, 350:596.

Izawa, K., Yamaguchi, H., Mastuda, Y., Shishido, H., Settai, R., and Onuki, Y. (2001). *Angular Position of Nodes in the Superconducting Gap of Quasi-2D Heavy-Fermion Superconductor $CeCoIn_5$*. *Phys. Rev. Lett.*, 87:057002.

Johnson, S. T., Forgan, E. M., Lloyd, S. H., Aegerter, C. M., Lee, S. L., Cubitt, R., Kealey, P. G., Ager, C., Tajima, S., Rykov, A., and Paul, D. M. (1999). *Flux-Line Lattice Structures in Untwinned $YBa_2Cu_3O_{7-\delta}$*. *Phys. Rev. Lett.*, 82:2792.

Jorgensen, J. D., Veal, B. W., Paulikas, A. P., Nowicki, L. J., Crabtree, G. W., Claus, H., and Kwok, W. K. (1990). *Structural properties of oxygen-deficient $YBa_2Cu_3O_{7-\delta}$*. *Phys. Rev. B*, 41:1863.

Kakuyanagi, K., Saitoh, M., Kumagai, K., Takashima, S., Nohora, M., Takagi, H., and Matsuda, Y. (2005). *Texture in the Superconducting Order Parameter of $CeCoIn_5$ Revealed by Nuclear Magnetic Resonance*. *Phys. Rev. Lett.*, 94:047602.

Kasahara, Y., Nakajima, Y., Izawa, K., Matsuda, Y., Behnia, K., Shishido, H., Settai, R., and Onuki, Y. (2005). *Anomalous quasiparticle transport in the superconducting state of $CeCoIn_5$*. *Phys. Rev. B*, 72:214515.

Keimer, B., Doğan, F., Aksay, I. A., Erwin, R. W., Lynn, J. W., and Sarikaya, M. (1993). *Inclined-Field Structure, Morphology, and Pinning of the Vortex Lattice in Microtwinned $YBa_2Cu_3O_7$*. *Science*, 83:262.

Keimer, B., Shih, W. Y., Erwin, R. W., Lynn, J. W., Dogan, F., and Aksay, I. A. (1994). *Vortex Lattice Symmetry and Electronic Structure in $YBa_2Cu_3O_7$*. *Phys. Rev. Lett.*, 73:3459.

Kenzelmann, M., Strässle, T., Niedermayer, C., Sigrist, M., Padmanabhan, B., Zolliker, M., Bianchi, A. D., Movshovich, R., Bauer, E. D., Sarrao, J. L., and Thompson, J. D. (2008). *Coupled Superconducting and Magnetic Order in $CeCoIn_5$*. *Science*, 321:1652.

Ketterson, J. B. and Song, S. N. (1999). *Superconductivity*. Cambridge University Press, 1st edition.

Khasanov, R., Shengalaya, A., Karpinski, J., Bussmann-Holder, A., Keller, H., and Müller, K. A. (2008). *s-Wave Symmetry Along the c-Axis and s + d In-plane Superconductivity in Bulk $YBa_2Cu_4O_8$*. *J. Supercond. Nov. Magn.*, 21:81.

Khasanov, R., Strässle, S., Castro, D. D., Masui, T., Miyasaka, S., Tajima, S., Bussmann-Holder, A., and Keller, H. (2007). *Multiple Gap Symmetries for the Order Parameter of Cuprate Superconductors from Penetration Depth Measurements*. *Phys. Rev. Lett.*, 99:237601.

Kirtley, J. R., Tsuei, C. C., Ariando, Verwijs, C. J. M., Harkema, S., and Hilgenkamp, H. (2006). *Angle-resolved phase-sensitive determination of the in-plane gap symmetry in $YBa_2Cu_3O_{7-\delta}$*. *Nat. Phys.*, 2:190.

Kleiner, W. H., Roth, L. M., and Autler, S. H. (1964). *Bulk Solution of Ginzburg-Landau Equations for Type II Superconductors: Upper Critical Field Region*. *Phys. Rev.*, 133:A1226.

Kogan, V. G. (1981). *London approach to anisotropic type-II superconductors*. *Phys. Rev. B*, 24:1572.

Kogan, V. G., Bullock, M., Harmon, B., Miranović, P., Dobrosavljević-Grujić, L., Gammel, P. L., and Bishop, D. J. (1997a). *Vortex lattice transitions in borocarbides*. *Phys. Rev. B*, 55:R8693.

Kogan, V. G., Gurevich, A., Cho, J. H., Johnson, D. C., Xu, M., Thompson, J. R., and Martynovich, A. (1996). *Nonlocal electrodynamics and low-temperature magnetization of clean high-κ superconductors*. *Phys. Rev. B*, 54:12386.

Kogan, V. G., Miranović, P., Dobrosavljević-Grujić, L., Pickett, W. E., and Christen, D. K. (1997b). *Vortex Lattices in Cubic Superconductors*. *Phys. Rev. Lett.*, 79:741.

Kogan, V. G. and Zhelezina, N. V. (2005). *Field dependence of the vortex core size*. *Phys. Rev. B*, 71:134505.

Koitzsch, A., Opahle, I., Elgazzar, S., Borisenko, S. V., Geck, J., Zabolotnyy, V. B., Inosov, D., Shiozawa, H., Richter, M., Knupfer, M., Fink, J., Büchner, B., Bauer, E. D., Sarrao, J. L., and Follath, R. (2009). *Electronic structure of $CeCoIn_5$ from angle-resolved photoemission spectroscopy*. *Phys. Rev. B*, 79:075104.

Koutroulakis, G., Mitrović, V. F., Horvatić, M., Berthier, C., Lapertot, G., and Flouquet, J. (2008). *Field Dependence of the Ground State in the Exotic Superconductor CeCoIn$_5$: A Nuclear Magnetic Resonance Investigation*. *Phys. Rev. Lett.*, 101:047004.

Kramer, L. and Pesch, W. (1974). *Core structure and low-energy spectrum of isolated vortex lines in clean superconductors at $T << T_c$*. *Z. Phys.*, 269:59.

Kumagai, K., Saitoh, M., Oyaizu, T., Furukawa, Y., Takashima, S., Nohara, M., Takagi, H., and Matsuda, Y. (2006). *Fulde-Ferrell-Larkin-Ovchinnikov State in a Perpendicular Field of Quasi-Two-Dimensional CeCoIn$_5$*. *Phys. Rev. Lett.*, 97:227002.

Landau, I. L. and Keller, H. (2007). *On the interpretation of muon-spin-rotation experiments in the mixed state of type-II superconductors*. *Physica C*, 466:131.

Landau, L. D. (1957). *The theory of a Fermi liquid*. *Sov. Phys. JETP*, 3:920.

Larkin, A. I. and Ovchinnikov, Y. N. (1965). *Inhomogeneous State of Superconductors*. *Sov. Phys. JETP*, 20:762.

Laughlin, R. B. (1998). *Magnetic Induction of $d_{x^2-y^2} + id_{xy}$ Order in High- T_c Superconductors*. *Phys. Rev. Lett.*, 80:5188.

Laver, M. (2007). *A study of the flux line lattice in niobium by small angle neutron scattering*. PhD thesis, University of Birmingham.

Laver, M., Bowell, C. J., Forgan, E. M., Abrahamsen, A. B., Fort, D., Dewhurst, C. D., Mühlbauer, S., Christen, D. K., Kohlbrecher, J., Cubitt, R., and Ramos, S. (2009). *Structure and degeneracy of vortex lattice domains in pure superconducting niobium: A small-angle neutron scattering study*. *Phys. Rev. B*, 79:014518.

Laver, M., Forgan, E. M., Brown, S. P., Charalambous, D., Fort, D., Bowell, C., Ramos, S., Lycett, R. J., Christen, D. K., Kohlbrecher, J., Dewhurst, C. D., and Paul, D. M. (2006). *Spontaneous Symmetry-Breaking Vortex Lattice Transitions in Pure Niobium*. *Phys. Rev. Lett.*, 96:167002.

Leibovitch, G., Beck, R., Dagan, Y., Hacohen, S., and Deutscher, G. (2008). *Field-induced nodal order parameter in the tunneling spectrum of YBa$_2$Cu$_3$O$_{7-x}$ superconductor*. *Phys. Rev. B*, 77:094522.

Levett, S. J., Dewhurst, C. D., and Paul, D. M. (2002). *Vortex-lattice transitions in YNi$_2$B$_2$C: Nature of the 45-degree reorientation*. *Phys. Rev. B*, 66:014515.

Liang, R., Bonn, D. A., and Hardy, W. N. (2006). *Evaluation of CuO$_2$ plane hole doping in YBa$_2$Cu$_3$O$_{6+x}$ single crystals*. *Phys. Rev.B*, 73:180505.

Lin, C. T. and Kulakov, A. (2004). *In situ observation of ferroelastic detwinning of YBCO single crystals by high temperature optical microscopy*. *Physica C*, 408:27.

Lin, C. T., Zhou, W., Liang, W., Schönherr, E., and Bender, H. (1991). *Growth of large and untwinned single crystal of YBCO*. *Physica C*, 195:291.

London, F. and London, H. (1935). *The Electromagnetic Equations of the Supraconductor*. *Proc. Roy. Soc. (London)*, A149:71.

Maeda, H., Tanaka, Y., Fukutomi, M., and Asano, T. (1988). *A New High-T_c Oxide Superconductor without a Rare Earth Element*. *Jpn. J. Appl. Phys.*, 27:L209.

Maggio-Aprile, I., Renner, C., Erb, A., Walker, E., and Fischer, Ø. (1997). *Critical currents approaching the depairing limit at a twin boundary in $YBa_2Cu_3O_{7-\delta}$*. *Nature (London)*, 390:487.

Maisuradze, A., Khasanov, R., Shengalaya, A., and Keller, H. (2009). *Comparison of different methods for analyzing μSR line shapes in the vortex state of type-II superconductors*. *J. Phys.: Condens. Matter*, 21:075701.

Martin, C., Agosta, C. C., Tozer, S. W., Radovan, H. A., Palm, E. C., Murphy, T. P., and Sarrao, J. L. (2005). *Evidence for the Fulde-Ferrell-Larkin-Ovchinnikov state in $CeCoIn_5$ from penetration depth measurements*. *Phys. Rev. B*, 71:020503.

Matsuda, Y. and Shimahara, H. (2007). *FuldeFerrellLarkinOvchinnikov State in Heavy Fermion Superconductors*. *J. Phys. Soc. Jpn.*, 76:051005.

McCormack, R., de Fontaine, D., and Ceder, G. (1992). *Oxygen configurations and their effect on charge transfer in off-stoichiometric $YBa_2Cu_3O_z$*. *Phys. Rev. B*, 45:12976.

Meissner, W. and Ochsenfeld, R. (1933). *Ein neuer Effekt bei Eintritt der Supraleitfähigkeit*. *Naturwissenschaften*, 21:787.

Misra, P. (2008). *Heavy-Fermion Systems*. Elsevier, 1st edition.

Mitrović, V. F., Horvatić, M., Berthier, C., Knebel, G., Lapertot, G., and Flouquet, J. (2006). *Observation of Spin Susceptibility Enhancement in the Possible Fulde-Ferrell-Larkin-Ovchinnikov State of $CeCoIn_5$*. *Phys. Rev. Lett.*, 97:117002.

Mizushima, T., Machida, K., and Ichioka, M. (2005). *Topological Structure of a Vortex in the Fulde-Ferrell-Larkin-Ovchinnikov State*. *Phys. Rev. Lett.*, 95:117003.

Mook, H. A., Dai, P., Dogan, F., and Hunt, R. D. (2000). *One-dimensional nature of the magnetic fluctuations in $YBa_2Cu_3O_{6.6}$*. *Nature (London)*, 404:729.

Movshovich, R., Jaime, M., Thompson, J. D., Petrovic, C., Fisk, Z., Pagliuso, P. G., and Sarrao, J. L. (2001). *Unconventional Superconductivity in $CeIrIn_5$ and $CeCoIn_5$: Specific Heat and Thermal Conductivity Studies*. *Phys. Rev. Lett.*, 86:5152.

Mühlschlegel, B. (1959). *Die thermodynamischen Funktionen des Supraleiters*. *Z. Phys.*, 155:313.

Nakai, N., Miranovć, P., Ichioka, M., and Machida, K. (2002). *Reentrant Vortex Lattice Transformation in Fourfold Symmetric Superconductors*. *Phys. Rev. Lett.*, 89:237004.

Neutron News, . (1992). *Neutron Scattering Lengths and Cross Sections of the Elements and Their Isotopes*. *Neutron News*, 3:29.

Ngai, J. H., Atkinson, W. A., and Wei, J. Y. T. (2007). *Tunneling Spectroscopy of c-Axis $Y_{1-x}Ca_xBa_2Cu_3O_{7-\delta}$ Thin-Film Superconductors*. *Phys. Rev. Lett.*, 98:177003.

O'Donovan, C. and Carbotte, J. P. (1997). *Effects of interlayer interaction on the superconducting state in $YBa_2Cu_3O_{7-\delta}$*. *Phys. Rev. B*, 55:1200.

Onnes, H. K. (1911). *The Superconductivity of Mercury*. *Comm. Phys. Lab. Univ. Leiden*, Nos. 122 and 124.

Orenstein, J. and Millis, A. J. (2000). *Advances in the Physics of High-Temperature Superconductivity*. *Science*, 288:468.

Ormeno, R. J., Sibley, A., Gough, C. E., Sebastian, S., and Fisher, I. R. (2002). *Microwave Conductivity and Penetration Depth in the Heavy Fermion Superconductor $CeCoIn_5$*. *Phys. Rev. Lett.*, 88:047005.

Özcan, S., Broun, D. M., Morgan, B., Haselwimmer, R. K. W., Sarrao, J. L., Kamal, S., Bidinosti, C. P., Turner, P. J., Raudsepp, M., and Waldram, J. R. (2003). *London penetration depth measurements of the heavy-fermion superconductor $CeCoIn_5$ near a magnetic quantum critical point*. *Europhys. Lett.*, 62:412.

Paglione, J., Tanatar, M. A., Hawthorn, D. G., Boaknin, E., Hill, R. W., Ronning, F., Sutherland, M., Taillefer, L., Petrovic, C., and Canfield, P. C. (2003). *Field-Induced Quantum Critical Point in $CeCoIn_5$*. *Phys. Rev. Lett.*, 91:246405.

Paul, D. M., Tomy, C. V., Aegerter, C. M., Cubitt, R., Lloyd, S. H., Forgan, E. M., Lee, S. L., and Yethiraj, M. (1998). *Nonlocal Effects and Vortex Lattice Transitions in YNi_2B_2C*. *Phys. Rev. Lett.*, 80:1517.

Pedersen, J. S., Posselt, D., and Mortensen, K. (1990). *Analytical treatment of the resolution function for small-angle scattering*. *J. Appl. Cryst.*, 23:321.

Petrovic, C., Movshovich, R., Jaime, M., Pagliuso, P., Hundley, M., Sarrao, J. L., Fisk, Z., and Thompson, J. D. (2001a). *A new heavy-fermion superconductor $CeIrIn_5$: A relative of the cuprates?* *Europhys. Lett.*, 53:354.

Petrovic, C., Pagliuso, P. G., Hundley, M. F., Movshovich, R., Sarrao, J. L., Thompson, J. D., Fisk, Z., and Monthoux, P. (2001b). *Heavy-fermion superconductivity in $CeCoIn_5$ at 2.3 K*. *J. Phys.: Condens. Matter*, 13:L337.

Pickett, W. E., Cohen, R. E., and Krakauer, H. (1990). *Precise band structure and Fermi-surface calculation for $YBa_2Cu_3O_7$: Importance of three-dimensional disperion*. *Phys. Rev. B*, 42:8764(R).

Pippard, A. B. (1953). *An Experimental and Theoretical Study of the Relation between Magnetic Field and Current in a Superconductor*. *Proc. Roy. Soc. (London)*, A216:547.

Renner, C. and Fischer, O. . (1995). *Vacuum tunneling spectroscopy and asymmetric density of states of $Bi_2Sr_2CaCu_2O_{8+\delta}$*. *Phys. Rev. B*, 51:9208.

Ronning, F., Capan, C., Bauer, E. D., Thompson, J. D., Sarrao, J. L., and Movshovich, R. (2006). *Pressure study of quantum criticality in $CeCoIn_5$*. *Phys. Rev. B*, 73:064519.

Roulin, M., Junod, A., Erb, A., and Walker, E. (1998). *Calorimetric Transitions on the Melting Line of the Vortex System as a Function of Oxygen Deficiency in High-Purity $YBa_2Cu_3O_x$*. *Phys. Rev. Lett.*, 80:1722.

Saint-James, D., Sarma, G., and Thomas, E. J. (1969). *Type II superconductivity*. Pergamon Press, 1st edition.

Schabel, M. C., Park, C. H., Matsura, A., Shen, Z. X., Bonn, D. A., Liang, R., and Hardy, W. N. (1998). *Angle-resolved photoemission on untwinned $YBa_2Cu_3O_{6.95}$. II. Determination of Fermi surfaces*. *Phys. Rev. B*, 57:6107.

Schiff, L. I. (1968). *Quantum Mechanics*. McGraw-Hill, 3rd edition.

Sekitani, T., Miura, N., Ikeda, S., Matsuda, Y. H., and Shiohara, Y. (2004). *Upper critical field for optimally-doped $YBa_2Cu_3O_{7-\delta}$*. *Physica B*, 346:319.

Settai, R., Shishido, H., Ikeda, S., Murakawa, Y., Nakashima, M., Aoki, D., Haga, Y., Harima, H., and Onuki, Y. (2001). *Quasi-two-dimensional Fermi surfaces and the de Haasvan Alphen oscillation in both the normal and superconducting mixed states of $CeCoIn_5$*. *J. Phys.: Condens. Matter*, 13:L627.

Settai, R., Takeuchi, T., and Onuki, Y. (2007). *Recent Advances in Ce-Based Heavy-Fermion Superconductivity and Fermi Surface Properties*. *J. Phys. Soc. Jpn.*, 76:051003.

Seyfarth, G., Brison, J. P., Knebel, G., Aoki, D., Lapertot, G., and Flouquet, J. (2008). *Multigap Superconductivity in the Heavy-Fermion System $CeCoIn_5$*. *Phys. Rev. Lett.*, 101:046401.

Sheng, Z. Z. and Hermann, A. M. (1988). *Bulk superconductivity at 120 K in the Tl-Ca/Ba-Cu-O System*. *Nature (London)*, 332:138.

Shibata, K., Maki, M., Nishizaki, T., and Kobayashi, N. (2003). *Scanning tunneling spectroscopy studies on vortices in $YBa_2Cu_3O_y$ single crystals*. *Physica C*, 392:323.

Shiraishi, J., Kohmoto, M., and Maki, K. (1999). *Vortex lattice transition in d-wave superconductors*. *Phys. Rev. B*, 59:4497.

Simon, C., Pautrat, A., Poullain, G., Goupil, C., Leblond-Harnois, C., Chaud, X., and Brûlet, A. (2004). *Influence of twin boundaries on the flux-line-lattice structure in $YBa_2Cu_3O_{7-\delta}$: A small-angle neutron scattering*. *Phys. Rev. B*, 70:024502.

Smilde, H. J. H., Golubov, A. A., Ariando, Rijnders, G., Dekkers, J. M., Harkema, S., Blank, D. H. A., Rogalla, H., and Hilgenkamp, H. (2005). *Admixtures to d-Wave Gap Symmetry in Untwinned $YBa_2Cu_3O_7$ Superconducting Films Measured by Angle-Resolved Electron Tunneling*. *Phys. Rev. Lett.*, 95:257001.

Soininen, P. I., Kallin, C., and Berlinsky, A. J. (1994). *Structure of a vortex line in a $d_{x^2-y^2}$ superconductor*. *Phys. Rev. B*, 50:13883.

Sonier, J. E., Brewer, J. H., Kiefl, R. F., Morris, G. D., Miller, R. I., Bonn, D. A., Chakhalian, J., Heffner, R. H., Hardy, W. N., and Liang, R. (1999). *Field Induced Reduction of the Low-Temperature Superfluid Density in $YBa_2Cu_3O_{6.95}$*. *Phys. Rev. Lett.*, 83:4156.

Sonier, J. E., Kiefl, R. F., Brewer, J. H., Bonn, D. A., Carolan, J. F., Chow, K. H., Dosanjh, P., Hardy, W. N., Liang, R., MacFarlane, W. A., Mendels, P., Morris, G. D., Riseman, T. M., and Schneider, J. W. (1994). *New muon-spin-rotation measurement of the temperature dependence of the magnetic penetration depth in $YBa_2Cu_3O_{6.95}$*. *Phys. Rev. Lett.*, 72:744.

Squires, G. L. (1996). *Introduction to the Theory of Thermal Neutron Scattering*. Dover, 1st edition.

Steglich, F., Aarts, J., Bredl, C. D., Lieke, W., Meschede, D., Franz, W., and Schäfer, H. (1979). *Superconductivity in the Presence of Strong Pauli Paramagnetism: $CeCu_2Si_2$*. *Phys. Rev. Lett.*, 43:1892.

Sun, A. G., Han, S. H., Katz, A. S., Gajewski, D. A., Maple, M. B., and Dynes, R. C. (1995). *Anisotropy of the penetration depth in $YBa_2Cu_3O_{7-\delta}$: Josephson-tunneling studies*. *Phys. Rev. B*, 52:R15731.

Tachiki, M., Takahashi, S., Gegenwart, P., Weiden, M., Lang, M., Geibel, C., Steglich, F., Modler, R., Paulsen, C., and Onuki, Y. (1996). *Generalized Fulde-Ferrell-Larkin-Ovchinnikov state in heavy-fermion and intermediate-valence systems*. *Z. Phys. B*, 100:369.

Tallon, J. L., Bernhard, C., Binninger, U., Hofer, A., Williams, G. V. M., Ansaldo, E. J., Budnick, J. I., and Niedermayer, C. (1995). *In-Plane Anisotropy of the Penetration Depth Due to Superconductivity on the Cu-O Chains in $YBa_2Cu_3O_{7-\delta}$, $Y_2Ba_4Cu_7O_{15-\delta}$, and $YBa_2Cu_4O_8$*. *Phys. Rev. Lett.*, 74:1008.

Tayama, T., Harita, A., Sakakibara, T., Haga, Y., Shishido, H., Settai, R., and Onuki, Y. (2002). *Unconventional heavy-fermion superconductor $CeCoIn_5$: dc magnetization study at temperatures down to 50 mK*. *Phys. Rev. B*, 65:180504.

Thiemann, S. L., Radović, Z., and Kogan, V. G. (1989). *Field structure of vortex lattices in uniaxial superconductors*. *Phys. Rev. B*, 39:11406.

Tinkham, M. (1996). *Introduction to Superconductivity*. Dover, 2nd edition.

Tranquada, J. M., Cox, D. E., Kunnmann, W., Moudden, H., Shirane, G., Suenaga, M., Zolliker, P., Vaknin, D., Sinha, S. K., Alvarez, M. S., Jacobson, A. J., and Johnston, D. C. (1988). *Neutron-Diffraction Determination of Antiferromagnetic Structure of Cu Ions in $YBa_2Cu_3O_{6+x}$ with x=0.0 and 0.15*. *Phys. Rev. Lett.*, 60:156.

Tranquada, J. M., Sternlieb, B. J., Axe, J. D., Nakamura, Y., and Uchida, S. (1995). *Evidence for stripe correlations of spins and holes in copper oxide superconductors*. *Nature (London)*, 375:561.

Tsuei, C. C. and Kirtley, J. R. (2000). *Pairing symmetry in cuprate superconductors*. *Rev. Mod. Phys.*, 72:969.

Veal, B. W. and Paulikas, A. P. (1991). *Dependence of hole concentration on oxygen vacancy order in $YBa_2Cu_3O_{7-\delta}$: A chemical valence model*. *Physica C*, 184:321.

Vorontsov, A. and Vekhter, I. (2006). *Nodal Structure of Quasi-Two-Dimensional Superconductors Probed by a Magnetic Field*. *Phys. Rev. Lett.*, 96:237001.

Walker, M. B. and Timusk, T. (1995). *Interpretation of the oblique Abrikosov flux lattice in $YBa_2Cu_3O_7$*. *Phys. Rev. B*, 52:97.

Watanabe, T., Fujii, T., and Matsuda, A. (1997). *Anisotropic Resistivities of Precisely Oxygen Controlled Single-Crystal $Bi_2Sr_2CaCu_2O_{8+\delta}$: Systematic Study on "Spin Gap" Effect*. *Phys. Rev. Lett.*, 79:2113.

White, J. S., Brown, S. P., Forgan, E. M., Laver, M., Bowell, C. J., Lycett, R. J., Charalambous, D., Hinkov, V., Erb, A., and Kohlbrecher, J. (2008). *Observations of the configuration of the high-field vortex lattice in $YBa_2Cu_3O_7$: Dependence upon temperature and angle of applied field*. *Phys. Rev. B*, 78:174513.

Wu, M. K., Ashburn, J. R., Torng, C. J., Hor, P. H., Meng, R. L., Gao, L., Huang, Z. J., Wang, Y. Q., and Chu, C. W. (1987). *Superconductivity at 93 K in a new mixed-phase Y-Ba-Cu-O compound system at ambient pressure*. *Phys. Rev. Lett.*, 58:908.

Xiang, T. and Wheatley, J. M. (1996). *Superfluid Anisotropy in YBCO: Evidence for Pair Tunneling Superconductivity*. *Phys. Rev. Lett.*, 76:134.

Xu, J.-H., Ren, Y., and Ting, C.-S. (1996). *Structures of single vortex and vortex lattice in a d-wave superconductor*. *Phys. Rev. B*, 53:R2991.

Yaouanc, A. J., Dalmas de Réotier, P., and Brandt, E. H. (1997). *Effect of the vortex core on the magnetic field in hard superconductors*. *Phys. Rev. B*, 55:11107.

Yethiraj, M., Christen, D. K., Paul, D. M., Miranovic, P., and Thompson, J. R. (1999). *Flux Lattice Symmetry in V_3Si: Nonlocal Effects in a High-κ Superconductor*. *Phys. Rev. Lett.*, 82:5112.

Yethiraj, M., Mook, H. A., Wignall, G. D., Cubitt, R., Forgan, E. M., Lee, S. L., Paul, D. M., and Armstrong, T. (1993a). *Anisotropic vortex lattice in $YBa_2Cu_3O_7$*. *Phys. Rev. Lett.*, 71:3019.

Yethiraj, M., Mook, H. A., Wignall, G. D., Cubitt, R., Forgan, E. M., Paul, D. M., and Armstrong, T. (1993b). *Small-angle neutron scattering study of flux line lattices in twinned $YBa_2Cu_3O_7$*. *Phys. Rev. Lett.*, 70:857.

Young, B.-L., Urbano, R. R., Curro, N. J., Thompson, J. D., Sarrao, J. L., Vorontsov, A. B., and Graf, M. J. (2007). *Microscopic Evidence for Field-Induced Magnetism in $CeCoIn_5$*. *Phys. Rev. Lett.*, 98:036402.

Zaanen, J. and Gunnarsson, O. (1989). *Charged magnetic domain lines and the magnetism of high-T_c oxides*. *Phys. Rev. B*, 40:7391.

Zabolotnyy, V. B., Borisenko, S. V., Kordyuk, A. A., Geck, J., Inosov, D. S., Koitzsch, A., Fink, J., Knupfer, M., Büchner, B., Drechsler, S. L., Berger, H., Erb, A., Lambacher, M., Patthey, L., Hinkov, V., and Keimer, B. (2007). *Momentum and temperature dependence of renormalization effects in the high-temperature superconductor $YBa_2Cu_3O_{7-\delta}$*. *Phys. Rev. B*, 76:064519.

Zhang, F. C. and Rice, T. M. (1988). *Effective Hamiltonian for the superconducting Cu oxides*. *Phys. Rev. B*, 37:3759.

Zhang, K., Bonn, D. A., Kamal, S., Liang, R., Baar, D. J., Hardy, W. N., Basov, D., and Timusk, T. (1994). *Measurement of the ab Plane Anisotropy of Microwave Surface Impedance of Untwinned $YBa_2Cu_3O_{6.95}$ Single Crystals*. *Phys. Rev. Lett.*, 73:2484.